Structural trends in off-stoichiometric kesterite type compound $Cu_2ZnSnSe_4$ semiconductor

Dissertation zur Erlangung des akademischen Grades
Doktor der Naturwissenschaften
(Dr. rer. nat.)

vorgelegt von

Laura Elisa Valle Rios

Eingereicht am Fachbereich Geowissenschaften

der Freien Universität Berlin

Angefertigt am Helmholtz-Zentrum Berlin für Materialen und Energie
Abteilung Struktur und Dynamik von Energiematerialien und im Rahmen der
Graduiertenschule „Materials for Solar Energy Conversion“

Die Arbeit ist in englischer Sprache verfasst

Berlin, September 2016

Erstgutachter:	Prof. Dr. Susan Schorr
Zweitgutachter:	PD Dr. Ralf Milke

Tag der Disputation: 05.12.2016

Abstract

Quaternary $Cu_2ZnSnSe_4$ is a promising low cost alternative absorber material for thin film solar cells. The current record conversion efficiency of 12.6% [1] for a $Cu_2ZnSn(S,Se)_4$ based thin film solar cell was reached when the polycrystalline CZTSSe absorber layer exhibits an off-stoichiometric composition. Deviations from stoichiometry in the absorber layer causes intrinsic point defects (vacancies, anti-site, interstitials) [2, 3] which determine significantly the electronic properties of the semiconductor, and in the efficiency of the solar cell device. Unfortunately, the current number of reported literature on intrinsic point defects of kesterites is very limited and mainly theoretical work.

This work focuses on the synthesis and characterization of off-stoichiometric CZTSe. In order to perform experimental analysis of defect types and concentrations, polycrystalline powder samples have been synthesized by solid state reaction within different off-stoichiometric compositions suggested by [4, 5]. Chemical and structural characterization by WDX spectroscopy and XRD has been performed. The main results show, that all synthesized samples present kesterite type CZTSe with an off-stoichiometric composition as the main phase. Moreover, the formation of single phase off-stoichiometric kesterite type CZTSe has been observed.

Further structural analyses by neutron powder diffraction experiments were carried out. As main outcome the cation distribution were determined, from which the intrinsic cation point defects and their concentrations have been evaluated. The occurrence of the corresponding off-stoichiometry type specific point defects could be proven. The results show, that it is possible to deduce the occurring point defect types from the chemical composition (cation ratios) of the kesterite phase. Additionally, the Cu-Zn disorder, which causes Zn_{Cu} and Cu_{Zn} anti site defects, has been determined within all off-stoichiometric CZTSe phases.

Zusammenfassung

Quaternäre $Cu_2ZnSnSe_4$-Verbindungen (CZTSe) sind eine vielversprechende, kostengünstige Alternative als Absorberschichtmaterial in Dünnschichtsolarzellen. Der gegenwärtige Rekordwirkungsgrad von 12.6% [1] für eine $Cu_2ZnSn(S,Se)_4$-basierte Dünnschichtsolarzelle wurde für polykristalline Absorberschichten erreicht, die eine nicht-stöchiometrische Zusammensetzung aufweisen. Abweichungen von der Stöchiometrie führen zu intrinsischen Punktdefekten (Leerstellen, Substitionen, Zwischengitteratome) [2, 3], welche erheblich die elektronischen Eigenschaften und somit den Wirkungsgrad von Solarzellen bestimmen. Allerdings ist die Anzahl an Veröffentlichungen hinsichtlich intrinsischer Punktdefekte in Kesteriten sehr begrenzt und hauptsächlich theoretischer Natur.

Diese Arbeit richtet sich auf die Synthese und Charakterisierung von nicht-stöchiometrischem CZTSe. Um experimentelle Analysen von Defekttypen und -konzentrationen durchzuführen, wurden polykristalline Pulverproben innerhalb der von [4, 5] vorgeschlagenen nicht-stöchiometrischen Zusammensetzungen mittels Festkörperreaktion synthetisiert. Chemische sowie strukturelle Charakterisierung durch WDX-Spektroskopie und XRD ist durchgeführt worden. Die wichtigsten Ergebnisse zeigen, dass sämtliche synthetisierten Proben Kesterit-Typ CZTSe als Hauptphase mit einer nicht-stöchiometrischen Zusammensetzung aufzeigen. Darüber hinaus konnte die Bildung von einphasigen, nicht-stöchiometrischen Kesterit-Typ CZTSe beobachtet werden. Weitere, auf Pulver-Neutronenbeugungsexperimenten basierende, strukturelle Analysen wurden einbezogen. Als wichtigstes Ergebnis wurde die Kationenverteilung bestimmt, mit welcher die intrinsischen Punktdefekte sowie deren Konzentrationen ausgewertet worden sind. Das Auftreten korrespondierender, nicht-stöchiometrischer Typ-spezifischer Punktdefekte konnte nachgewiesen werden. Die Ergebnisse zeigen, dass es möglich ist, die auftretenden Punktdefekte von der chemischen Zusammensetzung (Kationenverhältnisse) der Kesteritphase abzuleiten. Zusätzlich ist die Cu-Zn-Unordnung, welche Zn_{Cu}- und Cu_{Zn}-Fehlstellen hervorruft, in allen nicht-stöchiometrischen CZTSe-Phasen bestimmt worden.

Table of Contents

Tables list

Figures list

Abbreviations list

CZTSe	$Cu_2ZnSnSe_4$
Cu	copper
Zn	zinc
Sn	tin
Se	selenium
Z	atomic number
WDX	wavelength dispersive X-ray spectroscopy
BSE	back-scattered electron
XRD	X-ray powder diffraction
SEM	scanning electron microscope
θ	theta diffracted angle
λ	wavelength
fm	femtometers (10^{-15} meters)
T.O.F	neutron time of flight
V_{Cu}	copper vacancy defect
Cu_i	copper interstitial defect
Zn_{Cu}	zinc on copper antisite defect
Cu_{Zn}	copper on zinc antisite defect
Zn_{Sn}	zinc on tin antisite defect
occ	site occupation factors
b	neutron scattering length
$\overline{b}^{exp}$	experimental average neutron scattering length
$\overline{b}^{calc}$	calculated average neutron scattering length
eV	electro volt
Eg	band gap
PN	*p* and *n* type semiconductors junction
MIT	Metal–insulator transitions

Motivation

During the last century, the energy demand has exponentially increased along with human population. Currently the main energy supply is based on fossil fuels, which is a limited resource. Additionally, combustion of fuel causes negative environment impacts such as global warming due to the exhaust of carbon dioxide (CO_2). Therefore, moving toward renewable energy and lower CO_2 emission is required.

Solar energy is an unlimited energy source and a CO_2 free emissions alternative. One of its main applications is by photovoltaics (PV) technology which converts solar energy into direct current electricity. Currently, silicon based PV-modules are the most commercialized devices; however, silicon involves high cost in producing high-quality pure Si. Additionally, silicon has also some physical disadvantages such as its indirect band gap which exhibits a low absorption coefficient resulting in the need of a thicker absorber layer (100-300 µm). Therefore, in order to reduce the production cost and optimize the solar cells performances, alternative solar cell technologies so called thin film solar cells are being developed.

Thin film solar cells are known as the second generation of hetero-junction solar cells; which use materials with higher absorption coefficient to reduce the thickness of the absorber layer up to 1-5 µm. Up to now, the most common thin absorber layers are based on chalcogenide semiconductor materials such as cadmium telluride (CdTe) and copper indium gallium diselenide $Cu(In,Ga)Se_2$ solar cell devices based on such compounds have reached energy conversion efficiencies above 20% [6]. Nevertheless, these thin film technologies present some inconveniences due to the toxicity of cadmium and the need of scarce elements in the earth crust such as indium and gallium.

Low cost alternative materials for thin film solar cells being investigated are the kesterite type compounds $Cu_2ZnSn(S,Se)_4$ (CZTS,Se). Kesterite based solar cells present similar properties and work function with the existing technology based on chalcopyrite type compounds Cu(In,Ga)Se_2 (CIGS). Kesterite and chalcopyrite type compound have related crystal structures but kesterite compounds replaced the need of indium and gallium by nontoxic and earth abundant elements such as zinc and tin. CZTSSe kesterite type semiconductors CZTSSe present suitable physical properties for photovoltaic applications such as: *p*-type semiconductor behavior, direct band-gap between 1.0-1.5 eV and high absorption coefficient $>10^4$ cm^{-1}. The current record conversion efficiency of 12.6% [1] for a $Cu_2ZnSn(S,Se)_4$ based thin film solar cell was reached when the polycrystalline CZTSSe absorber layer exhibits an off-stoichiometric composition. The role of off-stoichiometry in the absorber layer has been already studied on chalcopyrite type compounds and it is known that deviations from stoichiometry cause intrinsic point defects (vacancies, anti-site, interstitials) [2, 3] which determine significantly the electronic properties of the semiconductor, which mean they play a crucial role in the efficiency of the solar cell device. Unfortunately, the current number of reported literature on intrinsic point defects of kesterites is very limited and mainly theoretical work.

This work is focused on selenide kesterite compounds $Cu_2ZnSnSe_4$. In order to perform experimental analysis of defect types and concentrations, polycrystalline powder samples have been synthesized by solid state reaction with different intended off-stoichiometric compositions. The samples have been chemically and structurally characterized. As a main outcome, different types and concentrations of intrinsic point defects and the Cu-Zn disorder defect have been determined within all the off-stoichiometry CZTSe samples.

This work is highly appreciated within the kesterite based solar cells research community. Knowledge of occurrences of secondary phases, concentrations of intrinsic point defects and structure parameters like the tetragonal deformation are important to understand the role of off-stoichiometry composition within the kesterite absorber layer.

1. Introduction

1.1 Crystal structure of I_2-II-IV-VI_4 compounds

I_2-II-IV-VI_4 quaternary compounds accordingly to literature [7, 8], might crystallize in kesterite-type structure, stannite-type structure (both belong to the tetragonal crystal system), wurtzite-kesterite-type structure (monoclinic) or wurtzite-stannite-type structure (orthorhombic).

Wurtz-stannite and wurtz-kesterite-type structures derived from the wurzite-type crystal structure in a similar way as the kesterite and stannite-type structures are derived from the sphalerite-type structure. Doubling the unit cell of the wurtzite-type structure as sphalerite type structure respectively in the direction of the crystallographic *c* axis and introducing three different cations in an ordered way. The majority of the reported wurtz-stannite-type structures can be predicted as an orthorhombic superstructure of the wurtzite-type structure with unit cell dimension $a_{or} \sim 2a_w$, $b_{or} \sim \sqrt{3}a_w$ and $c_{or} \sim c_w$ (subscripts *or* and *w* represent orthorhombic and wurtzite respectively) [8].

Theoretical studies from *S.Chen et al.* [7] reported calculations for two fundamental structures with 16-atom primitive unit cell: the wurtzite-kesterite and wurtzite-stannite structures, which correspond to the zinc-blende ZB-derived kesterite and stannite structure, respectively. *S.Chen* first-principles total energy calculations shown that the energy stability between the zinc-blende ZB- and wurtzite WZ-derived structures exhibits a clear dependence on the cation size difference and the ionicity of the I_2-II-IV-VI_4 compounds. Generally speaking, quaternary semiconductors with small and strongly ionic elements such as Ag_2ZnGeS_4 prefer crystallize in the wurtzite-kesterite type structure or Cu_2CdSiS_4 compounds prefer the wurtzite-stannite structures. Moreover, those calculations [7] reported the total energy (meV/atom) of $Cu_2ZnSnSe_4$ compound in different crystal structures types. The results are listed in Table 1; where the asterisk indicates the ground-state (T=0 K), thus kesterite-type structure is the ground state structure in $Cu_2ZnSnSe_4$ compounds. The energy for wurtz-kesterite and wurtz stannite is too high; therefore, the formation of those structures in $Cu_2ZnSnSe_4$ compounds is highly unexpected.

Table 1 *Total energy (meV/atom) of CZTSe in different crystal structures relative to the kesterite structure. The asterisk indicate the ground-state structure at T=0 K [7].*

$Cu_2ZnSnSe_4$	meV/atom
Kesterite	0.0*
Stannite	3.3
Wurtz-kesterite	8.0
Wurtz- stannite	9.6

Theoretically, the energy difference between kesterite and stannite type structure is very small. Experimentally the kesterite structure could be confused with stannite structure due to both structures are closely related; their symmetry differs by different distribution of cation resulting in different space groups: kesterite $I\bar{4}$ and stannite $I\bar{4}2m$ (Figure *1*).

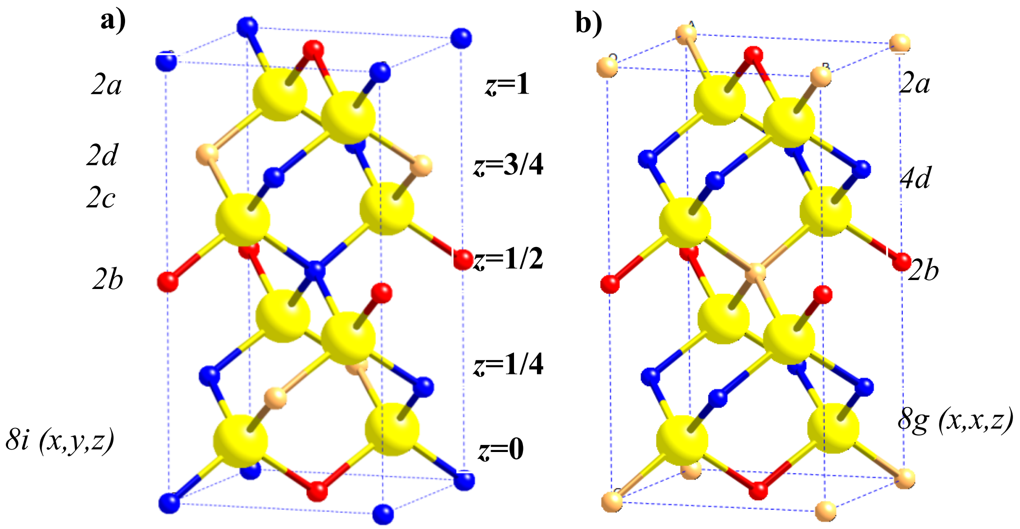

Figure 1 a) *Kesterite-type-structure space group* $\boldsymbol{I\bar{4}}$ *and* ***b)*** *stannite-type-structure space structure group* $\boldsymbol{I\bar{4}2m}$*. Cation distribution Cu-blue, Zn-orange, Sn-red and yellow big spheres represent the Se anions. The corresponding Wyckoff positions and lattice planes are given.*

The kesterite structure is characterized by alternating cation layers of CuSn, CuZn, CuSn and CuZn at z=0,1/4,1/2 and 3/4, respectively. Thus one copper occupies the $2a$ (0,0,0) position with zinc and the remaining copper ordered at $2c$ (0,1/2,1/4) and $2d$ (0,1/2,3/4) resulting in the space group $I\bar{4}$. The stannite-type structure space group ($I\bar{4}2m$) ZnSn layer alternate with Cu_2 layers, with the divalent cation located at the origin ($2a$) and the monovalent cation at the $4d$ position (0,1/2,1/4). In both structures Sn is located at the same $2b$ (0,0,1/2) structural site [9].

Another structural difference between kesterite and stannite-type structure, is the anion position. In the stannite structure the anion lies on the (110) mirror plane on a (*x,x,z*) position. In the kesterite structure the anion occupies a (*x,y,z*) position. Therefore, the mirror symmetry vanishes in the kesterite structure, however, the anion position difference between x and y is very small. Also the cations Zn^{2+} and Cu^{+} have a same number of electrons, so it is almost impossible to distinguish with high accuracy between the kesterite and stannite structures from X-ray powder diffraction data. A proper determination must be done by neutron powder diffraction along with Rietveld analysis. Such experiments have proved that stoichiometric $Cu_2ZnSnSe_4$ as well as Cu_2ZnSnS_4 crystallize in the kesterite type structure [9], but on the other hand, Cu_2FeSnS_4 have been reported to crystallizes in the stannite structure [10].

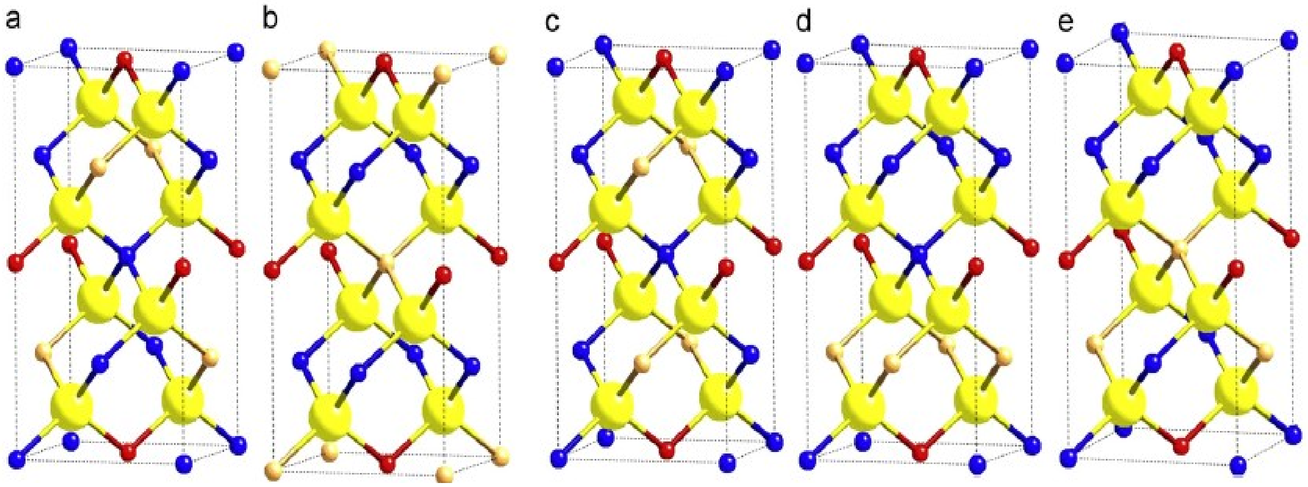

Figure 2 a) *Kesterite space group* $\boldsymbol{I\bar{4}}$, ***b)*** *stannite space group* $\boldsymbol{I\bar{4}2m}$ *;* ***c),d)*** *and* ***e)*** *the three different structural modifications with space groups:* $\boldsymbol{P\bar{4}2c}$, $\boldsymbol{P\bar{4}2_1m}$ *and* $\boldsymbol{P2}$, *respectively. Colours; Copper-blue, Zinc-orange, Tin-red and yellow big spheres represent the anions Se [Schorr, S. Sol. Energ. Mat. Sol (2011)95(6): 1482-1488].*

In addition to the stannite-type structure and kesterite-type structure, different polytypes based on a tetragonal unit cell have been suggested in literature [9, 11]. Those structural modifications belong to the tetragonal space group: $P\overline{4}2c,\ P\overline{4}2_1m$ and $P2$. The symmetry difference is related only to the order of the cations; nevertheless, the modifications are restricted to the exchange of two ions on the cation sublattice see Figure *2*.

Symmetry differences between those suggested polytypes are:

- Space group$P\overline{4}2c$; the Cu and Zn atoms in the layer *z*=1/4 are exchanged, creating a "stacking" fault with respect to the based-centered-tetragonal kesterite.
- Space group $P\overline{4}2_1m$; Cu and Zn atoms are exchanged between two layers to yield complete Zn and Cu layers at z=1/4 and z=3/4.
- Space group $P2$; a Cu atom at z=1/2 is exchanged with the Zn atom at z=3/4. This recovers the stannite structure at the layers z=1/2 and z=3/4, but maintains the kesterite structure in the others two layers.

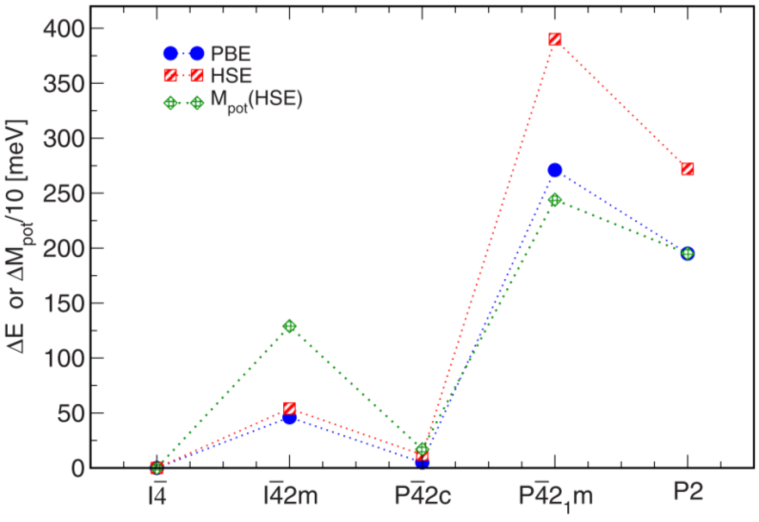

Figure 3 *Total energy differences obtained using theoretical calculations, where the energy zero refers to (the most stable) kesterite structure [Paier, J., et al., Physical Review B, (2009). 79(11): p. 115126].*

In literature [11, 12] those polytype modifications were introduced by first-principles calculations based on the density functional theory (PBE) and hybrid functional (HSE). It has been found that the total energy for such modifications is always larger than the energy required for the kesterite type structure. From Figure 3, it can be observed that the total energy for $P\bar{4}2_1m$ and $P2$ modifications are the highest (~200-400 meV), followed by the stannite structure (~50 meV). Remarkably the $P\bar{4}2c$ modification is very close in energy to kesterite $I\bar{4}$ structure. As mentioned above, in space group $P\bar{4}2c$, the Cu and Zn atoms are exchanged in z=1/4 plane [11]. Those theoretical calculations are in a good agreement with experimental literature from *S. Schorr* [9] where an intermixing of Cu and Zn was observed in the Cu-Zn layers within stoichiometric CZTS and CZTSe.

In summary, theoretical calculations support that the kesterite-type structure is the most stable structure for CZTSSe; however an intermixing within Cu and Zn layer is highly expected because its costs only very little energy. Such intermixing is known as “Cu-Zn disorder defect” where Cu_{Zn} and Zn_{Cu} antisite defects are formed. Nevertheless, this disorder is limited to the 2c and 2d Wyckoff position in the planes z=1/4 and z=3/4 and the other copper occupied the 2a Wyckoff position. So, if the small difference between the anion position (*x,x,z*) for stannite and (*x,y,z*) for kesterite would be disregarded; the disordered kesterite may be described in the space group $I\bar{4}2m$ with a statistical distribution of copper and zinc on the 4d Wyckoff position. However, in the disordered kesterite the 2a Wyckoff position is occupied by copper instead of zinc, therefore, is not correct to attribute this intermixing cation distribution to the stannite-type structure [8] [9].

1.2 $Cu_2ZnSnSe_4$ compound in photovoltaic applications

Currently most of thin-film solar cells being developed are based on the chalcogenide polycrystalline absorber materials cadmium telluride (CdTe) or copper indium gallium diselenide (CIGS). Both technologies have already reached energy conversion efficiencies above 20%. Nevertheless, their costs are one of the main drawbacks of those technologies due to constraints imposed by mineral scarcity. Figure 4(a) shows the earth’s crust abundance and costs of some of the most relevant elements for thin-film photovoltaics. As observed, the price of gallium and indium are significantly high, followed by cadmium and tellurium. Furthermore the annual production of indium and gallium is remarkably lower compared to other elements (see Figure 4b) [13]. Therefore, the use of other materials beside CIGS is needed.

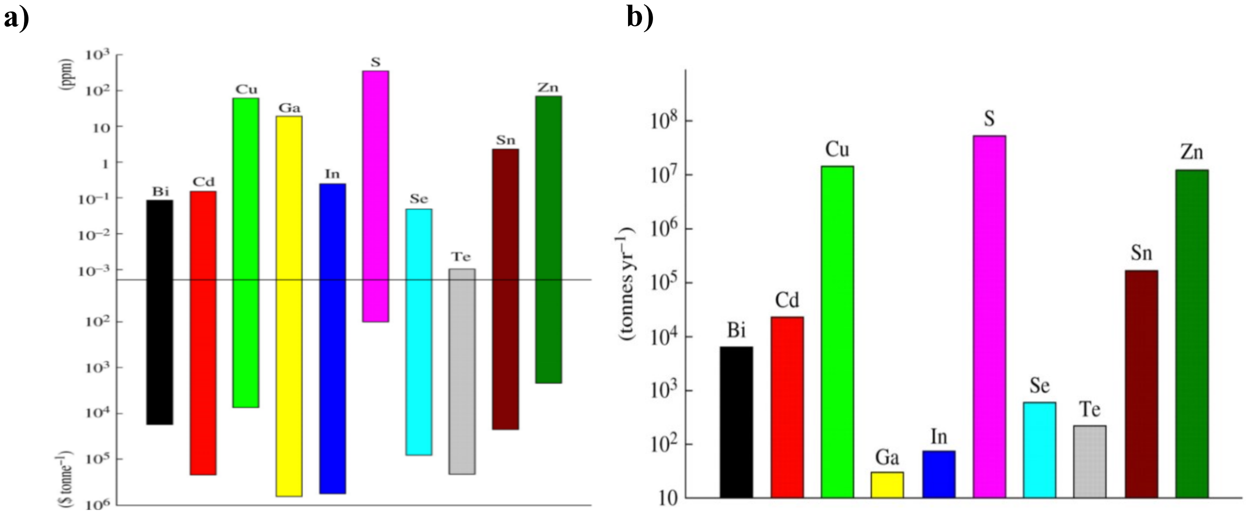

Figure 4 a) *Occurrence in the Earth's crust and current costs of some of the elements relevant to thin-film photovoltaics****.*** ***b)*** *Annual production of some of the elements relevant for photovoltaics [Peter, L. M. Phil. Trans.R.Soc. A (2011)369, 1840-1856].*

In addition, the foreseen of CdTe is quite pessimistic, because tellurium is one of the rarest elements in the Earth's crust, moreover, cadmium is a toxic heavy metal (10 times more toxic than lead or mercury), thus in Europe cadmium has been listed by the European Union's restriction on hazardous substances (RoHs). This directive bans certain hazardous substances in electrical and electronic equipment [14].

For those reasons, there is a clear need to expand the range of materials used in thin film solar cell toward lower costs, abundant and non-toxic elements. One promising alternative material is kesterite type compound $Cu_2ZnSnSe_4$ (CZTSe); consists of nontoxic, low cost and earth's crust abundant metals: copper, zinc and tin which replace the need of indium and gallium. On the other hand, non-metal selenium is chemically related to sulfur and tellurium. CZTSe based solar cells have reached energy conversion efficiency up to 11.6% [15] and CZTS based solar cells up to 9.2% efficiency [16]. Therefore, solar cells based on kesterite compounds are attractive for further investigation and development.

Quaternary $Cu_2ZnSnSe_4$ (CZTSe) compound present a semiconductor behavior which is crucial for its application in solar cells devices. In general, the electronic properties of semiconductors materials can be explained in terms of the energy distribution of their density of states. The primary features of an energy diagram for a crystalline semiconductor are: the valence band (E_v - occupied state), the conduction band (E_c - unoccupied state) and the energy band gap (E_g). The band gap is the minimum energy difference between the highest occupied state in the valence band and the lowest unoccupied state in the conduction band. The E_g value of a semiconductor is crucial to determine its functionality in an electronic device. However, when the E_g is significantly large (>9eV) the material behave then like an insulator. Figure 5a, shows a simplified schema of a semiconductor energy diagram because the valence and conduction bands are actually composed of a finite number of very closely spaced electron energy levels.

In particular, for kesterite type $Cu_2ZnSnSe_4$ (CZTSe) semiconductor compounds, a direct band gap with a value about ~1 eV (see Figure 5b) has been reported [17, 18]. Direct band gap feature is an advantage compared with silicon based absorbers for solar cells. In a direct band gap the top of the E_v and the bottom of the E_c occur at the same value of crystal momentum; this feature enhanced light absorption allowing the use of thinner absorber layers (1-5 μm thick).

In general semiconductors are poor conductors because a current requires the flow of electrons, and semiconductors have their valence band filled, preventing the entry flow of electrons. But conductivity can be enhanced by adding doping impurities (extrinsically) or by intrinsic doping (intrinsically), because doping causes an unbalanced number of electrons which allow a current to flow through the material; impurities can be either donor or acceptor. For instance, a deficit in the number of valence electrons in the material introduces electron-accepting levels just above the top of the valance band, and causes more holes to be introduced into the valence band. So, the majority charge carriers are positive holes (and electrons are the minority carriers), therefore called *p*-type semiconductor, opposite to *n*-type semiconductors, where electrons are the majority carriers due to excess of electrons which may be easily excited from the donor level into the conduction band. In *p*-type semiconductors, the Fermi level lies closer to the valence band than the conduction band. The doping behavior in kesterite $Cu_2ZnSnSe_4$ has been reported to be controlled by intrinsic doping [19].

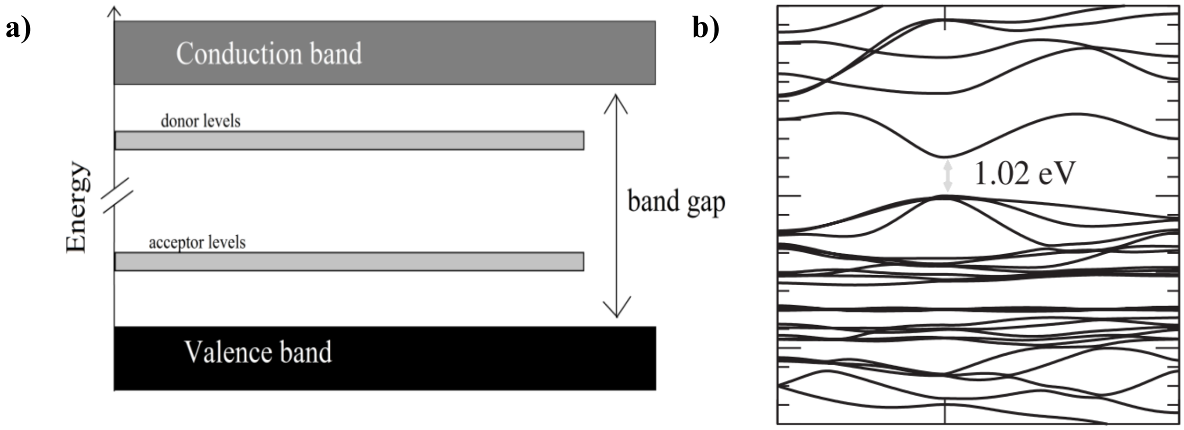

Figure 5 a) *Energy diagram of a semiconductor material* ***b)*** *direct band gap semiconductor of kesterite CZTSe [Botti et al. Appl. Phys. Lett. (2011) 98(24)]*

When light shines upon a semiconductor with a photon energy higher than its band gap energy ($h\nu > E_g$) the photon's energy is given to an electron in the crystal lattice. This electron is covalent bonded with neighboring atoms in the valence band, but when this electron absorbs the energy given by the photon, it is exited into the conduction band where it is free to move. The network of covalent bonds where the electron was previously a part of now has one fewer electron or so called "hole". Consequently, absorption of light (photons) by a suitable band gap semiconductor generates electro-hole pairs (charge carriers) free to move within the material. This light absorption effect that generates an electric potential (or voltage) in a material due to the separation of charges is the principle behind the photovoltaic effect [20], therefore, semiconducting materials that exhibit the photovoltaic effect are used to produce photovoltaics (PV) technology. A typical PV module consists of several connected solar cells which produce direct current (DC) electricity from sun light.

Mostly of the current thin film solar cells based on CZTSe absorbers, are built from *p*-type and *n*-type semiconductors, so called PN hetero-junction configuration (see Figure 6a). The *n*-type layer which has an excess of electrons is deposited above the *p*-type layer (excess of holes). The *n*-type layer is usually kept thin to allow light to pass through to the PN junction. The region where electrons and holes diffuse across the PN junction is called the depletion region where electrons move towards the *n*-type layer and the holes move towards the *p*-type layer. When illuminating the solar cell creating free carriers, the free electron and hole has sufficient energy to jump out of the depletion zone. If a wire is connected from the cathode (*n*-type) to the anode (*p*-type); electrons flow though the wire. Electrons are attracted to the positive charge and travels through the external load creating a flow of electric current. The holes are attracted to the negative charge and migrate to the back electrical contact.

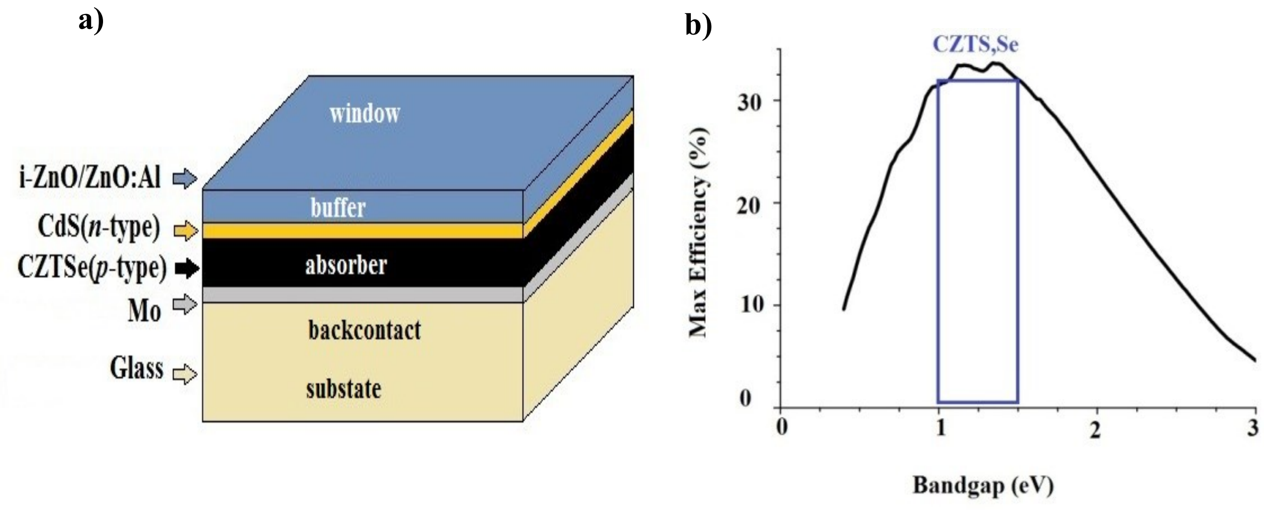

Figure 6 a) *Schema of a kesterite thin film solar cell based on p-type and n-type semiconductors configuration, so called PN junction* ***b)*** *Shockley-Queisser theoretical efficiency for CZTS,Se absorbers materials .*

The thermodynamic efficiency limit for solar energy conversion is known as the Shockley-Queisser limit [21], who calculated this limit as a function of the band gap from semiconductors used in a single PN junction solar cell. Shockley-Queisser calculations consider standard Earth's atmosphere air mass conditions AM 1.5, resulting in a maximum efficiency approximately of 30% for single solar cells with band gaps range of 1.2-1.4 eV. Solar cells based on kesterite semiconductor compounds (CZTS,Se) present a near optimum band gap between 1-1.5 eV (see Figure 6b), which supposed to be ideal for effective photo absorption, in fact, a high absorption coefficient has been reported for CZTSe materials ($>10^4$ cm^{-1}) [22].

In general, the quaternary compound semiconductor $Cu_2ZnSnSe_4$ (CZTSe) is a promising low cost alternative material for photovoltaic applications because it replaced the need of expensive elements (In,Ga) for non-toxic and earth's abundant Zn and Sn. CZTSe fulfills suitable criteria for absorber layer in thin film solar cells such as: *p*-type intrinsic semiconductor behavior, direct band gap ~ 1 eV and high absorption coefficient [23].

Theoretically kesterite based solar cells could reach efficiencies up to 30%. However, despite all its potential physical properties, the current record energy conversion efficiency experimentally achieved for kesterite based thin solar cells is 12.6%. This record have been reached with a polycrystalline CZTSSe absorber with copper-poor / zinc-rich off-stoichiometric composition [1]. In general, kesterite based solar cells are produced either by chemical or physical growth routes. All devices exhibit the best performance when the absorber layer exhibit an off-stoichiometric composition. Nevertheless, there are plenty of factors that influence the performance of solar cells e.g.: chemical composition, growth conditions, deposition process, grain size, grain boundaries, interface recombination, energy band alignments (spike/cliff like), secondary phases, etc. Therefore, a fundamental study of the absorber layer material regardless of complications presented in a solar cell is of great importance.

1.3 The role of intrinsic point defects

The kesterite structure (space group $I\overline{4}$) derives from the tetragonal chalcopyrite structure (space group $I\overline{4}2d$); hence kesterite structure inherits certain electronic characteristics. The doping of chalcopyrite CIGS semiconductors materials is controlled by variations of stoichiometry. CIGS semiconductors are doped by intrinsic defect rather than extrinsic impurities. Theoretical calculations *Chen et al.* [2] have reported that the defect complex of $2V_{Cu}$+In_{Cu} ($CuInSe_2$) and $2V_{Cu}$+Ga_{Cu} ($CuGaSe_2$) have the lowest energy of formations, which is in good agreement with experimental data presented by *C. Stephan* [24] where a remarkable tolerance of the chalcopyrite structure by the presence of high concentrations of defects complexes $2V_{Cu}$+In_{Cu} were found. This is one of the reasons why CIGS solar cells achieved high efficiencies (current record 22.3% [6]). Although a similar electronic behavior is predicted for kesterites, its situation is more complex because kesterite is a quaternary compound. Thus there are more possible point defects compared with binary or ternary compounds.

Unfortunately, the current experimental data available on intrinsic point defects in kesterites are very limited. The majority of publications are theoretical studies based on first-principles approach, for instance [2, 25-31]. The density functional theory (DFT) approach has been applied to calculate the defect formation energies depending on composition and on the Fermi level. DFT approach might has limitations predicting defects levels [18, 32]. However, general trends can be extracted out of the defect formation energies which can be considered correct [23]. All publications agree that Cu_{Zn} antisite is the defect with the lowest energy of formation, therefore, is the most probable acceptor defect which could explain that CZTS and CZTSe have experimentally shown *p*-type conductivity.

Cu_{Zn} antisite and copper vacancy V_{Cu} have a relatively deeper acceptor level, in comparison with the Cu vacancy in ternary chalcopyrite. In general, donor defects have higher formation energies than acceptors, leading to difficult *n*-type doping; thus there are no reports on *n*-type kesterite compounds.

Referring to *Chen et al* [2] where defect formations energies of expected point defects of $Cu_2ZnSnSe_4$ have been calculated. Those results are shown in Figure 7. The Fermi energy shifts from the valance to the conduction band; thus formation energy of the negatively charged acceptor defects such as Cu_{Zn}, V_{Cu} and Zn_{Sn} decreases, opposite to the formation energy of positively charged donors such as Zn_{Cu}, Cu_i and Sn_{Zn} which increases as the Fermi energy moves toward the conduction band. Accordingly, due to its lowest energy of formation, it can be assumed that Cu_{Zn} or V_{Cu} with compensation from the Zn_{Cu} make discrete energy levels appear allowing the *p*-type character. Moreover, those predicted low energy defects (Cu_{Zn} and Zn_{Cu}) could explain the Cu-Zn disorder experimentally observed on the 2*c* site and 2*d* crystallographic sites within stoichiometric kesterites CZTS and CZTSe [9].

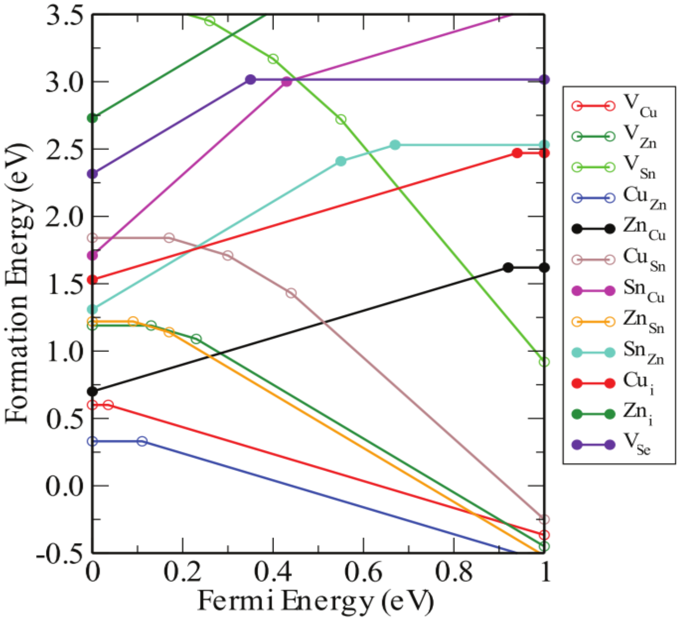

***Figure** 7 Change of the defect formation energy as a function of Fermi energy [Chen et al. Adv. Mater. (2013), 25, 1522-1539].*

Nevertheless, those theoretical calculations are based on single phase CZTSe with a stoichiometric composition. By co-existences of secondary phases or off-stoichiometric compositions; the formation energies and population of different defects can be changed dramatically, so the dominant defect such as Cu_{Zn} could be a different one. Further analysis of off-stoichiometry composition, formation of secondary phases, defect types and concentrations is crucial to understand their possible effect on kesterite based solar cells performances.

1.4 Phase stability and expected secondary phases

Moving from ternary chalcopyrite compounds into quaternary kesterite compounds increase the complexity associated with the multi-component system. For example, a higher probability of secondary phases. Ternary phase diagrams are useful because they give information concerning the kesterite phase and secondary phases, at certain temperature and composition.

The phase equilibria in the Cu_2Se-ZnSe-$SnSe_2$ system has been reported by *Dudchak et al.* [33] Figure 8 shows the isothermal section of the quasi-ternary Cu_2Se-ZnSe-$SnSe_2$ system at 670 K consists of the homogeneity ranges of the α-,β-,γ-, and δ'-solid solutions of Cu_2Se, ZnSe, $SnSe_2$ and the low-temperature modification of the quaternary $Cu_2ZnSnSe_4$. Cu_2Se solubility is lower than 2 mol. % and is elongated along the Cu_2Se-$SnSe_2$ boundary side, in ZnSe and $SnSe_2$ it is lower than 1 mol. % and in Cu_2SnSe_3 lower than 0.5 mol. %. The $Cu_2ZnSnSe_4$ phase was found to be 3 mol. % along the triangulated section Cu_2SnSe_3-ZnSe [33].

According to this phase diagram (Figure 8), kesterite phase has a narrow region where it can be present without secondary phases. In fact, its stability region is narrower in comparison with chalcopyrites. Due to the multiple constituents in the Cu-Zn-Sn-Se system and the possibility of multiple metal oxidation states, the occurrence of a large number of secondary phases (binary as well as ternary) are easy to co-exist with the kesterite phase. Consequently, the synthesis of high quality devices without any adverse effect of secondary phases is highly difficult.

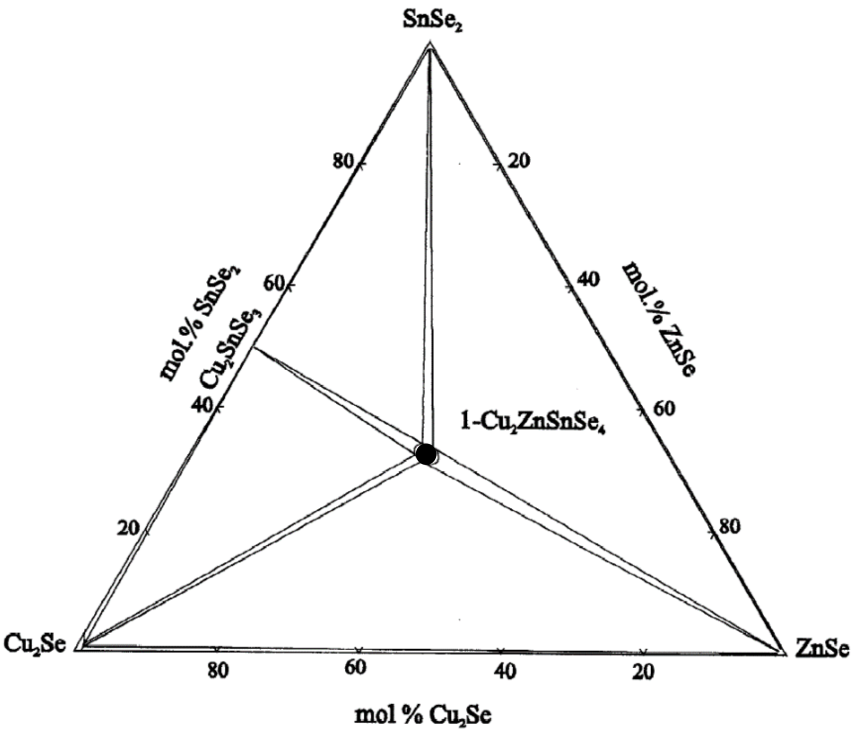

Figure 8 *Isothermal section of the* Cu_2Se*-ZnSe-*$SnSe_2$ *system at 670 K [Dudchak et al. J. Alloys Compd. (2003) 351:145-150].*

The most common secondary phases in the Cu-Zn-Sn-Se system are listed in Table 2 with their respective band gap values [34]. Secondary phases are considered harmful to the solar cell device performance depending on their position in the film as well as on their electro-optical properties.

For instance, secondary phases with high band gap might increase series resistance in the device when situated at the back contact. They also could act as barrier to the charge carriers when situated at the PN junction. Low band gap materials at the PN junction are usually responsible for a decrease in open-circuit voltage (V_{oc}) when shunt the device. It is therefore important to detect and identify the presence of the secondary phases in order to improve the solar cell device performance.

Table 2 *The most common secondary phases in the Cu-Zn-Sn-Se system [34, 35]*

Compound	Band gap (eV)
Cu_2SnSe_3	0.8
ZnSe	2.7
$SnSe_2$	1.0-1.6
SnSe	1.3
Cu_2Se	1.2
CuSe	2.03

1.5 Off-stoichiometry – cation substitutions

Off-stoichiometric compositions play an important role in the semiconductor materials used in thin film solar cells devices. Deviations from the stoichiometric composition lead the formation of point defects such as: vacancies, anti-sites, and/or interstitials [2, 3]. Defects in semiconductors materials act like intrinsic doping because create discrete energy levels within the band gap (donor or acceptors) which directly affect the generation, separation and recombination of electron-hole pairs. Therefore, off-stoichiometry and intrinsic defects have a significant influence in the opto-electronic properties of semiconductors. However mostly of available literature in kesterite defects are theoretical studies, thus the need to prove the formation of such defects experimentally is crucial to breakthrough understanding the fundamental property of the material and optimizing the growth processes of the absorber layer.

An experimental study on the flexibility of the kesterite structure and its ability to deviate from stoichiometry was introduced by *A. Lafond et al*. [4]. Following cation substitutions observed in CIGS compounds and taking into account charge balance in CZTS materials; *A. Lafond* proposed four different cation substitution reactions and intrinsic point defect complex formations.

Two substitution processes in the copper poor region so called: A-type Cu-poor/Zn-rich where copper is substituted forming a copper vacancy (V_{Cu}) and zinc on copper antisite (Zn_{Cu}) and B-type Cu-poor/Zn-rich where copper and tin are substituted by zinc forming zinc on copper (Zn_{Cu}) and zinc on tin (Zn_{Sn}) defects. The remaining two cation substitution processes in the copper rich region are: C-type Cu-rich/Zn-poor where zinc is substituted by copper and tin to form copper on zinc (Cu_{Zn}) and tin on zinc (Sn_{Zn}) antisite defects and last the D-type Cu-rich/Zn-poor where copper substitute zinc forming copper on zinc antisite (Cu_{Zn}) with extra copper interstitial (Cu_i). See in Table 3 summarized the cation substitution reactions and the intrinsic point defects derived from this reaction. A complementary illustration is presented in Figure 9.

Table 3 *Off-stoichiometric cation substation reactions, intrinsic point defects and formula for A,B,C,D-type [4] and E,F-type [5].*

type	Composition	Cation substitution reaction	Intrinsic point defects	Formula
A	Cu-poor/Zn-rich/Sn-const.	$2\ Cu^+ \rightarrow Zn^{2+}$	$V_{Cu} + Zn^{2+}_{Cu}$	$Cu_{2-2x}Zn_{1+x}SnSe_4$
B	Cu-poor/Zn-rich/Sn-poor	$2\ Cu^+ + Sn^{4+} \rightarrow 3Zn^{2+}$	$2\ Zn^{2+}_{Cu} + Zn^{2+}_{Sn}$	$Cu_{2-2y}Zn_{1+3y}Sn_{1-y}Se_4$
C	Cu-rich/Zn-poor/Sn-rich	$3\ Zn^{2+} \rightarrow 2\ Cu^+ + Sn^{4+}$	$2\ Cu^+_{Zn} + Sn^{4+}_{Zn}$	$Cu_{2+2z}Zn_{1-3z}Sn_{1+z}Se_4$
D	Cu-rich/Zn-poor/Sn-const.	$Zn^{2+} \rightarrow 2Cu^+$	$Cu^+_{Zn} + Cu^+_i$	$Cu_{2+2m}Zn_{1-m}SnSe_4$
E	Cu-poor/Zn-poor/Sn-rich	$2Cu^+ + Zn^{2+} \rightarrow Sn^{4+}$	$2V_{Cu}+Sn^{4+}_{Zn}$ $Sn^{4+}_{Cu}+V_{Cu}+V_{Zn}$	$Cu_{2-2w}Zn_{1-w}Sn_{1+w}Se_4$
F	Cu-rich/Zn-rich/Sn-poor	$Sn^{4+} \rightarrow Zn^{2+} + 2Cu^+$	$Zn^{2+}_{Sn} + 2Cu^+_i$ or $Cu^+_{Sn} + Cu^+_i + Zn^{2+}_i$	$Cu_{2(2-k)}Zn_{2-k}Sn_kSe_4$

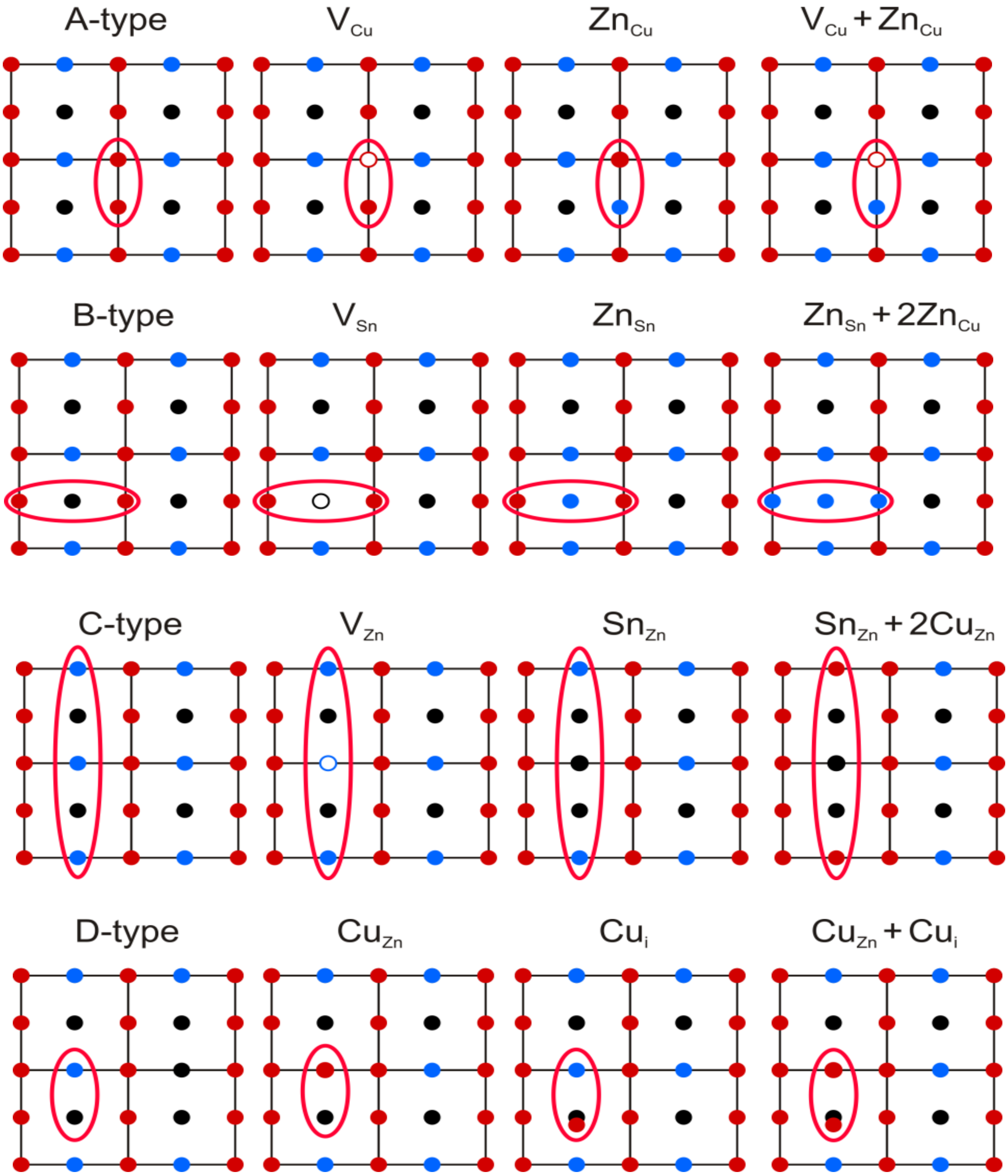

Figure 9 *Illustration of the cation substation process corresponding to the A,B,C and D-types. Colors represent: copper-red; zinc-blue, tin-black [Valle-Rios et al. J. Alloys Compd (2016)657: 408-413].*

Additionally, two more reactions have been introduced by *Valle-Rios et al.* [5] assuming the cation substitution reaction: $Sn^{4+} \rightarrow Zn^{2+} + 2Cu^{+}$ with a copper and zinc rich and tin poor composition leads to the defect complex $Zn_{Sn} + 2Cu_i$ or $Cu_{Sn} + Cu_i + Zn_i$, respectively. This reaction called F-type has a general formula $Cu_{2(2-k)}Zn_{2-k}Sn_kSe_4$. Moreover, a copper and zinc poor and tin rich composition lead to a reaction of $2Cu^{+} + Zn^{2+} \rightarrow Sn^{+4}$ with defect complex $2V_{Cu}+Sn^{4+}_{Zn}$ or $Sn^{4+}_{Cu}+V_{Cu}+V_{Zn}$ which correspond to E-type with a general formula $Cu_{2-2w}Zn_{1-w}Sn_{1+w}Se_{4}$.

The chemical formulae in Table 3 resulted from each cation susbtition can be used to plot the off-stoichiometry type lines in the Cu_2Se-$ZnSe$-$SnSe_2$ system as shown in Figure 10a. Nonetheless a better overview of a quaternary compound like kesterite is given with a cation ratios plot Cu/(Zn+Sn) vs Zn/Sn (see Figure 10b). When the cation ratios are ≠ 1, then they are considered as off-stoichiometric.

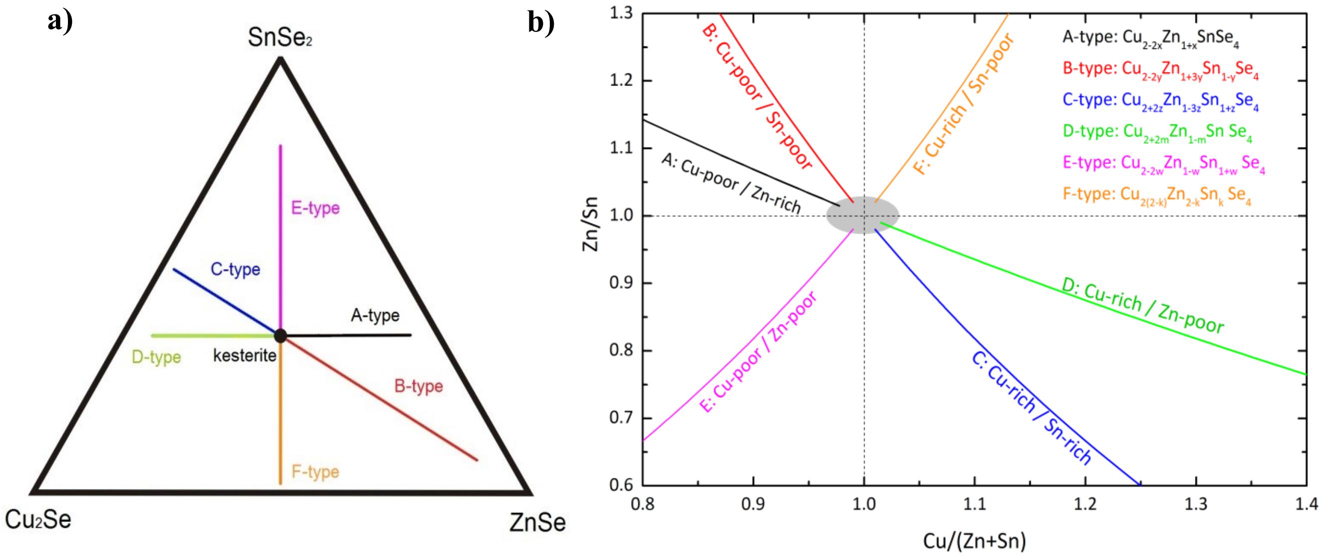

Figure 10 a) *Off-stoichiometry type lines in the pseudo-ternary Cu_2Se-$ZnSe$-$SnSe_2$ diagram,* ***b)*** *off-stoichiometry type lines in the cation ratios Cu/(Zn+Sn) vs Zn/Sn.*

2.Experimental: Materials and methods

2.1 Powder samples synthesis by solid state reaction

Synthesis starts from the pure (99.999%) elements Cu, Zn, Sn and Se. All elements are precisely weighed according the intended composition by following chemical formulae introduced in Table 3. Afterwards all the elements are placed in a pyrolytic graphite boat, the loaded boats laid inside silica tubes which are evacuated to 10^{-5} mbar vacuum and sealed with H_2/O_2 flame.

The solid state reaction took place below the material melting point; in the case of CZTSe compounds its melting point is at 790°C [36, 37]. The sealed ampoules are placed inside a one zone tubular furnace which are heated (10°C/h rate) up to 750°C; in order to avoid explosion of the tubes, several intermediate temperature steps (250°C,450°C and 600°C) were introduced in between. After the first step, reacted material are ground in an agate mortar and pressed into pellet for further annealing, the pellets are placed again into an evacuated silica tube. For the second reaction step the samples were heated up (50°C/h rate) to the final temperature of 750°C. Synthesis steps and reaction temperatures are summarized in Table 4 and illustrated in Figure *11*.

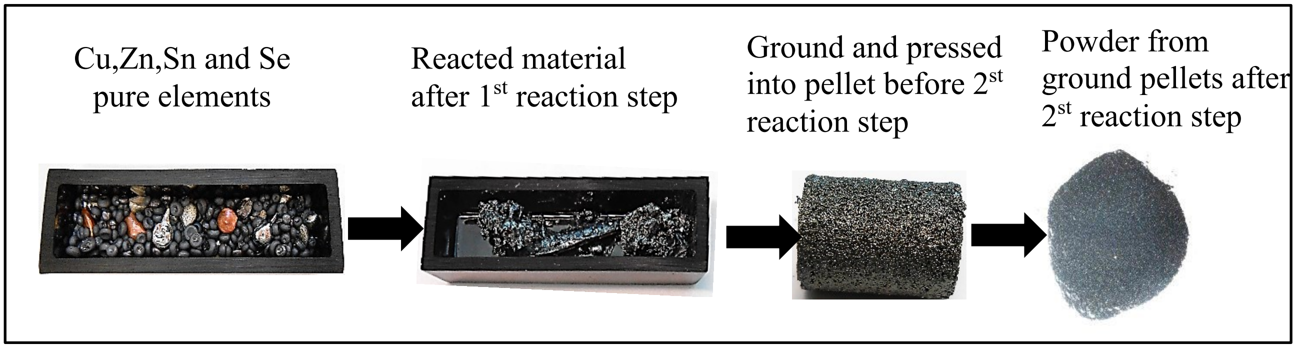

Figure 11 *Synthesis route - solid state reaction of CZTSe powder samples.*

Table 4 *Optimized temperature program for the synthesis of CZTSe powder material.*

Synthesis		CZTSe
1st reaction step Solid state reaction	1st heating stage	250°C, heating rate 10 K/h hold for 48 h
	2nd heating stage	450°C, heating rate 10 K/h hold for 48 h
	3rd heating stage	600°C, heating rate 10 K/h hold for 48 h
	final heating stage	750°C, which is 40°C below the CZTSe melting point of 790°C hold for 240 h [*Olekseyuk et al. PCSS V1,p195-200*]
	cooling	naturally cooled to room temperature (furnace switch-off)
homogenization step		grinding of the material pressed to pellets which are placed in sealed silica tubes
2nd reaction step	heating stage	750°C, heating rate 50 K/h hold for 240 h
	cooling	naturally cooled to room temperature (furnace switch-off)

As a small remark; the grinding step before pressing the powder into pellets was done by an agate mortar during the first two syntheses, afterwards this step was optimized by using a Fritsch vibratory, where the mortar vibrates electromagnetically grinding the reacted material through impact and friction between the grinding ball and the wall, this equipment is ideal for mixing homogeneously.

After the first reaction, the CZTSe samples were cooled down to room temperature by switching off the furnace, the same cooling procedure was applied after the second reaction (annealing). The furnace cooling profile was measured with a thermocouple device (see Figure 12b), it displays a decrease of temperature from 750°C to 400°C in 4 hours. After this point the cooling rate decreased slower and the samples reached room temperature after approximately 24 hours.

In this work all intended composition within the A, B, C and D off-stoichiometry type have been calculated by using the formulae from *Table 3*. Compositions within the E and F type line were not intended. In addition to the precisely weighed elements a 2% excess selenium was added for the first and second reaction in order to assure the reaction of all cations. After annealing the pellets were ground and the resulted powders have been characterized.

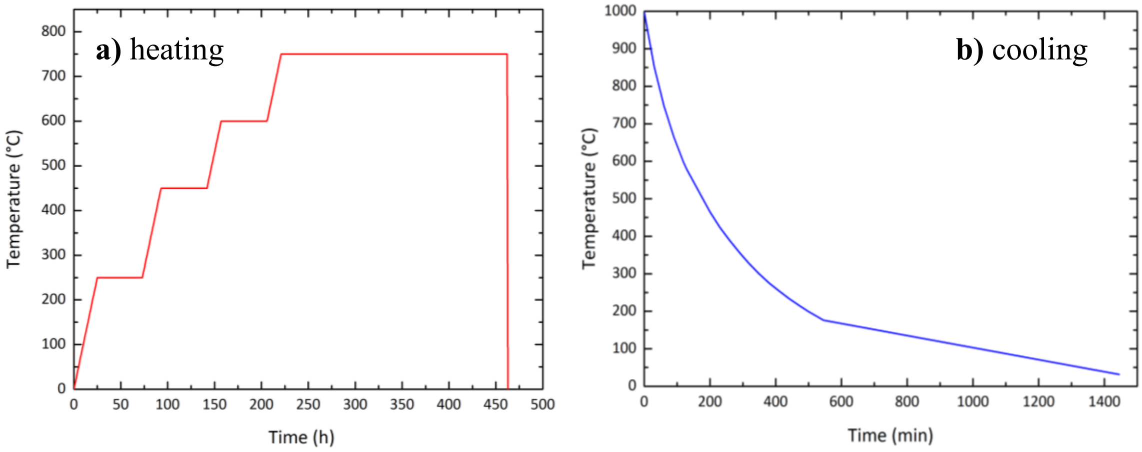

Figure 12a) *Temperature heating profile used for synthesis* ***b)*** *cooling profile measured by a thermocouple.*

2.2 Chemical characterization

Chemical characterizations have been performed at the Institute of Geological sciences of the Freie Universität Berlin; Laboratory for electron microprobe analysis (EMPA) using an JEOL JXA 8200 super Probe unit, equipped with a wavelength dispersive X-ray spectroscopy (WDS) and an energy dispersive X-ray spectrometer (EDS). This instrument is used for basic research in diverse range of materials, such as minerals, semiconductors, ceramics, etc. It provides a reliable quantitative and qualitative analysis of polycrystalline powder samples. A schematic representation of an electron microprobe is shown in Figure *13*.

In principle, the EMPA unit analyzes which elements compose a sample, by irradiating an electron beam onto the specimen surface and measuring the characteristic X-ray that is generated from it. In other words, when a specimen is bombarded by a focused electron beam at a certain accelerating voltage, the incident electrons collide with electrons in the inner shells of atoms with sufficient energy to eject an inner-shell electron from its orbit, leaving a vacancy, an electron from an outer shell at a higher energy level comes down to take the place of the ejected electron. This movement between energy levels is accompanied by the emission of an X-ray with a wavelength that is equivalent to the energy difference. Since the energy level of an element is unique to each element, by investigating the wavelength of the X-ray emitted, or the energy, it is possible to identify which elements compose the specimen being examined. With the EMPA unit, the signals of characteristic-X-rays, secondary electrons, and backscattered electrons, etc. can be detected by an appropriate detector.

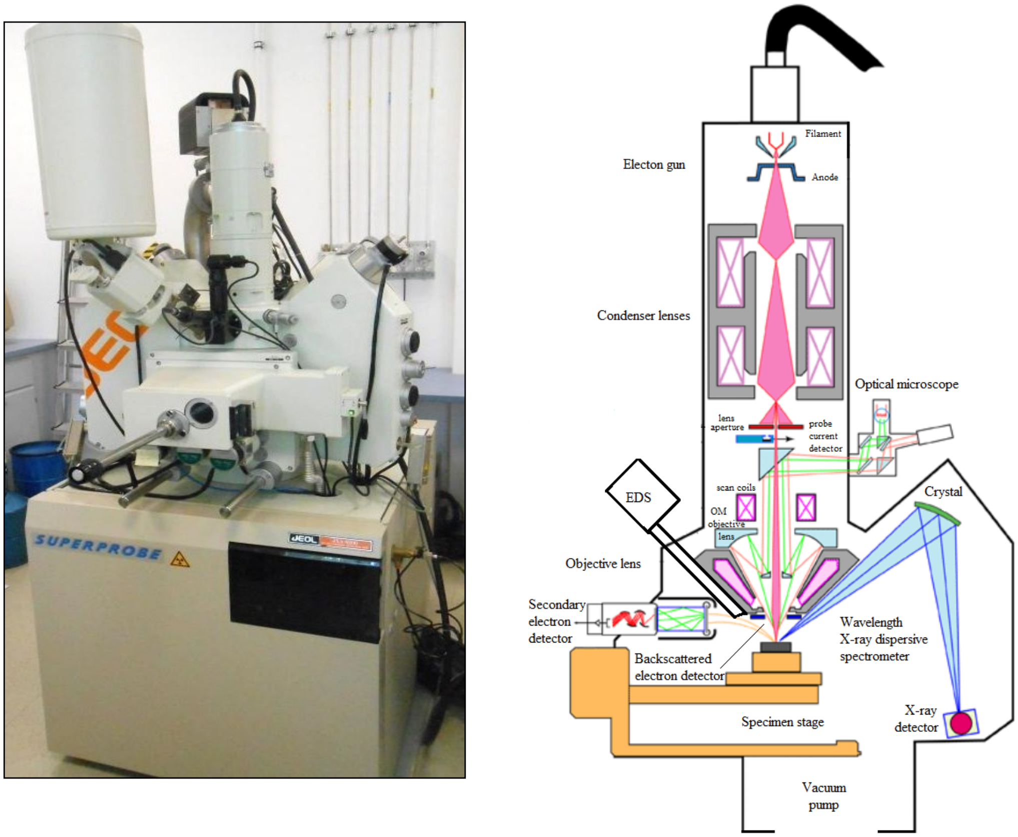

Figure 13 *Schematic diagram of an electron microprobe (EMPA).*

Energy dispersive spectrometer (EDS) sort the X-rays based on their energy. A solid state detector converts the energy of individual X-rays into electrical voltages of proportional size; the electrical pulses correspond to the characteristic X-rays of the element; while, wavelength dispersive spectrometer (WDS) sort the X-rays based on their wavelengths. WDS detection system use X-ray diffraction (Bragg diffraction) as the means by which they separate X-rays of different wavelengths. The spectrometer consists of a specimen surface, analyzing crystal, and x-ray detector. Since a single analyzing crystal cannot be used to analyze all elements, normally, there is several diffraction elements incorporated into one instrument. WDS can analyze only one element at a time, while EDS offers simultaneous analyses of multiple elements within short time. However, the energy resolution for EDS is lower than for WDS; this means that the amount of overlap between peaks of similar energies is much smaller on the WDS system. Moreover, EDS system has lower count rates and poor reproducibility, typically a WDS system has a count rate about 10x higher than an EDS system. Therefore, for highly reliable quantitative analyses WDS is generally a more precise technique [38].

For this work, to analyze the phase content and chemical composition within the synthesized powder samples; a random portion of the powder was selected to be embedded in epoxy and mechanically polished to achieve a clean surface. Previous to every EMPA measurements, a carbon evaporation device Leica EM SCD 500 has been use to deposit a conductive carbon tin film onto the polished surface. To calibrate EMPA quantitative analysis, standard crystals of each Cu, Zn, Sn and Se element have been selected within the 5 channels and performing an element peak search within the chosen standard condition.

A backscattered electron detector is integrated into the EMPA unit, back-scattered electron micrograph images (BSE) are quickly obtained (depending on the scan rate) at different magnifications, since heavy atoms with a higher atomic number Z scatter stronger than the light ones, BSE are useful for imaging a surface to preliminary distinguishing different phases. During the measurements BSE images have been digitally captured and used as a sample map for locating analyzed spots. Additionally, the optical microscope has been used to ensure the appropriate focus before set the spot to measure. For each sample 25-35 grains were selected to be measured and on each grain 10 measurement points were averaged. Mass and atomic percentages outcome values ~100% of Cu, Zn, Sn and Se out of each measured grains which were identified to belong to the same phase (same amount of Cu and/or Zn and/or Sn and/or Se within the 2% error of the WDS measurement) were averaged and attributed to belong to the same phase, for example to the kesterite phase. In case that the values deviate further than 2% error, then it is an indication that more than one kesterite phase has been formed and so this sample must be re-annealed to expected the formation of only one kesterite main phase.

From this kesterite phase averaged values, the Cu/(Zn+Sn) and Zn/Sn ratios have been calculated, in the same way the composition of the secondary phases (if any) have been obtained. An example of a back-scattered electron micrographs images (BSE) is shows in Figure *14* with x40 (left) and x200 (right) magnifications. In this particular example; the kesterite (CZTSe) phase was detected with an off-stoichiometric composition along with few amounts of secondary phases: zinc selenide (ZnSe) and tin diselenide ($SnSe_2$).

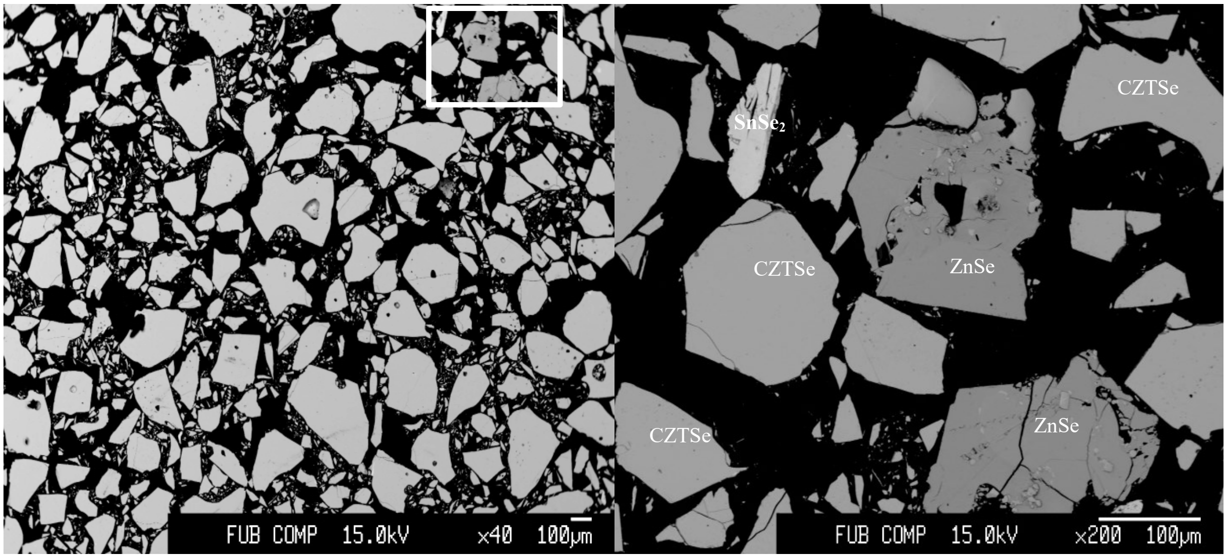

Figure 14 *Backscattered electron micrographs of polished synthesized powder sample at different magnifications x40 (left) and x200 (right). CZTSe were detected in light grey grains, along with secondary phases* $SnSe_2$ *and ZnSe.*

2.2.1 Determination of the off-stoichiometric chemical composition

Cation ratios Cu/(Zn+Sn) and Zn/Sn of the kesterite main phase are calculated out of the resulted atomic percentages from electron microprobe WDX spectroscopy analysis. The Cu/(Zn+Sn) vs. Zn/Sn cation ratio plot gives a better overview of the quaternary system, since the off-stoichiometric type lines (see Table *3*) are included; it is possible to recognize the off-stoichiometry type of the sample. Moreover, if a sample is a mixture of two off-stoichiometry types; the type fraction can be deduced by a graphical approach. Thereby taking into account the respective fraction and the off-stoichiometry type formula, the chemical composition can be deduced [4]. An example of the determination of the off-stoichiometric composition and type fraction by graphical approach is given next.

Cation ratio plot in Figure *15* shows an example of a sample with kesterite phase cation ratios Cu/(Zn+Sn)=0.890 and Zn/Sn=1.134. The kesterite phase is located between the off-stoichiometry type lines; A-type: $Cu_{2-2x}Zn_{1+x}SnSe_4$, and B-type: $Cu_{2-2y}Zn_{1+3y}Sn_{1-y}Se_4$.

The value of "x" of formula $Cu_{2-2x}Zn_{1+x}SnSe_4$ and value of "y" of formula $Cu_{2-2y}Zn_{1+3y}Sn_{1-y}Se_4$ are graphically deduced according to this particular location of the kesterite phase within the cation ratio plot. In the case of this example presented in Figure *15*: the values of "x" of A-type formula is equal to 0.134 and the value of "y" of B-type formula is equal to 0.032.

The type fractions have been deduced by a linear interpolation. This kesterite phase is 0.37 (37%) A-type and 0.63 (63%) B-type. Finally, the composition of each cation is calculated by summing the corresponding types formulae (A-and B-type) times its fraction as is shown below:

Copper: $(2-2x)*(fraction_{A-type})+(2-2y)*(fraction_{B-type})$

Zinc: $(1+x)*(fraction_{A-type})+(1+3y)*(fraction_{B-type})$

Tin: $(1)*(fraction_{A-type})+(1-y)*(fraction_{B-type})$

The off-stoichiometric chemical composition of this 37% A-type and 63% B-type kesterite phase is then equal to: $Cu_{1.859}Zn_{1.111}Sn_{0.980}Se_4$

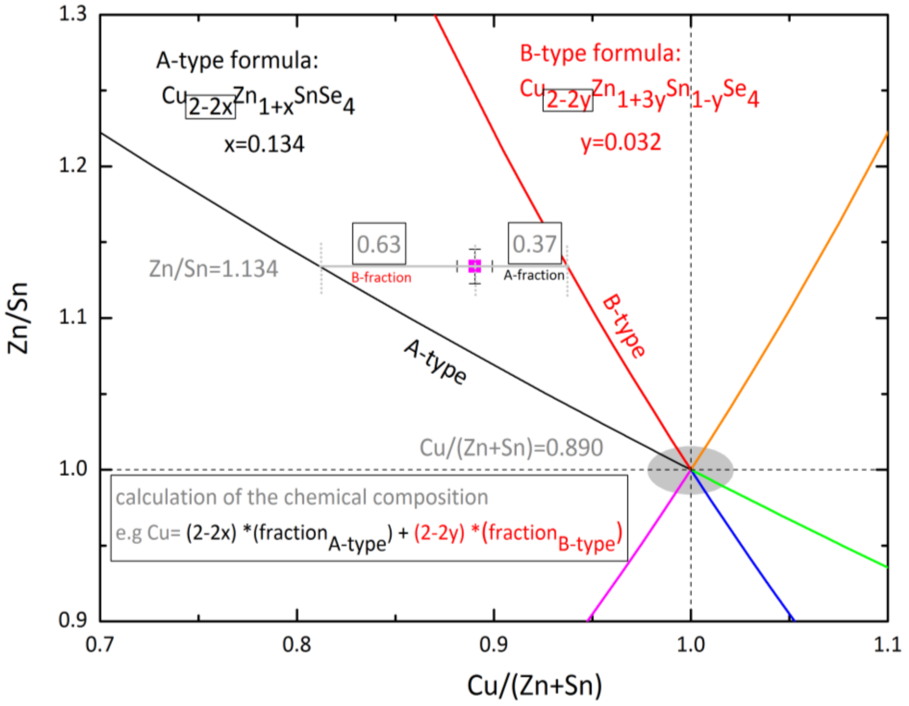

Figure 15 *A-B type mixture sample with cation ratios Cu/(Zn+Sn)=0.890 and Zn/Sn=1.134, 63%B-type and 37% A-type, chemical composition:* $Cu_{1.859}Zn_{1.111}Sn_{0.980}Se_4$

2.3 Structural characterization

2.3.1 X-Ray powder diffraction (XRD)

Structure characterization was done by X-ray powder diffraction (XRD) which is a rapid analytical technique used to study crystal structures and atomic spacing. Generally, a diffractometer consists of three basis components: X-ray tube, sample holder and detector. In principle, X-rays are generated by a cathode ray tube by heating a filament to produce electrons; the electrons bombard a target with sufficient energy to dislodge inner shell electrons of the target material and characteristic X-ray spectra are produced. The most common components of these spectra consist of K_α ($K_{\alpha 1}$-$K_{\alpha 2}$) and K_β radiation. Wavelengths are characteristic of the target materials; copper is the most common target material with CuK_α=1.5418 Å. Afterwards, filtering is required to produce monochromatic radiation. The X-rays are collimated to concentrate and directed to a sample, in our case a mass of finely ground powder sample. Powder samples consist of randomly oriented crystallites (polycrystalline). The interaction of the incident rays with the polycrystalline material produces a diffracted ray when condition satisfy Bragg's law "$n\lambda = 2d_{hkl} \sin\theta$", Where n is the order of reflection or diffraction, λ wavelength, d_{hkl} lattice plane spacing and θ is the diffraction angle. Finally, the diffracted X-rays are then detected, processed and counted, by scanning the sample through a range of 2θ angles. The scattering of X-rays from atoms produces a diffraction pattern, which contains information about the atomic arrangement within the crystal [39].

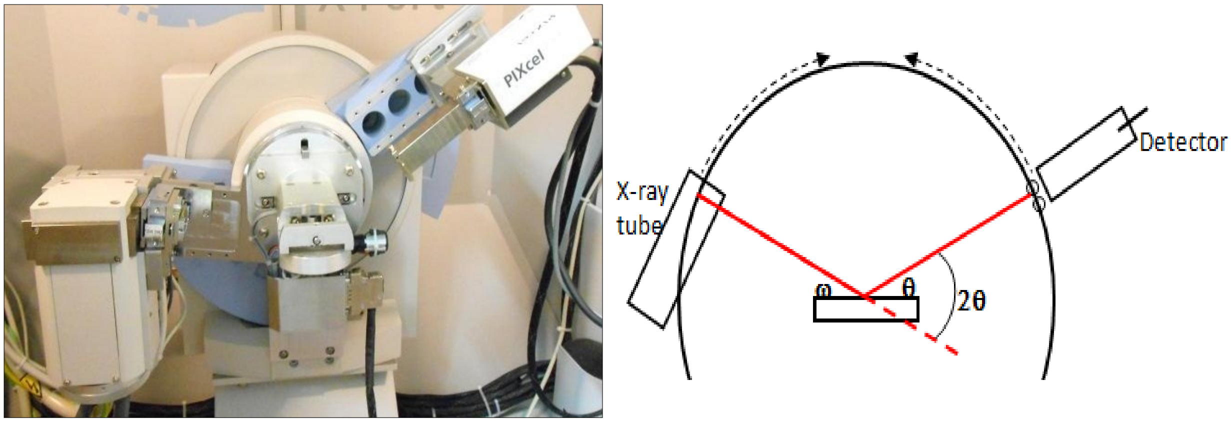

Figure 16 *PANalytical XRD under Bragg-Brentano geometry.*

For this work XRD measurements were performed at the Helmholtz Zentrum Berlin using a PANalytical X'Pert PRO MRD diffractometer under a Bragg-Brentano geometry (see Figure *16*). In this geometry, the incident angle is defined by omega (ω) between the X-ray source and the sample. While the diffraction angle 2θ, is defined between the incident beam and the detector. The incident angles ω is always ½ of the detector angle 2θ. In this diffractometer, the sample remains fixed while the X-ray tube and the detector rotate. All measurements were performed at room temperature with a sample spinner stage where the finely ground powder sample was placed on a zero background holder. Before the measurement, a smooth flat surface was carefully prepared to ensure the random orientation of the crystallites and prevent preferred orientations. Absolute scan was settle in a 2θ range from 10° to 130° with a step size of 0.01313° using the PIXcel detector, soller slit, 5mm mask and ¼° divergence slit with a power supply of 40 kV and 30mA.

2.3.2 Neutron powder diffraction (NPD)

Neutron powder diffraction was selected for further structure characterizations. Its principle is similar to X-rays diffraction, but in this case a beam of neutron impinges on a crystalline sample which scatters under a limited number of well-defined angles according to the Bragg's law that describes X-ray diffraction. The main difference between neutrons and X-rays is that they interact differently with the matter. X-rays interact primarily with the electron shell of the atom; therefore, diffracted X-ray intensity is larger for atoms with higher atomic number (Z). On the other hand, neutrons interact with atomic nuclei via the short-range strong nuclear force. Since the energy of the neutron remained unchanged by the collision, the scattering is then said to be elastic [40]. Furthermore, the amplitude of the neutron wave scattered by the nucleus depends on the strength of the interaction between the neutron and the nucleus. The Scattering length referred as *b*, measures the strength of such interactions which is not correlated with atomic number and varies even from isotope to isotope. Opposite to the angular dependence of the X-ray amplitude scattered by an atom called the atomic scattering factor *f*; for X-rays, the scattering power of various atoms and ions is proportional to the number of core electrons. The X-ray scattering factor *f* depends on the radial distribution of the electron density around the nucleus, and they are also functions of the Bragg angle ($\sin\theta/\lambda$).

When neutrons are of concern, their coherent scattering by nuclei is independent of the Bragg angle and the corresponding factors remain constant for any Bragg reflections.

Scattering factors of different isotopes are represented in terms of coherent scattering lengths of a neutron and are expressed in femtometers (1 fm=10^{-15}m), in the majority of cases of interest, *b* has been determined by experiment, and it can be found in literature, e.g. [41].

In Figure **17**a,b, the atomic scattering factors *f* and neutron scattering lengths *b* of our elements of interest copper and zinc are compared due to $Cu_2ZnSnSe_4$ contains isoelectric cation Cu^+ and Zn^{2+} which cannot be distinguished by X-ray due to their similar atomic scattering factors (see Figure 17a), but their neutron scattering lengths (b_{Cu}=7.718 fm; b_{Zn}=5.680 fm) are different enough to distinguish (see Figure 17b), therefore, the use of neutron powder diffraction is a suitable way to determine the ordering of those cations in the crystal structure of kesterites as have been previously reported by *S. Schorr* [9].

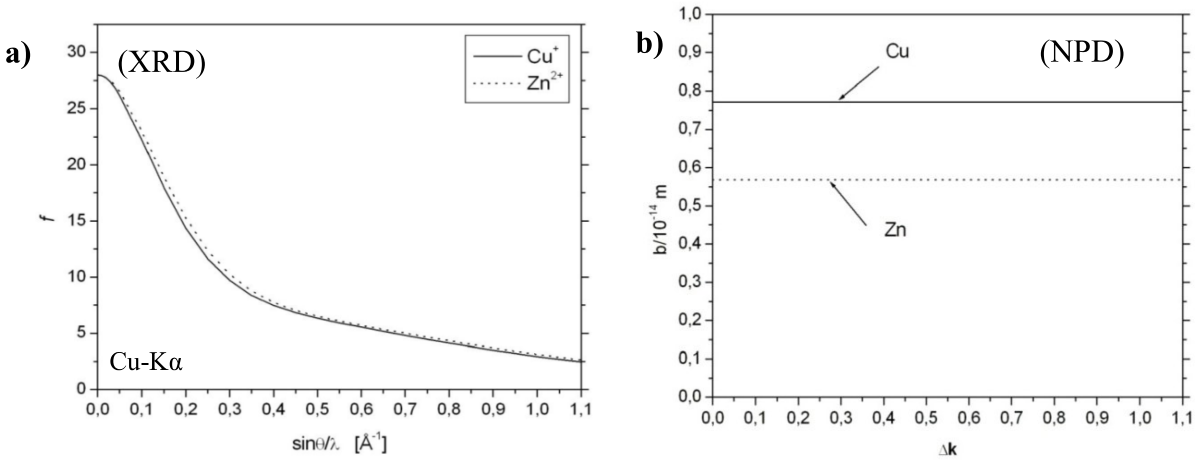

Figure 17 a) *Atomic scattering factors "f" as function of Bragg angle of* Cu^+ *and* Zn^{2+} ***b)*** *Neutron scattering length, b, for Cu and Zn as a function of wave vector.*

In general, any diffraction experiment is a Fourier transformation from real space into reciprocal space yielding intensity data in reciprocal space. Detectors register intensities *I(hkl)* of a Bragg-reflection in X-ray or neutron diffraction experiments which are directly proportional to the squares of the crystallographic structure factors *F(hkl)*; $I \propto |F_{hkl}|^2$. The general formula for neutron diffraction is given in following equation:

$$\boldsymbol{F_{hkl} = \sum b_j \cdot exp\left[2\pi i(hx_j + ky_j + lz_j)\right]}$$

Equation 1

Where:

- For the case of neutron diffraction, the X-ray scattering factor f_i has been substituted for the neutron scattering length b_j
- *hkl* = the Miller indices
- *xyz* = the relative atomic positions in the unit cell

For this work, all $Cu_2ZnSnSe_4$ off-stoichiometric powder samples have been characterized by neutron powder diffraction, two beam times for neutron sources have been gained under proposal submission at two different large scale neutron source facilities.

First measurements were done at the Spallation Neutron Source (SNS) of Oak Ridge National Laboratory, which currently provides the most intense pulsed neutron beam in the world. Generally in a powder diffractometer of a pulsed neutron source, the sample is irradiated by a pulsed beam of neutrons with a wide spectrum of energies, so scattered neutrons are recorded in banks of detectors located at different scattering angles, and the time at which each scattered neutron arrives to the detector is recorded at a particular scattering angle; resulting in a diffraction pattern [40]. This kind of pattern differs to others diffraction patterns because the independent variable is the neutron's time of flight (T.O.F) rather than the scattering angle. The time of flight is easily deduced from the arrival time of the neutron because its known when the pulse of neutrons left the source. In this research measurements were done using the POWGEN BL-11A powder diffractometer where time of flight (T.O.F) data was collected at room temperature (300 K) using a 60 Hz frequency at two frames with center wavelengths of 1.066 Å and 2.665 Å, covering a *d*-spacing range of 0.2760-4.6064 Å and 1.1038-9.2129 Å, respectively.

Additional neutron powder diffraction measurements were performed at the Berlin Research Reactor (BER II) of the Helmholtz-Zentrum Berlin for Materials and Energy (HZB). In principle, in a powder diffractometer at a reactor neutron source, a beam of neutrons with a single wavelength is selected by a device called a monochromator and directed toward a powder sample. The monochromator is usually an assembly of single crystals, each correctly oriented to diffract a mono-energetic beam of neutrons toward the scattering sample. The neutrons scattered from a powder sample are counted by suitable detectors and recorded as a function of the angle through which they were scattered by the sample. Each Bragg peak in a typical diffraction pattern corresponds to diffraction from atomic planes with different interplanar spacing, *d*, [40]. In this research, all measurements were done using the fine resolution powder diffractometer FIREPOD (E9); the data was collected at room temperature with a wavelength λ=1.79725Å, covering the 2θ range up to 140°. At both neutron source facilities, a vanadium-can of 6mm diameter was used as a sample container because this element (V) is a strong scatter of X-rays, but its nuclei hardly scatter neutrons.

2.3.3 Anomalous diffraction of synchrotron X-rays

Further structure characterizations were performed with synchrotron X-ray radiation. The use of this radiation has several advantages over the laboratory XRD for carrying out high quality powder diffraction measurements. In principle, synchrotron radiation is emitted when accelerated charged particles travelling at relativistic speeds change velocity, such as when they are made to follow a curved trajectory (synchrotron rings) controlled by a magnetic field. Synchrotron radiation is emitted tangentially in these curved sections, which can therefore serve as the source of X-ray for experiments. Its output power exceeds that of the conventional X-ray tube by many orders of magnitude [42]. Moreover, the wavelength can be tuned over a large energy range to be optimum for a particular measurement, for e.g. tuning to the absorption edge of an element in the sample to exploit anomalous scattering phenomena.

Normal X-ray scattering factor f_0 describes the scatter ability of different atoms as a $\sin\theta/\lambda$ function therefore it is wavelength independent. However, when the X-ray energy is nearly coincident with the binding energy of any of the electrons in an atom, the scattering process is affected by the possible absorption of the photon, so, there is a sharp rise in the X-ray absorption with increasing photon energy at each of the electron binding energies (hence the term *"absorption edge"*). The principal effect to the coherent scattering is a shift in the phase between the incident wave and the scattered wave *via* a resonance effect. This phase shift created an imaginary component to the atomic scattering factor as well as a modification of the real part. As the effect is largely of concern for absorption via inner shell (K for light elements and L for heavier ones) electrons that have distributions confined close to the atomic nucleus, these anomalous scattering factors are independent of $\sin\theta/\lambda$ but are strongly dependent on λ. By taking into account those two additional parameters, the overall scattering factor of each chemical element is presented in the following form [39]:

$$\boldsymbol{f^{j}(s) = f_0^{j}(s) + \Delta f^{j'} + i\Delta f^{j''}} \qquad \textit{\textbf{Equation 2}}$$

Where:

- $s = \sin\frac{\theta}{\lambda}$
- f_0^j = normal atomic scattering factor that depends only on the type of the scattering atom (number of electrons) and is a function of $\sin\theta/\lambda$
- $\Delta f^{j'}$ and $\Delta f^{j''}$ = the real and imaginary components, respectively, of the anomalous scattering factors and they depend on both the atom type and the wavelength λ

Generally, the magnitude of the anomalous scattering factors is proportional to the wavelength, and inversely proportional to the number of electrons in an atom. Thus anomalous scattering becomes stronger, and reached its maximum when the wavelength is near to the corresponding absorption edge of an atom, this effect may be used for contrast enhancement to discriminate atoms that have similar conventional scattering factors. This contrast enhancement is useful for kesterite compounds because copper and zinc have similar number of electrons but with different K-edge absorption values: 8979 eV for copper and 9659 eV for zinc (see Table 5). Although the best f’ contrast enhancement is found close to the absorption edge, the uncertainty of f’ is also highest in this region, therefore, the use of multiple wavelengths near to the edge is suggested.

Table 5 *Anomalous scattering factors f' of copper and zinc from the Cromer and Liberman values [43]*

Energy [eV]	**Zn^{2+} Δ f'**	**Cu^{+} Δ f'**
8048 eV	-1.5465	-1.9635
8919 eV	-2.2235	-4.6172
8955 eV	-2.2689	-5.5884
8969 eV	-2.2866	-6.5604
8974 eV	-2.2929	- 7.4207
9376 eV	-3.1232	-2.3273
9599 eV	-4.6777	-1.8036
9635 eV	-5.6561	-1.7422
9649 eV	-6.6476	-1.7185
9654 eV	-7.5581	-1.7100
12398 eV	-0.4026	-0.0745

In this work anomalous diffraction of synchrotron X-rays has been used to differentiate between Cu and Zn cation within different off-stoichiometric $Cu_2ZnSnSe_4$ powder samples. Measurements were gained under proposal submission at the Helmholtz-Zentrum Berlin for Materials and Energy, where the diffraction end station of the KMC-2 beamline of BESSY II has been selected (Figure 18a). KMC-2 provides X-ray radiation with both very stable energies and intensities [44], its accessible energy range of 4-14 keV is ideally suited for the K-edges of Cu (8979 eV) and Zn (9659 eV). The experiments were conducted at ambient conditions, with 10 different selected energies: first selected energy was near the CuK_α radiation (8048 eV), next one in the middle of the absorption edges (9376 eV) and four below the Cu and Zn absorption K-edge respectively (see Figure 18b).

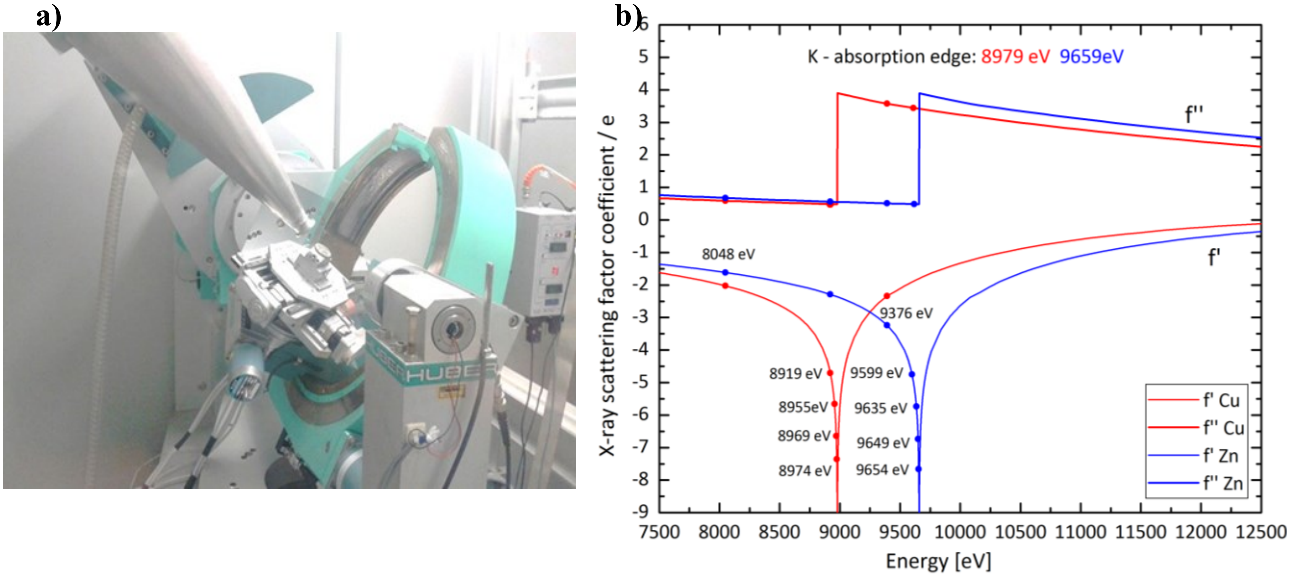

Figure 18 a) *Diffraction end station of the KMC-2 beamline of BESSY II at HZB and* **b)** *Cu and Zn anomalous scattering factors as a function of photon energy [according to Cromer and Liberman].*

2.3.4 Rietveld refinement method

Rietveld analysis has been chosen for a detailed structural analysis of collected powder diffraction data. This method is a structure refinement procedure which considers the entire powder diffraction pattern; its approach is not a structure solution method thus a reasonably good starting model is needed. Rietveld refinement uses a complex minimization procedure which sought the best least-squares fit between the experimental step-scanned intensity value (observed) and the calculated pattern. The quantity minimized in the least-squares refinements is the residual, S [45]:

$$\mathbf{S = \sum_i w_i (y_i - y_{ci})^2} \qquad \textit{Equation 3}$$

Where:

- w_i = the weight of each observation point
- y_i =observed intensity at each step 2θ

- y_{ci} = calculated intensity at each step
- the sum is overall data points

Typically, many Bragg reflections contribute to the intensity (y_i) observed at any arbitrary chosen point (i) in the pattern. The calculated intensities, y_{ci}, are determined from the $|F_{hkl}|^2$ values calculated from the structural model by summing of the calculated contributions from Bragg reflections plus the background [45], see following equation:

$$\mathbf{y_{ci} = s \sum_K L_K |F_K|^2 \varphi(2\theta_i - 2\theta_K) P_K A + y_{bi}} \qquad \textit{Equation 4}$$

Where:

- s= scale factor
- k = Miller indices *hkl* of a Bragg peak
- L_K= Lorentz, polarization and multiplicity factors
- φ_k = the reflection profile function of the Bragg peak
- P_k = preferred orientation function
- A= absorption factor
- F_K= the structure factor
- y_{bi}= background intensity

The idea behind the Rietveld method is to consider the entire powder diffraction pattern using a variety of refinable parameters. The refinements are carried out based on the refined model for the crystal structure, diffraction optics effects, instrumental factors, and other specimen characteristics (e.g. lattice parameters). Moreover, the sequence into which the different parameters are being refined need to be done carefully. The quality of the refinement is reflected by the R-Bragg (R_{bragg}) and chi-square (χ^2) values. In the following section the refine procedure for X-ray, neutrons and synchrotron diffraction data is described. For all refinements the FullProf suite software package has been used [46].

2.3.4.1 Rietveld refinements of XRD data

The Thompson-Cox-Hasting pseudo-Voigt convoluted function [47] (Npr=7 in FullProf) [48] has been applied to describe the peak shape profile. The kesterite structure (space group $I\bar{4}$) was used as starting model in the refinement as well as a model of the corresponding secondary phases detected by WDX spectroscopy analysis. The refinement parameters were: zero-shift, scale factor, lattice parameters, peak shape and asymmetry parameters and background. The lattice parameters and phase weight fraction values have been extracted from the refinements. Figure 19a, shows the simulation of the kesterite diffraction pattern from the inorganic structures database ICSD-95117 [49] and Figure 19b an example of a refinement pattern from a single phase sample $Cu_{1.950}Zn_{1.104}Sn_{0.961}Se_4$. The quality of the refinement is reflected by the R-Bragg (7.83) and chi-square (1.58).

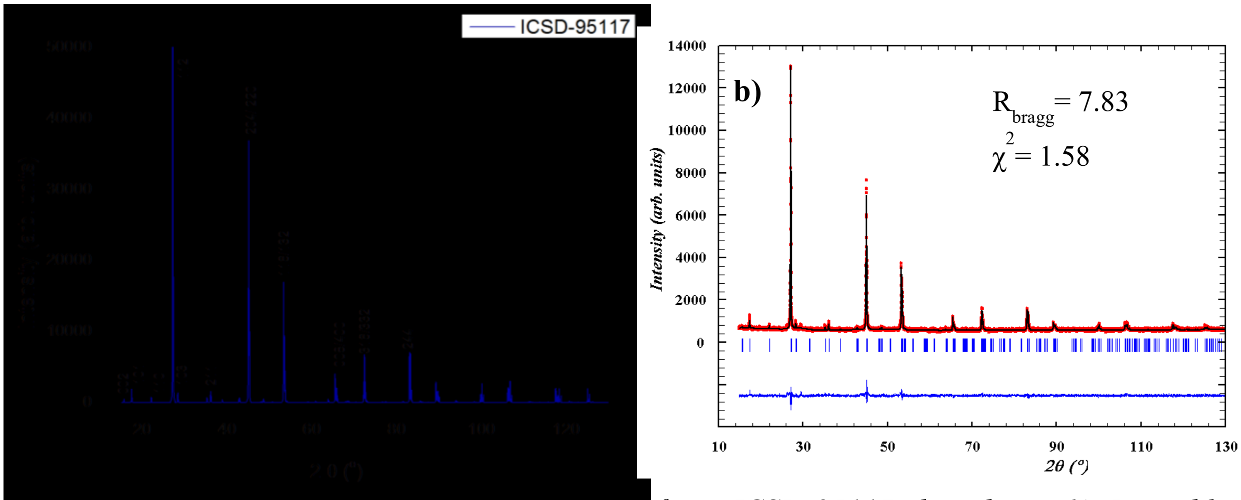

*Figure 19 **a)** Simulation of kesterite pattern from ICSD-95117 data base, **b)** Rietveld refinement example of a pattern of a single phase sample $Cu_{1.950}Zn_{1.104}Sn_{0.961}Se_4$; red color pattern represents Y_{obs} - observed, black Y_{calc}- calculated and blue line Y_{obs}-Y_{calc} - is the subtraction of observed minus calculated patterns.*

2.3.4.2 Rietveld refinements of anomalous X-Ray diffraction data

The peak shape profile function used was also the Thompson-Cox-Hasting pseudo-Voigt convoluted function [47], in this case, only the kesterite structure (space group $I\bar{4}$) was used as starting model since all the analyzed samples by anomalous diffraction were single phase. The X-ray anomalous scattering factors f' and f'' of each element (Cu, Zn, Sn and Se) for all selected energy: 8048eV, 8919eV, 8955eV, 8969 eV, 8974eV, 9376eV, 9599eV, 9635eV, 9649eV and 9654eV were included in the refinement file (see Table 6). In this case the f' and f'' values have been taken from E.A Merrit website [50]. These scattering factors data were calculated using the subroutine library by Brennan and Cowan [51], in turn using the theoretical approximation developed by Cromer and Liberman. Those values between tabulated energies were derived by linear interpolation as explained by *Többens et al.* [52].

Table 6 *Anomalous scattering factors f' of copper and zinc; values marked * have been adjusted from the Cromer and Liberman value given in brackets [52].*

Energy / eV	*f'* (Cu)	*f'* (Zn)
8048	-1.9635	-1.5465
8919	-4.6172	-2.2235
8955	-5.5884	-2.2689
8969	-6.26* (-6.5604)	-2.2866
8974	-6.70* (-7.4207)	-2.2929
9376	-2.3273	-3.1232
9599	-1.8036	-4.6777
9635	-1.7422	-5.6561
9649	-1.7185	-6.6476
9654	-1.7100	-7.20* (-7.5581)
12398	-0.0745	-0.4026

Each data set taken with different energies were refined separately. Profile parameters and background have been first refined by LeBail method and the extracted parameters were kept fixed in the subsequent Rietveld refinements. Anisotropic displacement parameters were taken from a single-crystal refined structure of CZTSe [53] and kept. Cation occupation in the structure model was; 2*a* - Cu, 2*c* - Cu, 2*d* - Zn. The 2*b,* Sn was set according with the chemical composition. The anion coordinates *x,y,z* were refined from

8048eV energy by LeBail and kept fixed for the refinements by different energies. The occupation factors of 2*a* ,2*c* and 2*d* sites were refined independently out if all energies data set. Detailed information about the refinements procedure and method have been published by *Többens et al.* [52, 54]

2.3.4.3 Rietveld refinements of neutron powder diffraction data

The neutron diffraction data collected from the spallation neutron source at Oak Ridge National Laboratory has been refined with the peak shape function for neutron Time of flight data (T.O.F.) convolution pseudo-Voigt (Npr 9 in FullProf). As the starting crystal structure model for the CZTSe main phase the kesterite ordered type structure (space group $I\overline{4}$) with Cu on 2*a*: (0,0,0), Cu on 2*c*: (0,½,¼), Zn on 2*d*: (0,½,¾), Sn on 2*b*: (½,½,0) and Se on 8*g*: (*x*-0.74124, *y*-0.74201, *z*-0.62874) [53]. Additionally, the corresponding secondary phases were included for the refinements.

The refined parameters were: zero-shift, scale factor, lattice parameters, peak shape and asymmetry parameters, background, anion coordinates, isotropic temperature factors and site occupancies without any constraints. For each sample both from the 2 frames pattern were refined simultaneously (with center wavelengths of 1.066 Å and 2.665 Å, covering a *d*-spacing range of 0.2760-4.6064 Å and 1.1038-9.2129 Å, respectively) see Figure *21*a, b.

Further Rietveld refinements were done from neutron data collected at the fine resolution powder diffractometer FIREPOD (E9) of Berlin Research Reactor (BER II) at the Helmholtz-Zentrum Berlin for Materials and Energy (HZB).

The refinement procedure (see Figure 21) has been the same as described above, differing only by the use of the Thompson-Cox-Hasting pseudo-Voigt convoluted peak shape profile function (Npr=7 in FullProf). Also the absorption correction coefficient (μR) has been calculated for the corresponding compositions.

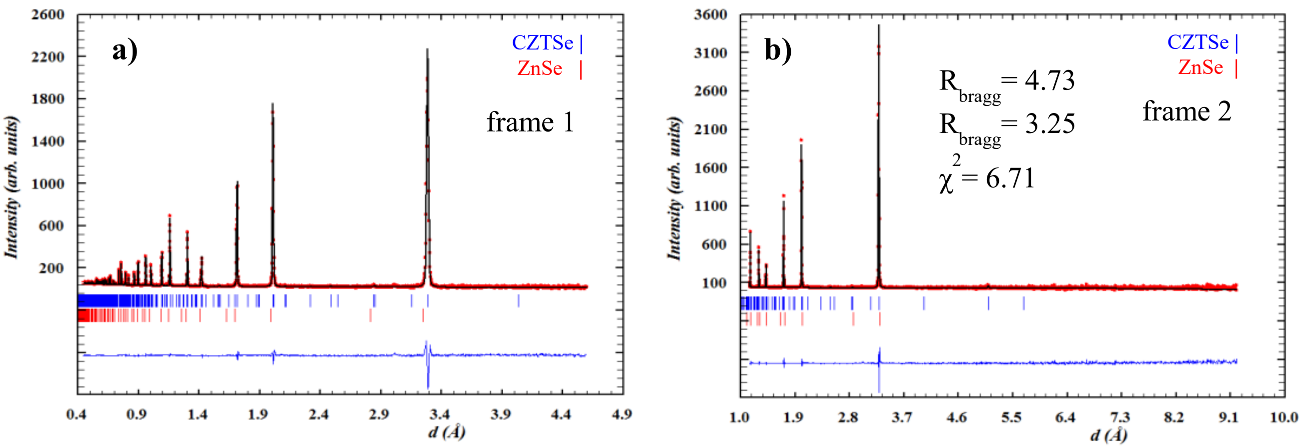

Figure 21 a) *frame 1 and* ***b)*** *frame 2 of Rietveld analysis of a neutron diffraction pattern for the kesterite sample* $Cu_{1.86}Zn_{1.11}Sn_{0.98}Se_4$ ($I\bar{4}$) *with secondary phase ZnSe* ($F\bar{4}3m$)*; red color pattern represents* Y_{obs} *- observed, black* Y_{calc}*- calculated and blue line* Y_{obs}*-*Y_{calc} *- is the subtraction of observed minus calculated patterns.*

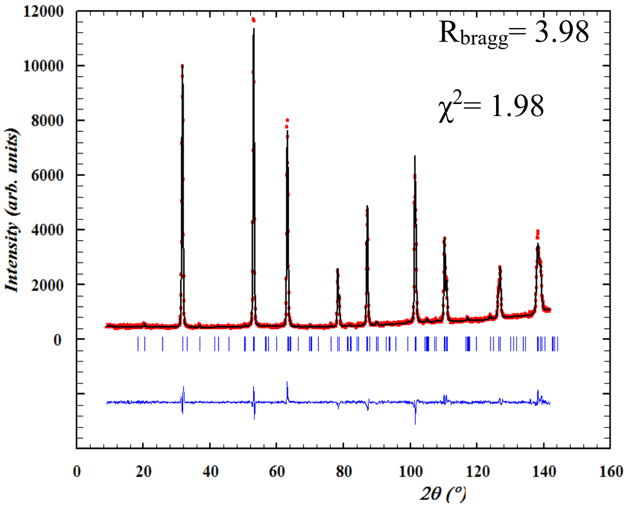

Figure 21 **c)** *Rietveld refinement example of a pattern of a single phase sample:* $Cu_{1.892}Zn_{1.101}Sn_{0.977}Se_4$. ($I\bar{4}$)*; red color pattern represents* Y_{obs} *- observed, black* Y_{calc}*-calculated and blue line* Y_{obs}*-*Y_{calc} *- is the subtraction of observed minus calculated patterns.*

2.3.5 Average neutron scattering length method

The application of the average neutron scattering length method has been demonstrated to be a reliable way to determine the cation distribution and intrinsic point defects in the kesterite type compounds [9, 10] In this method the experimental average neutron scattering length of each Wyckoff position, when the kesterite type structure as a model in the refinement was used. The positions are calculated according to the following equation:

$$\overline{\boldsymbol{b}}_{2a}^{exp} = occ_{2a} \cdot b_{Cu} \qquad \overline{\boldsymbol{b}}_{2c}^{exp} = occ_{2c} \cdot b_{Cu}$$

Equation 5

$$\overline{\boldsymbol{b}}_{2d}^{exp} = occ_{2d} \cdot b_{Zn} \qquad \overline{\boldsymbol{b}}_{2b}^{exp} = occ_{2b} \cdot b_{Sn}$$

Where:

- $\overline{b}^{exp}$= experimental average neutron scattering length
- *occ*= site occupation factors obtained from Rietveld refinements of the corresponding site.
- *b*= neutron scattering length of the element (b_{Cu}=7.718 fm, b_{Zn}=5.680 fm, b_{Sn}=6.225 fm)

Complementary, a calculated average neutron scattering length is deduced by the following equation:

$$\overline{\boldsymbol{b}}_{j}^{calc} = X_j \cdot b_X + Y_j \cdot b_Y$$

Equation 6

Where:

- $\overline{b}^{calc}$= calculated average neutron scattering length
- j= a Wyckoff position (2a, 2c, 2d or 2b)
- X, Y= fractions of cation (Cu, Zn and/or Sn)
- *b*= neutron scattering length of the element (b_{Cu}=7.718 fm, b_{Zn}=5.680 fm, b_{Sn}=6.225 fm)

Considering that each site could be occupied by more than one cation, the sum (equation 6) will be equal to one for a full occupied site or less than one if vacancies are presented. The total amount of the distributed cations on each of the crystallographic sites must be in a good agreement with the chemical composition. Furthermore, when modeling the distributions of the cations, it must be keep in mind that $\bar{b}^{calc}$ must lie within the error bar from the $\bar{b}^{exp}$. The errors are extracted from FullProf suite software by refining the site occupation factors (occ). Basically, in order to build a reasonable cation distribution model, $\bar{b}^{exp}$ and $\bar{b}^{calc}$ should be plotted simultaneously. Below an example of the application of the average neutron scattering length method is presented (see Figure 22).

In this particular example, a Cu-rich/ Zn-poor / Sn-rich composition has been chosen. This CZSTe present cation ratios of Cu/(Zn+Sn)=1.174 and Zn/Sn=0.777 (determined by WDX spectroscopy analyses) and exhibit a C-D type mixture off-stoichiometry with 81% C-type and 19% D-type, those percentages have been deduced by linear combination, as described in section 2.2.1 (page 27). The chemical composition of this kesterite phase is: $Cu_{2.181}Zn_{0.814}Sn_{1.048}Se_4$. From Rietveld refinements, the obtained site occupations (occ) on each site are: $2a$ 0.98886 (0.028), $2c$ 0.92909 (0.038), $2d$ 1.12358 (0.053) and $2b$ 1.00122 (0.034). Taking previous equations into account $\bar{b}^{exp}$ is obtained by multiplying those occ values times their corresponding neutron scattering length. By other hand $\bar{b}^{calc}$ is deduced out of the cation distribution model for each Wyckoff position ($2a$, $2c$, $2d$ or $2b$). By summing each cation fraction multiplied by their corresponding neutron scattering length. The resulted model from this particular CZSTe is presented in the following Table 7*:*

***Table** 7 Cation distribution example model of an off-stoichiometry C-D type mixture kesterite $Cu_{2.181}Zn_{0.814}Sn_{1.048}Se_4$. Calculated and experimental average neutron scattering length results are presented on the last two columns.*

Model	**Cu**	**Zn**	**Sn**	$\bar{b}^{calc}$	$\bar{b}^{exp}$
2a (Cu)	1	0	0	7.718	7.632
2c (Cu)	0.85	0.15	0	7.4123	7.171
2d (Zn)	0.288	0.664	0.048	6.2931	6.382
2b (Sn)	0	0	1	6.225	6.233
sum	2.138	0.814	1.048		
Cu_i	0.043				

Figure 22a plotted simultaneously $\bar{b}^{exp}$ and $\bar{b}^{calc}$; in square symbols the experimental scattering length with its error and in stars the calculated neutron scattering length out of the cation fractions from Table 7. This model is in a good agreement with the chemical composition $Cu_{2.181}Zn_{0.814}Sn_{1.048}Se_4$ and $\bar{b}^{calc}$ lie within the $\bar{b}^{exp}$ errors.

From Figure 22a, it can be observed that $\bar{b}^{exp}$ at 2*a* and 2*b* site lie within the neutron scattering length value of the corresponding elements (b_{Cu}=7.718 fm, b_{Sn}=6.225 fm) so those positions are fully occupied by copper and tin respectively. Whereas, 2*c* and 2*d* are significantly lower and higher as expected, this is an indication of presence of point defects such as the antisite defect due to an element with higher or lower neutron scattering length that is located at that site.

When the model has been proved, the percentages of each cation can be plotted versus each crystallographic sites (100% mean a fully occupied site), such plot is shown in Figure 22b. Since this CZTSe is Cu-rich/ Zn-poor / Sn-rich 81% C-type and 19% D-type mixture; the Cu_{Zn} antisite defect is expected, therefore, the (15%) Zn_{Cu} antisite on the 2*c* Wyckoff position is attributed to the Cu-Zn disorder defect, thereby, the amount of Cu_{Zn} antisite defect on the 2*d* site (28.8%-15%=13.8%) is attributed to C-type (9.5%) and to D-types (4.3%) because this defect is expected on both types. Additionally, the presence of tin on zinc antisite (Sn_{Zn}=4.8%) expected for C-type and copper interstitials (Cu_i =4.3%) expected on D-type have been observed.

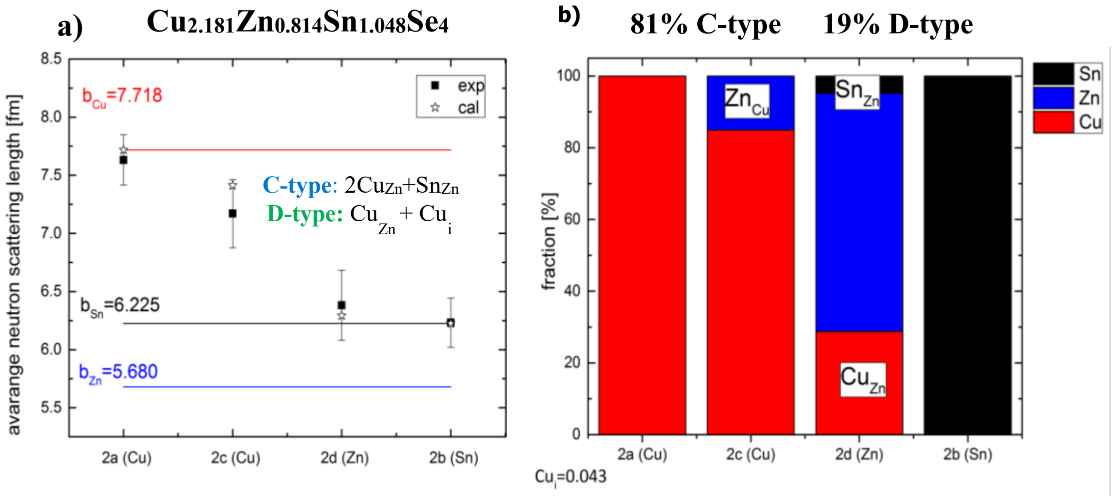

Figure 22 a) *Neutron scattering lengths where the square symbols represent* $\bar{b}^{exp}$*with its error bars and the star symbols represent* $\bar{b}^{calc}$ ***b)*** *cation distribution of each crystallographic site with its percentages of point defects.*

2.4 Electrical characterization: Temperature dependence of CZTSe resistivity

Electrical resistivity is an important intrinsic physical property of a material; independently of the size or shape of a sample it describes how much a material resists the flow of electric current. Resistivity is represented by the Greek letter ρ, by other hand, electrical conductivity represented by the Greek letter σ, is defined as the inverse of the resistivity ($\sigma=\mathbf{1}/\rho$). Conductivity of a material is determined by two factors: the concentration of free carriers available to conduct current and their mobility. In a crystalline solid exhibiting band transport in delocalized states (long carrier mean free paths), the mobility dependence on temperature is dictated by two types of scattering mechanisms: the impurity scattering and the lattice vibration (phonons). At high temperatures, lattice phonons will inhibit carrier motion but at low temperatures, phonons are "frozen", so impurity scattering dominates. Moreover, introduction of disorder into a perfect crystal disrupts the delocalization of charge carriers throughout the entire solid. In semiconductor materials, disruption in crystalline order creates localized states (also called traps) between valence and conduction band (given donor and acceptor states). Those localized states have a profound effect on the overall electronic properties, because carriers (electrons and holes) may fall into it and become immobilized (trapped), so to become mobile carriers must jump or "hop" from one localized state to another [55]. In this case, electronic transport in structural disordered materials is proposed to occur through "hopping" mechanism. The electron's mobility associated with this type of hopping motion among localized states is thermally assisted by thermal vibrations of the lattice or directly from an external electrical field.

In semiconductor materials, two types of conduction mechanisms are usually observed: at high temperatures the conductivity can be described by free charge carriers. But at low temperatures the conductivity is explained in terms of hopping conduction associated with defects in the band gap of the material.

There are three different types of hopping conductivity:

1) The nearest neighbor hopping (NNH)

In semiconductors, e.g., *n*- or *p*-type there are ionized donors or acceptors. Because of those ionized impurities the energy levels are affected by potential fluctuation. Electrons hop between there spatially fluctuated levels by emitting or absorbing phonons to surmount the potential barrier to the nearest neighbor site, thus, this type of hopping is called nearest neighbor hopping.

2) Mott-type variable range hopping (M-VRH)

The hopping impurity conduction at sufficient low temperatures, resistances between neighboring impurities typical become larger than those connecting some remote impurities whose unoccupied localized levels happened to be concentrated in a narrow band near the Fermi level. This range hopping takes place when the electron density of state (DOS) at the fermi level is constant. The characteristic hopping length increases with lowering the temperature (hence the name Mott variable-range hopping or M-VRH) [56].

3) Efros - Shklovskii variable range hopping (SE-VRH)

Efros and Shklovskii [57] proposed that multi-particle Coulomb interactions between electrons can decrease the density of states at the Fermi level, thus this modification from Mott variable-range hopping is then called Efros-Shklovskii Variable Range Hopping. In the region of the SE-VRH a Coulomb gap is formed, because of influence of the long-range Coulomb correlations between hopping charge carrier. SE-VRH is found when the DOS has a parabolic quasi-gap.

In Figure 23, schematic representation of variable range hopping regimes of the density of states (DOS) in the acceptor band near the edge of the valence band. The delocalized states at the center of the acceptor band and localized states at the edges have been taken into account. In Figure 23a) region of Mott VRH, density of state (DOS) is constant around the Fermi level and Figure 23b) in the region of SE VRH, a Coulomb gap is formed.

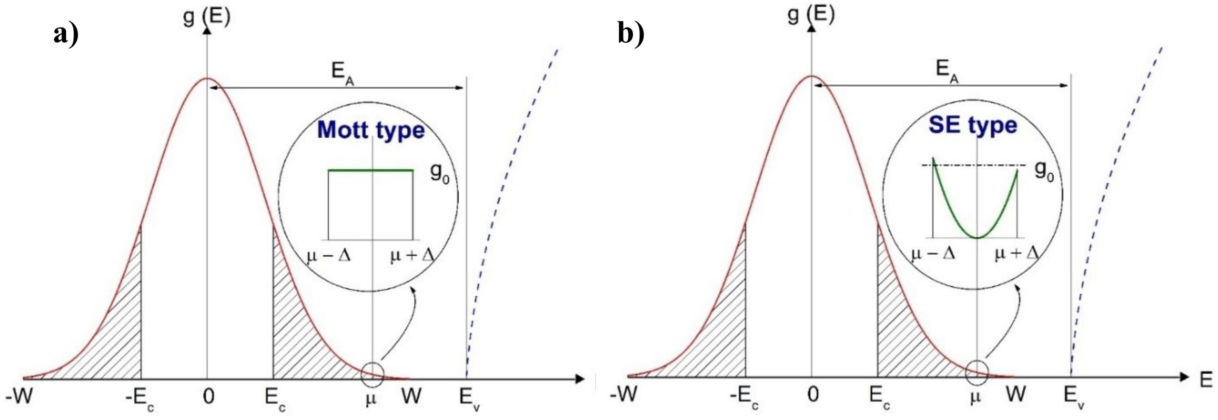

Figure 23 *Schematic representation of the density of states (DOS) in the acceptor band near the edge of the valence band.* ***a)*** *Region of Mott VRH, where DOS is constant around the Fermi level and* ***b)*** *in the region of SE VRH where a Coulomb gap is formed [Guc, M., et al. (2014). "Variable-range hopping conductivity in* $Cu_2ZnGeSe_4$ *single crystals." Solar Energy Materials and Solar Cells 127: 87-91].*

The resistivity in cases of hopping conductivity can be expressed as:

$$\rho(T) = A_p T^m \exp\left[\left(\frac{T_{0p}}{T}\right)^{1/p}\right]$$ ***Equation 7***

Where:

$T_{0\rho}$ is the characteristic hopping temperature

m=1/ ρ; ρ=1 in nearest neighbor hopping (NNH), ρ=2 in Efros - Shklovskii (S-E VRH) regime and ρ=4 in the Mott variable range hopping (M-VHR).

The variable range hopping VRH conduction regime could be determined according to the the temperature dependence of the resistivity in accordance with above equation 7.

In this work, temperature dependence resistivity measurements ρ(T) of off-stoichiometric CZTSe powder samples were performed at the Institute of Applied Physics of the Academy of Sciences at Chisinau Moldova. Only single phase samples were selected to disregard the influences of the secondary phases. Powder samples were pressed into homogenous pellets with approximately 5mm diameter and 1mm thickness. Four point electric contacts made by silver paste were assembled onto the pellets obeying the Van der Pauw method which allows measurements on samples of arbitrary shape [58] see Figure 24a,b. Measurements took place in the temperature range from 50-300 K, to avoid uncontrolled heating of the sample during the measurements, the applied current was kept below than 100µA. The study of temperature dependence of electrical conductivity of the semiconductor material is important for understanding the transport and the conductivity mechanism of the charge carriers.

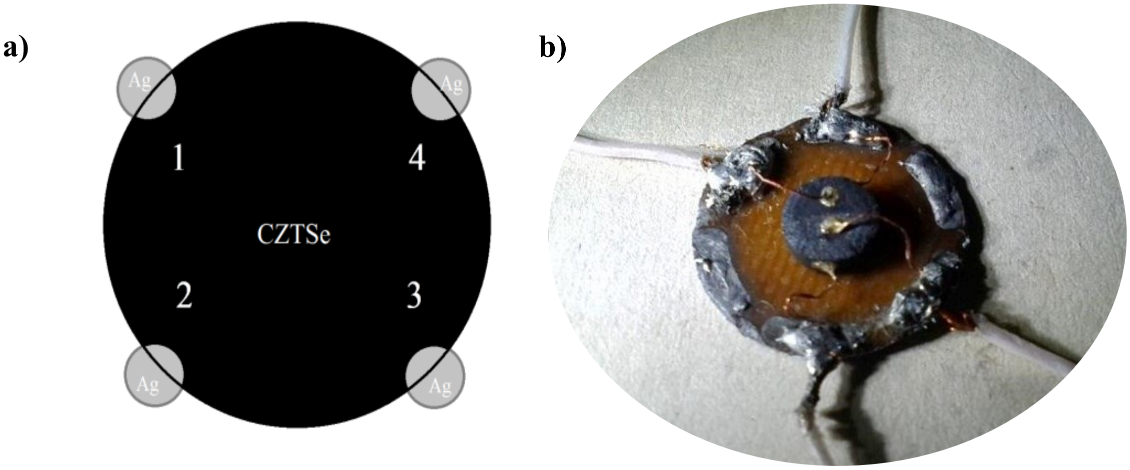

Figure 24 a) *Schema of CZTSe pellets under Van der Pauw configuration* ***b)*** *CZTSe pellet with 4 silver contacts.*

3.Results and Discussions

3.1 Synthesis and Phase analysis

3.1.1 Copper poor region

Synthesis of kesterites inside the copper poor region are of great interests because the best reported kesterite based solar cells energy conversion efficiencies are reported within this region. Figure 25 shows the best efficiencies according to their cation ratios [59]. The current record 12.6% is not included but also exhibits cation ratios in the copper poor region: Cu/(Zn+Sn)=0.8 and Zn/Sn=1.1 [1].

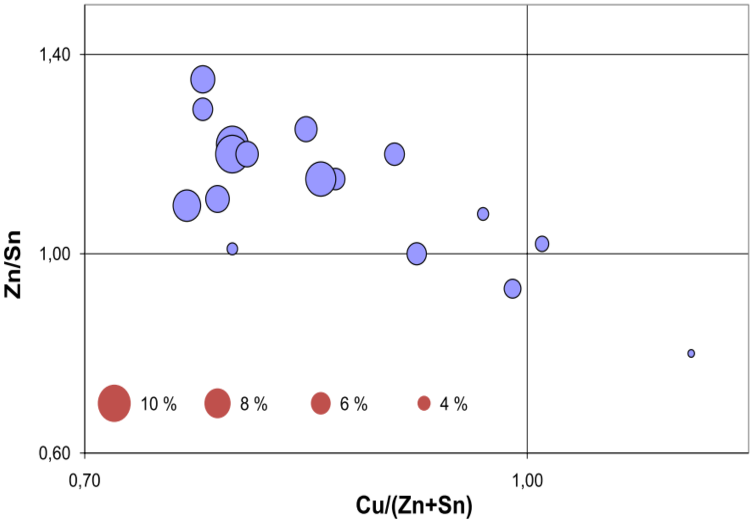

Figure 25 *Best kesterite solar cell within the cation ratios; the diameter of the circles is proportional to the conversion efficiency [Delbos, S. (2012). "Kësterite thin films for photovoltaics: a review." EPJ Photovolt. 3: 35004].*

For this work, polycrystalline powder samples in the copper poor region have been synthesized as described in section 2.1 "*Powder samples synthesis by solid state reaction*" (page 21).

Intended composition have been calculated according to the corresponding off-stoichiometry A- and B-type formulae, as described in Table 3 of section 1.5 "*Off-stoichiometry – cation substitutions*" (page 17).

- **A-type: copper poor, zinc poor and tin constant**

For synthesis of samples with an intended copper poor, zinc poor and tin constant composition, the A-type line $Cu_{2-2x}Zn_{1+x}SnSe$ formula has been used. The values of "*x*" varied from 0.025 to 0.125. See the following Table 8 which shows the corresponding intended formulae and intended cation ratios. In total 10 samples inside this range have been synthesized.

Table 8 *Intended composition within the A-type off-stoichiometry line.*

No.	x	$Cu_{2-2x}Zn_{1+x}SnSe_4$	Cu/(Zn+Sn)	Zn/Sn
1	0.025	$Cu_{1.950}Zn_{1.025}SnSe_4$	0.963	1.025
2	0.050	$Cu_{1.900}Zn_{1.050}SnSe_4$	0.927	1.050
3	0.075	$Cu_{1.850}Zn_{1.075}SnSe_4$	0.892	1.075
4	0.100	$Cu_{1.800}Zn_{1.100}SnSe_4$	0.857	1.100
5	0.125	$Cu_{1.750}Zn_{1.125}SnSe_4$	0.824	1.125

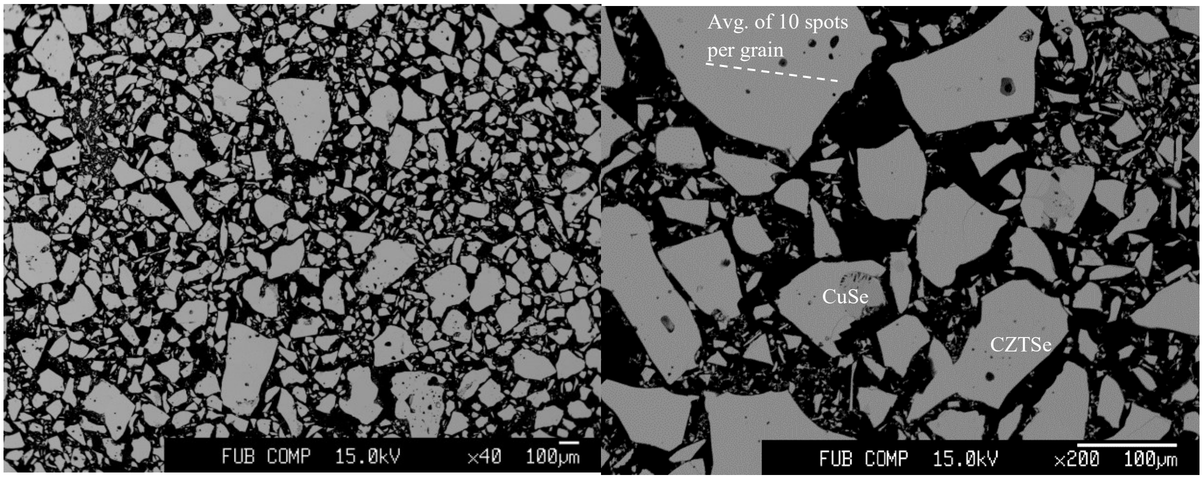

Figure 26 *Backscattered electron micrographs of polished powder sample at different magnifications x40 (left) and x200 (right). In total 35 grains have been selected and 10 points where measured and averaged.*

The cation ratios Cu/(Zn+Sn) and Zn/Sn of the kesterite main phase have been obtained from WDX spectroscopy analyses, as described in section 2.2 “*Chemical characterization”* (page 23). An example of a backscattered electron micrograph of a synthesized sample is presented in Figure 26, out of this sample 35 grains were selected, on each grain 10 points where measured and averaged.

To prove the homogeneity of the kesterite phase, the resulted WDX based averaged atomic percentages of each measured grain were plotted as shown in Figure 27. The values within the 2% error of the microprobe were averaged. Thus the cation ratios Cu/(Zn+Sn)=0.979 and Zn/Sn=1.075 of the kesterite phase have been deduced. It has been then proved that the sample contains only one kesterite phase and exhibit a copper poor (Cu/(Zn+Sn) < 1) and zinc rich (Zn/Sn>1) composition. Grains where secondary phases have been detected were averaged separately.

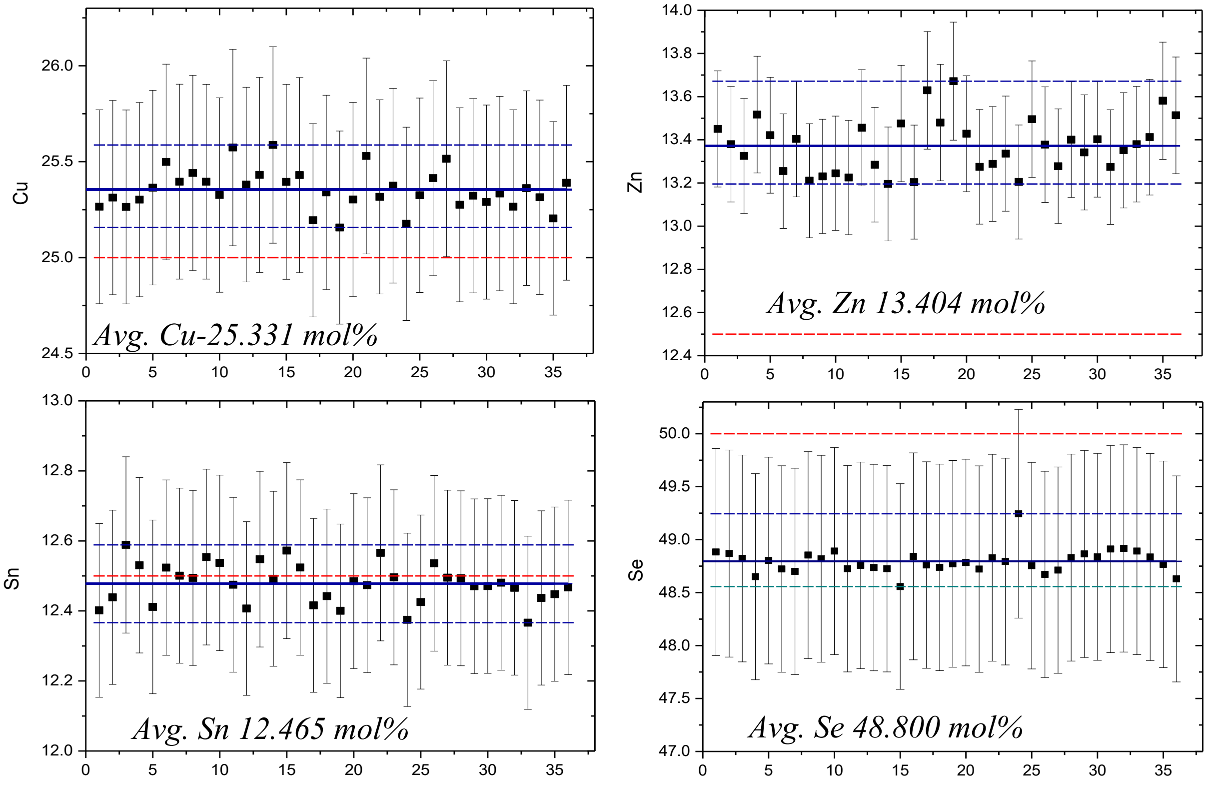

Figure 27 *Averaged mol% Cu,Zn,Sn and Se out of 35 grains measured on a powder sample. The results proved that it has only one kesterite phase with copper poor and zinc rich composition: cation ratios Cu/(Zn+Sn)=0.979 Zn/Sn=1.075.*

In fact, secondary phases have not been detected with an exactly binary composition. They instead have a solid solution composition with more than two elements. However, to simplify this section all secondary phases will be described as binary compounds since their real chemical composition is indeed significantly close to the binary compounds. The solid solution compositions of all secondary phases are described in the section: *3.1.6 Secondary phases – overview* in page 72.

As mentioned above, in total 10 samples with intended A-type composition (see Table 8) have been analyzed by chemical characterization. The resulted occurrences of secondary phases are following discussed.

As expected in zinc rich region, zinc selenide "ZnSe" was the most predominant secondary phase. ZnSe phase has been detected in 5 of those 10 samples. Additionally, tin diselenide phase "$SnSe_2$" has been detected in 3 samples. Less expected secondary phases such as copper (II) selenide "CuSe" and copper (I) selenide "Cu_2Se" have been detected in 2 and 1 samples respectively. Remarkably three samples have been found to be single phase but with an off-stoichiometric kesterite composition. An overview of the secondary phases formation is given is Figure 28 *a,b*. The samples are colored according to the occurrence of secondary phases; red - single phase (kesterite), magenta - ZnSe, green - $SnSe_2$ and blue-CuSe and/or Cu_2Se.

Furthermore, Figure 28*a,b* also show the intended A-type composition (star symbols) compared to the real obtained cation ratios (square symbols) of the 10 synthesized samples. All obtained ratios exhibit a deviation from the intended.

For instance, the square symbol labeled as number "1" in Figure 28a, corresponds to the intended values of Cu/(Zn+Sn)=0.963 and Zn/Sn=1.025 when x=0.025 (see Table 8). But the obtained ratios (see square symbol labeled as "1" in Figure 28a) exhibit a Cu/(Zn+Sn)= 0.950 and Zn/Sn=1.099, thus ratios differ from the intended. However, it can be assumed that the reason of such shift was due the formation of secondary phase "CuSe" which reduced the amount of copper from the main phase kesterite. Also, losses of tin shift the sample out of the A-type line (tin constant).

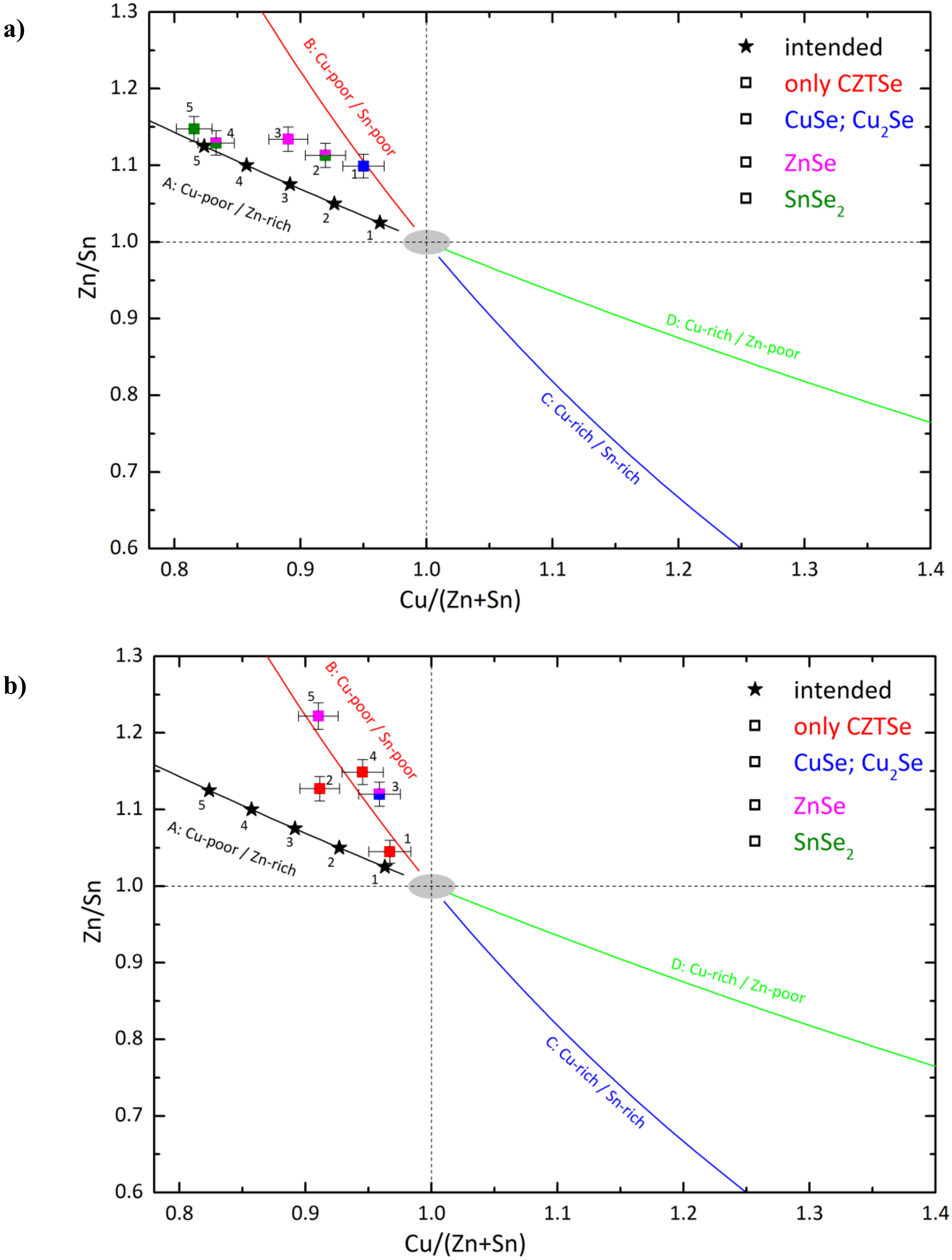

Figure 28 a), b) *A-type: Intended (stars) vs obtained (squares) cation ratios with the corresponding color of detected secondary phases: red - single phase (kesterite), magenta - ZnSe, green -* $SnSe_2$ *and blue-CuSe and/or* Cu_2Se

Remarkably, the sample No. "1" of Figure 28b has been found to be a single phase kesterite sample with cation ratios; Cu/(Zn+Sn)= 0.967 and Zn/Sn=1.045. Those obtained ratios are significantly closer to the intended (Cu/(Zn+Sn)=0.963 and Zn/Sn=1.025). The slightly deviation may have occurred due to small losses of tin.

Nevertheless, finding a reason of deviation from each intended vs obtained cation ratios is not always obvious. For instances, sample No. "2" of Figure 28b: its deviation indicate that some copper and tin have been lost from the kesterite phase, however, none secondary phases have been detected within this sample.

An explanation of such element losses can be found by considering the synthesis procedure (see section 2.1). The solid state reaction takes place inside a vacuum and sealed silica ampule. For the first reaction multiples temperatures have been selected (250°, 450°, 600° and 750°C). Following by an annealing step at 750° C. It is then likely that during the reaction some losses of elements occur or form a secondary compound. In fact, some materials have been observed deposited on the silica ampule surface. Such materials have been analyzed, the results are presented in the further section: *3.1.5 Elements losses during synthesis – SEM, EDS"* in page 68.

- **B-type: copper poor, zinc rich and tin poor composition**

Further synthesis in copper poor region were intended to follow the B-type line with a copper poor, zinc rich and tin poor composition. For this synthesis the formula: $Cu_{2-2y}Zn_{1+3y}Sn_{1-y}Se_4$ has been used and the values of "*y*" vary from 0.025 to 0.075. See Table 9 with the corresponding intended chemical composition and cation ratios. In total 6 samples have been synthesized in this range.

***Table 9** Intended composition within the B-type off-stoichiometry line.*

No.	**y**	**$Cu_{2-2y}Zn_{1+3y}Sn_{1-y}Se_4$**	**Cu/(Zn+Sn)**	**Zn/Sn**
1	0.025	$Cu_{1.950}Zn_{1.075}Sn_{0.975}Se_4$	0.951	1.103
2	0.050	$Cu_{1.900}Zn_{1.150}Sn_{0.950}Se_4$	0.905	1.211
3	0.075	$Cu_{1.850}Zn_{1.225}Sn_{0.925}Se_4$	0.860	1.324

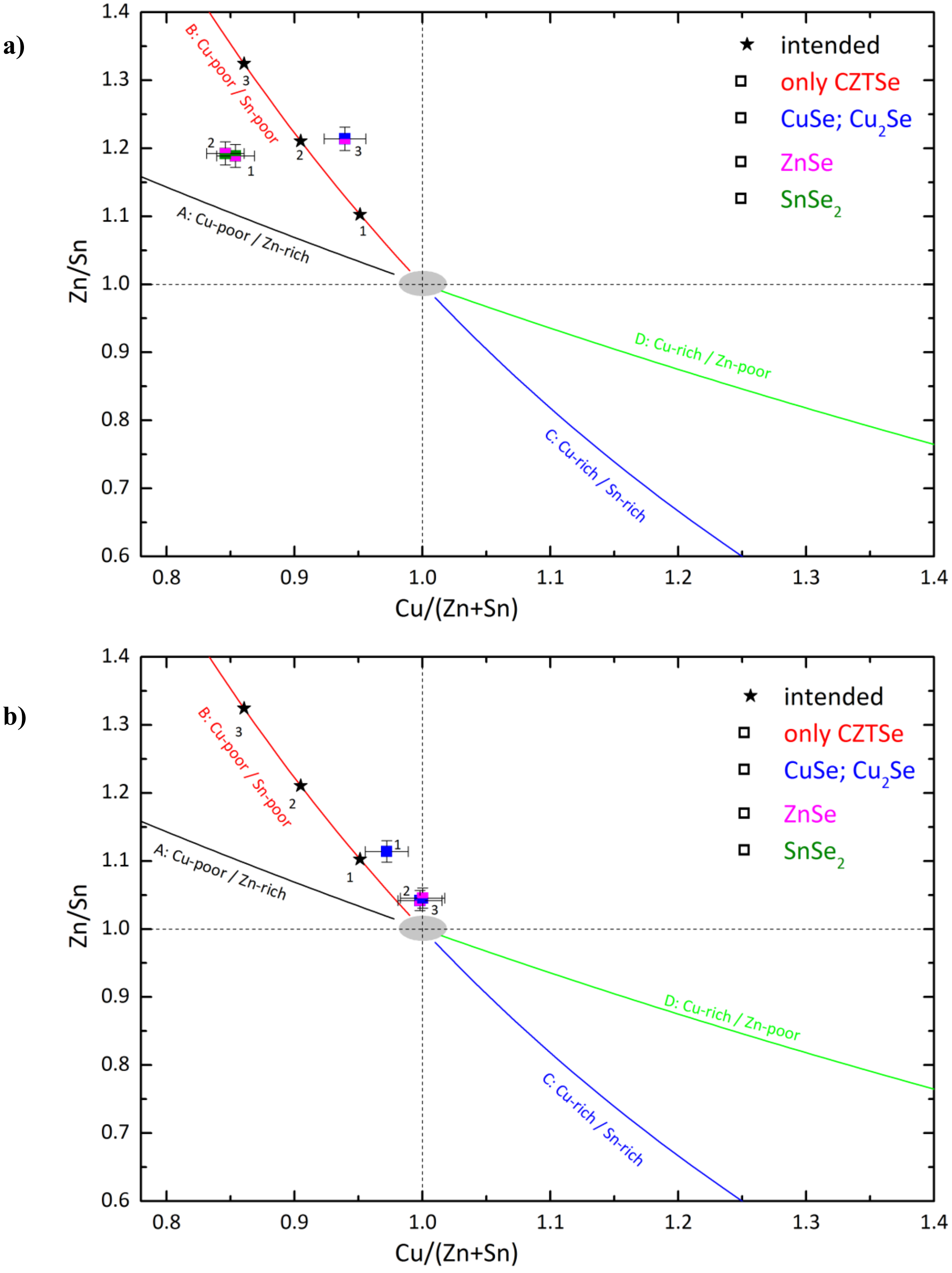

Figure 29 a, b *B-type: Intended (stars) vs obtained (squares) cation ratios with the corresponding color of detected secondary phases: red - single phase (kesterite), magenta - ZnSe, green -* $SnSe_2$ *and blue-CuSe and/or* Cu_2Se

The chemical characterization procedure applied on these 6 intended B-type samples was exactly the same as explained for the intended A-type samples. Figure 29*a,b* present the samples by colors according to the occurrences of secondary phases. Also the cation ratios deviation from ideal B-type line (star symbols) versus the obtained ratios (square symbols) is observed.

Phase analysis shows that zinc selenide “ZnSe” was the predominant secondary phase, as it is expected in zinc rich region. ZnSe was detected in 5 out of 6 total samples. Additionally, “$SnSe_2$” phase has been detected in 2 samples. Also “CuSe” has been detected in 3 samples and “Cu_2Se” phase only in 1 sample.

The cation ratios deviation, for example, on samples labeled as No. “1” and No. “2” (see Figure 29a) were intended to have values of y=0.025 and y=0.050, respectively (see Table 9). But both samples shifted into a copper poorer region despite that no copper secondary phases were detected. Maybe the shift in Sample No. “1” might occur due to losses of tin related with the formation of $SnSe_2$ phase.

Moreover, in Figure 29b samples labeled as No. “2” and No. “3” were intended to have values of y=0.050 and y=0.075, respectively. However, both samples ended overlapping near to the stoichiometric region. One reason of these deviations might be due to zinc losses related with the formation of “ZnSe” phase.

Conclusions

By comparing the results out of samples with A- and B-type indented compositions have been found that:

i. “ZnSe” in both cases was the most preferred secondary phase. It has been detected: between the A- and B- type line, after the B- type line, as well as near to the stoichiometric region.
ii. “CuSe” and “Cu_2Se” which are not expected in copper poor region. Have been detected starting from the B-type line and also near to the stoichiometric region.
iii. Copper selenides phases usually occurred together with zinc selenide phase.

iv. "$SnSe_2$" has been detected only between the A- and B- type line.
v. Single phase kesterites have been detected between the A- and B- type lines as well as on the B-type line. Single phase kesterite were observed only on intended A-type samples.
vi. Deviations of cation ratios from intended vs obtained were more pronounced on B-type samples in comparison with A-type samples.
vii. Mostly all deviations within the copper poor region occurred due losses of tin.
viii. It is difficult to explain all deviations by just taking into account the presence of secondary phases. The synthesis conditions strongly influence the final product.

Further discussions of tin losses during the reaction are presented in section: *3.1.5 Elements losses during synthesis – SEM, EDS"* in page 68.

3.1.2 Copper rich region

Although most of the kesterite based solar cells are produced inside the copper poor region because this is where higher efficiencies have been reported. Analyses in the copper rich region are also of great importance in order to understand which factors might influence the performances of a kesterite based solar cell. For instances, study the occurrences of secondary phases is important, because as presented in Table 2 secondary phases have different band gap values than the kesterite phase. Therefore, the presence of some secondary phases, especially the ones with a lower bandgap could be harmful for the solar cell device. For this reason, intended samples within the copper rich region have been synthesized following the C- and D-type formulae described in Table 3.

- **C-type: copper rich zinc poor and tin rich**

The copper rich, zinc poor and tin rich composition follow the C-type line with an off-stoichiometric formula: $Cu_{2+2z}Zn_{1-3z}Sn_{1+z}Se_4$. The selected values of "*z*" varied from 0.025

to 0.075. Table 10 presents the corresponding intended chemical composition and cation ratios. In total 7 samples have been synthesized within this range.

Table 10 *Intended composition within the C-type off-stoichiometry line*

No.	z	$Cu_{2+2z}Zn_{1-3z}Sn_{1+z}Se_4$	Cu/(Zn+Sn)	Zn/Sn
1,2,3,4	0.025	$Cu_{2.050}Zn_{0.925}Sn_{1.025}Se_4$	1.051	0.902
5,6	0.050	$Cu_{2.100}Zn_{0.850}Sn_{1.050}Se_4$	1.105	0.810
7	0.075	$Cu_{2.150}Zn_{0.775}Sn_{1.075}Se_4$	1.162	0.721

The results from chemical analyses out of these 7 intended C-type samples have been plotted by colors according to the occurrence of secondary phases (see Figure 30). It can be observed that copper selenides secondary phases: "CuSe" and "Cu_2Se" (in blue) were the predominant. In fact, the detection of such phases is expected inside the copper rich region.

Two samples intended to be *z*=0.025 (see Table 10) are shown in Figure 30 as No. "1" and No. "2". In both cases, zinc selenide "ZnSe" (in magenta) has been only detected near to the stoichiometric region. Along with the "ZnSe" phase: "CuSe" and "Cu_2Se" phases were also detected. In the case of samples labeled as No. "4" and "5" the "CuSe" as well as the "Cu_2Se" secondary phases have been detected but in samples No. "3", "6" and "7" only "CuSe" has been detected as secondary phase.

Deviations of intended (stars) vs obtained (squares) cation ratios, also presented in Figure 30. The intended C-type ratios (star symbols) are compared with the obtained ratios (square symbols). Samples: No. "1, 2, 3" and "4" were intended to have a Cu/(Zn+Sn)=1.051 and Zn/Sn=0.902 (see Table 10). But their obtained cation ratios exhibit strong deviations. Especially on the Zn/Sn ratio which ended much higher than expected. Obtained values of Zn/Sn were found within a range from 0.995 to 1.132. But a smaller deviation was observed in the Cu/(Zn+Sn) ratio. The obtained values of Cu/(Zn+Sn) were found within a range from 0.996 to 1.027. In this case the formations of copper secondary phases might shifted the samples from intended Cu/(Zn+Sn)=1.051 into near stoichiometry region.

In the case of samples: No. "5" and No. "6", their obtained Cu/(Zn+Sn) ratio were: 1.088 and 1.103, respectively. These ratios are indeed quite near to their intended ratio

Cu/(Zn+Sn)=1.105. Concerning to the Zn/Sn ratio, the obtained values were: 0.871 for No.5 and 0.883 for No.6. Although these Zn/Sn ratios were higher than the intended Zn/Sn=0.810, the deviations of samples No. "5-6" were much lower in comparison with samples No. "1-4".

Finally, the obtained cation ratios of sample: No. "7": Cu/(Zn+Sn)=1.174 and Zn/Sn=0.777 exhibit a small deviation because those ratios are not too far from the intended ratios: Cu/(Zn+Sn)=1.162 and Zn/Sn=0.721 (see Table 10).

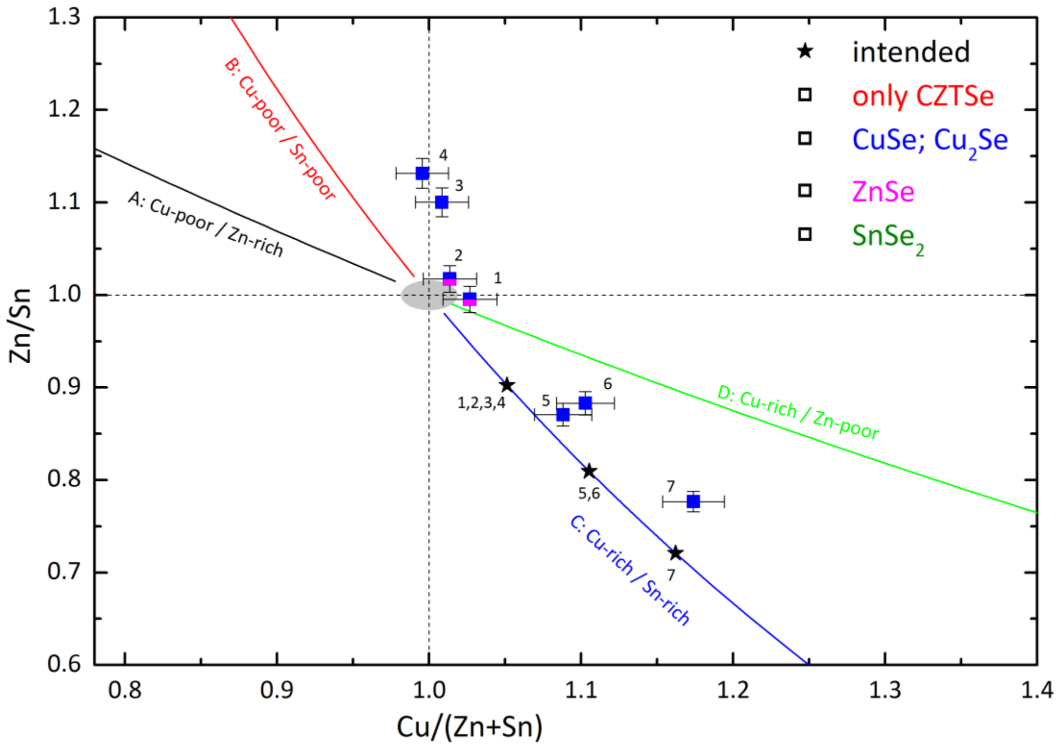

Figure 30 *C-type and Intended (stars) vs obtained (squares) cation ratios with the corresponding color of detected secondary phases: red - single phase (kesterite), magenta - ZnSe, green - SnSe2 and blue-CuSe and/or Cu2Se*

- **D-type: copper rich zinc poor and tin constant**

Further samples in the copper rich region have been synthesized with intended D-type off-stoichiometric composition: copper rich, zinc poor and tin constant. For this synthesis the formula: $Cu_{2+2m}Zn_{1-m}SnSe_4$ has been used and the values of "*m*" varied from 0.050 - 0.150. See Table 11 which presents the corresponding intended chemical composition and cation ratios. In total 3 samples have been synthesized within this range.

***Table 11** Intended composition within the D-type off-stoichiometry line*

No.	m	$Cu_{2+2m}Zn_{1-m}SnSe_4$	Cu/(Zn+Sn)	Zn/Sn
1	0.050	$Cu_{2.100}Zn_{0.950}SnSe_4$	1.077	0.950
2	0.100	$Cu_{2.200}Zn_{0.900}SnSe_4$	1.158	0.900
3	0.150	$Cu_{2.300}Zn_{0.850}SnSe_4$	1.243	0.850

Chemical analyses of intended D-type samples have been plotted by colors according to the occurrence of secondary phases (see Figure 31). In this case only copper selenides secondary phases (in blue) have been observed. "CuSe" phase have been detected in samples labeled as No. "1" and "2" and the "Cu_2Se" phase have been detected within all samples.

Intended D-type cation ratios (star symbols) versus the obtained cation ratios (square symbols) are also presented in Figure 31. All obtained cation ratios out of these intended D-type samples have been found inside the copper rich region (Cu/(Zn+Sn)>1).

Deviation of cation ratios were especially observed in sample: No. "1". It was intended to be *m*=0.050 (see Table 11). But its obtained cation ratios: Cu/(Zn+Sn)=1.023 and Zn/Sn=1.085 exhibit a strong deviation. Most likely this shift occurred due to copper secondary phases formations and large amount of tin loss.

Fortunately, samples: No. "2" and "3" ended quite near to the intended D-type off-stoichiometry line. Their obtained cation ratios were: Cu/(Zn+Sn)=1.100; Zn/Sn=0.961 for No."2" and Cu/(Zn+Sn)=1.145; Zn/Sn=0.910 for No."3". These cation ratios also shifted from the intended values (see Table 11) but with a smaller deviation in comparison with sample No. “1”.

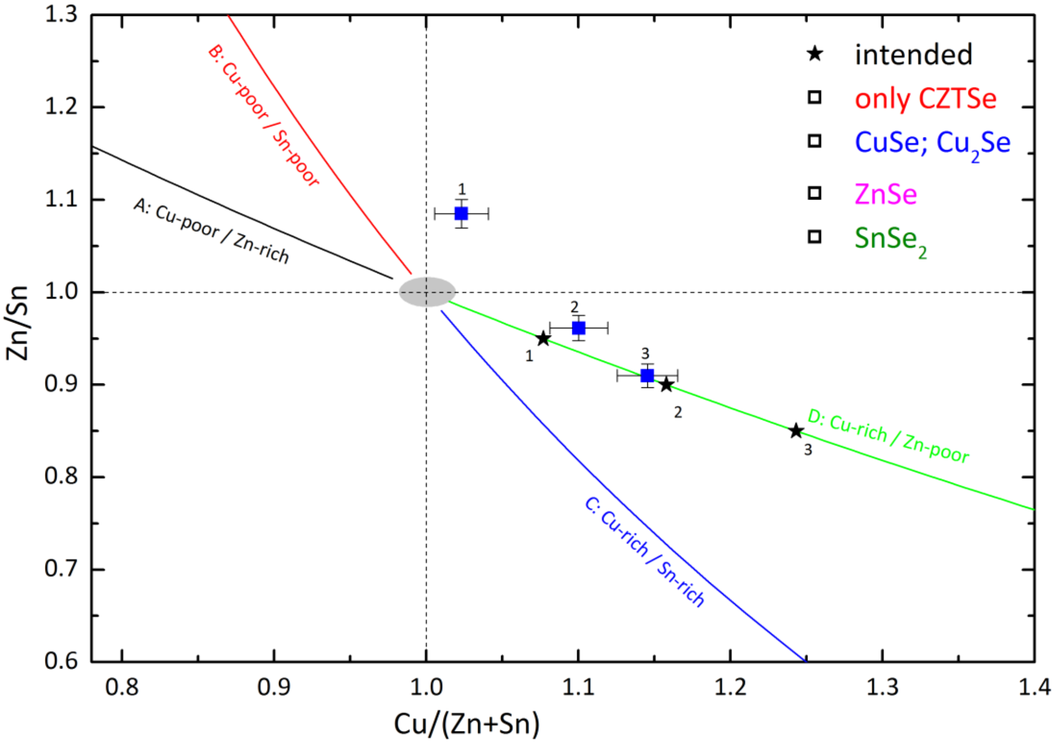

Figure 31 *D-type; Intended (stars) vs obtained (squares) cation ratios with the corresponding color of detected secondary phases: red - single phase (kesterite), magenta - ZnSe, green - SnSe$_2$ and blue-CuSe and/or Cu$_2$Se*

Conclusions

Summarizing the results inside the copper rich region of intended C- and D- type samples have been found that:

i. “CuSe” and “Cu$_2$Se” were the most preferred secondary phases and were usually detected together.
i. “CuSe” and “Cu$_2$Se” have been detected within all the Cu-rich region.
ii. Out of both copper selenides phases: the “CuSe” was the predominant.
iii. “ZnSe” secondary phase was detected only near to the stoichiometric region together with copper selenides phases.

iv. All obtained cation ratios have deviated from the intended C- and D-type compositions. Nevertheless, some samples have been obtained quite near to the C- and D- type lines.

v. Similar to copper poor A- and B- type intended samples, it is difficult to explain the shift from intended cation ratios by just taking into account the occurrences of secondary phases.

3.1.3 Stoichiometric region

Complementary to the Cu-poor and Cu-rich regions, the stoichiometric region is also interesting in order to study the influence of off-stoichiometric compositions. For this reason, 3 "$Cu_2ZnSnSe_4$" samples have been synthesized with intended cation ratios: Cu/(Zn+Sn) and Zn/Sn equal to 1.

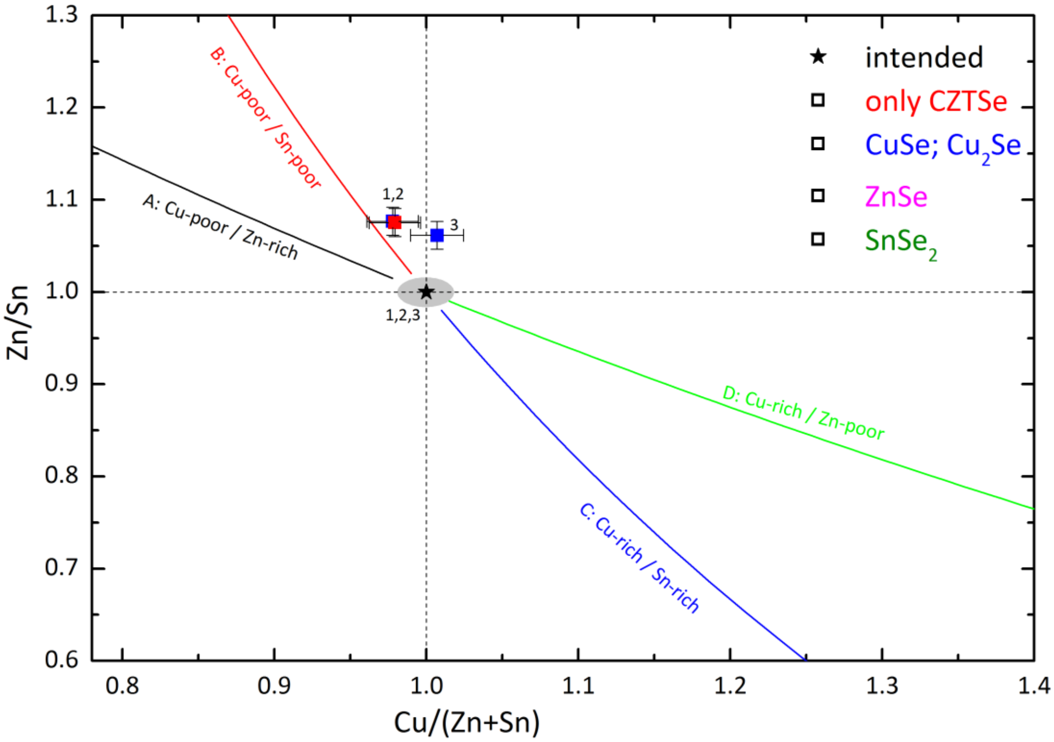

Figure 32 *Intended stoichiometric composition (star) vs obtained (squares) cation ratios with the corresponding color of detected secondary phases: red - single phase (kesterite), magenta - ZnSe, green -* $SnSe_2$ *and blue-CuSe and/or* Cu_2Se*.*

The results from chemical analyses out of these samples are presented in Figure 32. The samples are colored according to the occurrence of secondary phases: blue-CuSe and/or Cu_2Se and red - single phase (kesterite).

Secondary phases: “CuSe” and “Cu_2Se” have been detected in samples labeled as No. ”1” and No. “3” respectively. Although, the formation of “CuSe” is unexpected inside the copper poor region, similar results have been also observed in intended A- and B-type samples. Remarkably sample labeled as No. “2” has been found to be single phase kesterite. Detection of single phase kesterite near to the B-type line has been also observed in intended A-type samples (see Figure 28b).

All obtained cation ratios have deviated from the intended stoichiometric composition (see Figure 32). Samples labeled as No. “1” and No. “2” have shifted and overlapped in the copper poor and zinc rich region. Their obtained cation ratios are: Cu/(Zn+Sn)=0.979; Zn/Sn=1.075 for sample No.”1” and Cu/(Zn+Sn)=0.978; Zn/Sn=1.077 for sample No.”2”. In the case of sample No. “3”, its obtained ratio Cu/(Zn+Sn)=1.007 is almost as the intended value equal to 1 but its Zn/Sn=1.061 was slightly higher as the intended value.

Conclusions

i. Stoichiometric $Cu_2ZnSnSe_4$ have not been obtained.
ii. “CuSe” has been detected in the Cu-poor region (alike A- and B-type samples).
iii. “Cu_2Se” has been observed in the copper rich region (alike C- and D-type samples).
iv. Deviations from the intended stoichiometric composition suggest losses of tin.

3.1.4 Off-stoichiometric CZTSe - overview

An overview of all synthesized kesterites within different intended off-stoichiometric composition have been plotted according to obtained kesterite cation ratios Cu/(Zn+Sn) vs Zn/Sn, additionally the kesterites are colored according to the occurrence of secondary phases or single phase kesterites (Figure 33).

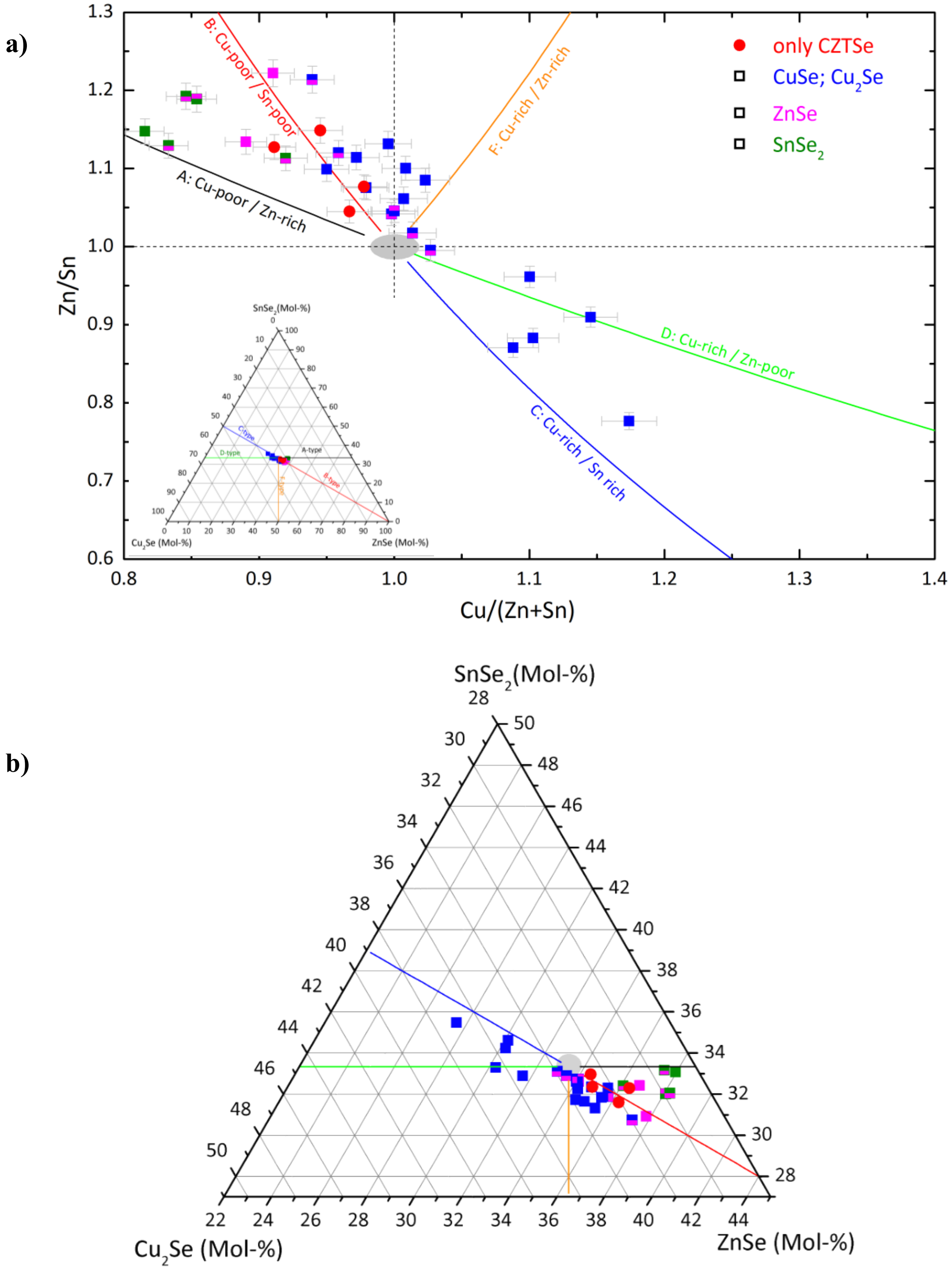

Figure 33 a) *Cation ratios plot of off-stoichiometric CZTSe powder sample and* ***b)*** *Cu_2Se-$ZnSe$-$SnSe_2$ pseudo-ternary diagram (zoom to 50%) colored according to detected secondary phases: red - single phase (kesterite), magenta - ZnSe, green - $SnSe_2$ and blue- CuSe and/or Cu_2Se.*

The cation ratios plot Cu/(Zn+Sn) vs Zn/Sn and the pseudo-ternary Cu_2Se-ZnSe-$SnSe_2$ phase diagram (100%) give an overview of all obtained off-stoichiometric kesterites (Figure 33a). But in order to have a better overview, the pseudo-ternary phase diagram was zoomed to 50% (Figure 33b). In total 29 samples have been synthesized, off-stoichiometric kesterite has been detected as the main phase within all the samples.

Results revealed that only few samples lie on the intended A-, B-, C- or D-type line. In fact, the majority of the kesterite phase ended as a mixture of two different types. For this reason, Figure 33 include additionally the Cu-rich, Zn-rich and Sn-poor F-type line (formula: $Cu_{2(2-k)}Zn_{2-k}Sn_kSe_4$). Although none intended F-type samples have been synthesized, some of the obtained kesterite phase can be considered as B-F type mixture. As a comment, the E-type off-stoichiometry line will be omitted, because neither intended samples have been synthesized as well as any kesterite phase ended near to its off-stoichiometric region (Cu-poor, Zn-poor and Sn-rich).

The occurrences of secondary phases within all 29 synthesized samples have been highlighted in Figure 34a, b, c and d. The area where $SnSe_2$ has been detected is colored in green (see Figure 34a). This secondary phase has been observed only within A- and A-B type mixture region. The green area covered a cation ratios range: Cu/(Zn+Sn)=0.816-0.920 and Zn/Sn=1.113-1.192.

Figure 34b shows in magenta color areas where ZnSe has been detected. The main area covers the range: Cu/(Zn+Sn)=0.833-1.027 and Zn/Sn=0.995-1.192. Another smaller area is located near the B-type line, at a zinc richer region with cation ratios range: Cu/(Zn+Sn)= 0.910-0.939 and Zn/Sn= 1.214-1.222. Despite some ZnSe secondary phase has been also detected near to the stoichiometric region, it can be concluded that the preferable region for zinc selenide formation is when Zn/Sn >1.

Figure 34c shows the area where CuSe and/or Cu_2Se phases have been detected. As expected, those phases were predominant in kesterite phase with Cu/(Zn+Sn)>1. In the case of Cu_2Se phase has been detected within 10 out of 29 total samples. Its range of detection covers: Cu/(Zn+Sn)= 0.959-1.145 and Zn/Sn= 0.883-1.132. On the other hand CuSe is widespread; it has been detected within 16 out of 29 samples inside a larger range of Cu/(Zn+Sn)= 0.939-1.174 and Zn/Sn= 0.777-1.214.

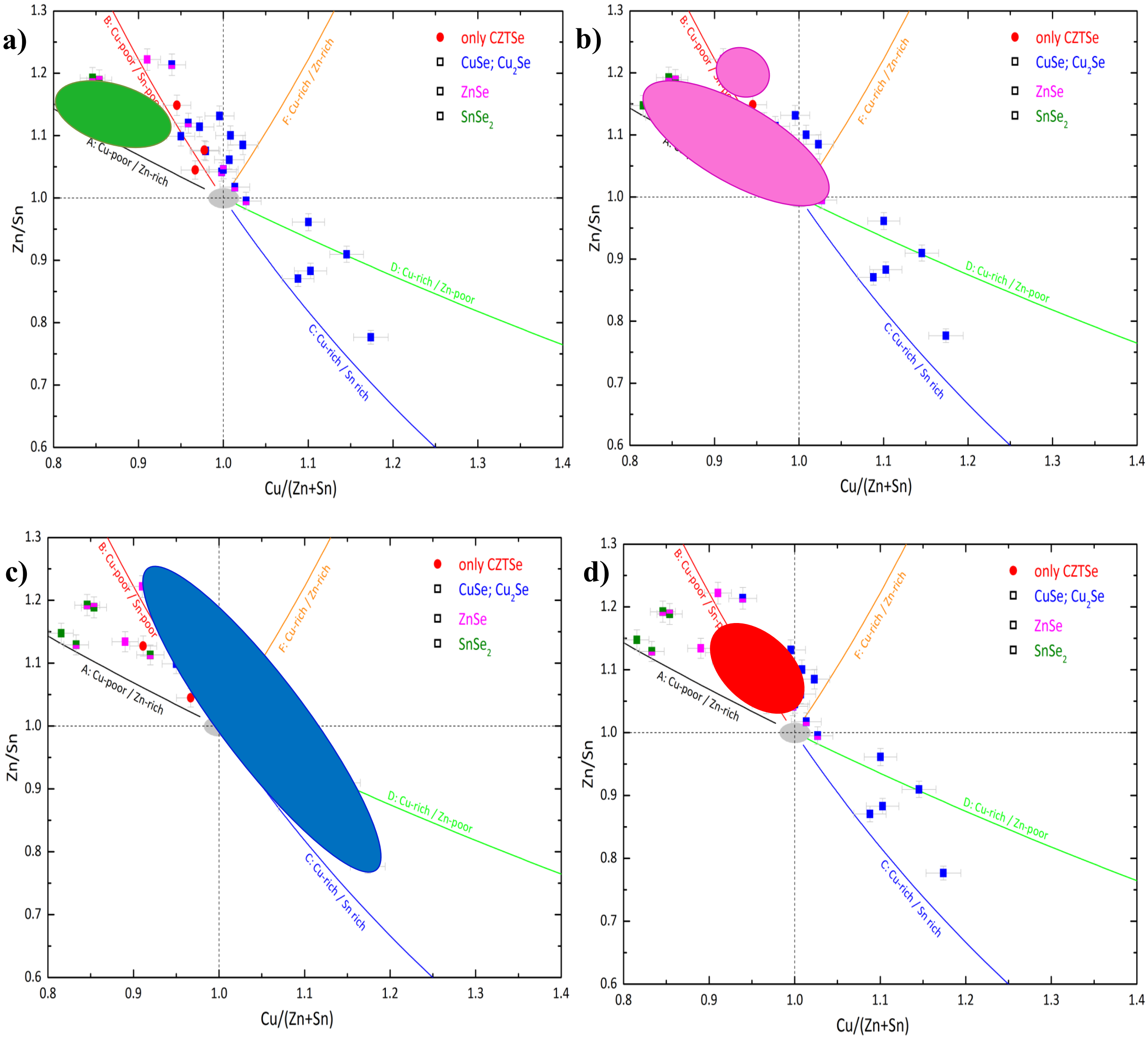

Figure 34 *Cation ratio plots according to occurrence of secondary phases**:** **a)** green - SnSe$_2$ **b)** magenta – ZnSe **c)** blue-CuSe and/or Cu$_2$Se and **d)** red - single phase (kesterite).*

As discussed in section 3.1.1 *Copper poor region* in page 49, the presence of copper selenides secondary phases are not expected when Cu/(Zn+Sn)<1. But as reported at *Valle-Rios et al.* [5] copper selenides secondary phases have been also detected within off-stoichiometric sulfide kesterites (CZTS). Nevertheless, the detection of those phases seems to be limited by the B-type line. For both CZTSe and CZTS, none copper selenide phases have been detected between the A- and B-type lines. Furthermore, the presence of copper selenides secondary phases between the A- and E-type off-stoichiometry lines is unsure, because no samples have been obtained inside this region.

Figure 34d highlighted in red the area where off-stoichiometric single phase kesterites have been found. Remarkably, all 4 single kesterite phase lie near to the B-type line. Its area of detection covers the cation ratios range: Cu/(Zn+Sn)= 0.911-0.978 and Zn/Sn=1.045-1.149. Two kesterite single phases are located near to the stoichiometric region but the other two exhibit a copper-tin poorer and zinc richer composition. Moreover, as reported in *Valle-Rios et al [5]*, the region where off-stoichiometric CZTSe single phases were detected is very similar to the region where off-stoichiometric CZTS single phases have been observed.

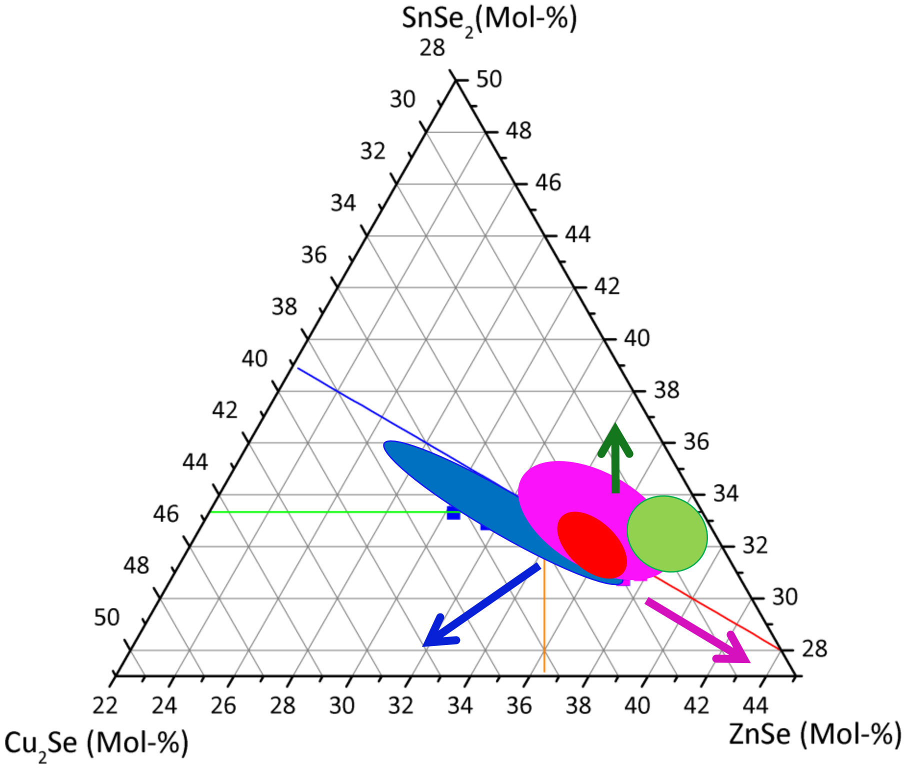

Figure 35 *Pseudo-ternary phase diagram with occurrence of secondary phases**:** green - $SnSe_2$, magenta – ZnSe, blue-CuSe and/or Cu_2Se and red - single phase (kesterite).*

A complementary overview of detected secondary phases is given by the pseudo-ternary phase diagram in Figure 35 (zoomed to 50%) where the trend of expected secondary phases is better observed.

Conclusions

i. Tolerance for single phase kesterite outside the stoichiometric region was observed.
ii. Off-stoichiometric single phase kesterites have been found near to the B-type line and close to the stoichiometric region, either on CZTSe or CZTSe compounds.
iii. Occurrences of secondary phases are highly expected, even inside the stoichiometric region.
iv. CuSe and/or Cu_2Se were detected within the Cu-poor region, however, its occurrences seem to be limited by the B-type line (either on CZTSe or CZTSe).
v. Formation of off-stoichiometric kesterite phase might be limited to Zn/Sn<1.25, because all results from intended B-type samples with Zn/Sn=1.324 have shifted into lower Zn/Sn values. Nevertheless, to prove its limits further synthesis must be carried on.

3.1.5 Elements losses during synthesis – SEM, EDS

Chemical composition and properties of kesterite materials are strongly determined by its synthesis route and growth conditions. In this work polycrystalline powder samples have been synthesized by solid state reaction. As described in section 2.1"*Powder samples synthesis by solid state reaction*" (page 21), the reaction takes place inside a vacuum and sealed silica (SiO_2) ampule.

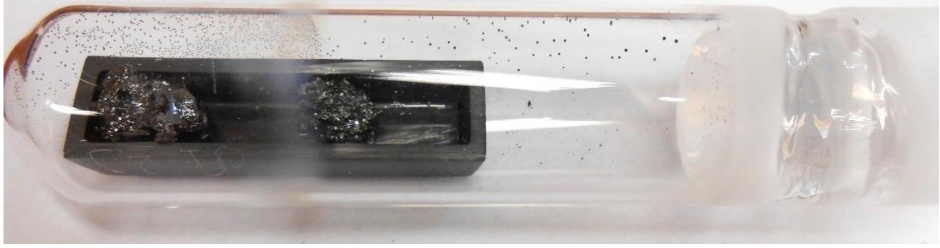

***Figure 36** Vacuum and sealed silica ampule after synthesis of CZTSe by solid state reaction.*

Occasionally after the first reaction or annealing step, the presence of deposited material onto the quartz surface have been observed (see an example in Figure 36). Precipitation of elements and/or compounds might be responsible of the observed deviations from intended vs obtained kesterite cation ratios.

In order to understand material losses during synthesis, some random pieces of ampoules with deposited materials (visible by eyes) were selected to be analyzed with 10kV Acc. voltage by a scanning electron microscope (SEM) equipped with an energy-dispersive X-ray spectroscopy (EDS). The results showed some traces of copper, zinc, tin and selenium elements but mainly big particles of tin and selenium.

As observed in Figure 37a, SEM micrograph with elements color mapping shows big selenium particles (>400µm). Also tin particles (see Figure 37b) have been found within a size range from 20-100µm. However, no big particles apart of the few traces of copper and zinc elements have been found.

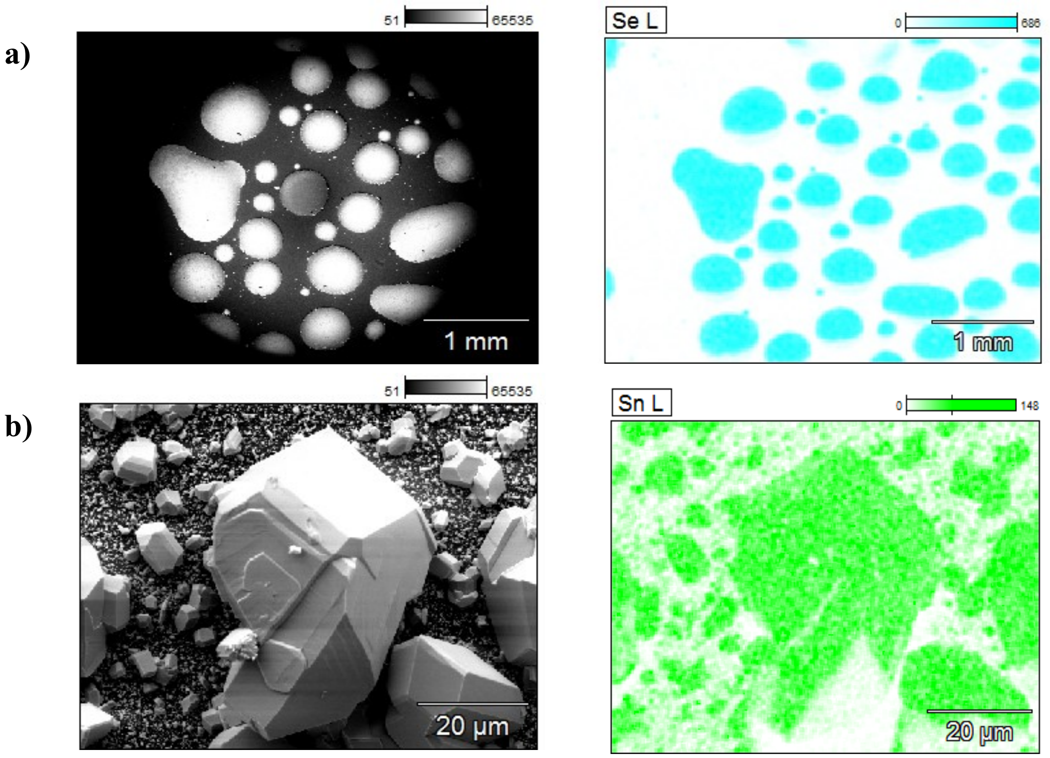

Figure 37 *SEM micrographs a) selenium (blue) and b) tin (green) particles.*

Moreover, few amount of small kesterite particles within a size range from 10-15 µm have been also detected (see Figure 38). CuSe tiny particle (~5µm) has been possibly detected but due to weak contrast of elements, it is difficult to confirm its presence. In the case of $SnSe_2$, ZnSe or a ternary compound have not been clearly evidence of its presence.

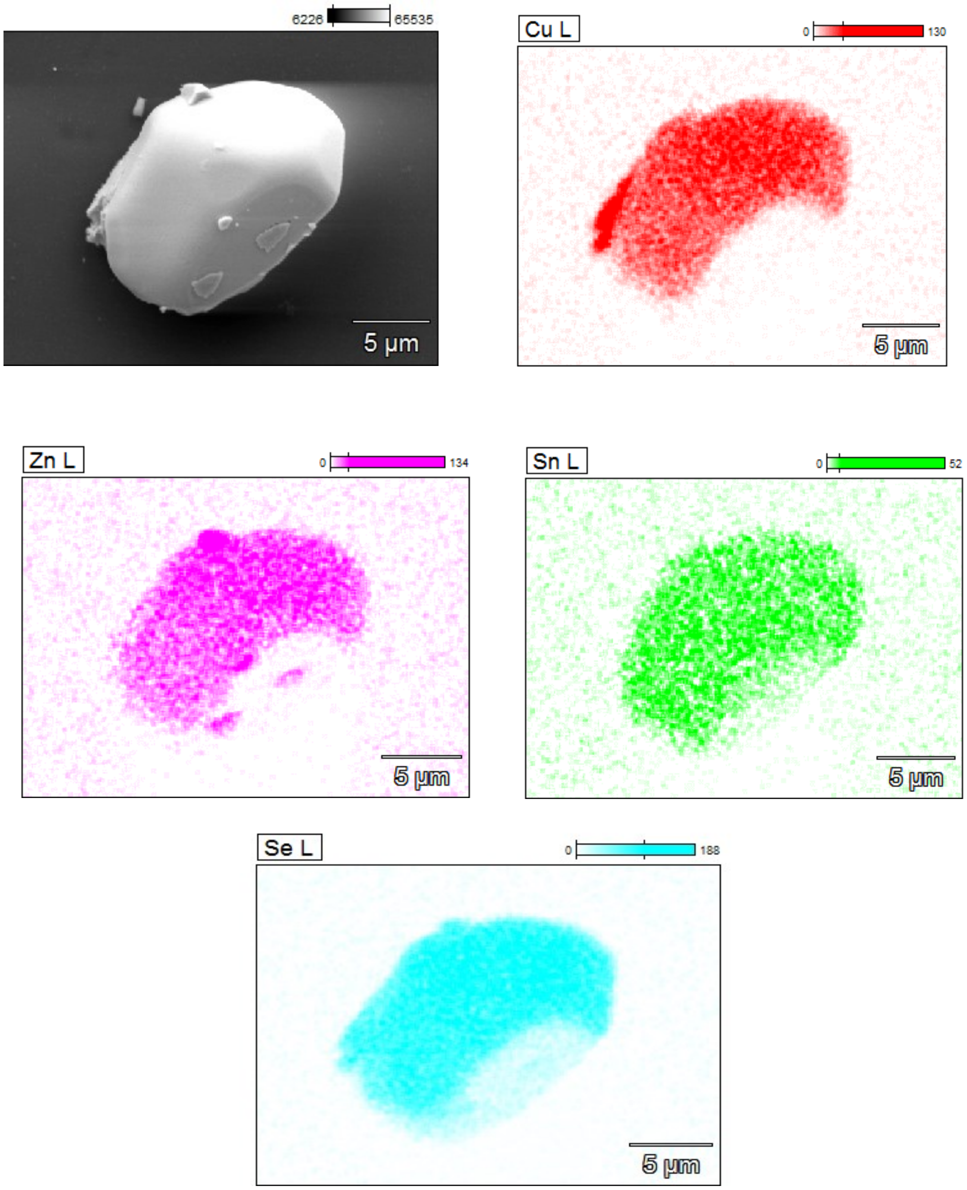

Figure 38 *SEM micrographs of a kesterite particle with element color mapping: copper - red, zinc-magenta, tin-green and selenium-blue.*

Tin losses have been also observed during the growth of kesterite materials by physical route as discussed in literature [60, 61]. *Weber et al.* [62] have proposed decomposition reaction which attributed the losses of Sn via desorption of SnSe. However, such proposed reaction is based on stoichiometric chemical equilibrium. In our case the occurrence of $SnSe_2$ as secondary phase has been confirmed by EMPA analysis but not evidenced of SnSe and/or $SnSe_2$ compounds onto the ampules have been observed by SEM and EDS spectroscopy.

SEM and EDS spectroscopy analyses have given a clue to understand deviations from intended vs obtained cation ratios of the kesterite phase (apart of the occurrences of secondary phases). Nevertheless, it is not clear what determined the losses of elements during the synthesis, especially tin and/or selenium, because losses of tin were more pronounced only within certain apparently random samples. For instance, during a same synthesis-batch, deposited particles might be observed only within 1 out of 6 quartz ampoules.

The condition of the ampoules before a reaction takes place have been attempted to be the same during each synthesis. For example, the vacuum region where reactions take place has been measured to be similar for every ampule before the synthesis. The ampoules used during the first reaction step have a diameter of ~2.5 cm. The length of the ampule where the carbon boat has been placed was measured to be ~8 cm, thus the volume during the first step reaction was ~39.27cm^3. In the case of annealing step, ampoules have a smaller diameter of ~1.5 cm. The length of the small ampoules has been measured to be ~5 cm, so the volume during the annealing step was ~8.83cm^3.

Moreover, same heating temperature rates have been selected, also a similar natural cooling have been applied for every synthesis as described, in Figure 12a) Temperature heating profile used for synthesis b) cooling profile measured by a thermocouple. Even the use of the same furnace was preferable.

Conclusions

1. Reactions took place within similar conditions, for instance, volumes and temperatures profiles were intended to be similar for every synthesis.
2. To optimize the synthesis and prevent losses of elements, especially, tin and/or selenium, further investigations are needed; for instance, control on vapor pressures.
3. SEM and EDX spectroscopy analyses helped to understand the deviation from intended vs composition kesterite cation ratios.
4. Beside observation of tin and selenium particles, small kesterite particles have been found.

3.1.6 Secondary phases – overview

So far, the secondary phases have been described as binary compounds. But in fact they consist of more than two elements. Nevertheless, their compositions are really similar to binary compounds. But in this case, secondary phases are considered as solid solutions, thus should not be confused with ternary or quaternary compounds. Table 12 presents the solid solutions compounds according to the cation ratios of the kesterite main phase where along with it, these secondary phases have been observed.

Solid solutions composition has been obtained according to mole % ratios and normalization of selenium from chemical characterization. However, out of WDX spectroscopy analyses, it is difficult determinate the percentages of secondary phases within a sample. Because only a small portion of the powder sample is selected randomly to be embedded in the epoxy and measure at the electron microprobe. But the amount of grains where secondary phases have been detected were the minority. Usually, secondary phases have been detected in a range from 3 to 8 grains out of 25-35 total measured grains (number of measures grains depended on the grain size). Nevertheless, WDX based results are correlated with X-ray diffraction analyses where the weigh fraction of a phase is extracted from Rietveld refinements (see section *3.2.1 Lattice parameters and phase weight fraction"* in page 77).

The chemical composition of detected secondary phases (solid solutions) are listed in Table *12*. As observed, those compositions are indeed really near to the binary compounds: CuSe, Cu_2Se, ZnSe and $SnSe_2$. Therefore, discussions of the occurrence of secondary phases given by binary composition are considered to be corrected.

The results out of these solid solutions show that in the case of A-B type mixture, the limited solubility of Cu and Sn in the ZnSe phase was found in: $Zn_{0.774}(Cu_{0.144}Sn_{0.082})Se$ and $Sn_{0.919}(Cu_{0.053}Zn_{0.028})Se_2$ for Cu and Zn in the $SnSe_2$ phase.

Limited solubility of Cu and Sn in ZnSe phase within the B-F type mixture was observed in: $Zn_{0.771}(Cu_{0.157}Sn_{0.072})Se$ and the limited solubility of Zn and Sn of CuSe and Cu_2Se phases have been observed in: $Cu_{0.822}(Zn_{0.075}Sn_{0.103})Se$ and $Cu_{1.979}(Zn_{0.017}Sn_{0.004})Se$ respectively.

F-D type mixture, the limited solubility of Cu and Sn of ZnSe phase was observed at: $Zn_{0.924}(Cu_{0.054}Sn_{0.022})Se$. Also, $Cu_{0.950}(Zn_{0.011}Sn_{0.039})Se$ and $Cu_{1.987}(Zn_{0.011}Sn_{0.002})Se$ were the limited solubility found of Zn and Sn within CuSe and Cu_2Se phases.

Finally, in the case of C-D type mixture, limited solubility found of Zn and Sn within CuSe and Cu_2Se phases were observed in: $Cu_{0.803}(Zn_{0.1}Sn_{0.097})Se$ and $Cu_{1.985}(Zn_{0.013}Sn_{0.002})Se$, respectively.

Table 12 *Secondary phases - solution composition and cation ratios*

Cu/(Zn+Sn)	**Zn/Sn**	**Type**	**Solution – secondary phases**
0.833	1.129	AB	$Zn_{0.961}(Cu_{0.037}Sn_{0.002})Se$; $Sn_{0.956}(Cu_{0.027}Zn_{0.017})Se_2$
0.816	1.147	AB	$Sn_{0.92}(Cu_{0.05}Zn_{0.03})Se_2$
0.846	1.192	AB	$Zn_{0.774}(Cu_{0.144}Sn_{0.082})Se$; $Sn_{0.935}(Cu_{0.038}Zn_{0.027})Se_2$
0.890	1.134	AB	$Zn_{0.910}(Cu_{0.071}Sn_{0.019})Se$
0.854	1.189	AB	$Zn_{0.787}(Cu_{0.142}Sn_{0.071})Se$;$Sn_{0.940}(Cu_{0.036}Zn_{0.024})Se_2$
0.967	1.045	AB	-
0.920	1.113	AB	$Zn_{0.792}(Cu_{0.140}Sn_{0.068})Se$; $Sn_{0.919}(Cu_{0.053}Zn_{0.028})Se_2$
0.911	1.127	AB	-
0.950	1.099	AB	$Cu_{0.998}(Sn_{0.002})Se$
0.910	1.222	FB	$Zn_{0.771}(Cu_{0.157}Sn_{0.072})Se$
0.945	1.149	FB	-
0.959	1.120	FB	$Cu_{0.990}(Zn_{0.009}Sn_{0.001})Se$; $Zn_{0.795}(Cu_{0.151}Sn_{0.054})Se$; $Cu_{1.991}(Zn_{0.008}Sn_{0.001})Se$
0.939	1.214	FB	$Cu_{0.991}(Zn_{0.008}Sn_{0.001})Se$; $Zn_{0.774}(Cu_{0.157}Sn_{0.069})Se$
0.978	1.077	FB	-
0.979	1.075	FB	$Cu_{0.991}(Zn_{0.008}Sn_{0.001})Se$
0.972	1.114	FB	$Cu_{1.988}(Zn_{0.011}Sn_{0.001})Se$; $Cu_{0.822}(Zn_{0.075}Sn_{0.103})Se$
0.998	1.042	FB	$Cu_{0.990}(Zn_{0.009}Sn_{0.001})Se$; $Zn_{0.941}(Cu_{0.046}Sn_{0.013})Se$
0.996	1.132	FB	$Cu_{0.923}(Zn_{0.044}Sn_{0.033})Se$; $Cu_{1.979}(Zn_{0.017}Sn_{0.004})Se$
1.000	1.046	FB	$Zn_{0.950}(Cu_{0.039}Sn_{0.011})Se$; $Cu_{0.976}(Zn_{0.021}Sn_{0.003})Se$
1.008	1.100	FB	$Cu_{0.982}(Zn_{0.013}Sn_{0.005})Se$
1.007	1.061	FB	$Cu_{1.986}(Zn_{0.012}Sn_{0.002})Se$
1.023	1.085	FB	$Cu_{1.985}(Zn_{0.011}Sn_{0.004})Se$; $Cu_{0.988}(Zn_{0.010}Sn_{0.002})Se$
1.145	0.910	FD	$Cu_{1.987}(Zn_{0.011}Sn_{0.002})Se$
1.100	0.961	FD	$Cu_{1.988}(Zn_{0.010}Sn_{0.002})Se$;$Cu_{0.989}(Zn_{0.010}Sn_{0.002})Se$
1.027	0.995	FD	$Zn_{0.924}(Cu_{0.054}Sn_{0.022})Se$; $Cu_{0.994}(Zn_{0.006})Se$; $Cu_{1.993}(Zn_{0.006}Sn_{0.001})Se$
1.014	1.017	FD	$Cu_{1.992}(Zn_{0.007}Sn_{0.001})Se$; $Zn_{0.945}(Cu_{0.044}Sn_{0.011})Se$; $Cu_{0.950}(Zn_{0.011}Sn_{0.039})Se$
1.088	0.871	CD	$Cu_{0.99}(Zn_{0.01})Se$
1.174	0.777	CD	$Cu_{0.99}(Zn_{0.01})Se$
1.103	0.883	CD	$Cu_{1.985}(Zn_{0.013}Sn_{0.002})Se$; $Cu_{0.803}(Zn_{0.1}Sn_{0.097})Se$

Conclusions

All secondary phase samples have been detected as solid solutions, by comparing all solid solutions listed in Table 12, the observed limited solubility according to the 29 synthesized samples are summarized below:

i. Cu and Zn in $SnSe_2$ phase: $Sn_{0.919}(Cu_{0.053}Zn_{0.028})Se_2$ (A-B type mixture).
ii. Cu and Sn in ZnSe phase: $Zn_{0.771}(Cu_{0.157}Sn_{0.072})Se$ (B-F type mixture).
iii. Zn and Sn in Cu_2Se phase: $Cu_{1.979}(Zn_{0.017}Sn_{0.004})Se$ (B-F type mixture).
iv. Zn and Sn in CuSe phase: $Cu_{0.803}(Zn_{0.1}Sn_{0.097})Se$ (C-D type mixture).

3.1.7 Type fractions and chemical composition – linear combination.

As previously discussed in section 3.1.4 *Off-stoichiometric CZTSe - overview*" (page 63), the majority of kesterite phases are located between two different off-stoichiometry type lines (-A,-B,-C,-D,-F). Therefore, type fractions and chemical composition have been deduced by a linear interpolation (described in section 2.2.1). Results are summarized by type percentages in following Table 13.

In total 9 kesterites are considered A-B type mixture. Those kesterite mixtures cover a cation ratios range: Cu/(Zn+Sn) from 0.816 to 0.967 and Zn/Sn from 1.045 to 1.192. Kesterites phases were wider spread within the Cu/(Zn+Sn) ration. Copper exhibits a significant variation in composition; the lowest amount of copper was found in kesterite phase with a chemical composition: $Cu_{1.740}Zn_{1.141}Sn_{0.994}Se_4$. All tin (Sn) values were < 1, however, the variation on tin composition within A-B type mixtures has been less pronounced compared with variations of copper and zinc.

A large number of kesterites phases are considered as B-F type mixture. In total 13 have been found within the Cu/(Zn+Sn) cation ratios range from 0.910 to 1.023 and Zn/Sn ratio from 1.042 to 1.222. In this case, a stronger variation was observed over the Zn/Sn ratio. The zinc richest kesterite phase has a chemical composition: $Cu_{1.910}Zn_{1.155}Sn_{0.945}Se_4$. And the tin poorest: $Cu_{1.953}Zn_{1.142}Sn_{0.941}Se_4$.

Table 13 *Kesterite type fractions and chemical composition - linear combination*

Cu/(Zn+Sn)	Zn/Sn	Formulae	Type fraction (%)			
0.833	1.129	$Cu_{1.766}Zn_{1.125}Sn_{0.996}Se_4$	A	88	B	12
0.816	1.147	$Cu_{1.740}Zn_{1.141}Sn_{0.994}Se_4$	A	84	B	16
0.846	1.192	$Cu_{1.797}Zn_{1.158}Sn_{0.971}Se_4$	A	38	B	62
0.890	1.134	$Cu_{1.859}Zn_{1.111}Sn_{0.980}Se_4$	A	37	B	63
0.854	1.189	$Cu_{1.810}Zn_{1.154}Sn_{0.971}Se_4$	A	35	B	65
0.967	1.045	$Cu_{1.961}Zn_{1.036}Sn_{0.992}Se_4$	A	25	B	75
0.920	1.113	$Cu_{1.902}Zn_{1.090}Sn_{0.979}Se_4$	A	25	B	75
0.911	1.127	$Cu_{1.892}Zn_{1.101}Sn_{0.977}Se_4$	A	24	B	76
0.950	1.099	$Cu_{1.947}Zn_{1.073}Sn_{0.977}Se_4$	A	3	B	97
0.910	1.222	$Cu_{1.910}Zn_{1.155}Sn_{0.945}Se_4$	F	5	B	95
0.945	1.149	$Cu_{1.950}Zn_{1.104}Sn_{0.961}Se_4$	F	10	B	90
0.959	1.120	$Cu_{1.965}Zn_{1.083}Sn_{0.967}Se_4$	F	14	B	86
0.939	1.214	$Cu_{1.953}Zn_{1.142}Sn_{0.941}Se_4$	F	19	B	81
0.978	1.077	$Cu_{1.985}Zn_{1.053}Sn_{0.978}Se_4$	F	20	B	80
0.979	1.075	$Cu_{1.986}Zn_{1.051}Sn_{0.978}Se_4$	F	21	B	79
0.972	1.114	$Cu_{1.984}Zn_{1.076}Sn_{0.966}Se_4$	F	24	B	76
0.998	1.042	$Cu_{2.007}Zn_{1.026}Sn_{0.985}Se_4$	F	45	B	55
0.996	1.132	$Cu_{2.023}Zn_{1.080}Sn_{0.954}Se_4$	F	46	B	54
1.000	1.046	$Cu_{2.011}Zn_{1.028}Sn_{0.983}Se_4$	F	50	B	50
1.008	1.100	$Cu_{2.036}Zn_{1.058}Sn_{0.962}Se_4$	F	59	B	41
1.007	1.061	$Cu_{2.025}Zn_{1.036}Sn_{0.976}Se_4$	F	62	B	38
1.023	1.085	$Cu_{2.055}Zn_{1.045}Sn_{0.964}Se_4$	F	78	B	22
1.145	0.910	$Cu_{2.185}Zn_{0.909}Sn_{0.999}Se_4$	F	1	D	99
1.100	0.961	$Cu_{2.136}Zn_{0.950}Sn_{0.991}Se_4$	F	9	D	91
1.027	0.995	$Cu_{2.039}Zn_{0.990}Sn_{0.955}Se_4$	F	18	D	82
1.014	1.017	$Cu_{2.025}Zn_{1.007}Sn_{0.990}Se_4$	F	72	D	28
1.088	0.871	$Cu_{2.093}Zn_{0.896}Sn_{1.029}Se_4$	C	86	D	14
1.174	0.777	$Cu_{2.181}Zn_{0.814}Sn_{1.048}Se_4$	C	81	D	19
1.103	0.883	$Cu_{2.117}Zn_{0.901}Sn_{1.020}Se_4$	C	67	D	33

In total 4 kesterite phases could be considered as F-D type mixture. Two of them lie close to the D-type line: $Cu_{2.185}Zn_{0.909}Sn_{0.999}Se_4$ and $Cu_{2.136}Zn_{0.950}Sn_{0.991}Se_4$. The others appear to be close to the D and F type line respectively. But those two kesterite phases are indeed close to the stoichiometric region; the uncertainties of type fractions near to this region could be higher than estimated (up to ~5%).

The last 3 kesterites are C-D type mixture. Those kesterites cover the cation ratio range: Cu/(Zn+Sn) from 1.088 to 1.174 and Zn/Sn from 0.777 to 0.833. The variation in composition is stronger over the Zn/Sn ratio. The tin richest and zinc poorest composition observed with in all 29 kesterite phases is the: $Cu_{2.181}Zn_{0.814}Sn_{1.048}Se_4$.

Conclusions

i. Chemical composition has been deduced from linear interpolation and exhibit off-stoichiometric compositions.
ii. All samples can be considered as a mixture of two different off-stoichiometry types.
iii. Classification of the kesterite phase according to their type fractions is really important to study the presence of intrinsic point defects.
iv. Copper poorest: $Cu_{1.740}Zn_{1.141}Sn_{0.994}Se_4$ and copper richest: $Cu_{2.181}Zn_{0.814}Sn_{1.048}Se_4$ compositions have been observed.

3.2 Structural parameters by Rietveld refinements

3.2.1 Lattice parameters and phase weight fraction

Diffraction data collected from X-ray powder diffraction experiments have been analyzed by Rietveld refinements as have been explained in section 2.3.4.1 *Rietveld refinements of XRD data" (page 38).*

As a starting model of the refinements, kesterite type structure (space group $I\bar{4}$) has been selected. Additionally, secondary phases; $SnSe_2$ (space group $P\bar{3}m1$), ZnSe (space group $F\bar{4}3m$), Cu_2Se (space group $Fm\bar{3}m$) and CuSe (space group$P6_3/mmc$) have been included in the corresponding refinement file.

The Bragg position of the ZnSe phase overlap with the reflexes of the kesterite phase. It used to be believed that it is not possible to distinguish the presence of ZnSe. But recent studies of a master work by A. Pereira [63] revealed that a small shoulder appear in the 220 peak by the presence of ZnSe. However, this influence is particularly visible when the amount of ZnSe is higher than 10%. Thus shoulder of the 220 peak was not found in the diffraction patterns from synthesized samples.

Lattice parameters of the kesterite phase weight fractions have been extracted from Rietveld analyses. The obtained values of lattice parameters a and c are listed in Table 14. But a better overview of resulted lattice parameters is giving in Figure 39a,b.

Lattice parameters have been plotted according to the kesterite cation ratios (Figure 39). As observed, the lattice parameter "a" exhibit lower values in the copper rich, zinc poor region (see Figure 39a). Whereas, the lattice parameter "c" (Figure 39b) increases along the Cu/(Zn+Sn) ratio, from copper poor to copper rich. The reduction in the unit cells could be attributed to the presence of point defects such as copper vacancies. Also due to exchange of Zn^{2+} with Cu^{+}, because copper has a smaller size compared to zinc [64].

Moreover, the obtained phase weight fractions (%) from Rietveld refinements are summarized in Table 15. Percentages of the kesterite main phase are presented in Figure 40 according to its cation ratios. As observed, the higher amount of kesterite phase has been found when Cu/(Zn+Sn) < 1 and Zn/Sn > 1. On the other hand, a preferable region for secondary phases have been found mainly when Cu/(Zn+Sn) and Zn/Sn are higher than 1.

Table 14 *Lattice parameters, $\eta=c/2a$ and percentages of kesterite main phase*

Cu/(Zn+Sn)	Zn/Sn	*a(Å)*	*c(Å)*	$\eta=c/2a$	Kesterite (%)
0.833	1.129	5.697	11.337	0.9951	97.47%
0.816	1.147	5.699	11.344	0.9952	99.89%
0.846	1.192	5.700	11.358	0.9963	92.12 %
0.890	1.134	5.699	11.343	0.9952	82.59%
0.854	1.189	5.699	11.357	0.9964	77.45%
0.967	1.045	5.701	11.362	0.9966	100%
0.920	1.113	5.699	11.345	0.9953	79.61%
0.911	1.127	5.699	11.344	0.9952	100%
0.950	1.099	5.701	11.353	0.9957	99.81%
0.910	1.222	5.696	11.336	0.9951	82.85%
0.945	1.149	5.697	11.339	0.9951	100%
0.959	1.120	5.698	11.355	0.9964	85.07%
0.939	1.214	5.696	11.352	0.9964	79.88%
0.978	1.077	5.701	11.354	0.9959	100%
0.979	1.075	5.697	11.353	0.9964	99.5%
0.972	1.114	5.700	11.357	0.9963	75.83%
0.998	1.042	5.697	11.354	0.9965	77.17%
0.996	1.132	5.698	11.353	0.9963	72.97%
1.000	1.046	5.698	11.352	0.9961	94.77%
1.008	1.100	5.696	11.354	0.9966	99.52%
1.007	1.061	5.703	11.356	0.9956	68.65%
1.023	1.085	5.697	11.353	0.9963	79.77%
1.145	0.910	5.688	11.340	0.9968	73.77%
1.100	0.961	5.696	11.348	0.9962	98.46%
1.027	0.995	5.698	11.354	0.9963	71.45%
1.014	1.017	5.697	11.353	0.9965	85.08%
1.088	0.871	5.698	11.362	0.9970	99.88%
1.174	0.777	5.696	11.358	0.9970	99.89%
1.103	0.883	5.692	11.349	0.9969	85.12%

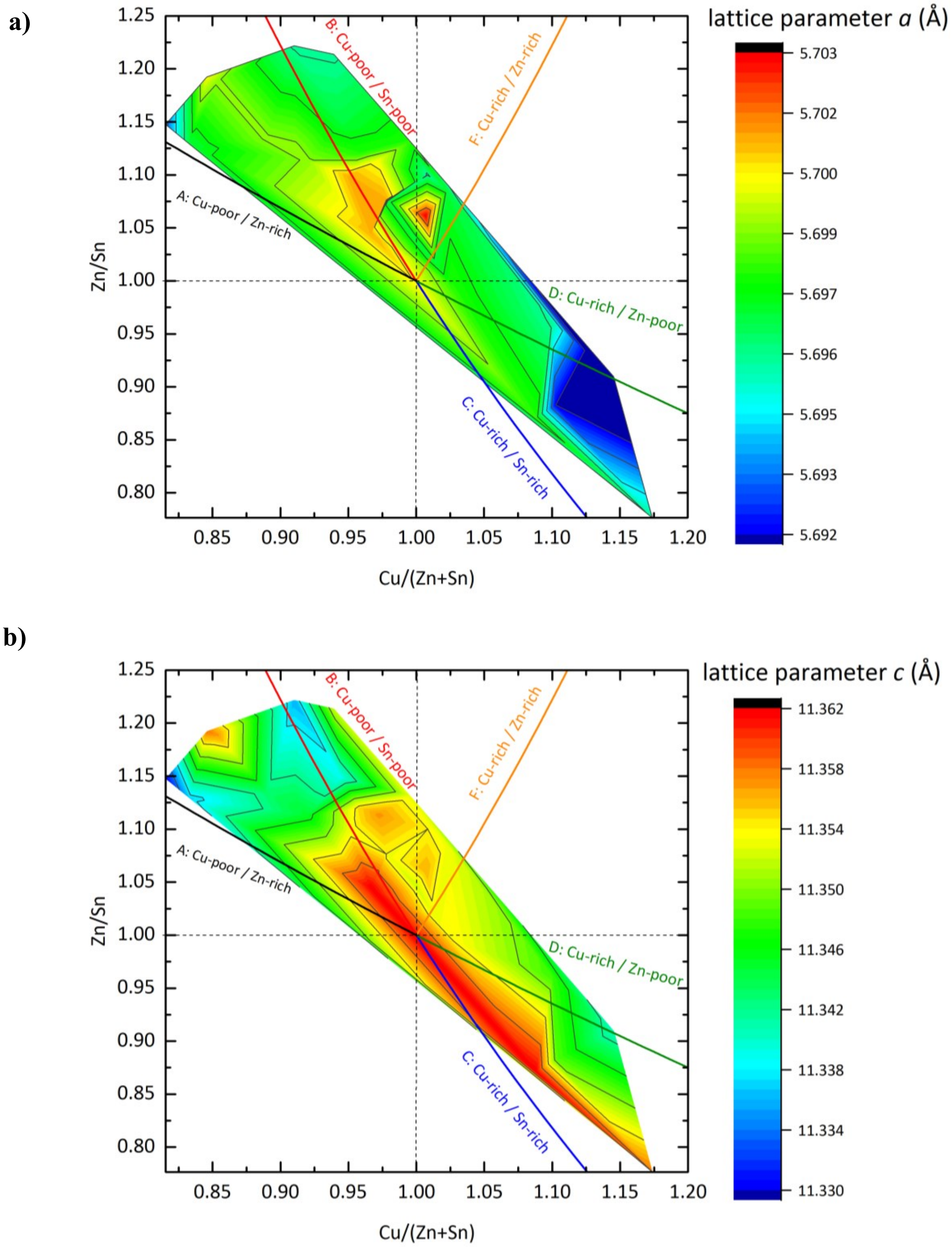

Figure 39a,b *Lattice parameter "a" and "c" (Å) of the kesterite main phase (XRD) in relation to cation ratio plot of the kesterite phase.*

Table 15 *Secondary phase weight fraction (%) – in relation to kesterite cation ratio*

Cu/(Zn+Sn)	**Zn/Sn**	**secondary phases – weight fractions**
0.833	1.129	$Zn_{0.96}(Cu_{0.04})Se$ (2.44%); $Sn_{0.96}(Cu_{0.03}Zn_{0.01})Se_2$ (0.08%)
0.816	1.147	$Sn_{0.92}(Cu_{0.05}Zn_{0.03})Se_2$ (0.11%)
0.846	1.192	$Zn_{0.8}(Cu_{0.1}Sn_{0.1})Se$ (7.55%);$Sn_{0.94}(Cu_{0.04}Zn_{0.02})Se_2$ (0.33%)
0.890	1.134	$Zn_{0.91}(Cu_{0.07}Sn_{0.02})Se$ (17.41%)
0.854	1.189	$Zn_{0.8}(Cu_{0.1}Sn_{0.1})Se$ (21.96%);$Sn_{0.94}(Cu_{0.04}Zn_{0.02})Se_2$ (0.58%)
0.967	1.045	-
0.920	1.113	$Zn_{0.8}(Cu_{0.1}Sn_{0.1})Se$ (19.64%);$Sn_{0.92}(Cu_{0.05}Zn_{0.03})Se_2$ (0.75%)
0.911	1.127	-
0.950	1.099	Cu Se (0.19%)
0.910	1.222	$Zn_{0.8}(Cu_{0.1}Sn_{0.1})Se$ (17.15%)
0.945	1.149	-
0.959	1.120	$Cu_{0.99}(Zn_{0.01})Se$ (0.4%); $Zn_{0.8}(Cu_{0.1}Sn_{0.1})Se$ (13.65%); $Cu_{1.99}(Zn_{0.01})Se$ (0.88%)
0.939	1.214	$Cu_{0.99}(Zn_{0.01})Se$ (0.18%); $Zn_{0.8}(Cu_{0.1}Sn_{0.1})Se$ (19.94%)
0.978	1.077	-
0.979	1.075	$Cu_{0.99}(Zn_{0.01})Se$ (0.5%)
0.972	1.114	$Cu_{1.99}(Zn_{0.01})Se$ (23.77%); $Cu_{0.8}(Zn_{0.1}Sn_{0.1})Se$ (0.39%)
0.998	1.042	$Cu_{0.99}(Zn_{0.01})Se$ (0.45%); $Zn_{0.94}(Cu_{0.05}Sn_{0.01})Se$ (22.38%)
0.996	1.132	$Cu_{0.93}(Zn_{0.04}Sn_{0.03})Se$ (0.29%); $Cu_{1.98}(Zn_{0.02})Se$ (26.74%)
1.000	1.046	$Zn_{0.95}(Cu_{0.04}Sn_{0.01})Se$ (2.95%); $Cu_{0.98}(Zn_{0.02})Se$ (2.28%)
1.008	1.100	$Cu_{0.98}(Zn_{0.01}Sn_{0.01})Se$ (0.48%)
1.007	1.061	$Cu_{1.99}(Zn_{0.01})Se$ (31.35%)
1.023	1.085	$Cu_{1.99}(Zn_{0.01})Se$ (20.09%); $Cu_{0.99}(Zn_{0.01})Se$ (0.14%)
1.145	0.910	$Cu_{1.99}(Zn_{0.01})Se$ (26.23%)
1.100	0.961	$Cu_{1.99}(Zn_{0.01})Se$ (1.35%); $Cu_{0.99}(Zn_{0.01})Se$ (0.19%)
1.027	0.995	$Zn_{0.93}(Cu_{0.05}Sn_{0.02})Se$ (8.63%); $Cu_{0.99}(Zn_{0.01})Se$ (0.63%); $Cu_{1.99}(Zn_{0.01})Se$ (19.29%)
1.014	1.017	$Cu_{1.99}(Zn_{0.01})Se$ (1.7%); $Zn_{0.95}(Cu_{0.05})Se$ (12.45%); $Cu_{0.95}(Zn_{0.01}Sn_{0.04})Se$ (0.77%)
1.088	0.871	$Cu_{0.99}(Zn_{0.01})Se$ (0.12%)
1.174	0.777	$Cu_{0.99}(Zn_{0.01})Se$ (0.11%)
1.103	0.883	$Cu_{1.99}(Zn_{0.01})$ (0.12%); $Cu_{0.8}(Zn_{0.1}Sn_{0.1})Se$ (14.76%)

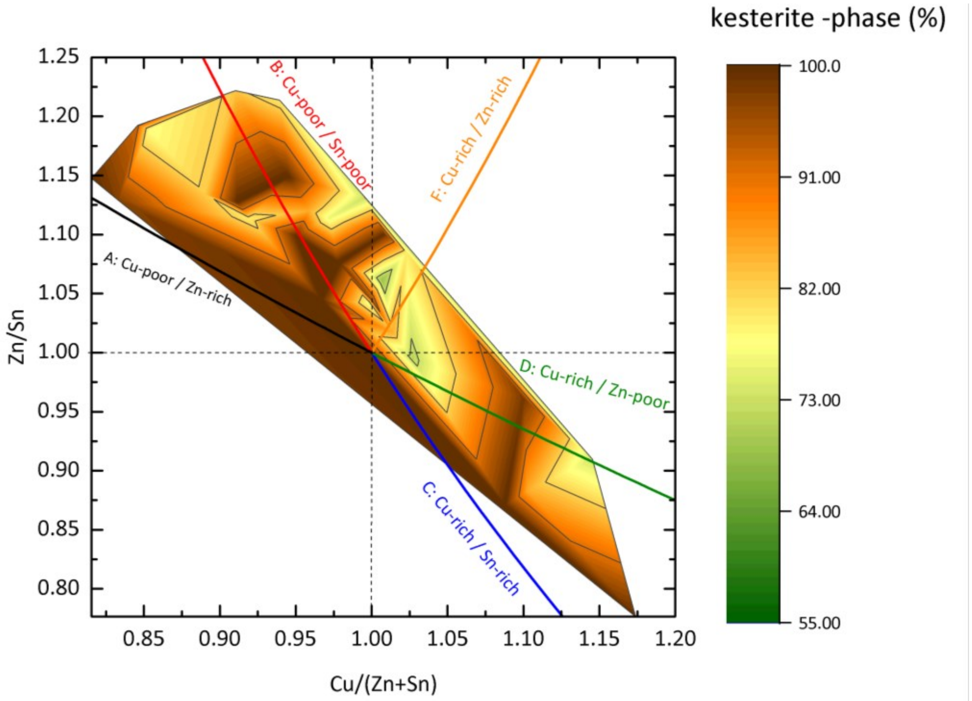

Figure 40 Kesterite phase percentages in relation to cation ratios**.**

Conclusions

i. The obtained weight fraction from Rietveld refinements proved that kesterite is the main phase within all synthesized samples (in agreement to chemical characterization by WDX).

ii. The higher percentages of the kesterite phase has been found near to the A- and A-B type mixture.

iii. Highest percentage of secondary phases was 26.74% of Cu_2Se (Cu/(Zn+Sn)=0996).

iv. Variation in lattice parameter *c* is slightly higher than lattice parameter *a.*

v. The reduction in the unit cells could be attributed due to the presence of point defects, for example copper vacancies.

3.2.2 Tetragonal deformation

Tetragonal deformation η=*c*/2*a* describes the deviation of the ratio of the long axis "*c*" over two times the short axis "a" (see Figure 41). Tetragonal deformation within off-stoichiometric CZTSe polycrystalline samples has been deduced experimentally from lattice parameters values obtained by Rietveld refinements of XRD data. η= *c*/2*a* values have listed before in Table 14.

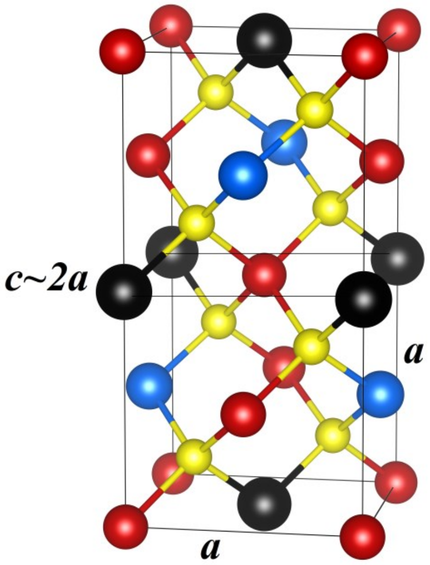

Figure 41 *Body-centered tetragonal kesterite structure with c ~ 2a (pseudo-cubic ratio)*

Deviation *c/2a* ≠1 is an interesting structural parameter because of its relation with the crystal field splitting Δ_{CF}. For instance, lattice parameters and tetragonal deformation of $Cu_2ZnSnSe_4$ have been theoretically calculated by *Chen et.al* [65] for the kesterite and stannite structures. It has been reported that the tetragonal deformation η=0.998 of kesterite structure is slightly smaller than stannite structure η=1.000 and that the crystal field splitting $\Delta_{CF}=\Gamma_{5v}-\Gamma_{4v}$ [66], which is determined partially by η= *c*/2*a* [67] follows the same trend. The kesterite structure has a smaller and negative crystal field splitting Δ_{CF}=-0.031eV while the stannite structure has a larger and positive value Δ_{CF}= 0.066 eV. The sign of the crystal field is important for the symmetry of the topmost valence band [23] therefore it has an impact in the electronic structure and properties of semiconductor materials.

The tetragonal deformation for $Cu_2ZnSnSe_4$ within available ICDD data gives a *c/2a* ratio of just slightly < 1. Moreover, some of the reported values in literature where *c*/2*a* has been deduced either experimentally or theoretically are listed in Table 16. As observed, either for stannite or kesterite structure *c*/2*a* =1 or below 1. Opposite to Cu_2ZnSnS_4 compounds, where c/2a >1 have been reported (for example *c*/2*a* =1.0015 by *Siebentritt et a.l* [23]).

Table 16 *$Cu_2ZnSnSe_4$ - Literature review of lattice constant and tetragonal deformation reported from stannite (ST) and kesterite (KT) structure.*

structure	***a*** **(Å)**	***c*** **(Å)**	**η**	**reference**
ST	5.681 (1)	11.340 (2)	0.9981 (2)	*Villars et al.*[68]
ST	5.688 (1)	11.338 (2)	0.9967 (2)	*Olekseyuk et. al* [69]
ST	5.603 (1)	11.206 (2)	1.0000 (2)	*Gürel* [12]
ST	5.604 (1)	11.208 (2)	1.0000 (2)	*Persson* [22]
ST	5.762 (1)	11.524 (2)	1.0000 (2)	*Chen et al.*[65]
KT	5.605 (1)	11.200 (2)	0.9991 (2)	*Persson* [22]
KT	5.680 (1)	11.360 (2)	1.0000 (2)	*Babu et al.* [70]
KT	5.604 (1)	11.202 (2)	0.9995 (2)	*Gürel* [12]
KT	5.695 (1)	11.345 (2)	0.9960 (2)	*Siebentritt et al.* [23]
KT	5.763 (1)	11.503 (2)	0.9980 (2)	*Chen et al.*[65]

In the case of off-stoichiometric polycrystalline CZTSe samples, all values of tetragonal deformation have been found below one (*c*/2*a* <1) which is in a good agreement with literature (see *Table 16*).

However, a dependency on composition, especially of copper content has been observed (see *Figure 42*). Lowest tetragonal deformation has been observed in the copper poor region and the values increase in the copper rich region.

In fact those results have been correlated with CZTSe thin film solar cells by *Marquez et al.* [71] where it has been observed that the open circuit voltage (V_{oc}) of the kesterite based solar cell significantly increase by a decrease of the tetragonal deformation. When the CZTSe based solar cell have an absorber layer composition inside the copper poor region. A high V_{oc}=434mV and 8.1% energy conversion efficiency have been reached when the absorber layer exhibited a tetragonal deformation $c/2a$ =0.9950. Remarkably, its V_{oc} is higher compared with the current record of CZTSe based solar cells: V_{oc}=423mV and 11.6% efficiency [15]. Due to its possible influences in the electronic structure, the tetragonal deformation of the absorber layer might have a critical effect over the overall performance of the solar cell. This topic is open for further investigations.

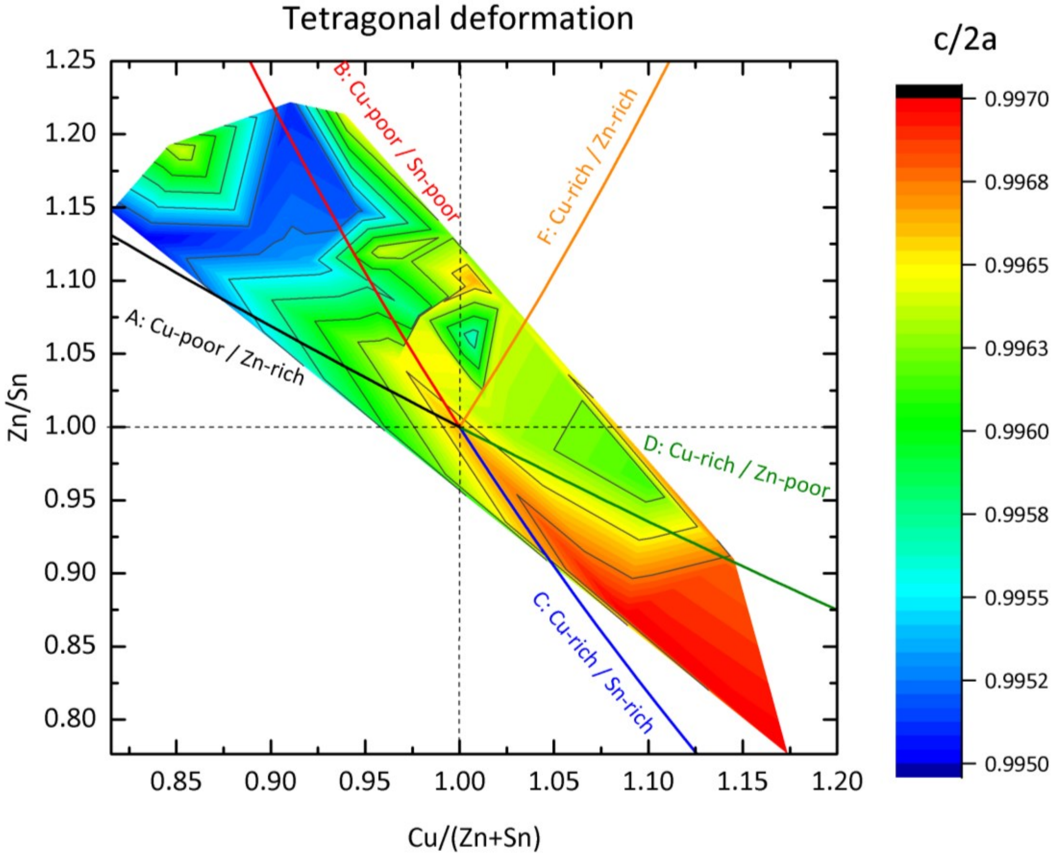

Figure 42 *Tetragonal deformation in relation to the kesterite cation ratios.*

Conclusions

1. Deficit of open circuit voltage (V_{oc}) is one of the main challenges of kesterite based solar cells. Enhancement of V_{oc} directly improves the fill factor (FF) and the efficiency.
2. Lower tetragonal deformation $c/2a$ were found in the copper poor region (A-type), where high solar cell efficiencies have been also reported.
3. The values of $c/2a$ increase when Cu/(Zn+Sn)>1, especially, between the C-D type mixture region.
4. The influences of the tetragonal deformation of the absorber layer over of the kesterite based solar cell performances should be further investigated.

3.2.3 Tetragonal distortion

Selenium anion position (8*g*) have been obtained from Rietveld analysis. Data was refined with the kesterite (space group $I\bar{4}$) structure model derivate from cubic sphalerite type structure F-43*m* with an origin at 4c: 0.25, 0.25, 0.25. The anion position of the kesterite structure derived from *x*+0.5, *y*+0.5, *z*+0.5. In this case the ideal anion position are (*x,y,z*)=*3/4,3/,4,5/8 [53].*

When the anion position is displaced from its ideal values lead to the definition of tetragonal distortion. Anion position within all synthesized polycrystalline powder samples shown a displacement from the ideal selenium anion position (*0.75, 0.75, 0.625*). Therefore, the tetragonal distortion has been calculated accordingly: u=0.75-x, u=0.75-y and u=0.625-z.

The results are presented in Figure 43 according to the composition of kesterite phase in relation with the cation ratios Cu/(Zn+Sn) vs Zn/Sn. The highest distortion of anion coordinate "*x"* was observed in the copper-poor, zinc-rich region near to the A-type line whereas in the copper-rich region remained more stable. The anion coordinate "*y*" exhibit the highest deviation, particularly between the B- and F-type lines. The highest distortion of anion "*y*" coordinate is observed near to the B-type line in the copper poor region and C-type line in the copper rich region. In the case of anion coordinate "*z*" exhibits the highest distortion within the copper rich region. Distortion is less in the copper poor region, especially near to the A-type line.

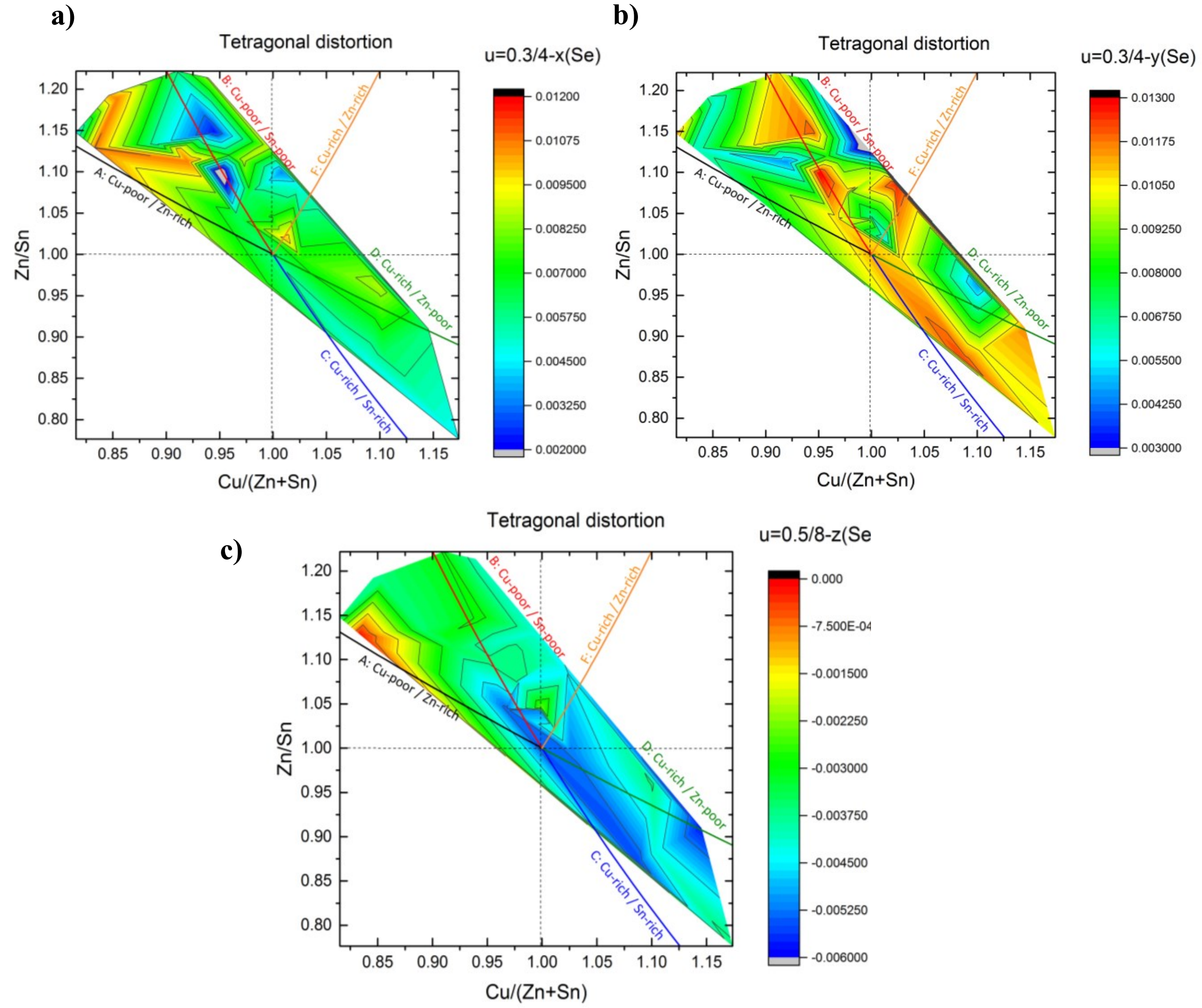

Figure 43 *Tetragonal distortion of selenium position (x,y,z) according to cation ratios Zn/Zn vs Cu/(Zn+Sn) of kesterite phase.*

Furthermore the tetragonal deformation it is an important crystal structure parameter, η=*c*/2*a* describes the deviation of lattice parameters ratio of the long axis "*c*" over two times the short axis "*a*". As has been presented in Figure 42, the tetragonal deformation is also influenced by the chemical composition of the kesterite phase. When comparing those independent structure parameters (see Figure 44); tetragonal distortion vs tetragonal deformation according to kesterite cation ratio Cu/(Zn+Sn). It seems like the anion coordinate "*z*" is the most affected by the tetragonal deformation (Δ=1-η).

Tetragonal distortion coordinate "*z*" is lower in the copper poor region Cu/(Zn+Sn)< 1. Also values of tetragonal deformation η= *c*/2*a* were lower in the copper poor region so the crystal structure it is compressed compared to the copper rich region where values of *c*/2*a* have been found closer to 1 thus Δ=1-η decreased.

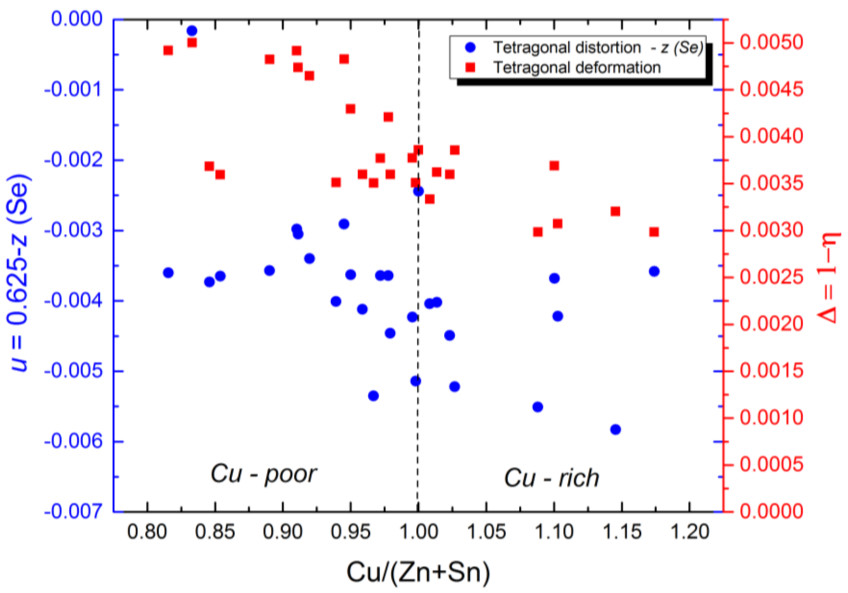

Figure 44 *Tetragonal distortion and tetragonal deformation according to kesterite ratio Cu/(Zn+Sn).*

Conclusion

i. All selenium anion position (*x,y,z*) have been displaced from the ideal coordinates.
ii. Influence of the chemical composition, in particular between Cu-poor and Cu-rich regions has been observed.
iii. Anion coordinate "*z*" seems to be affected by the tetragonal deformation (*c*/2*a)*.

3.2.4 Bond lengths and angles

- **Bond lengths**

In the previous section, the displacement of the anion position has been discussed. Anion displacement occur from differences in bond lengths (distances) of the cation-anion bonds (Cu-Se Zn-Se, Sn-Se) thus the anion is shifted from the middle of the anion tetrahedral (XA_2BC), therefore, the tetrahedral is considered to be distorted.

Bond lengths of kesterite compounds $Cu_2ZnSnSe_4$ have theoretically calculated by *C. Persson* [22] and *T. Gürel* [12] the values are presented in Table 17.

Table 17 *Calculated bond lengths (Å) of kesterite* $Cu_2ZnSnSe_4$*.*

CZTSe	Gürel [12]	Persson [22]
Cu-2a	2.376 Å	2.395 Å
Cu-2c	2.369 Å	2.392 Å
Zn-2d	2.433 Å	2.458 Å
Sn-2b	2.533 Å	2.606 Å

In this work the lengths of the cation-anion bonds of off-stoichiometric kesterite phase have been experimentally obtained from Rietveld refinements. Experimental results are presented in angstroms in Figure 45 according to kesterite cation ratios. Results have been correlated with the results obtained by neutron powder diffraction data analyses discussed in section 3.3.2 *Concentrations of intrinsic point defects* page 102.

Figure 45a, bond length (2a) – Se (8g), all obtained values were higher compared to the theoretical values (see Table 17). Bond lengths in the copper rich region are longer than in the copper poor region. Shortest bond has been found near to the A-type line.

Figure 45b, similar to the other copper bond length, all (2c) – Se (8g) bonds values were higher than theoretical values. Deviation of (2c) – Se (8g) lengths was higher compared with (2a) – Se (8g). But the longer bond value was found near to the B-type line where also the highest concentration of copper-zinc disorder defect has been detected (disorder effect concentrations discussed in page 112).

In the case of bond length (2d) – Se (8g) (see Figure 45c), experimental values exhibit similar values to the proposed by theoretical calculations (Table 17), especially in the copper poor region (between A- and B-type lines), but also in the copper rich and zinc poor region (near to the D-type line). Shortest bond lengths have been found in the copper rich region between the C and D-type lines, (2d) – Se (8g) exhibit a significant deviation.

In Figure 45d, bond lengths (2b) – Se (8g) in the copper poor region are closer to the value proposed by *Gürel* 2.533 (see Table 17). As noticed, bond lengths were longer in the copper rich and tin rich region.

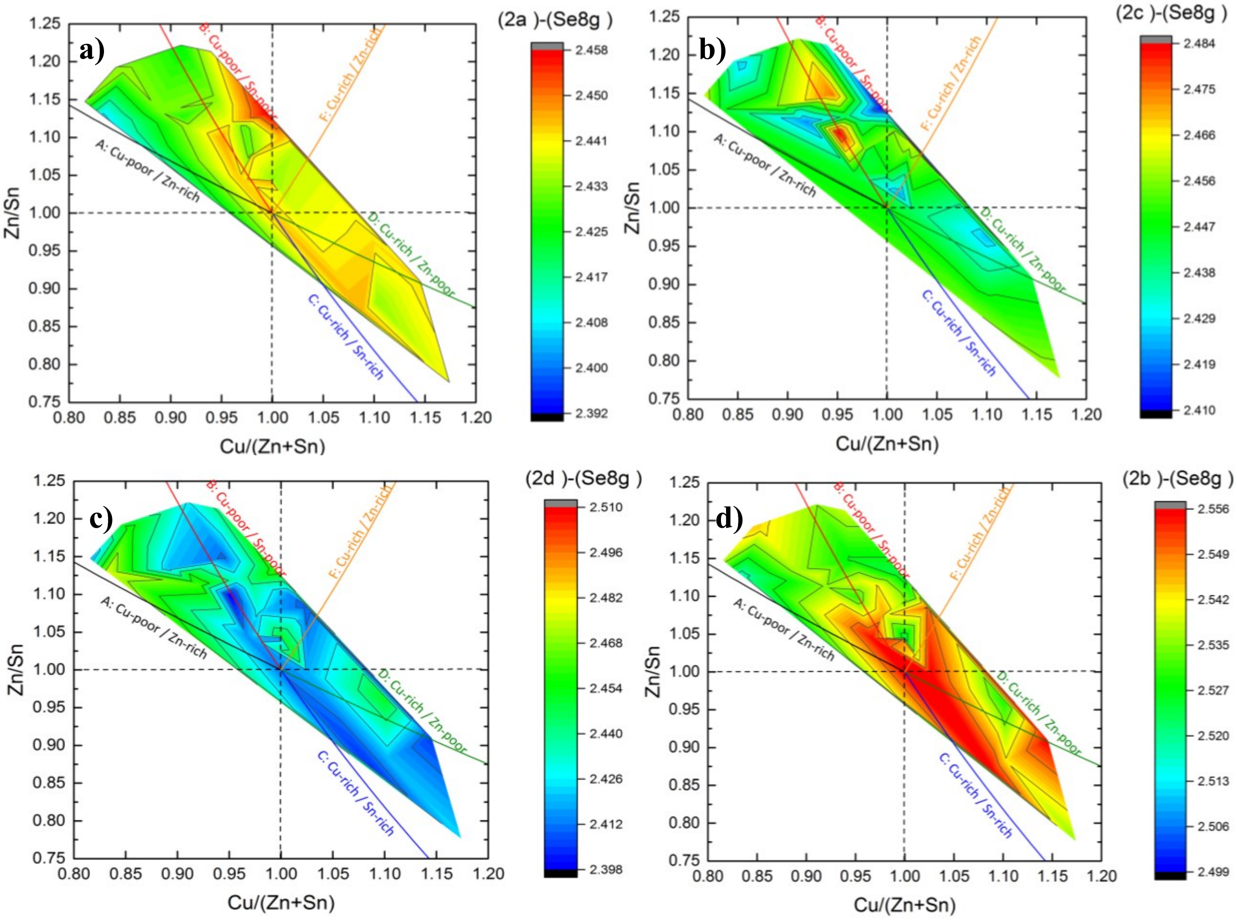

Figure 45 *Bond lengths in the kesterite phase* ***a)*** *(2a)–Se (8g),* ***b)*** *(2c)–Se (8g),* ***c)*** *(2d)–Se (8g) and* ***d)*** *(2b)–Se (8g) [Å].*

According to standard deviation formula, higher standard deviation has been found in (2d) – Se (8g) and (2c) – Se (8g) bond lengths as the result of copper-zinc disorder defect and the most stable was the (2a) – Se (8g) where less cations substitutions occurred.

- **Bond angles**

Furthermore, the bond angles of cation-anion-cation of off-stoichiometric kesterite phase have been also obtained from Rietveld refinements. As discussed in previous sections, variation of bond lengths and anion positions have been observed. It is then expected a distorted tetrahedron, thus its angles vary from the ideal angle 109.4712°. The distorted tetrahedron is then reflected in the cation-anion-cation bond angles.

Experimental results of cation-anion-cation angles of kesterite type structure from off-stoichiometric CZTSe are presented. In Figure 46, the angles of two kesterites are compared: a) a copper poor kesterite with a cation ratio Cu/(Zn+Sn)=0.833 vs b) copper rich kesterite with cation ratio Cu/(Zn+Sn)=1.174.

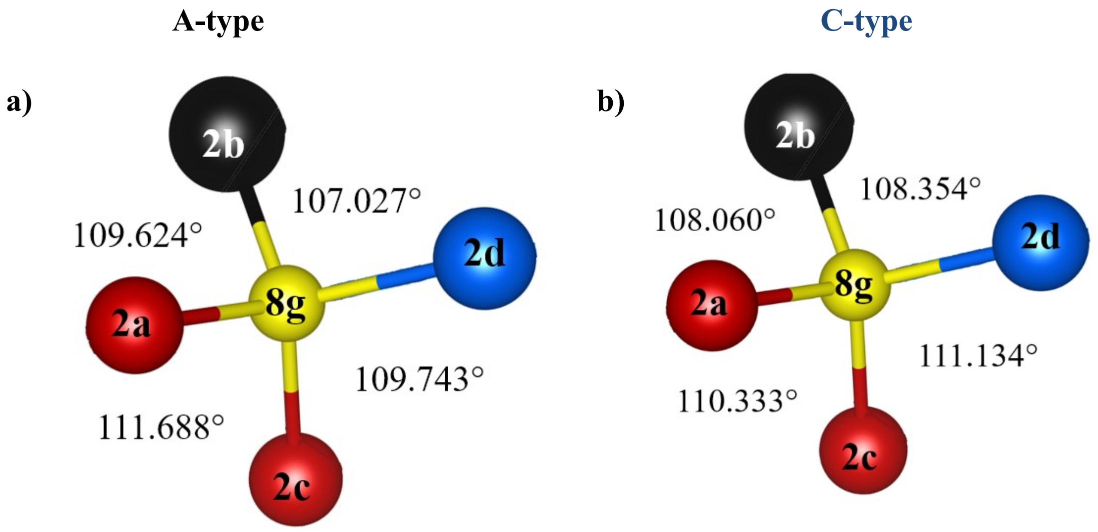

Figure 46 *Cation-anion-cation bond angles in the tetrahedron of kesterite type structure: a) Cu poorest CZTSe and b) Cu richest CZTSe.*

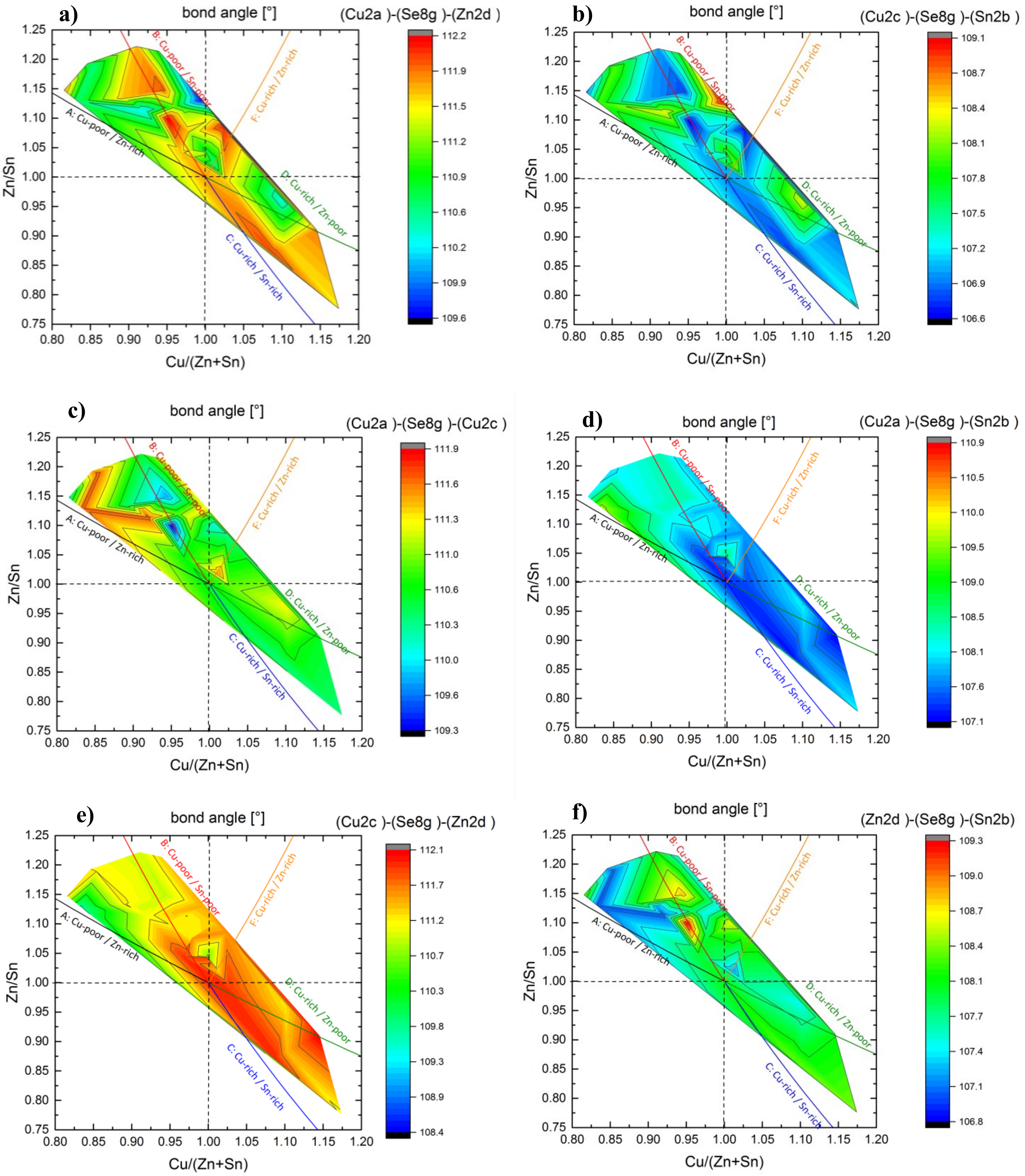

Figure 47 *Cation-anion-cation bond angles in the tetrahedron of kesterite type structure according to kesterite cation ratios*

As expected all cation-anion-cation angles exhibit a distorted tetrahedron ≠ 109.5°. In the copper poor CZTSe Figure 46a, strong deviation from ideal value was observed in the (Cu2a)-(Se8g)-(Cu2c)= 111.688° which can be explained because it was the region where vacancies on 2a and 2c are present. (Cu2a)-(Se8g)-(Sn2b)= 109.624° and angle (Cu2c)-(Se8g)-(Cu2d)= 109.743° are slightly closer to the ideal. In this region near to the A-type line also a lower copper-zinc disorder defect in the 2c and 2d site has been observed by neutron diffraction analysis as discussed in page112.

In the case of copper rich kesterite Figure 46b, compared with the other cation-anion-cation angles the (Cu2c)-(Se8g)-(Cu2d)= 111.134° deviated the most from the ideal value. This Cu-rich CZTSe exhibit a higher copper-zinc disorder defect compared with the copper poor kesterite. Additionally, in this copper rich kesterite the highest concentration of copper on zinc (Cu_{Zn}) and tin on zinc (Sn_{Zn}) antisite defects have been detected. It seems like a more distorted tetrahedron occurred in copper rich kesterite because none of its angles are near to the ideal angle (109.5°).

Cation-anion-cation angles of all 29 off-stoichiometric kesterite phase are presented in Figure 47 according to Cu/(Zn+Sn) and Zn/Sn ratios. By applying a standard deviation formula within these obtained values, a high deviation of 0.646 occurred in (Cu2a)-(Se8g)-(Cu2d) angle and a lower deviation of 0.457 was found in the angle (Cu2c)-(Se8g)-(Zn2d).

Conclusion

i. Variations of bond lengths and bond angles according to the chemical composition (Cu-poor vs Cu-rich) have been observed.
ii. So far no experimental data of kesterite bond angles and lengths have been reported for off-stoichiometric compositions.
iii. Bond lengths and angles are really important for theoretical calculations because they could be used as approximation values to determine for example vibrational modes or elastic constants.
iv. But it is important to keep in mind that some of the observed trends might be inside the uncertainties of the refinements since often the given errors are underestimated.

3.3 Neutron powder diffraction and Rietveld refinements

3.3.1 Average neutron scattering length and cation distributions

3.3.1.1 Intrinsic point defect in copper poor region

Off-stoichiometric polycrystalline powder samples have been measured by neutron diffraction as described in section 2.3.2 (page 30). The collected data has been analyzed by Rietveld refinements (see page 40) and further application of the average neutron scattering length method allows to determine the distribution of the cation and intrinsic point defects.

In total 9 kesterites have been obtained with a copper poor zinc rich composition. These kesterites could be described as mixtures of A-type: copper poor and zinc rich and B-type: copper poor and tin poor (see 3.1.7 page 75). In Figure 48, three A-B kesterites are presented as an example of the average neutron scattering length analysis method. In circle symbols, the experimental neutron scattering length $\bar{b}^{exp}$, extracted from Rietveld refinements, and in star symbols $\bar{b}^{calc}$, the calculated average neutron scattering length is shown. The later in agreement with the chemical composition (as described in page 41).

In the kesterite type structure the crystallographic sites 2*a* and 2*c* are expected to be fully occupied by copper (neutron scattering length b_{Cu}=7.718 fm). However, these copper poor kesterite phases exhibit $\bar{b}_{2a}^{exp}$ and $\bar{b}_{2c}^{exp}$<7.718 fm. As expected, a dependency of copper deficit within the kesterite phase is correlated with a deficit of the average neutron scattering length. For example, in the kesterite phase (84% A-type) which exhibits the lowest $\bar{b}_{2a}^{exp}$ and $\bar{b}_{2c}^{exp}$ values. This is an indication that 2a and 2c sites are not fully occupied by copper: $\bar{b}_{2a}^{exp}$ and $\bar{b}_{2c}^{exp}$ might decrease either by the presence of copper vacancies (V_{Cu}), zinc on copper and/or tin on copper (Zn_{Cu} /Sn_{Cu}) antisite defects because b_{Zn} and b_{Sn} are lower than $b_{Cu.}$

On the other hand, if the 2*d* site is fully occupied by zinc, the neutron scattering length would be b_{Zn}=5.680fm. But Figure 48 shows an increase of neutron scattering length

$\bar{b}_{2d}^{exp}$>5.680 fm. In this case $\bar{b}_{2d}^{exp}$ might increase by the presence of copper on zinc or tin on zinc antisites (Cu_{Zn}/Sn_{Zn}) because b_{Cu} and b_{Sn} are higher than b_{Zn}.

The crystallographic site 2*b* is expected to be fully occupied by tin (b_{Sn}=6.225 fm). Variations on this site were less noticeable in comparison with the other sites. A slightly decrease of $\bar{b}_{2b}^{exp}$ has been observed which might be due to the presence of tin vacancies (V_{Sn}) or zinc on tin (Zn_{Sn}) antisite because $b_{Zn} < b_{Sn}$.

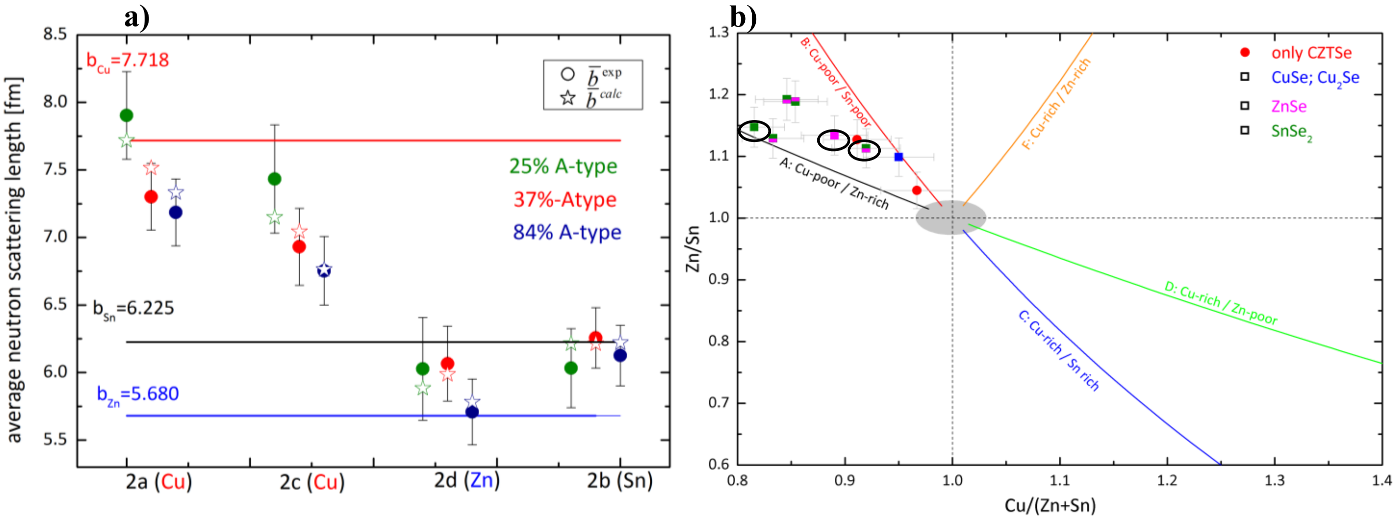

***Figure 48 a)** average neutron scattering length of 3 A-B kesterites **b)** kesterites examples are marked in a black circle in the cation ratio plot.*

Nevertheless, charge balance is taken into account by the cation substitutions, therefore, only the intrinsic point defects that keep the charge neutrality are allowed. The expected intrinsic point defects in this region are: copper vacancies and zinc on copper antisite defects for A-type (V_{Cu} + Zn^{2+}_{Cu}) and for B-type zinc on copper and zinc on tin antisite defects ($2Zn^{2+}_{Cu}$ + Zn^{2+}_{Sn}) (as described in section 1.5, page 17).

Two examples of the cation distribution of A-B kesterites are presented in Figure 49. The cation distribution of kesterite: $Cu_{1.902}Zn_{1.090}Sn_{0.979}Se_4$ (25% A-type // 75% B-type) shows that the 2a site is fully occupied by copper but copper vacancies have been observed on the

2c site, together with a high amount of zinc on copper antisite. Also a zinc on tin antisite was observed in the 2b site.

In the case of copper poor kesterite: $Cu_{1.740}$ $Zn_{1.141}Sn_{0.994}Se_4$ (84% A-type // 16% B-type), the cation distribution shows that copper vacancies have been observed in both 2*a* and 2*c* sites, also zinc on copper antisite was observed on the 2*c* site. Those observed defects are in a good agreement with the expected off-stoichiometry type defects. However, the presence of copper on zinc antisite defect observed on the 2*c* and 2*d* sites correspond to the copper-zinc disorder defect. This disorder defect has been introduced in section 1.1 page 3.

Theoretical calculations support that intermixing of Cu and Zn layer is highly expected because its costs only very little energy. Disordered kesterite has been already observed experimentally in stoichiometric CZTSe by *S.Schorr* [9]. Nevertheless, this disorder defect is limited to the 2*c* and 2*d* Wyckoff position in the planes *z*=1/4 and *z*=3/4.

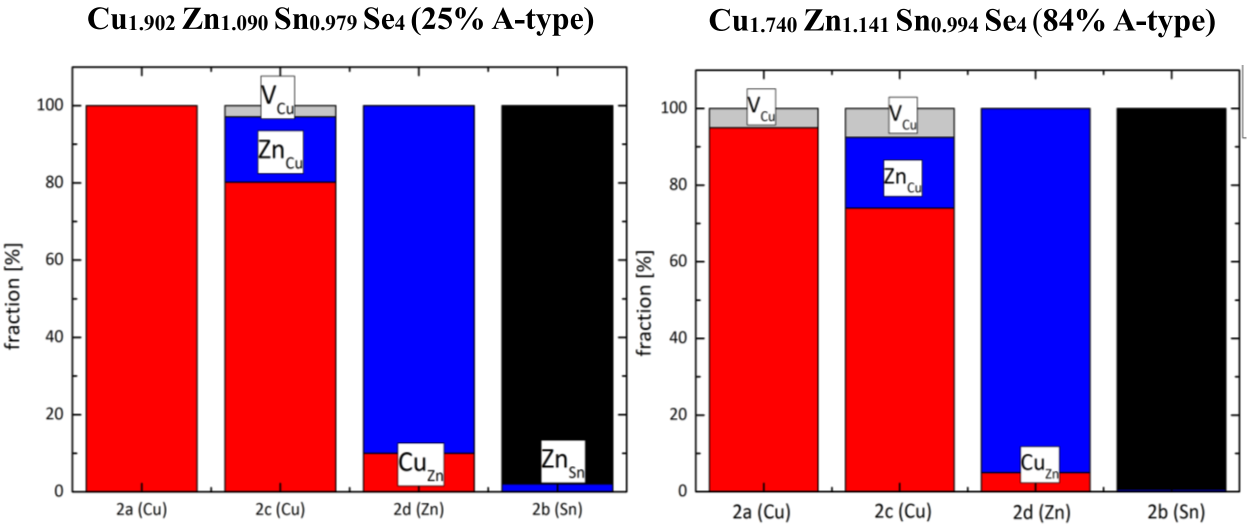
$Cu_{1.902}$ $Zn_{1.090}$ $Sn_{0.979}$ Se_4 (25% A-type)

$Cu_{1.740}$ $Zn_{1.141}$ $Sn_{0.994}$ Se_4 (84% A-type)

Figure 49 *Cation distribution and point defects of A-B kesterites: 25% and 84% A-type.*

The results out of 9 analyzed A-B kesterites within the copper poor region, have proved that they are indeed mixtures, thus the presence of both A- and B-type expected defects has been observed. Additionally, the copper-zinc disorder defect has been observed within all

A-B kesterites on the 2*c* and 2dWyckoff positions. Remarkable copper vacancies in 2a and 2c sites have been observed in copper poorest kesterites near to the A-type line, and vacancies only on the 2*c* site were observed between the A- and B- type line. Further discussion about the Cu-Zn disorder defect is presented in section 3.3.3 (page 112).

3.3.1.2 Intrinsic point defect in copper poor and copper rich region

The majority of the obtained kesterites are considered to be a mixture of B-type (copper poor, tin poor) and F-type (copper rich, zinc rich). This is a particular mixture because it includes both Cu-poor to Cu-rich regions. In total 13 kesterites are located within the Cu/(Zn+Sn) ratio range: from 0.910 to 1.023.

In Figure 50, three examples of B-F kesterites are presented. As expected, a trend with the amount of copper in Wyckoff position 2*a* and 2*c* is observed. In the case of copper poor kesterites, the average neutron scattering length $\bar{b}_{2a}^{exp}$ is lower than b_{Cu}=7.718 fm. But $\bar{b}_{2a}^{exp}$ rises up to b_{Cu}=7.718 fm in the copper rich kesterite. However, the average neutron scattering length $\bar{b}_{2c}^{exp}$ remains below b_{Cu}=7.718 even within a copper rich kesterite (see 22% B-type in Figure 50). It means that vacancies or/and an element with a lower average neutron scattering length might be presented on the 2*c* site.

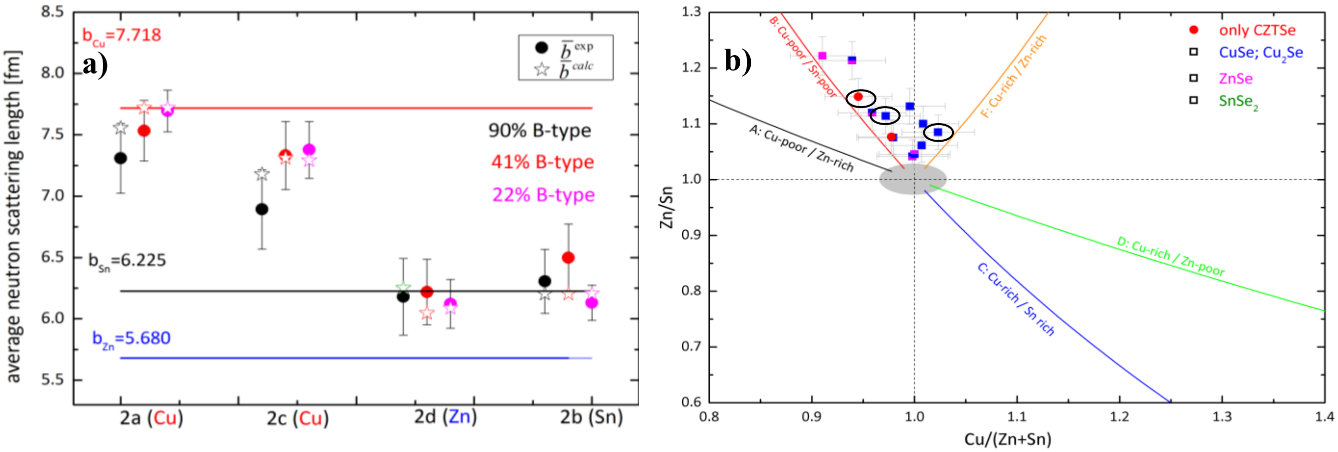

Figure 50 a) *average neutron scattering length of 3 B-F kesterites* ***b)*** *kesterites examples are marked in a black circle in the cation ratio plot.*

In the case of $2d$ and $2b$ sites which are expected to be fully occupied by zinc and tin respectively. A minor variation of the average neutron scattering lengths of the $2d$ and $2b$ sites ($\bar{b}_{2d}^{exp}$, $\bar{b}_{2b}^{exp}$) were observed in comparison with $2a$ and $2c$. Because both B- and F-type exhibit zinc rich and tin poor compositions.

As mentioned above, expected intrinsic point defects must keep the charge neutrality. B-type proposed defects are: $2Zn^{2+}{}_{Cu} + Zn^{2+}{}_{Sn}$. But in the case of F-type, the substitution of tin (Sn^{4+}) might lead to two different defects: $Zn^{2+}{}_{Sn} + 2Cu^{+}{}_{i}$ or $Cu^{+}{}_{Sn} + Cu^{+}{}_{i} + Zn^{2+}{}_{i}$. Although both of these F-type defects keep the charges neutrality, only $Zn^{2+}{}_{Sn}$+$2Cu^{+}{}_{i}$ defects have been so far observed.

Cation distribution examples of B-F kesterites are presented in Figure 51. Copper poor kesterite (90% B-type) presence zinc on copper (Zn_{Cu}) antisite defect on both $2a$ and $2c$ sites. Also zinc on tin (Zn_{Sn}) antisite on the $2b$ site was observed. Such observed defects are in a good agreement with expected B-type defects. Nevertheless, few copper interstitials (Cu_i) have been also observed, as the result of influences of the F-type defects.

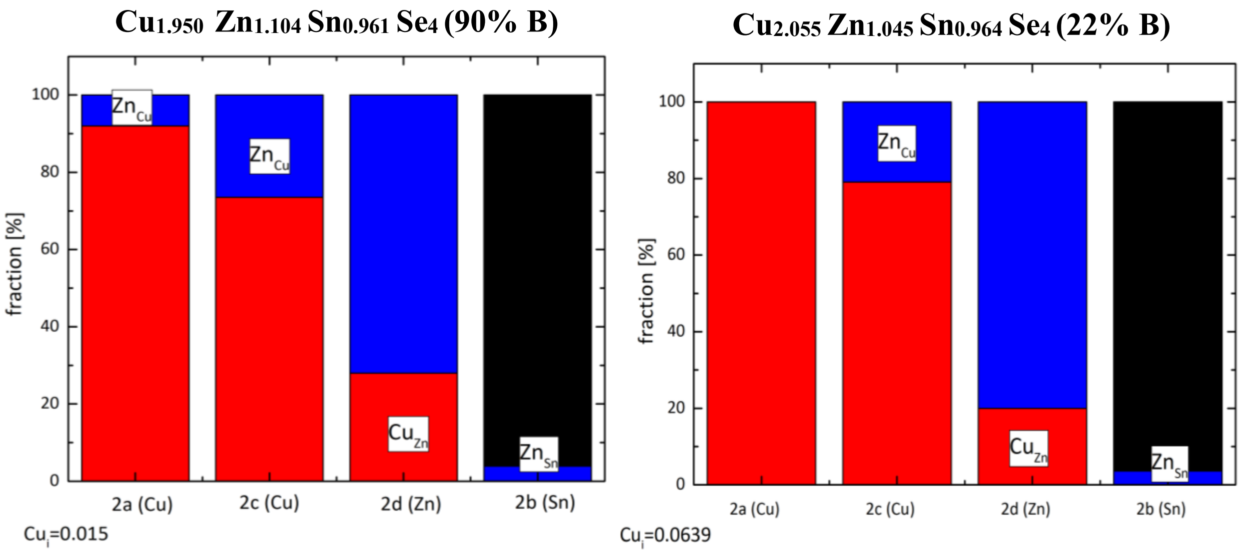
$Cu_{1.950}$ $Zn_{1.104}$ $Sn_{0.961}$ Se_4 (90% B)

$Cu_{2.055}$ $Zn_{1.045}$ $Sn_{0.964}$ Se_4 (22% B)

Figure 51 *Cation distribution and point defects of B-F kesterites: 22% and 90% B-type.*

On the other hand, copper rich kesterite (78% F-type) presents zinc on tin (Zn_{Sn}) antisite defect together with a higher amount of copper interstitials (Cu_i). Those defects are expected within the copper, zinc rich and tin poor region. Additionally, the copper-zinc disorder defect (Zn_{Cu} - Cu_{Zn}) has been also observed on the 2*c* and 2*c* sites within all B-F kesterites.

3.3.1.3 Intrinsic point defect in copper rich and zinc poor region

In comparison with the copper poor, less of off-stoichiometric kesterites have been obtained within the copper rich and zinc poor region. In total 4 kesterites could be considered as a mixture of F-type (copper rich, zinc rich) and D-type (copper rich zinc poor). However, two of these kesterites are indeed quite near to the stoichiometric region and the other two lie closer to the D-type than the F-type.

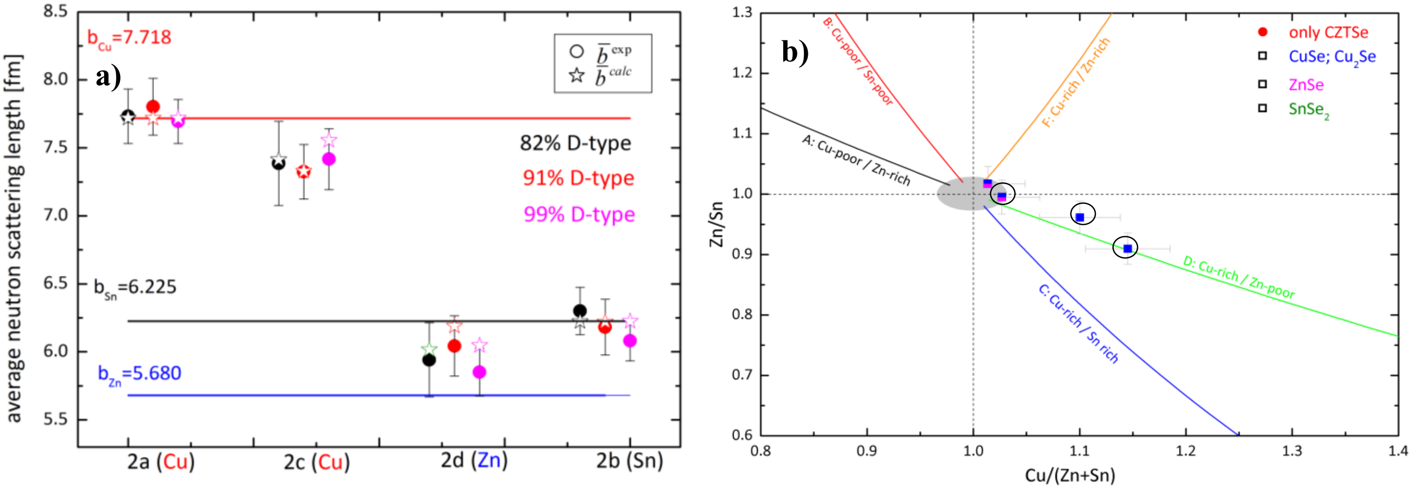

***Figure 52 a)** average neutron scattering length of 3 F-D kesterites **b)** kesterites examples are marked in a black circle in the cation ratio plot.*

In Figure 52a,b, three examples of F-D kesterites are presented. The one in black symbols (82% D-type) is located near to the stoichiometric region where the uncertainties of type percentages deduced by linear combination became higher. However, the average neutron scattering lengths $\bar{b}_{2c}^{exp}$ and $\bar{b}_{2d}^{exp}$ differ from b_{Cu} and b_{Zn} values. This is an indication that intrinsic point defects are present even within kesterites close to the stoichiometry region. In both 91% and 99% D-type kesterites (copper rich zinc poor), the 2*a* site is fully occupied by copper, but 2*c* and 2*d* sites exhibit deviations from b_{Cu} and b_{Zn} values. This might be due to Cu-Zn disorder defect as well as copper on zinc antisite defect, Cu_{Zn} is in fact an expected D-type defect. D-type defects occurred by the substitution of Zn^{2+} for Cu^{+}_{Zn} + Cu^{+}_{i}.

In Figure 53, two cation distribution examples of F-D kesterites are shown. In the case of a kesterite with 82% D-type, which is indeed close to the stoichiometry region. But the presence of expected D-type defects as well as few amount of F-type expected defects have been observed.

Expected D-type defects have been observed in the 99% D-type kesterite. Copper on zinc antisite and copper interstitial defects have been detected with a higher concentration, in comparison with the 82% D-type kesterite. Additionally, the Cu-Zn disorder defect has been also observed within all F-D kesterites.

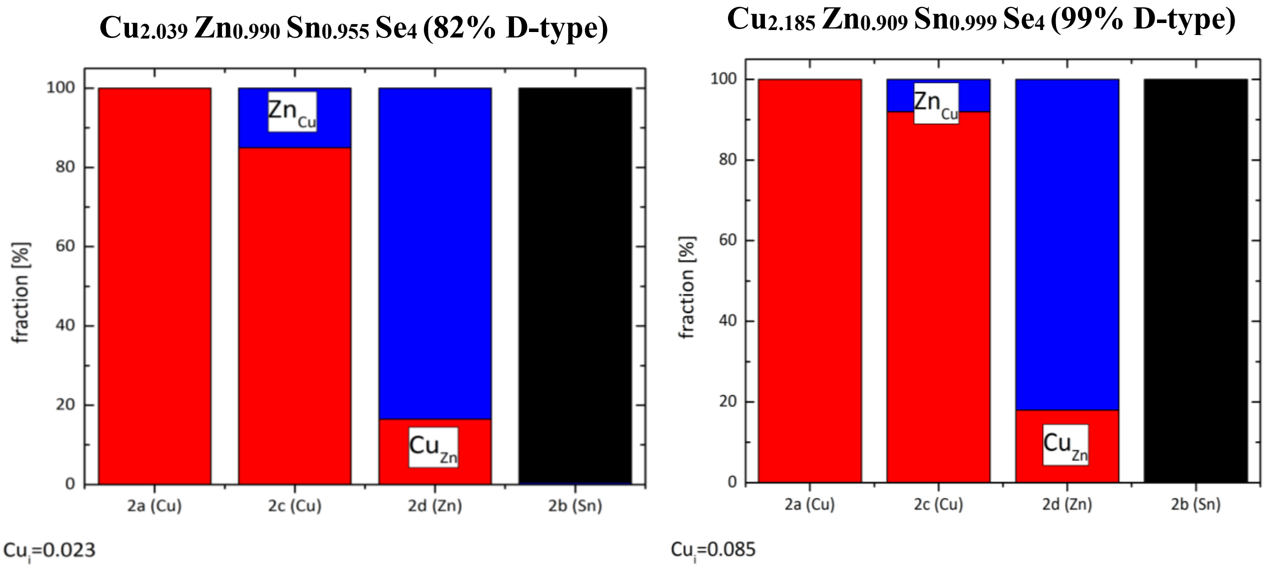
$Cu_{2.039}$ $Zn_{0.990}$ $Sn_{0.955}$ Se_4 (82% D-type)

$Cu_{2.185}$ $Zn_{0.909}$ $Sn_{0.999}$ Se_4 (99% D-type)

Figure 53 *Cation distribution and point defects of F-D kesterites: 82% and 99% D-type.*

The detection of Cu-Zn disorder defect in the copper rich region, slightly differ from the copper poor region. For instances, in the Cu-poor region, the presence of Cu-Zn disorder defect is deduced by the occurrence of copper on zinc antisite (Cu_{Zn}) on the 2*d* site. But in the copper rich region, the presence of this defect is deduced by the occurrence of zinc on copper (Zn_{Cu}) antisite defect on the 2*c* site. Nevertheless, it is important to keep in mind that the amount of Zn_{Cu} on the 2*c* site correspond to the Cu-Zn disorder defect, will be equally reflected as Cu_{Zn} on the 2*d* site. Only what it is remained of Cu_{Zn} on the 2*d* site is considered as D-type defect. Further information concerning the concentration of intrinsic point defects is presented in the section 3.3.2 *Concentrations of intrinsic point defects* (page 102).

3.3.1.4 Intrinsic point defect in copper rich and tin rich region

In total 3 kesterites could be considered as a mixture of C-type (copper rich tin rich) and D-type (copper rich zinc poor). But two of them are located closer to the C-type than to the D-type line. In Figure 54a, the average neutron scattering lengths are presented. For all these kesterites their $\bar{b}_{2a}^{exp}$ and $\bar{b}_{2b}^{exp}$ remain quite stable with values near to b_{Cu} and b_{Sn}. But $\bar{b}_{2c}^{exp}$ and $\bar{b}_{2d}^{exp}$ deviate from b_{Cu} and b_{Zn} respectively.

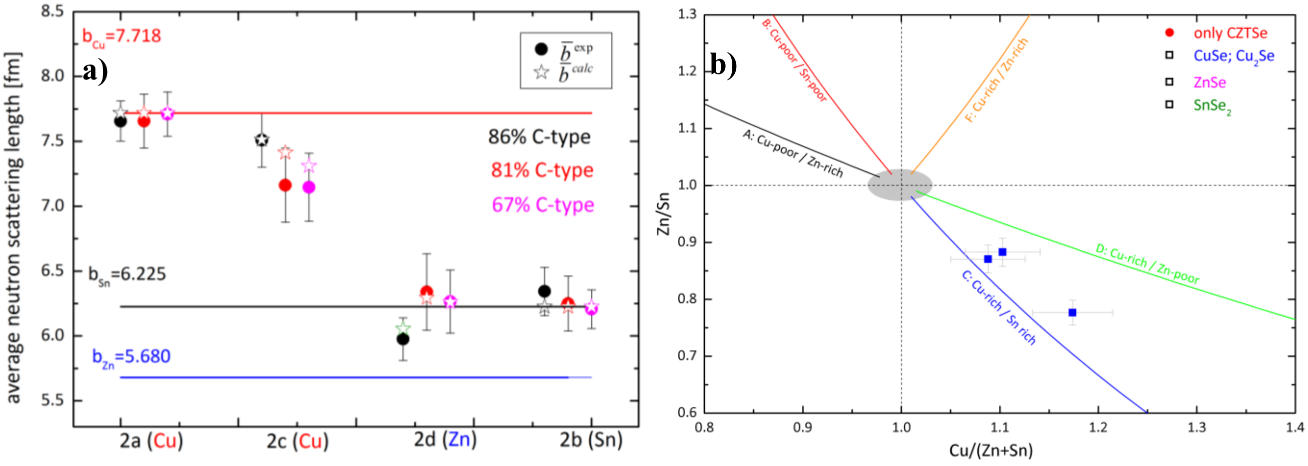

Figure 54 a) *average neutron scattering length of 3 C-D kesterites* ***b)*** *kesterites examples in the cation ratio plot.*

The expected C-type defects from substitution of Zn^{2+} are: 2 Cu^{+}_{Zn} + Sn^{4+}_{Zn}. In Figure 55, two cation distributions of C-D kesterites are shown. These two kesterites exhibit a Sn-rich composition, thus the presence of tin on zinc (Sn_{Zn}) antisite defect has been observed. In these kesterites, the 2a and 2b sites are fully occupied by copper and tin respectively. But the Cu-Zn disorder defects have been observed in the 2*c* and 2*d* sites. Additionally, copper on zinc (Cu_{Zn}) antisite defect on the 2d site have been detected, which is an expected defect for C-type and D-type.

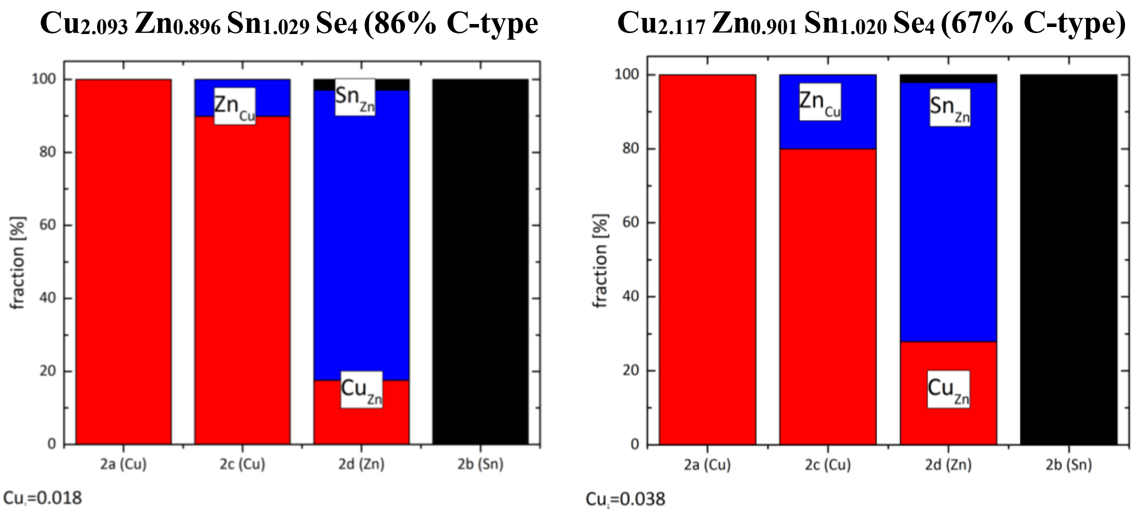
$Cu_{2.093}$ $Zn_{0.896}$ $Sn_{1.029}$ Se_4 (86% C-type

$Cu_{2.117}$ $Zn_{0.901}$ $Sn_{1.020}$ Se_4 (67% C-type)

Figure 55 *Cation distribution and point defects of C-D kesterites: 86% and 67% C-type.*

3.3.2 Concentrations of intrinsic point defects

3.3.2.1 Copper vacancies

In order to have a better overview of the intrinsic point defects, the defect concentrations of each intrinsic point defect per cubic centimeter (cm^{-3}) have been calculated. The volume of a unit cell is deduced according to extracted lattice parameters from Rietveld refinements. Multiplying the volume by the defect fractions on each Wyckoff positions 2*a*, 2*c*, 2*d*, 2*b* (see previous section 3.3.1 *Average neutron scattering length and cation distributions)* the defect concentrations of a defect is obtained per cubic centimeter cm^{-3}.

The fractions of copper vacancies are given by percentages (see Figure 56a). If the same defect has been observed on two Wyckoff positions, for example on the 2*a* and 2*c* sites, the fraction of both sites are summed. This was the case of two kesterites lying near to the A-type line.

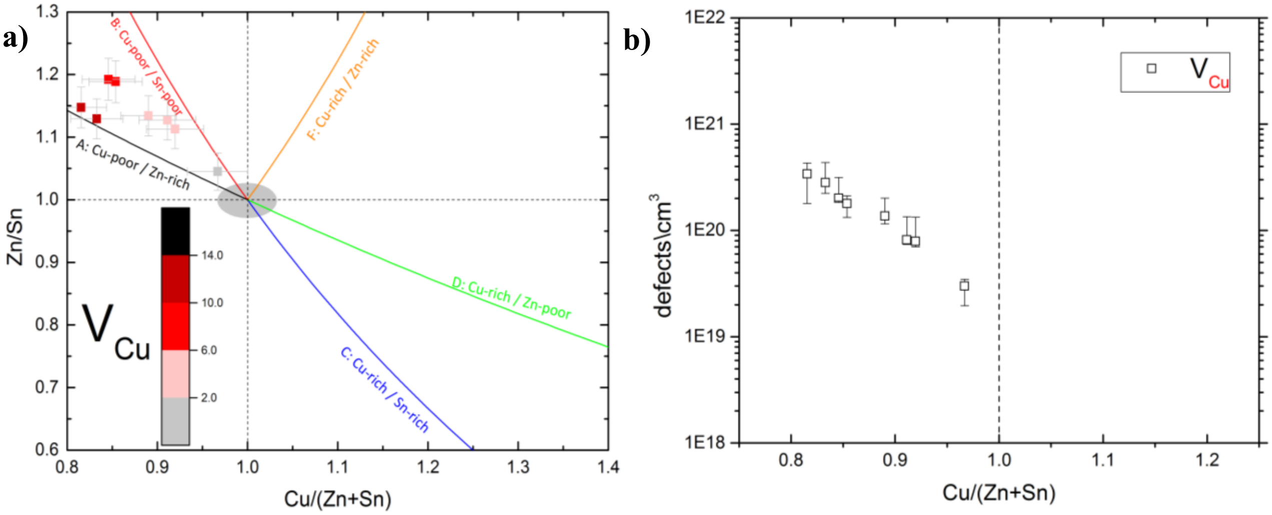

Figure 56 a) *percentages of V_{Cu} according to kesterite cation ratios (%) and* ***b)*** *defect concentrations of copper vacancies by 1/cm^{3}in relation to kesterite Cu/(Zn+Sn) ratio.*

The concentrations of copper vacancies are presented in Figure 56b according to kesterite ratio Cu/(Zn+Sn). As expected, the highest concentration (V_{Cu}~$3.4x10^{20}$cm^{-3}) has been observed in the cooper poorest kesterite which lies close to the A-type line. Concentrations of copper vacancies decrease proportionally to the Cu/(Zn+Sn) ratio. In the case of kesterites located between the A- and B-type lines, copper vacancies have been observed only on the 2*c* site.

In summary, concentrations of V_{Cu} are in a range from: ~$7.8x10^{19}$ to ~$2.0x10^{20}$ cm^{-3}. The lowest concentration (~$2.9x10^{19}$ cm^{-3}) was detected close to the stoichiometry region. No copper vacancies have been detected beyond the B-type line.

3.3.2.2 Zinc on copper and copper on zinc antisites

In this section copper on zinc (Cu_{Zn}) and zinc on copper (Zn_{Cu}) antisite defects are discussed. The fractions of Zn_{Cu} inside the Cu-poor region together with the fractions of Cu_{Zn} inside the Cu-rich region are shown in Figure 57. But it is important not to confuse these intrinsic defects with the Cu-Zn disorder defect, because these fractions are separated from the disorder defect.

For example, in a B-type kesterite, the Zn_{Cu} antisite is observed on the 2*c* site, therefore the Cu_{Zn} observed in the 2*d* site is attributed to the Cu-Zn disorder defect. Thus the same amount of Cu_{Zn} on the 2*d* site is subtracted from the Zn_{Cu} on the 2*c* site. Thus, what is left of Zn_{Cu} antisite on the 2*c* site is summed with the Zn_{Cu} on the 2*a* site (if any). The Cu-Zn disorder defect is limited to the 2*c* and 2*d* Wyckoff positions, further discussion on this defects are presented in section *3.3.3 Copper – zinc disorder defect concentration (*CuZn+ZnCu *(*page 112).

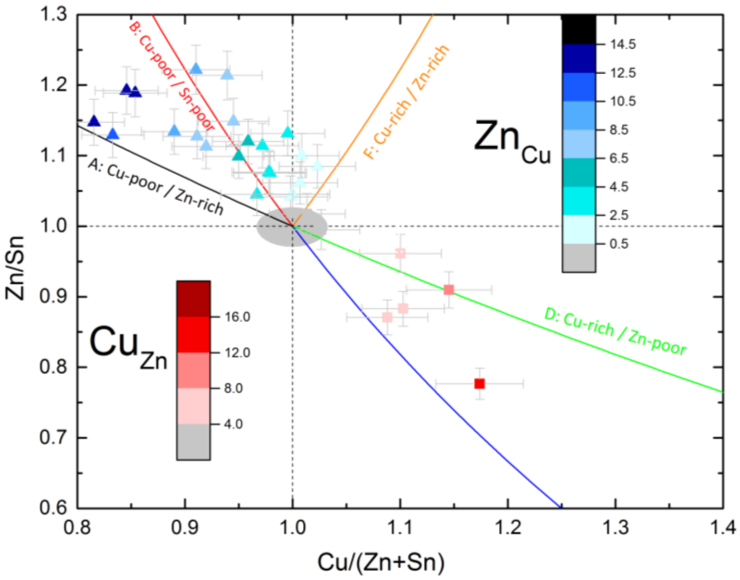

Figure 57 *Percentages of Zn_{Cu} and Cu_{Zn} according to kesterite cation ratios (%).*

Concentrations of zinc on copper (Zn_{Cu}) antisite are presented in *Figure 58*a according to Cu/(Zn+Sn) kesterite ratio. The highest concentration (Zn_{Cu}~$3.68x10^{20}$ cm^{-3}) has been observed in the Cu-poorest kesterite which lies close to the A-type line. High concentrations ~$3.50x10^{20}$ cm^{-3} have been observed within two A-B kesterites with zinc rich composition (~Zn/Sn=1.19). The lowest concentration ~$2.45x10^{19}$cm^{-3} has been detected in a kesterite with Cu/(Zn+Sn)=1.023 and Zn/Sn=1.085.

Zinc on copper (Zn_{Cu}) antisite defect is widely spread along the Zn-rich region, because it is an expected defect for both A- and B-types. However, it has been also observed, but at lower concentrations within B-F kesterites when Cu/(Zn+Sn)>1. In fact, Zn_{Cu} antisite is unexpected inside the Cu-rich region. But, it seems like the influence of B-type on F-type (and vice versa) is strong within B-F kesterites. The region between B-F kesterites differ from the other mixtures because a transition from the Cu-poor to Cu-rich composition occurred. Furthermore, according to theoretical calculations *Chen et al* [2], the formation energy of Zn_{Cu} is lower compared to Zn_{Sn}, thus low energy could have been also beneficial for occurrences of Zn_{Cu} within Cu/(Zn+Sn)>1.

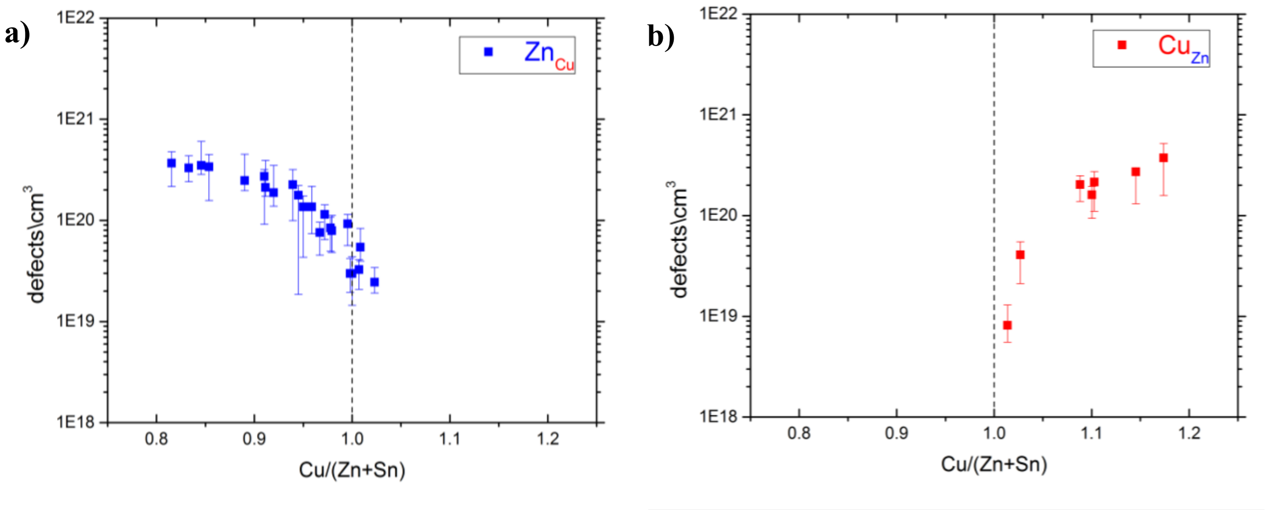

***Figure 58 a)** defect concentrations of zinc on copper (Zn_{Cu}) and **b)** copper on zinc (Cu_{Zn}) by 1/cm^3 in relation to kesterite Cu/(Zn+Sn) ratio.*

In *Figure 58*b, the concentrations of the copper on zinc antisite defects (Cu_{Zn}) are presented. Despite of less amount Cu-rich kesterites in comparison with Cu-poor composition were obtained, it is possible to observe a clear trend of Cu_{Zn} defect concentrations increasing proportionally to the Cu/(Zn+Sn) ratio.

The highest Cu_{Zn} concentration (~$3.75\text{x}10^{20}$ cm^{-3}) has been observed when Cu/(Zn+Sn)=1.174 and the lowest concentration (~$8.16\text{x}10^{18}$ cm^{-3}) was detected close to the stoichiometric region: Cu/(Zn+Sn)=1.014. According to theoretical calculations, the formation energy of Cu_{Zn} is equally low as the formation of Zn_{Cu} [2]. But unlike Zn_{Cu} defect observed when Cu/(Zn+Sn)>1, no Cu_{Zn} defect has been observed when Cu/(Zn+Sn)<1.

3.3.2.3 Zinc on tin and tin on zinc antisites

Fractions of Zn_{Sn} and Sn_{Zn} are shown in Figure 59. The presence of Zn_{Sn} antisite defect has been observed in 23 kesterites. In contrast to the Sn_{Zn} antisite defect, has been detected only within 3 kesterites because fewer synthesis of kesterite were carried out inside the Zn-rich region. Nevertheless, the high occurrence of Zn_{Sn} antisite defect might be also related to its lower energy of formation in comparison with Sn_{Zn} defect which exhibit a higher formation energy [2].

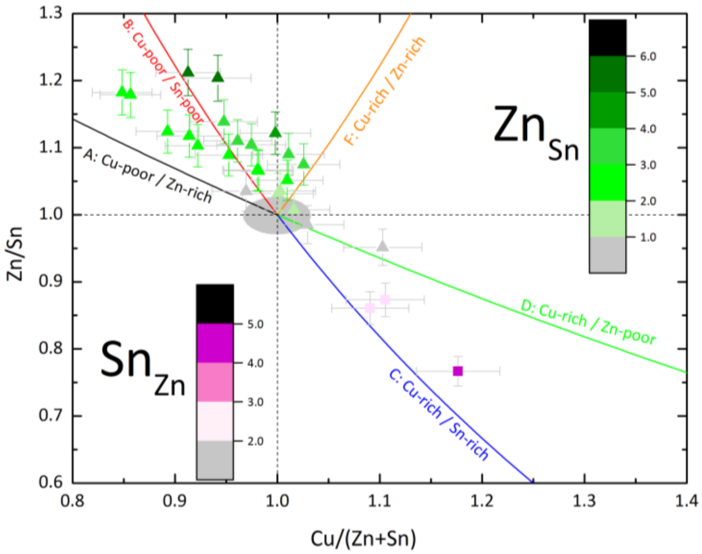

Figure 59 *Percentages of* Zn_{Sn} *and* Sn_{Zn} *according to kesterite cation ratios (%).*

Defect concentrations of zinc on tin (Zn_{Sn}) antisite are presented in Figure 60a. For this defects a better overview is given over the Zn/Sn ratio. The highest concentration (~1.60×10^{20} cm^{-3}) was observed in a kesterite with Zn/Sn=1.214. As expected, concentrations decrease proportionally to the Zn/Sn ratio. However, the lowest concentration (~1.36×10^{19} cm^{-3}) has been detected close to the stoichiometric region (Zn/Sn=0.995) rather than at the lowest ratio (Zn/Sn=0.961). The reason is because the amount of tin near stoichiometry is almost one, so less room for substitution of tin is possible. In the other hand, the kesterite with Zn/Sn=0.961 is located close to the D-type stoichiometry and exhibits a tin poor composition, thus tin substitution by zinc occurred.

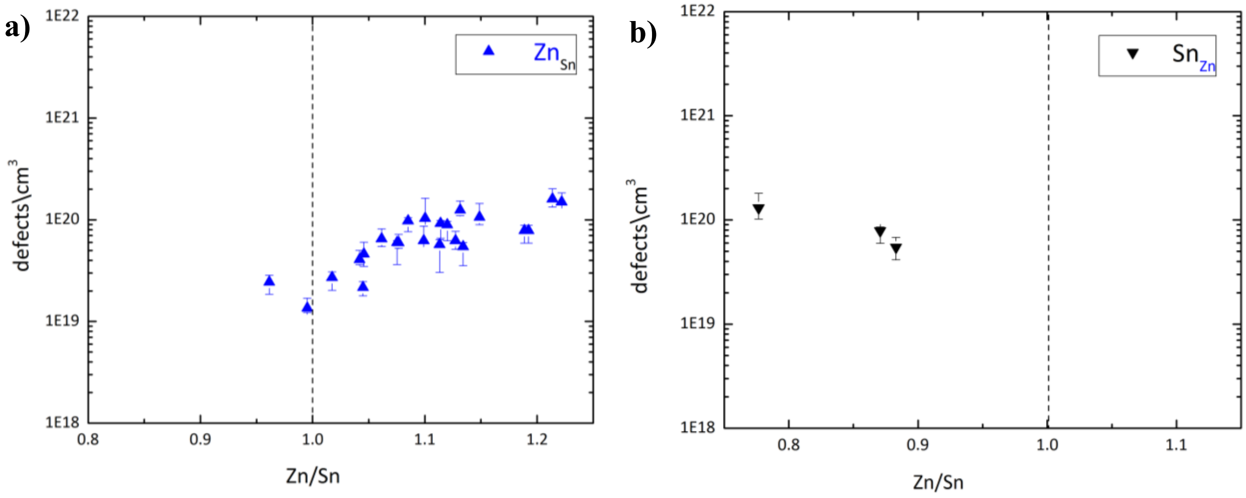

***Figure 60 a)** defect concentrations of zinc on tin (Zn_{Sn}) and **b)** tin on zinc (Sn_{Zn}) 1/cm^3 in relation to kesterite Cu/(Zn+Sn) ratio.*

Defect concentrations of tin on zinc antisite (Sn_{Zn}) are shown in Figure 60b. Despite the small amount of obtained kesterite within the zinc poor region, the increase of concentrations proportionally to Zn/Sn ratio is clearly observed. The highest concentration (~1.30×10^{20} cm^{-3}) was detected within the zinc poorest kesterite (Zn/Sn=0.777) close to C-type stoichiometry. The lowest concentration (~5.45×10^{19} cm^{-3}) has been observed at Zn/Sn=0.883. However, lower concentrations might occur if approaching the stoichiometric region.

3.3.2.4 Copper interstitials

The percentages of copper interstitials defects are given in Figure 61a. This defect differs from the others because it has not a fixed Wyckoff position. Thus the fraction of Cu_i is deduced when the others sites (2*a*, 2*c*, 2*d*, 2*b*) are fully occupied, so the remained excess of copper is then considered as interstitials. The kesterite structure can self-adapt to hold interstitials defects, however, in this work the percentages of Cu_i defects were lower than 10%, and therefore its influences in the crystal structure might be too small to be clearly observed in an experimental diffraction pattern.

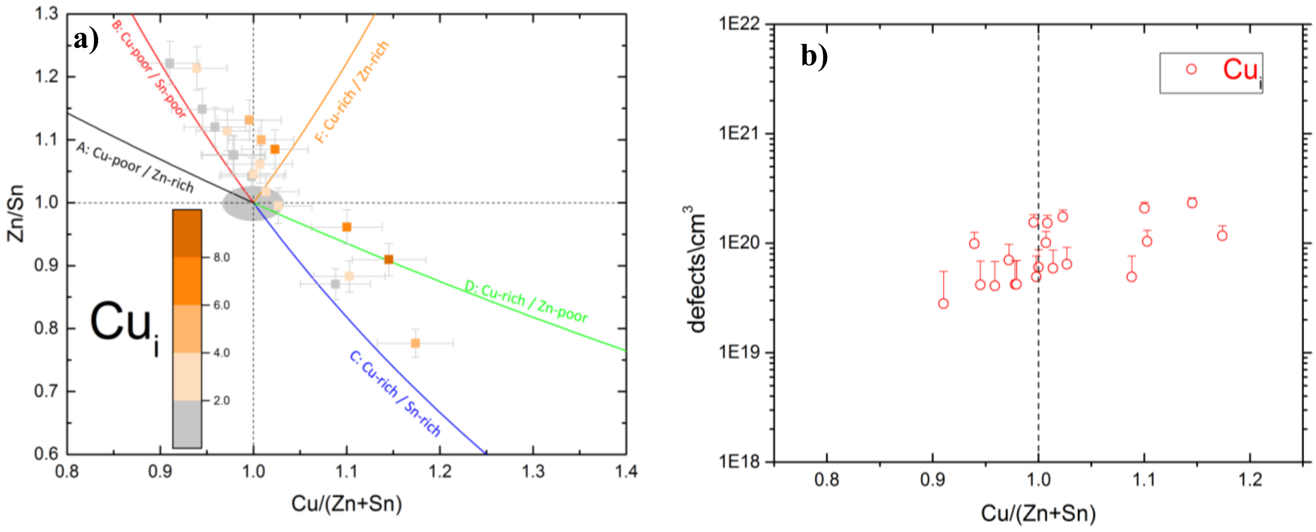

Figure 61 a) *percentages of Cu_i according to kesterite cation ratios (%) and* ***b)*** *defect concentrations of copper interstitials by 1/cm^3 in relation to kesterite Cu/(Zn+Sn) ratio.*

Copper interstitials have been detected within 20 kesterites, the defect concentrations are shown in Figure 61b. The highest concentration (~2.33x10^{20} cm^{-3}) has been detected close to the D-type stoichiometry with a Cu/(Zn+Sn)=1.145. The lowest concentration (~2.81x10^{19} cm^{-3}) has been unexpectedly detected inside the Cu-poor region with a Cu/(Zn+Sn)=0.910. However as discussed for the Zn_{Cu} defect, it seems like the influence of F-type on B-type (and vice versa) is strong within B-F kesterites. None Cu_i in copper poor region has been detected beyond the B-type line.

Furthermore, expected F-type defects by the substitution of tin ($Sn^{4+} \rightarrow Zn^{2+} + 2Cu^{+}$) might result in: Zn_{Sn}+2Cu_i or Cu_{Sn} + Cu_i + Zn_i defects [5]. However, experimentally only the "Zn_{Sn}+2Cu_i " defects have been observed. One of the reasons could be that according to theoretical calculations [2], the required energy for Cu_{Sn} and Zn_i defects formation is higher in comparison with Zn_{Sn}. Additionally, Cu_i defect formation requires very little energy which might also explain it occurrence even within the Cu-poor region.

3.3.2.5 Complementary discussion of experimental neutron diffraction data with reported theoretical calculations of intrinsic defects

Theoretical calculation by *Chen et al* [2] has reported the ionization levels of intrinsic defects in the band gap of $Cu_2ZnSnSe_4$ using density functional theory. In red lines the acceptor levels and the blue bars the donor levels (see Figure 62). The initial and final charge state are shown in parenthesis. Transition energy (ionization) levels derived according to the turning points shown in Figure 7 (see page 14). The band gap was corrected according to experimental value (1.0 eV). Nevertheless, the chemical potential on those calculations is limited to the stable region, so these results consider defects within stoichiometric CZTSe. If the chemical potential goes beyond the stable chemical potential region, the formation energies and the population of such defects could differ.

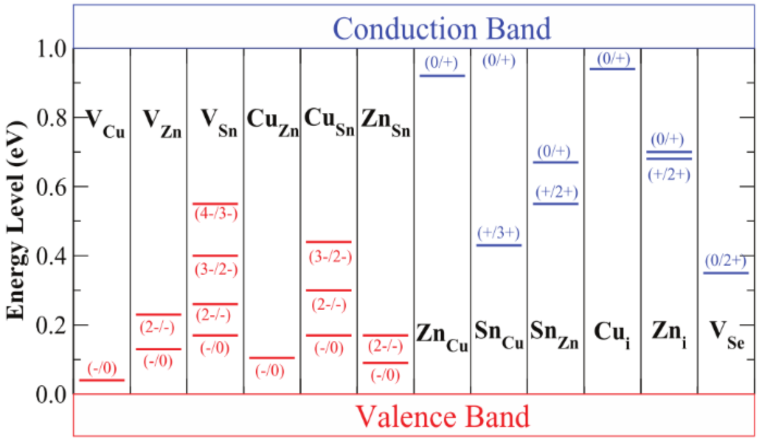

Figure 62 *Energetic levels of intrinsic defects from DFT calculations in 1eV band gap of* $Cu_2ZnSnSe_4$*. The red bars show the acceptor level and the blue bars show the donor level [Chen et al. Adv. Mater. (2013), 25, 1522-1539].*

In this work, occurrence of intrinsic point defects within off-stoichiometric CZTSe have been deduced by evaluation of experimental neutron diffraction data. The results of some intrinsic defects follow certain trends suggested by DFT calculations. Experimental results might help to validate theoretical approaches. Because it is important to keep in mind that it is still unclear how theoretically predicted defects formation, which are calculated under equilibrium could be transferred to real solar cell fabrication processes which involve off-stoichiometry and no equilibrium conditions. Therefore, further investigation on intrinsic defects under different kesterites synthesis routes and growth conditions are of great importance.

Moreover, donor-acceptor compensation has an electrical character; electron transfer occurs from donor to acceptor defect and there is a strong Coulomb attraction between the charge centers. According to theoretical calculations, considering the low energy of formation of intrinsic defects, self-compensated defects clusters can be formed (see Figure 63) [2]. This calculation shows that the overall formation energies of defect clusters significantly decreased compared to the intrinsic ones and correspond to a population range from 10^{11} to 10^{18} cm^{-3}. Population of clusters could influence the generation, separation and recombination of electro-hole pairs significantly.

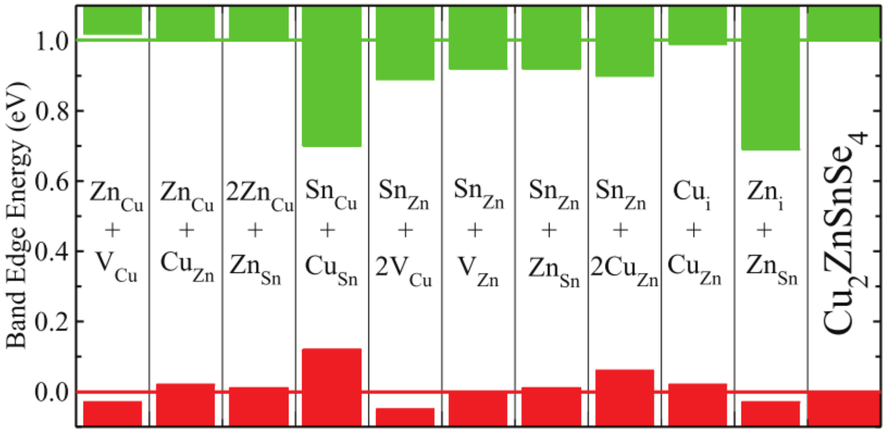

Figure 63 *Calculated valence and conduction band shifts caused by defect clusters. Position in valence (red) and conduction band (green) [Chen et al. Adv. Mater. (2013), 25, 1522-1539].*

On the other hand, the intrinsic point defects deduced from neutron powder diffraction analyses, are in a good agreement with proposed cation substitutions [4, 5]. Substitution process takes into account charges balance. Therefore, it is not possible to deduce clusters formation directly by compensating a positive donor defect with the negative acceptor defect concentrations. Nevertheless, it can be assumed that defect clusters would indeed occurred and its population would be in a lower concentration compared to the intrinsic point defects concentrations.

Conclusions: neutron powder diffraction and Rietveld refinements

i. Evaluation of neutron powder diffraction data by Rietveld analysis and the application of the average neutron scattering length method, have been a suitable way to determine the distribution of kesterites cations and concentrations of intrinsic point defects.
ii. Occurrences of the corresponding off-stoichiometry type defects are in a good agreement with proposed cation substitutions [4, 5].
iii. Intrinsic defect concentrations have been detected in an order $>10^{19}$ cm^{-3} but $< 10^{21}$ cm^{-3}.
iv. Evaluated kesterites are indeed mixtures of two different off-stoichiometry types thus influences of both respective type defects have been observed.
v. Strong influence of defects between B- and F-type has been observed, for example, by the occurrence of “Cu_i“ within Cu/(Zn+Sn)<1 and the occurrence of “Zn_{Cu}“ within Cu/(Zn+Sn)>1.
vi. Copper vacancies (V_{Cu}) on 2*a* and 2*c* sites have been observed only on kesterites phases close to A-type stoichiometry.
vii. F-type: “Cu_{Sn} + Cu_i + Zn_i” defects have not been experimentally observed.
viii. Cu-Zn disorder, which causes Zn_{Cu} and Cu_{Zn} anti site defects, has been determined within all off-stoichiometric kesterite type CZTSe phases.
ix. Results show that it is possible to deduce the occurring point defect types from the chemical composition (cation ratios) of the kesterite phase.

x. Experimental results of intrinsic defects follow certain trends suggested by DFT calculations [2].

3.3.3 Copper – zinc disorder defect concentration (Cu_{Zn}+Zn_{Cu})

Currently the Cu-Zn disorder defect has drawn significant attention inside the kesterite research community. Theoretical calculations support that an exchange of copper and zinc costs very little energy and is highly expected [11]. The Zn_{Cu} and Cu_{Zn} antisites have been reported with the lowest energy of donor and acceptor defect formation and their compensation leads to the antisite pair defect [Cu_{Zn}^{-}+Zn_{Cu}^{+}] [2].

The disorder defect has been first experimentally quantified by neutron powder diffraction analysis [9, 10]. Further evidence of disorder defect has been also proved by anomalous X-ray [52, 54] and others spectroscopy techniques such as: Raman spectroscopy [72], multinuclear NMR [73, 74] and photoluminescence [75, 76]. The intermixing of copper and zinc in the lattice plane at z=1/4 and 3/4 on 2c and 2d Wyckoff position causes a high concentration of Cu_{Zn} and Zn_{Cu} antisite defects, they have been observed even in stoichiometric kesterite compounds.

The evaluation of experimental data from neutron powder diffraction of off-stoichiometric CZTSe powder samples has proved that disorder defect has been observed with all 29 kesterites. The obtained fractions are given by percentages (see Figure 64a) according to the kesterite cation ratios. Fractions of Cu-Zn disorder defect have been found within a range from 0.05 to 0.38. Such fractions are higher compared with the intrinsic defects.

The concentrations of (Cu_{Zn}+Zn_{Cu}) disorder defect are shown in Figure 64b. The lowest concentration (~1.36×10^{20} cm^{-3}) has been found within a Cu-poor and Zn-rich kesterite (~85% A-type). The concentrations significantly increase by approaching the B-type off-stoichiometry line. The highest concentration (~1.04×10^{21} cm^{-3}) has been observed within a Cu-poor and Sn-poor kesterite (~90% B-type). In comparison with previous discussed intrinsic defects, the Cu-Zn disorder defect exhibits a higher concentration in the order of 10^{20}-10^{21} cm^{-3}.

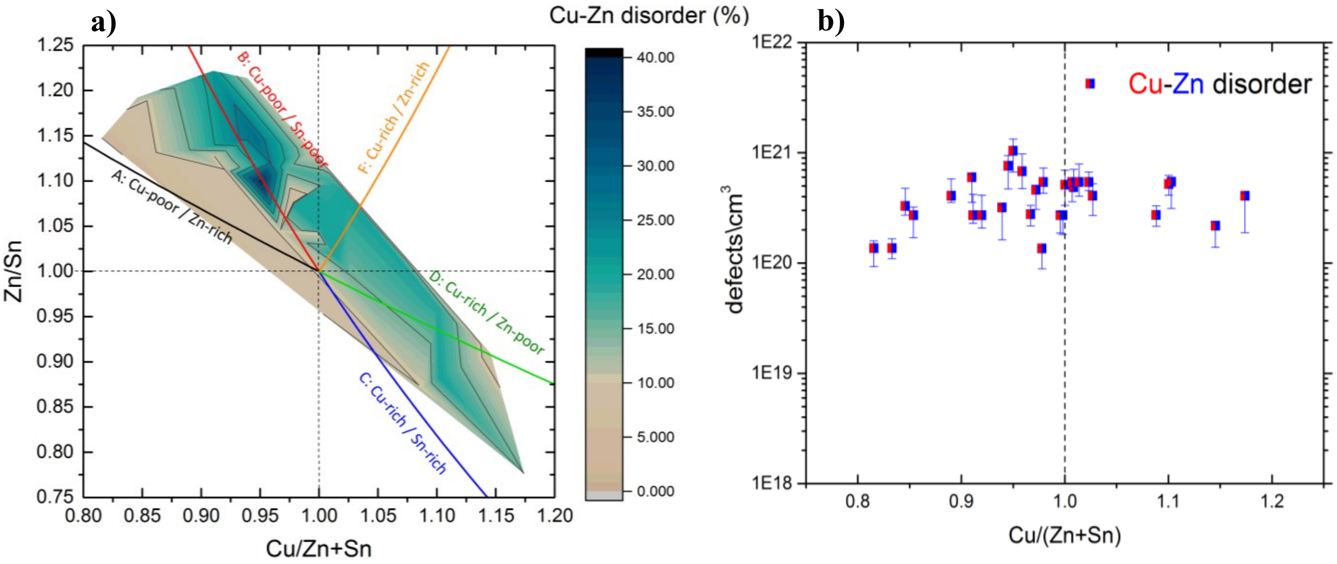

Figure 64 ***a)*** *percentages of disorder defect according to kesterite cation ratios (%) and* ***b)*** *defect concentrations of disorder defect by 1/cm*^{3}*in relation to kesterite Cu/(Zn+Sn) ratio.*

Off-stoichiometry A- and B-type are both located inside the Cu-poor region, however, the concentrations of Cu-Zn disorder defect significantly differ from A- to B.-type. It seems like the presence of copper vacancies (V_{Cu}) decrease the amount of (Cu_{Zn}+Zn_{Cu}) disorder defect. The lowest concentration has been detected within a kesterite where V_{Cu} on the 2*a* and 2*c* sites have been observed. Low disorder defect concentrations were also observed within A- and A-B kesterites with V_{Cu} on the 2c site. But the disorder defect increases when approaching the B-type stoichiometry where no further V_{Cu} have been detected. In fact, low concentrations of Cu-Zn disorder defect related with A-type defects (V_{Cu}+Zn_{Cu}) have been also experimentally reported by NMR and Raman spectroscopy [74]. It seems like A-type complexes, especially V_{Cu} have an impact on the level of Cu-Zn disorder defect.

Moreover, theoretical calculations by *Huang et al* [77] have suggested that disorder pair [Cu_{Zn}^-+Zn_{Cu}^+] and A-type complexes (Zn_{Cu}+V_{Cu}) are strongly correlated. The presence of A-type defects would decrease the formation energy of the Cu-Zn disorder defect. Additionally, it has been reported that disorder defect pair [Cu_{Zn}^-+Zn_{Cu}^+] and A-type defect complexes (Zn_{Cu}+V_{Cu}) affect the band gap energy in an opposite way: A-type defects increases the band gap whereas disorder defect decreases the band gap. These results suggest that the presence of A-type defects might not only limit the amount of disorder but also reduce the depth of band gap fluctuations.

Furthermore, *Scragg et al* [78] has recently suggested that one of the possible reason of low open circuit voltage (V_{oc}) occur due to the existence of band fluctuation with different possible origins. However, the disorder defect pair [Cu_{Zn}^{-}+Zn_{Cu}^{+}] might be the primary cause of such fluctuations. The deficit of open circuit voltage (V_{oc}) is currently the most challenging problem of kesterite based solar cells, therefore, increase V_{oc} is critical to achieve higher efficiencies. In fact, record efficiency of kesterite based solar cells has been achieved within the A-type composition [1, 15] thus one of the reasons might be due to low concentration of Cu-Zn disorder defect.

Nevertheless, the concentration of disorder defect is influenced by the thermal history and the growth method of kesterites, as suggested by [75, 76]. For the synthesis of our kesterite powder samples, an uncontrolled cooling (by switching off the furnace) has been applied. The measured temperature cooling profile has been presented in Figure 12.

Conclusion

i. Lowest concentration of Cu-Zn disorder defect has been detected within Cu-poor and Zn-rich compositions (A-type).
ii. Cu-Zn disorder defects exhibit the highest concentration in the order of 10^{20}-10^{21} cm^{-3} in comparison with the others intrinsic point defects.
iii. The presence of copper vacancies seems to decrease the amount of Cu-Zn disorder defect.
iv. This results are in a good agreement with literature [74] where low concentrations of Cu-Zn disorder defect have been also observed within A-type composition.
v. Literature [78] suggest that a A-type defects (Zn_{Cu}+V_{Cu}) have a positive impact on kesterite based solar cell devices by reducing the depth of band gap fluctuations.
vi. Growth conditions, in particular the thermal history of the kesterite would influence the concentration of the Cu-Zn disorder defect, as suggested by [75, 76].

3.4 Anomalous powder diffraction analysis

Further structure characterization was carried out by anomalous diffraction of synchrotron X-ray radiation as described in section 2.3.3 *Anomalous diffraction of synchrotron X-rays* (page 33). Data analysis has been performed in a copper poor and zinc rich single phase kesterite with a chemical composition: $Cu_{1.950}Zn_{1.104}Sn_{0.961}Se_4$ and cation ratios Cu/(Zn+Sn)=0.945 and Zn/Sn=1.149. This kesterite is located between the off-stoichiometry B-type (90%) and F-type (10%). The experiments were carried out at ambient conditions, the diffraction data has been collected from 10 different selected energies: 8048eV energy close to the CuK_α radiation, 9376eV in the middle of Cu and Zn K-absorption edges, additionally, 4 energies have been selected below the Cu K-edge (8979eV) and 4 more energies below the Zn K-edge (9659eV). The diffraction patterns are presented in Figure 65.

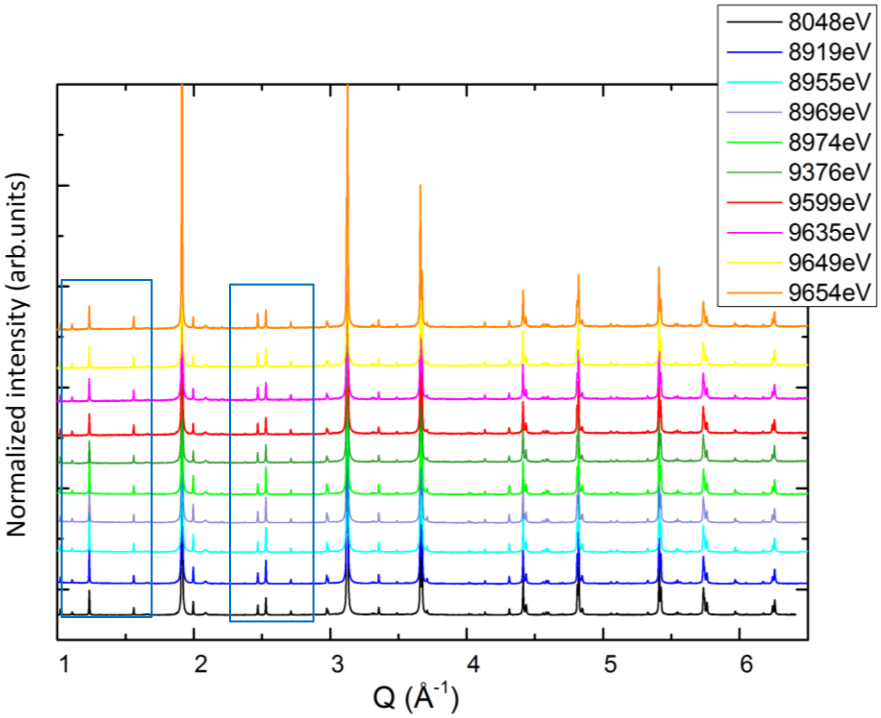

Figure 65 *Different energies set of anomalous diffraction patterns of synchrotron X-rays*

The diffraction patterns have been zoomed (see Figure 66) to observe the strongest variations of reflexes intensity within different set of energies. For example, the 101 reflex (Figure 66a) exhibits higher intensities at energies closer to the Cu K-edge (8979eV), whereas 110 reflex (Figure 66a) shows a higher intensity at energies near to the Zn K-edge (9659eV). Similar variations of intensities are observed at reflexes 202, 211 and 114 (Figure 66c). Therefore, the small Bragg peaks are the ones which contain the most information about the copper and zinc cations.

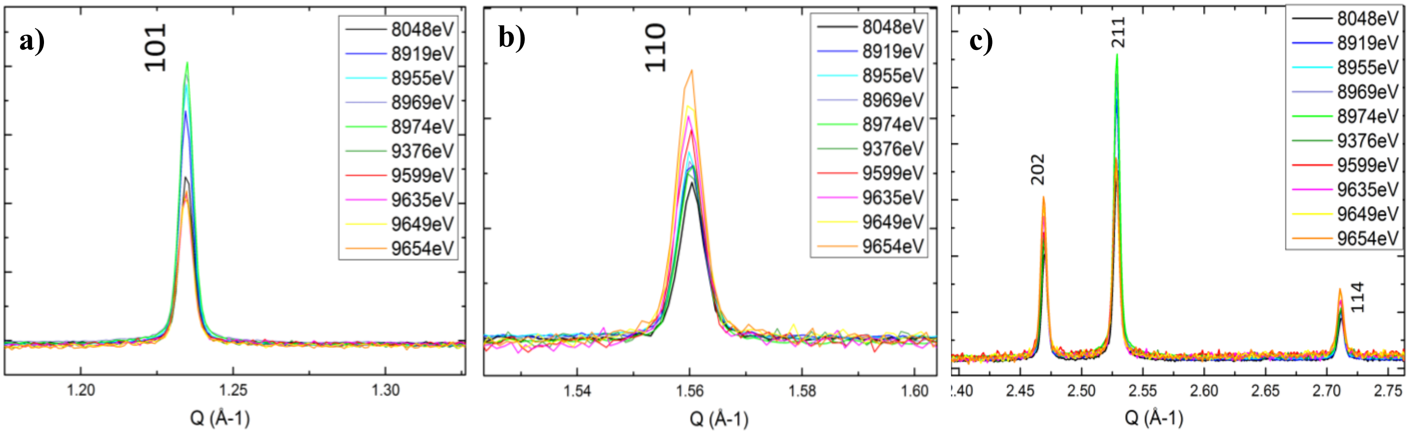

***Figure** 66 Diffraction patterns zoomed at 101, 110, 202, 211 and 114 reflexes.*

The collected diffraction data has been evaluated by Rietveld analysis. The refinements procedure has been described in section 2.3.4 (see page 40). Further detailed information about the refinement method has been recently reported by *Többens et al* [52]. In general, the occupation factors of the cations, for instance, copper on the 2*a* site is obtained by considering the following formula as a linear equation (y=mx+b) with a linear dependency on *f*(Zn)/*f*(Cu):

Equation 8

$$occ(\mathrm{Cu}) = sof(\mathrm{Zn}) \cdot \frac{f(\mathrm{Zn})}{f(Cu)} + sof(\mathrm{Cu})$$

Where:

f= scattering factors of copper and zinc

occ= model site occupation factor (to be deduced)

sof= site occupation factor from Rietveld refinements

In Figure 67, the intercept gives the amount of copper on the 2*a* site and the slope gives the amount of the other element, in this case zinc on the 2*a* site (if any). The scattering factors used for each energy set have been listed in Table 6.

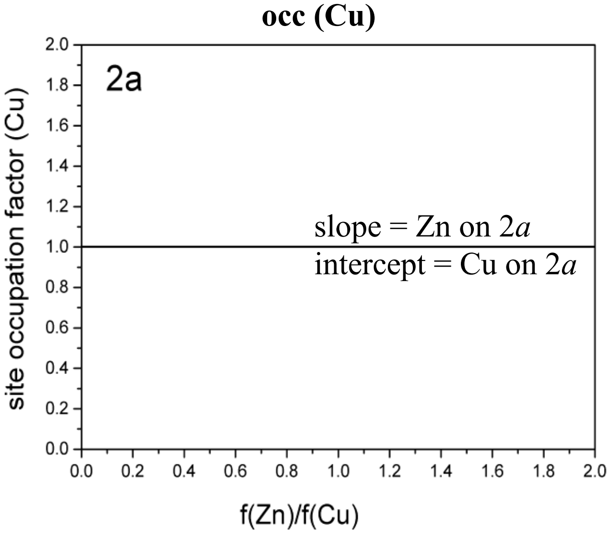

***Figure 67** site occupation of copper in the 2a site*

A linear fit (by using originLab software) was applied on the Wyckoff positions 2*a*, 2*c* and 2*d* and the results of each slope and intercept are shown in Figure 68. These results can be then translated as the amount of copper and zinc.

According to this results, the amount of copper on the 2*a* site is 0.957 and 0.827 on the 2c site. The amount of zinc on 2*d* site is 0.874. The presence of Cu_{Zn} and Zn_{Cu} antisite defects can be noticed, especially on the 2*c* site. The amount of Zn_{Cu} on the 2*c* site is 0.136 and the Cu_{Zn} on the site is 0.115.

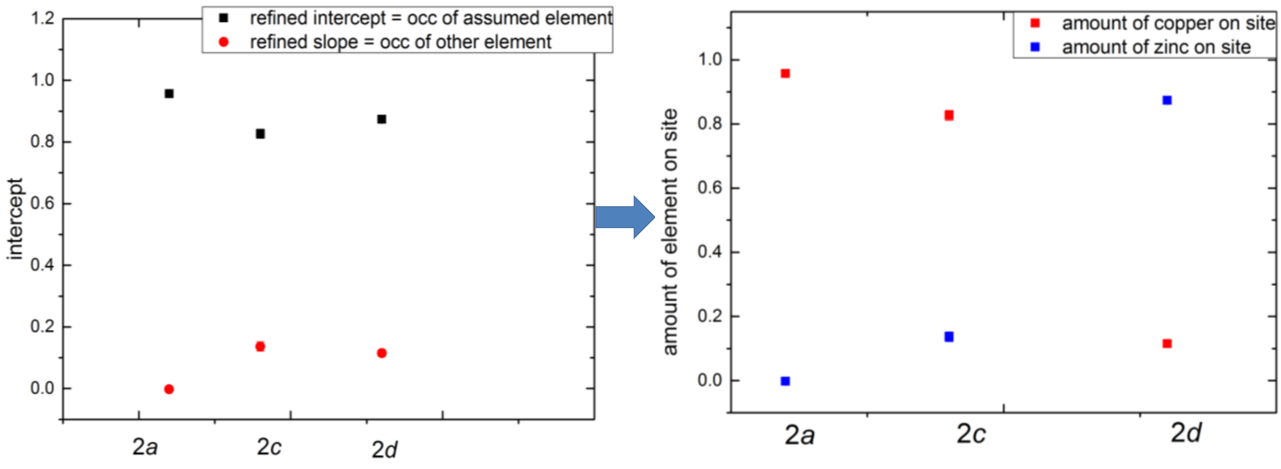

Figure 68 *Amount of copper and zinc distributed on the 2a, 2c and 2d Wyckoff positions.*

The results from anomalous diffraction slightly deviated from the neutron diffraction data where the amount of copper was; 0.92 on the 2*a* and 0.74 on the 2*c* site. The amount of zinc on the 2*d* site was 0.72. This kesterite exhibits a B-type off-stoichiometry, therefore zinc on copper antisite defect has been observed on the 2*a* site (Zn_{Cu}=0.01) and on the 2*c* site (Zn_{Cu}=0.27), also a high concentration of copper-zinc disorder defect has been observed (0.28).

The little amount of Zn_{Cu} on the 2*a* site might have been under the detection limit of anomalous diffraction experiments and could resulted in the underestimation of the disorder defect within this kesterite. However, some similarities between anomalous and neutron diffraction can be observed. For instances, even if the presence of zinc on copper was not detected on the 2*a* site, it is noticed that the 2*a* site is not fully occupied by copper because it is lower than one. Furthermore, the presence of Zn_{Cu} on the 2*c* site of Cu_{Zn} on 2*d* site is clearly observed.

Conclusion

i. Use of anomalous diffraction of synchrotron X-ray radiation to determine the ordering of kesterite cation has been just recently introduced [52].

ii. It has been proved to be a reliable alternative way to estimate the amount of Cu-Zn disorder defect on the 2*c* and 2*d* sites [54].

iii. In this work, evaluation of anomalous diffraction data exhibit similar results compared to neutron diffraction analyses.

iv. However, experiments and analyses of the anomalous diffraction is still open to improvements.

3.5 Temperature dependence resistivity analysis of off-stoichiometric single phase CZTSe

Temperature dependence resistivity measurements ρ(T) of off-stoichiometric CZTSe single phase samples (pellets) have been performed at the Institute of Applied Physics of the Academy of Sciences at Chisinau Moldova as has described in section 2.4 (page 45). The interpretation of results is acknowledged to Dr. Maxim Guc.

Temperature dependencies of resistivity measurements within a temperature range from 50 to 300 K are presented in Figure 69. The activation character was observed within all single phase kesterites. Data analysis has been performed in a similar way as reported for single crystals: Cu_2ZnSnS_4 [79], $Cu_2ZnSiSe_4$ [80], $Cu_2ZnGeSe_4$ [81] and for Cu_2ZnSnS_4 thin films[82]. The plot of the temperature dependence of conductivity in different coordinates allowed to determinate that within all kesterite pellets, the Mott type of variable range hopping (Mott-VRH) has been observed in a wide temperature range (see Figure 70). According to literature [56, 57] this conductivity mechanism can be described by the following equation:

$$\rho(T) = AT^{1/4}\exp\left[\left(\frac{T_{04}}{T}\right)^{1/4}\right]$$ **Equation 9**

Where:

A is an independent of T parameter

T_{04} is the characteristic temperature

These values have been determined by graphical analysis. The obtained values are presented in Table 18 according to the kesterite compositions. Here the width of the acceptor band $W = 0.5\, k_B\, (T_v^3 T_{04})^{1/4}$ [57] and T_v is the onset temperature of the Mott-VRH conductivity.

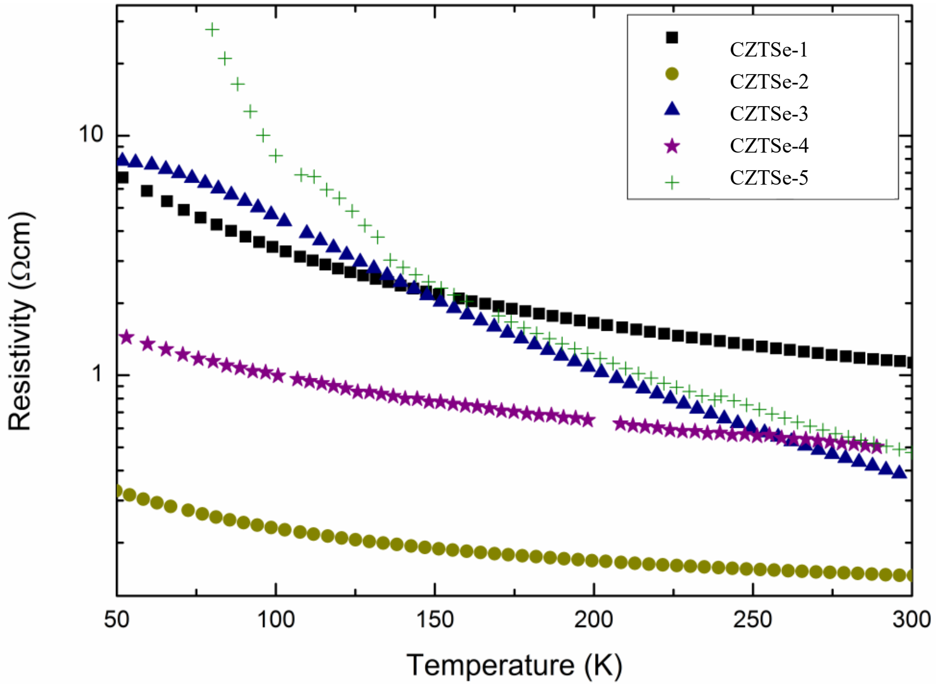

Figure 69 *Temperature dependence of resistivity of single phase CZTSe.*

Table 18 *Chemical composition of kesterite single phase and the macro parameters of Mott-VRH conductivity mechanism.*

Sample	**Cu**	**Zn**	**Sn**	**Se**	**d*T* (K)**	***T*₀₄ (K)**	***W* (meV)**
CZTSe-1	1.985	1.053	0.978	4.00	95–215	9.92×10^4	43
CZTSe-2	1.961	1.036	0.992	4.00	70–300	8.51×10^3	30
CZTSe-3	1.892	1.101	0.977	4.00	175–230	2.92×10^6	106
CZTSe-4	2.00	1.00	1.00	4.00	155–272	3.38×10^4	39
CZTSe-5	1.950	1.104	0.961	4.00	170–247	2.56×10^6	107

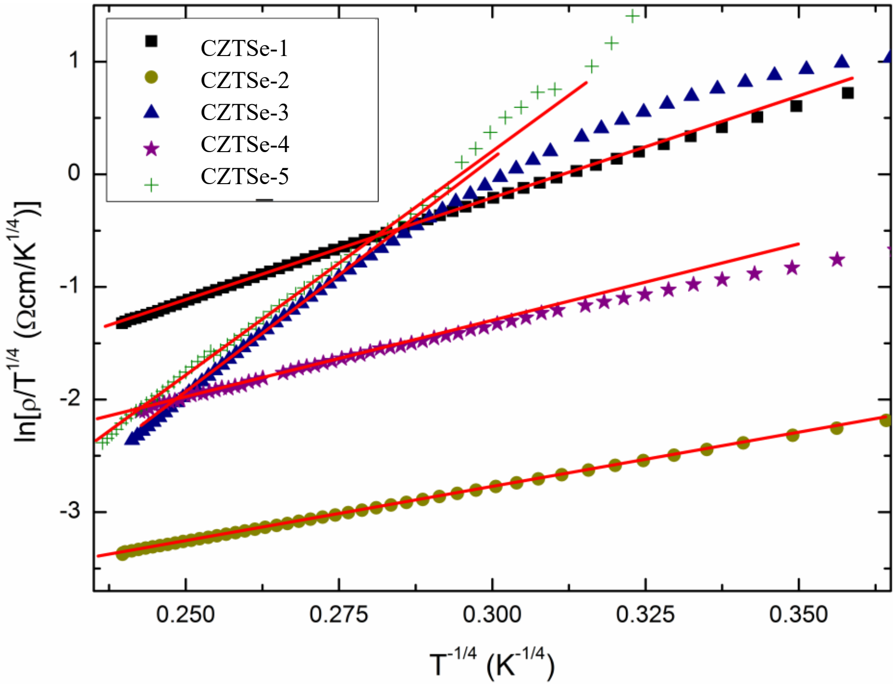

Figure 70 *The plots of* $ln(\rho/T^{1/4})$ *vs.* $T^{-1/4}$ *of single phase CZTSe.*

Following the model suggested in literature [79-82]. The acceptor band which consider the zone of delocalized states in the middle of the band, and two zones with localized states in the band edges, has been used. Making the approximation of the density of states (DOS) in acceptor band by the rectangular shape as presented in literature [79].

The values of relative acceptor concentration N/N_c and of relative localization radius a/a_0 have been calculated and summarized in Table 19. Where N_c referred to the critical concentration of metal-insulator transition (MIT) and a_0 is the localization radius far from the metal-insulator transition (MIT) [57].

Overlapped integrals reported in literature [79, 80] were used for the minimization process taking into account the theoretically calculated value of hole mass $m = 0.23\ m_0$ [83]. However, the use of J_0 proposed in [57] for the doped semiconductor [79] yielded the reliable value of dielectric permittivity $\kappa \approx 4.44$ with standard deviation value ≈ 0.09.

Values of Bohr radius a_B = 10.2 Å, acceptor band center E_0 = 159 meV, critical concentration of the MIT $N_c = 1.46\times10^{19}$ cm^{-3}, as well as of a/a_B, DOS at the Fermi level $g(\mu)$ and mobility threshold E_c, collected in Table 19, have been estimated for three samples (CZTSe-1, CZTSe-2 and CZTSe-4). The kesterite CZTSe-3 and CZTSe-5 were not taken into account as its relative concentration was quite low, suggesting that these kesterite samples are far from the MIT, while used approximation of DOS is valid only in case of semiconductors samples close to the MIT[57].

Table 19 *The relative cations concentration (Cu/Zn), the relative acceptor concentration (N/Nc), the localization radius in units of that far from the MIT (a/a0) and in units of the Bohr radius (a/aB), the DOS (g(μ)) and the mobility threshold (Ec).*

Sample	**Cu/Zn**	N/N_c	a/a_0	a/a_B	$g(\mu)$ **(meV^{-1} cm^{-3})**	E_c **(meV)**
CZTSe-1	1.88	0.64	2.77	2.92	1.09×10^{17}	28
CZTSe-2	1.88	0.81	5.14	5.04	1.97×10^{17}	24
CZTSe-3	1.71	0.33	1.50	–	–	–
CZTSe-4	2.00	0.73	3.67	3.66	1.37×10^{17}	28
CZTSe-5	1.766	0.35	1.55	–	–	–

The ratios of cations Cu/Zn are presented in Table 19, these ratios exhibit a strong dependence of different calculated parameters. In particular it is evident the decrease of relative acceptor concentration with decrease of Cu/Zn ratio. This leads to the conclusion that from two most discussed defects, which form the acceptor levels in the band gap of CZTSe semiconductors are the copper vacancies V_{Cu} and zinc on copper antisite Cu_{Zn} [5]. The electrical conductivity process of off-stoichiometric CZTSe polycrystalline powder samples have showed that by low Cu/Zn ratio, most likely lead to an increment of V_{Cu} and a decrease of Cu_{Zn} antisite defects. From the obtained results the decrease of acceptor concentration, which are involved in the electrical conductivity, with Cu/Zn ratio was determined. This correlates to decrease of Cu_{Zn} defects and contradicts to increase of V_{Cu}.

The results also proved that hopping is the preferable regime within the samples. A hopping conductivity is more favorable in comparison with inter grain diffusion.

Conclusion

i. Mott type of variable range hopping (Mott-VRH) has been observed in a wide temperature range.
ii. Hopping is the preferable regime which is more favorable in comparison with inter grain diffusion.
iii. Decrease of relative acceptor concentration with decrease of Cu/Zn ratio has been observed.
iv. Acceptor concentration involve the electrical conductivity, which could explain that CZTSe semiconductors exhibit a *p*-type conductivity.

4. Summary

This work presents a structural study on off-stoichiometric CZTSe kesterite compounds. All analyses have been performed on reference powder material. In total 29 polycrystalline powder samples have been synthesized by solid state reaction from pure elements in a sealed evacuated silica tubes. The first reaction took place at 750°C with several temperature steps (250°C, 450°C, 600°C) in between. After reaction all samples were ground, pressed in pellets and annealed again at 750°C. In order to study the influence of off-stoichiometry on kesterite compounds, intended composition have been selected according to suggested off-stoichiometric types, so called: A-type Cu-poor/Zn-rich, B-type Cu-poor/Sn-poor, C-type Cu-rich/Sn-rich and D-type Cu-rich/ Zn-poor [4].

To determine phase content and chemical composition of the obtained samples, an electron microprobe system equipped with a wavelength dispersive X-ray spectroscopy unit has been used. The results proved the presence of kesterite type CZTSe with an off-stoichiometric composition as the main phase within all synthesized samples. Binary selenides have been detected as secondary phases. Occurrences of secondary phases within the Cu-poor and Cu-rich region have been discussed. Moreover, the formation of single phase off-stoichiometric kesterite type CZTSe has been observed. In this way the ability of the kesterite type structure to tolerate deviations from stoichiometric composition without collapse of the crystal structure was proven [5]. The type fractions and chemical composition of the CZTSe phase have been deduced by linear interpolation graphical approach. The majority of obtained kesterites have been detected between two different off-stoichiometry types, thus the F-type Cu-rich/Zn-rich off-stoichiometry has been introduced.

Structural characterization by X-ray powder diffraction have been performed. The lattice parameters *a* and *c* of the CZTSe main phase have been determined by Rietveld analysis. Refinements were performed using FullProf software [48] with the kesterite structure model, because stoichiometric CZTSe crystallizes in the kesterite type structure [9].

Additionally, a correlation between the lattice parameter ratio *c*/2*a* (tetragonal deformation) and the cation ratios Cu/(Zn+Sn) and Zn/Sn was demonstrated.

Moreover, neutron powder diffraction experiments were performed at the Spallation Neutron Source (SNS) in Oak Ridge/US as well as at the Berlin Research Reactor BERII of HZB/Germany. The neutron scattering length of Cu and Zn is different, therefore it is possible to distinguish between cations Cu^+ and Zn^{2+} site occupation in the crystal structure. Further Rietveld refinements of neutron diffraction data additionally with the average neutron scattering length analysis method lead to the determination of cation distribution within the crystal structure. Thus the intrinsic point defects and their concentrations have been deduced. Defect concentrations have been detected in the order of: $>10^{19}$ cm^{-3} but $<$ 10^{21} cm^{-3}. The occurrence of the corresponding off-stoichiometry type specific point defects could be proven. The results show, that it is possible to deduce the occurring point defect types from the chemical composition (cation ratios) of the kesterite phase.

Furthermore, the Cu-Zn disorder defect, which causes Zn_{Cu} and Cu_{Zn} anti site defects has been determined within all off-stoichiometric kesterite type CZTSe phases. This defects exhibit the highest concentration compared to the others intrinsic defects, it has been found in the order of 10^{20}-10^{21} cm^{-3}. But its lowest concentration has been detected within Cu-poor and Zn-rich compositions (A-type). It seems like the presence of copper vacancies decrease the amount of Cu-Zn disorder defect.

Complementary structural analyses by anomalous diffraction of synchrotron X-ray radiation were carried out. This method have been recently introduced as an alternative way to determine the ordering of cation in the kesterite structure [52]. In this work, evaluation of anomalous diffraction data exhibit similar results compared to neutron diffraction analyses. However, experiments and analyses of the anomalous diffraction data are still open to improvements.

Temperature dependence resistivity measurements ρ(T) of off-stoichiometric single phase CZTSe powder samples were performed at the Institute of Applied Physics at Chisinau Moldova. The study of temperature dependence of electrical conductivity of the semiconductor material is important for understanding of the transport and the conductivity mechanism of the charge carriers. It has been found that hopping conductivity occur. Mott type of variable range hopping (Mott-VRH) has been observed in a wide temperature range.

This work is highly appreciated within the kesterite based solar cells research community. Knowledge of occurrences of secondary phases, concentrations of intrinsic point defects and structure parameters like the tetragonal deformation are important to understand the role of off-stoichiometry composition of the kesterite absorbers layer.

References

1. Wang, W., et al., Device Characteristics of CZTSSe Thin-Film Solar Cells with 12.6% Efficiency. Advanced Energy Materials, 2014. **4**(7).
2. Chen, S., et al., Classification of Lattice Defects in the Kesterite Cu2ZnSnS4 and Cu2ZnSnSe4 Earth-Abundant Solar Cell Absorbers. Advanced Materials, 2013. **25**(11): p. 1522-1539.
3. Gershon, T., et al., Photovoltaic Materials and Devices Based on the Alloyed Kesterite Absorber (AgxCu1–x) 2ZnSnSe4. Advanced Energy Materials, 2016.
4. Lafond, A., et al., Crystal Structures of Photovoltaic Chalcogenides, an Intricate Puzzle to Solve: the Cases of CIGSe and CZTS Materials. Zeitschrift für Anorganische und Allgemeine Chemie, 2012. **638**(15): p. 2571-2577.
5. Valle Rios, L.E., et al., Existence of off-stoichiometric single phase kesterite. Journal of Alloys and Compounds, 2016. **657**: p. 408-413.
6. PV-Magazine, solar frontier hits 22.3% on CIGS cell. Photovoltaic market and technology, 2015.
7. Chen, S., et al., Wurtzite-derived polytypes of kesterite and stannite quaternary chalcogenide semiconductors. Physical Review B, 2010. **82**(19): p. 195203.
8. Schorr, S., Crystallographic Aspects of Cu2ZnSnS4 (CZTS), in Copper Zinc Tin Sulfide-Based Thin-Film Solar Cells. 2014, John Wiley & Sons Ltd. p. 53-74.
9. Schorr, S., The crystal structure of kesterite type compounds: A neutron and X-ray diffraction study. Solar Energy Materials and Solar Cells, 2011. **95**(6): p. 1482-1488.
10. Schorr, S., H.-J. Hoebler, and M. Tovar, A neutron diffraction study of the stannite-kesterite solid solution series. European Journal of Mineralogy, 2007. **19**(1): p. 65-73.
11. Paier, J., et al., Cu2ZnSnS4 as a potential photovoltaic material: A hybrid Hartree-Fock density functional theory study. Physical Review B, 2009. **79**(11): p. 115126.
12. Gürel, T., C. Sevik, and T. Çağın, Characterization of vibrational and mechanical properties of quaternary compounds Cu2ZnSnS4 in kesterite and stannite structures. Physical Review B, 2011. **84**(20): p. 205201.
13. Peter, L.M., Towards sustainable photovoltaics: the search for new materials. Philosophical Transactions of the Royal Society of London A: Mathematical, Physical and Engineering Sciences, 2011. **369**(1942): p. 1840-1856.
14. Blazev, A.S., Photovoltaics for commercial and utilities power generation. 2013: Lulu Press, Inc.
15. Lee, Y.S., et al., Cu2ZnSnSe4 Thin-Film Solar Cells by Thermal Co-evaporation with 11.6% Efficiency and Improved Minority Carrier Diffusion Length. Advanced Energy Materials, 2015. **5**(7): p. n/a-n/a.
16. Kato, T., et al. Characterization of front and back interfaces on Cu2ZnSnS4 thin-film solar cells. in Proceedings of the 27th European photovoltaic solar energy conference and exhibition. 2012.

17. Ahn, S., et al., Determination of band gap energy (Eg) of Cu2ZnSnSe4 thin films: On the discrepancies of reported band gap values. Applied Physics Letters, 2010. **97**(2): p. 021905.
18. Botti, S., D. Kammerlander, and M.A.L. Marques, Band structures of Cu_2ZnSnS_4 and$Cu_2ZnSnSe_4$ from many-body methods. Applied Physics Letters, 2011. **98**(24): p. 241915-1--241915-3-241915.
19. Adhi Wibowo, R., et al., Pulsed laser deposition of quaternary Cu2ZnSnSe4 thin films. physica status solidi (a), 2007. **204**(10): p. 3373-3379.
20. Becquerel, A., Recherches sur les effets de la radiation chimique de la lumière solaire au moyen des courants électriques. Comptes Rendus de LAcadémie des Sciences, 1839. **9**: p. 145-149.
21. Shockley, W. and H.J. Queisser, Detailed Balance Limit of Efficiency of p-n Junction Solar Cells. Journal of Applied Physics, 1961. **32**(3): p. 510-519.
22. Persson, C., Electronic and optical properties of Cu_2ZnSnS_4 and $Cu_2ZnSnSe_4$. Journal of Applied Physics, 2010. **107**(5): p. 053710-1--053710-8-053710.
23. Siebentritt, S. and S. Schorr, Kesterites - a challenging material for solar cells. Progress in Photovoltaics: Research and Applications, 2012. **20**(5): p. 512-519.
24. Stephan, C., Structural trends in off stoichiometric chalcopyrite type compound semiconductors. 2011, Freie Universität Berlin.
25. Walsh, A., et al., Kesterite thin-film solar cells: advances in materials modelling of $Cu_2ZnSnSe_4$. Advanced Energy Materials, 2012. **2**(4): p. 400-409.
26. Chen, S., et al., Defect physics of the kesterite thin-film solar cell absorber Cu2ZnSnS4. Applied Physics Letters, 2010. **96**(2): p. 021902.
27. Chen, S., et al., Abundance of Cu_{Zn} + Sn_{Zn} and $2Cu_{Zn}$ + Sn_{Zn} defect clusters in kesterite solar cells. Applied Physics Letters, 2012. **101**(22): p. 223901-1--223901-4-223901.
28. Chen, S., et al., Intrinsic point defects and complexes in the quaternary kesterite semiconductor Cu_2ZnSnS_4. Physical Review B (Condensed Matter and Materials Physics), 2010. **81**(24): p. 245204---245204.
29. Nagoya, A., et al., Defect formation and phase stability of Cu2ZnSnS4 photovoltaic material. 2010. **81**(11): p. 113202.
30. Maeda, T., S. Nakamura, and T. Wada, First-principles calculations of vacancy formation in In-free photovoltaic semiconductor Cu 2 ZnSnSe 4. Thin Solid Films, 2011. **519**(21): p. 7513-7516.
31. Maeda, T., S. Nakamura, and T. Wada, First principles calculations of defect formation in in-free photovoltaic semiconductors Cu2ZnSnS4 and Cu2ZnSnSe4. Japanese Journal of Applied Physics, 2011. **50**(4S): p. 04DP07.
32. Siebentritt, S., et al., The electronic structure of chalcopyrites—bands, point defects and grain boundaries. Progress in Photovoltaics: Research and Applications, 2010. **18**(6): p. 390-410.
33. Dudchak, I.V. and L.V. Piskach, Phase equilibria in the Cu2SnSe3-SnSe2-ZnSe system. journal of alloys and compounds, 2003. **351**(1): p. 145-150.
34. Berg, D.M. and P.J. Dale, Kesterites, in Copper Zinc Tin Sulfide-Based Thin-Film Solar Cells. 2014, John Wiley & Sons Ltd. p. 107-132.

35. Gosavi, S.R., et al., Physical, optical and electrical properties of copper selenide (CuSe) thin films deposited by solution growth technique at room temperature. Journal of Alloys and Compounds, 2008. **448**(1–2): p. 344-348.
36. Matsushita, H., T. Ichikawa, and A. Katsui, Structural, thermodynamical and optical properties of Cu2-II-IV-VI4 quaternary compounds. Journal of materials science, 2005. **40**(8): p. 2003-2005.
37. Olekseyuk, I.D., I.V. Dudchak, and L.V. Piskach, Phase Equlibrium in the Quazythird-Timed System Cu2Se-ZnSe-Cu2SnSe3. PHYSICS AND CHEMISTRY OF SOLID STATE, 2001. **V.1**: p. 195-200.
38. Clarke, A.R., Microscopy techniques for materials science. 2002: Woodhead Publishing.
39. Pecharsky, V.K. and P.Y. Zavalij, Fundamentals of powder diffraction and structural characterization of materials. Vol. 69. 2009: Springer.
40. Pynn, R., Neutron Scattering-A Non-destructive Microscope for Seeing Inside Matter, in Neutron applications in earth, energy and environmental sciences, L. Liyuan, R. Rinaldi, and H. Schober, Editors. 2008, Springer Science & Business Media. p. 15-36.
41. Sears, V.F., Neutron scattering lengths and cross sections. Neutron news, 1992. **3**(3): p. 26-37.
42. Dinnebier, R.E. and S.J.L. Billinge, Powder diffraction: theory and practice. 2008: Royal Society of Chemistry.
43. Cromer, D.T. and D.A. Liberman, Anomalous dispersion calculations near to and on the long-wavelength side of an absorption edge. Acta Crystallographica Section A, 1981. **37**(2): p. 267-268.
44. Többens, D.M. and S. Zander, KMC-2: an X-ray beamline with dedicated diffraction and XAS endstations at BESSY II. Journal of large-scale research facilities JLSRF, 2016. **2**: p. A49.
45. Young, R.A., The Rietveld Method. 1995: Oxford University Press.
46. Rodrguez-Carvajal, J., An introduction to the program Fullprof. 2001.
47. Thompson, P., D.E. Cox, and J.B. Hastings, Rietveld refinement of Debye-Scherrer synchrotron X-ray data from Al2O3. Journal of Applied Crystallography, 1987. **20**(2): p. 79-83.
48. Rodriguez-Carvajal, J., FullProf Suite. 2012.
49. Karlsruhe, F. ICSD - database for completely identified inorganic crystal structures. Available from: https://icsd.fiz-karlsruhe.de.
50. EA., M. X-ray Anomalous Scattering Biomolecular Structure Center the University of Washington. 2014; Available from: http://skuld.bmsc.washington.edu/scatter/AS_index.html.
51. Brennan, S. and P. Cowan, A suite of programs for calculating x-ray absorption, reflection, and diffraction performance for a variety of materials at arbitrary wavelengths. Review of scientific instruments, 1992. **63**(1): p. 850-853.
52. Többens, D.M., et al., Quantitative anomalous powder diffraction analysis of cation disorder in kesterite semiconductors. Powder Diffraction, 2016. **FirstView**: p. 1-8.
53. Nateprov, A., et al., Single crystal X-ray structure investigation of Cu2ZnSnSe4. Электронная обработка материалов, 2013(5).

54. Többens, D.M., et al., Temperature dependency of Cu/Zn ordering in CZTSe kesterites determined by anomalous diffraction. physica status solidi (b), 2016: p. n/a-n/a.
55. Kasap, S.O., Principles of electronic materials and devices. 2006: McGraw-Hill.
56. Mott, N. and E. Davis, Electronic processes in non-crystalline solids. Clarendon, Oxford, 1979: p. 465.
57. Shklovskii, B.I. and A.L. Efros, Electronic properties of doped semiconductors. Springer Series in Solid-State Sciences. Vol. 45. 1984: Springer Berlin Heidelberg.
58. van der Pauw, L.J., A method of measuring specific resistivity and Hall effect of discs of arbitrary shape. Philips Res. Rep., 1958. **13**: p. 1-9.
59. Delbos, S., Kësterite thin films for photovoltaics : a review. EPJ Photovolt., 2012. **3**: p. 35004.
60. Redinger, A., et al., The consequences of kesterite equilibria for efficient solar cells. Journal of the American Chemical Society, 2011. **133**(10): p. 3320-3323.
61. Scragg, J.J., et al., Chemical Insights into the Instability of Cu2ZnSnS4 Films during Annealing. Chemistry of Materials, 2011. **23**(20): p. 4625-4633.
62. Weber, A., R. Mainz, and H.W. Schock, On the Sn loss from thin films of the material system Cu–Zn–Sn–S in high vacuum. Journal of Applied Physics, 2010. **107**(1): p. 013516.
63. Sousa, A.P.C.d., Investigation of detection limits of ZnSe and Cu2SnSe3 secondary phasses in Cu2ZnSnSe4, in Departamento de Fisica. 2016, Universidade de Coimbra.
64. Shannon, R., Revised effective ionic radii and systematic studies of interatomic distances in halides and chalcogenides. Acta Crystallographica Section A, 1976. **32**(5): p. 751-767.
65. Chen, S., et al., Crystal and electronic band structure of Cu_2ZnSnX_4 (X=S and Se) photovoltaic absorbers: first-principles insights. Applied Physics Letters, 2009. **94**(4): p. 041903-1--041903-3-041903.
66. Rowe, J.E. and J.L. Shay, Extension of the Quasicubic Model to Ternary Chalcopyrite Crystals. Physical Review B, 1971. **3**(2): p. 451-453.
67. Wei, S.-H. and A. Zunger, Optical properties of zinc-blende semiconductor alloys: Effects of epitaxial strain and atomic ordering. Physical Review B, 1994. **49**(20): p. 14337-14351.
68. Paufler, P., P. Villars, LD Calvert. Pearson's handbook of crystallographic data for intermetallic phases. American Society for Metals. Metals Park. Ohio. 1986. Vols. 1–3. 3258 pp, US $495.00 ISBN 0-87170-217-7. Crystal Research and Technology, 1987. **22**(11): p. 1436-1436.
69. Olekseyuk, I.D., et al., Single crystal preparation and crystal structure of the Cu2Zn/Cd,Hg/SnSe4 compounds. Journal of Alloys and Compounds, 2002. **340**(1–2): p. 141-145.
70. Babu, G.S., et al., Effect of post-deposition annealing on the growth of Cu2ZnSnSe4 thin films for a solar cell absorber layer. Semiconductor Science and Technology, 2008. **23**(8): p. 085023.

71. Márquez, J., et al., Systematic compositional changes and their influence on lattice and optoelectronic properties of Cu2ZnSnSe4 kesterite solar cells. Solar Energy Materials and Solar Cells, 2016. **144**: p. 579-585.
72. Valakh, M.Y., et al., Raman scattering and disorder effect in Cu_2ZnSnS_4. physica status solidi (RRL) – Rapid Research Letters, 2013. **7**(4): p. 258-261.
73. Choubrac, L., et al., Multinuclear (67Zn, 119Sn and 65Cu) NMR spectroscopy - an ideal technique to probe the cationic ordering in Cu2ZnSnS4 photovoltaic materials. Physical Chemistry Chemical Physics, 2013. **15**(26): p. 10722-10725.
74. Paris, M., et al., Solid-State NMR and Raman Spectroscopy To Address the Local Structure of Defects and the Tricky Issue of the Cu/Zn Disorder in Cu-Poor, Zn-Rich CZTS Materials. Inorganic Chemistry, 2014. **53**(16): p. 8646-8653.
75. Scragg, J.J.S., et al., A low-temperature order-disorder transition in Cu2ZnSnS4 thin films. Applied Physics Letters, 2014. **104**(4): p. -.
76. Rey, G., et al., The band gap of Cu2ZnSnSe4: Effect of order-disorder. Applied Physics Letters, 2014. **105**(11): p. 112106.
77. Huang, D. and C. Persson, Band gap change induced by defect complexes in Cu2ZnSnS4. Thin Solid Films, 2013. **535**: p. 265-269.
78. Scragg, J.J.S., et al., Cu–Zn disorder and band gap fluctuations in Cu2ZnSn(S,Se)4: Theoretical and experimental investigations. physica status solidi (b), 2016. **253**(2): p. 247-254.
79. Lisunov, K.G., et al., Features of the acceptor band and properties of localized carriers from studies of the variable-range hopping conduction in single crystals of p-Cu2ZnSnS4. Solar Energy Materials and Solar Cells, 2013. **112**: p. 127-133.
80. Lisunov, K.G., et al., Energy spectrum of near-edge holes and conduction mechanisms in Cu2ZnSiSe4 single crystals. Journal of Alloys and Compounds, 2013. **580**: p. 481-486.
81. Guc, M., et al., Variable-range hopping conductivity in Cu 2 ZnGeSe 4 single crystals. Solar Energy Materials and Solar Cells, 2014. **127**: p. 87-91.
82. Guc, M., et al., Disorder and variable-range hopping conductivity in Cu2ZnSnS4 thin films prepared by flash evaporation and post-thermal treatment. Journal of Alloys and Compounds, 2014. **596**: p. 140-144.
83. Liu, H.-R., et al., First-principles study on the effective masses of zinc-blend-derived $Cu_2Zn\text{-}IV\text{-}VI_4$ (IV = Sn, Ge, Si and VI = S, Se). Journal of Applied Physics, 2012. **112**(9): p. 093717-1--093717-6-093717.

Appendix: A1. Rietveld refinements of neutron data and BSE micrographs

Sample A0050-1

Cu (Zn+Sn)	Zn/Sn	Cu	Zn	Sn	Se	type	%	%
0.9113	1.1273	1.892	1.101	0.977	4	A-B	76 % B	24 % A

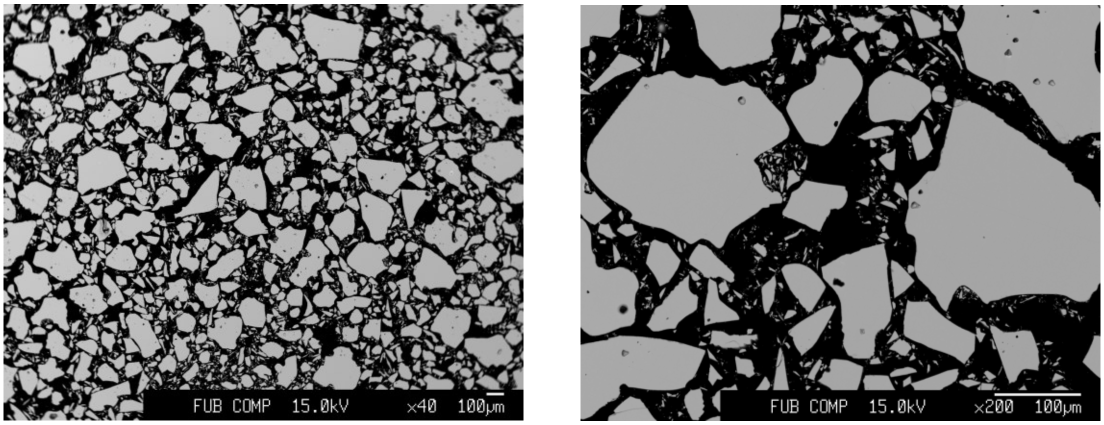

BSE micrograph

Refined phases: Kesterite (space group $I\bar{4}$)

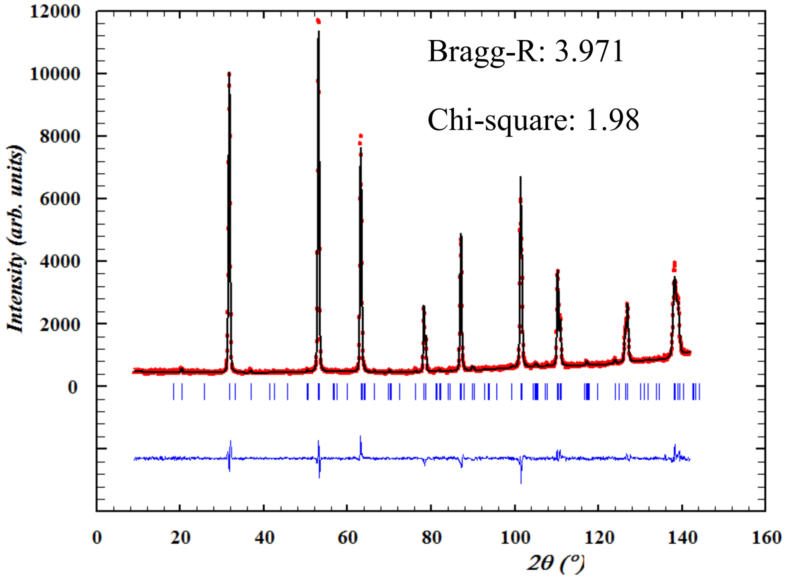

Rietveld refinement of neutron powder diffraction pattern collected at E9.

Sample A0100-1

Cu (Zn+Sn)	Zn/Sn	Cu	Zn	Sn	Se	type	%	%
0.8330	1.1292	1.766	1.125	0.996	4	A-B	12 % B	88% A

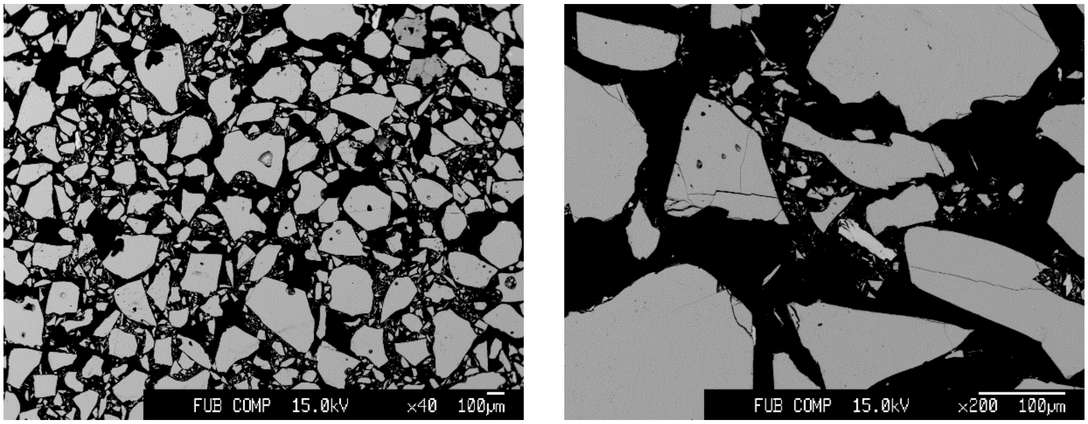

BSE micrograph

Refined phases: Kesterite (space group $I\bar{4}$)
$SnSe_2$ (space group $P\bar{3}m1$)
ZnSe (space group $F\bar{4}3m$)

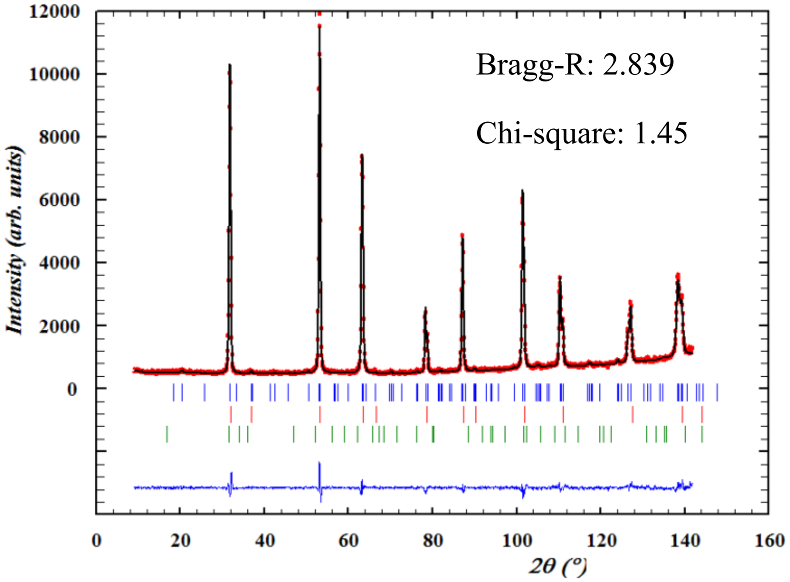

Rietveld refinement of neutron powder diffraction pattern collected at E9.

Sample A0125-1

Cu (Zn+Sn)	Zn/Sn	Cu	Zn	Sn	Se	type	%	%
0.8155	1.1475	1.740	1.141	0.994	4	A-B	16 % B	84% A

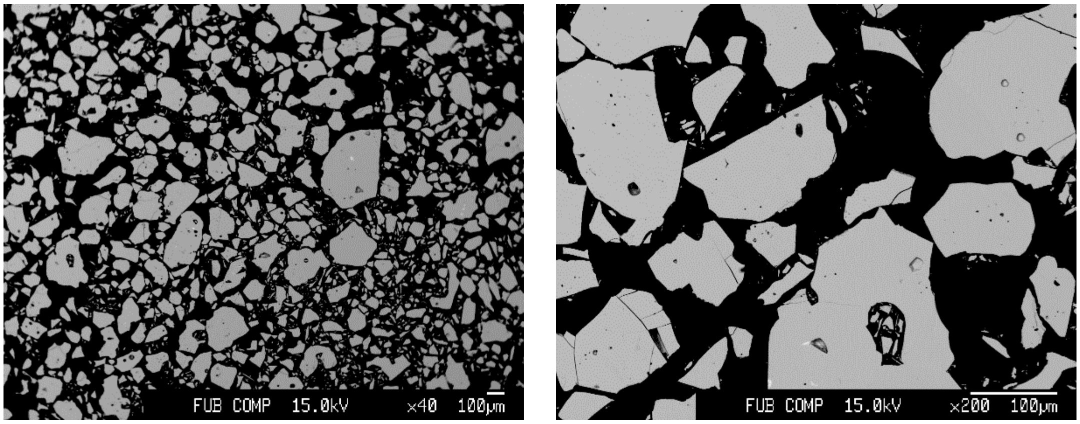

BSE micrograph

Refined phases: Kesterite (space group $I\bar{4}$)
SnSe$_2$ (space group $P\bar{3}m1$)

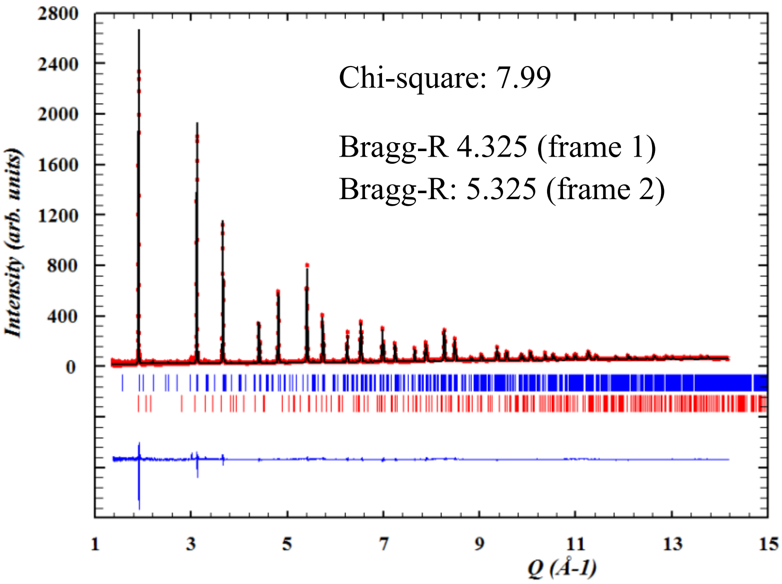

Rietveld refinement of neutron powder diffraction pattern (frame 1) collected at Oak Ridge.

Sample A0025-3

Cu (Zn+Sn)	Zn/Sn	Cu	Zn	Sn	Se	type	%	%
0.9669	1.0449	1.961	1.036	0.992	4	A-B	75 % B	25% A

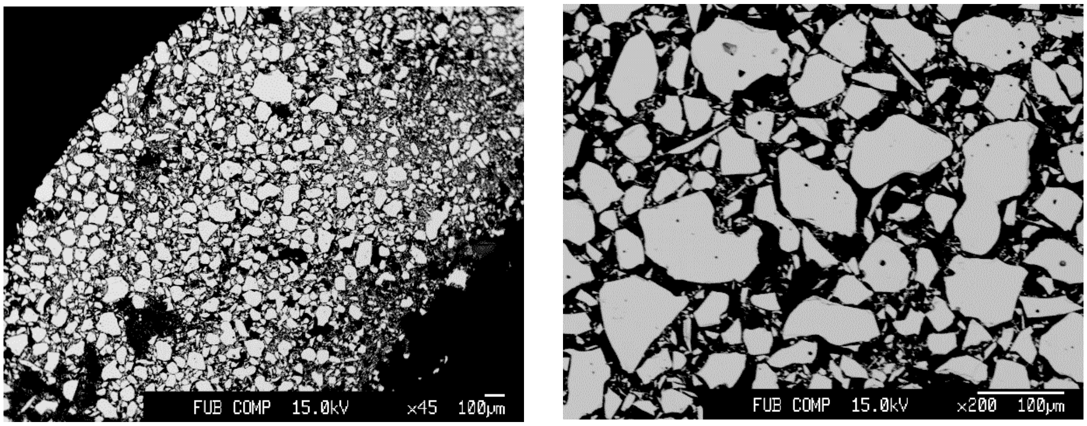

BSE micrograph

Refined phases: Kesterite (space group $I\overline{4}$)

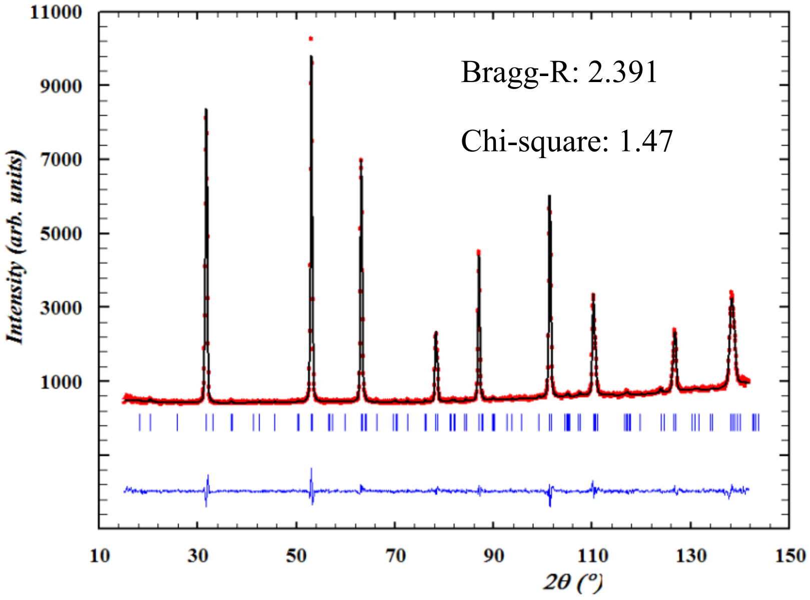

Rietveld refinement of neutron powder diffraction pattern collected at E9.

Sample B0025-5

Cu (Zn+Sn)	Zn/Sn	Cu	Zn	Sn	Se	type	%	%
0.8538	1.1887	1.810	1.154	0.971	4	A-B	65 % B	35% A

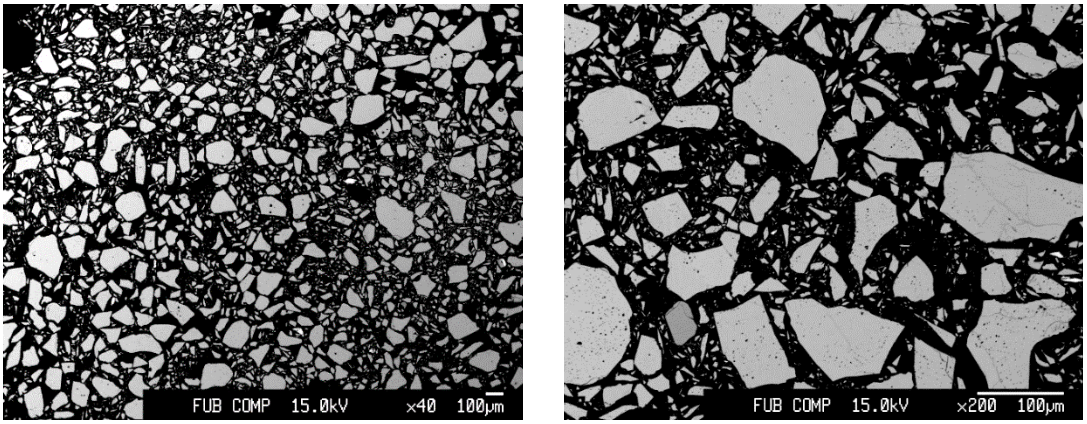

BSE micrograph

Refined phases: Kesterite (space group $I\bar{4}$)

$SnSe_2$ (space group $P\bar{3}m1$)

ZnSe (space group $F\bar{4}3m$)

Se (space group $P3_121$)

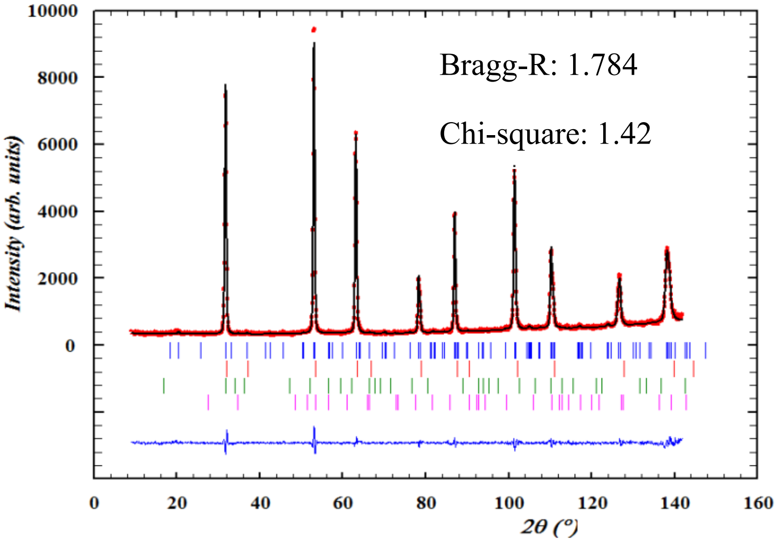

Rietveld refinement of neutron powder diffraction pattern collected at E9.

Sample B0050-5

Cu (Zn+Sn)	Zn/Sn	Cu	Zn	Sn	Se	type	%	%
0.8458	1.1924	1.797	1.158	0.971	4	A-B	62 % B	38% A

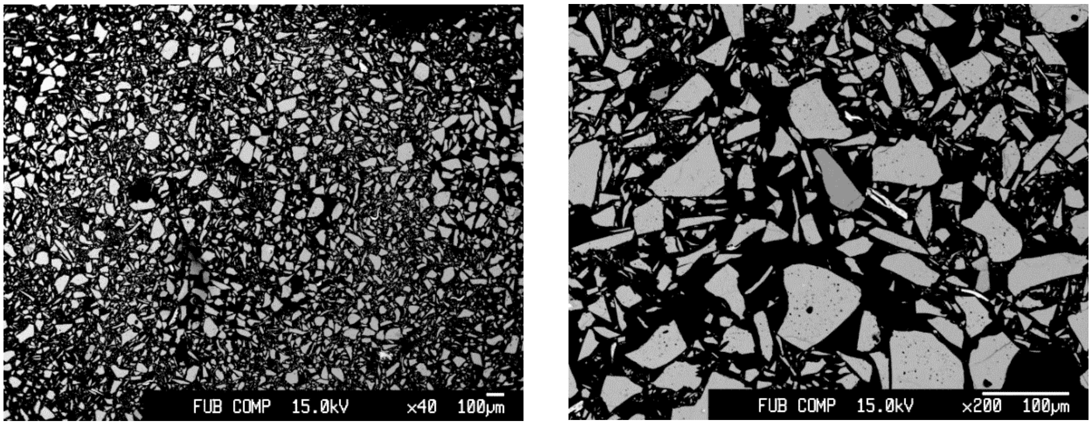

BSE micrograph

Refined phases: Kesterite (space group $I\bar{4}$)

$SnSe_2$ (space group $P\bar{3}m1$)

ZnSe (space group $F\bar{4}3m$)

Se (space group $P3_121$)

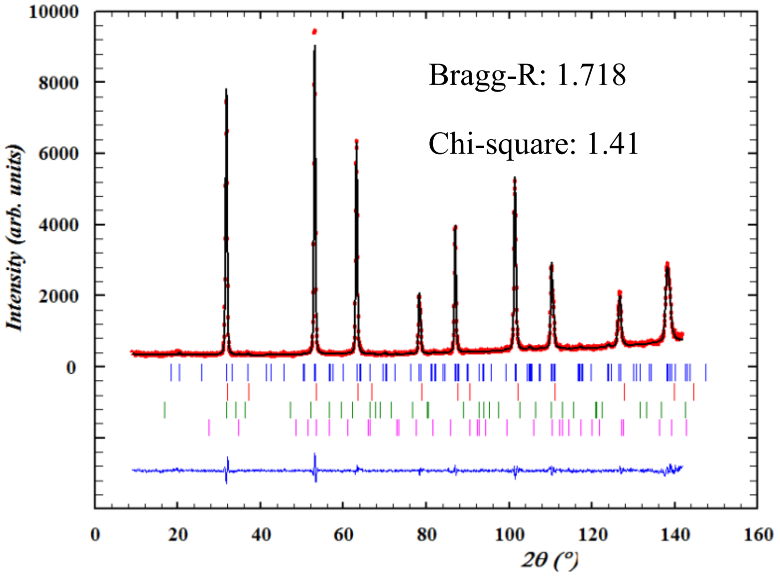

Rietveld refinement of neutron powder diffraction pattern collected at E9.

Sample A0025-6

Cu (Zn+Sn)	Zn/Sn	Cu	Zn	Sn	Se	type	%	%
0.9500	1.0990	1.947	1.073	0.977	4	A-B	97 % B	3 % A

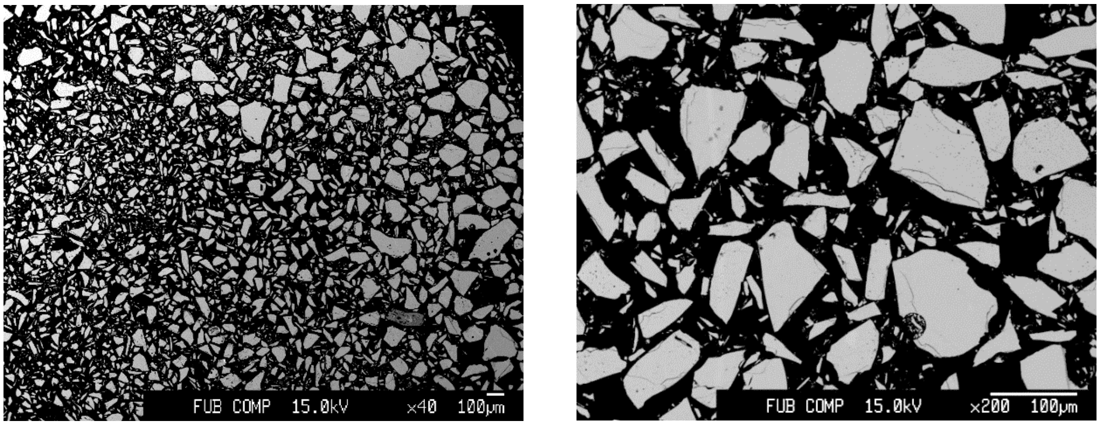

BSE micrograph

Refined phases: Kesterite (space group $I\overline{4}$)
CuSe (space group $P6_3/mmc$)
Se (space group $P3_121$)

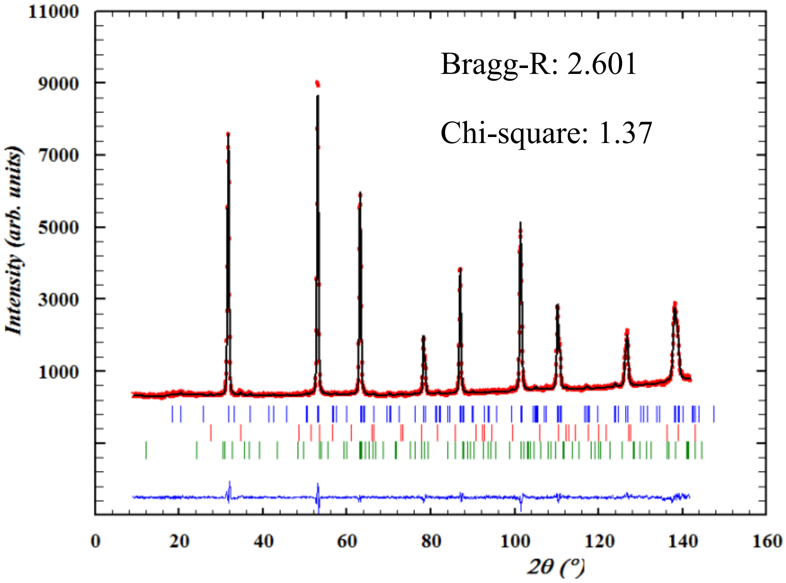

Rietveld refinement of neutron powder diffraction pattern collected at E9.

Sample A0050-6

Cu (Zn+Sn)	Zn/Sn	Cu	Zn	Sn	Se	type	%	%
0.9197	1.1131	1.902	1.090	0.979	4	A-B	75 % B	25 % A

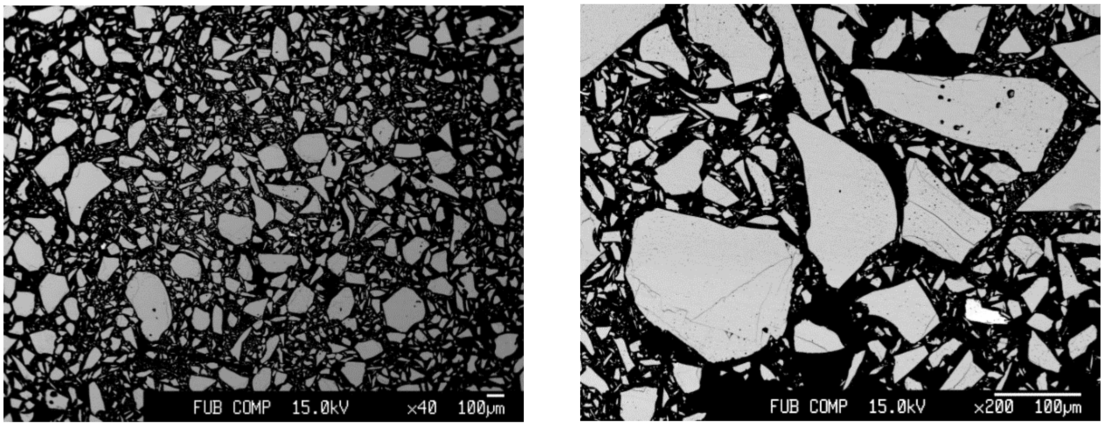

BSE micrograph

Refined phases: Kesterite (space group $I\bar{4}$)

$SnSe_2$ (space group $P\bar{3}m1$)

ZnSe (space group $F\bar{4}3m$)

Se (space group $P3_121$)

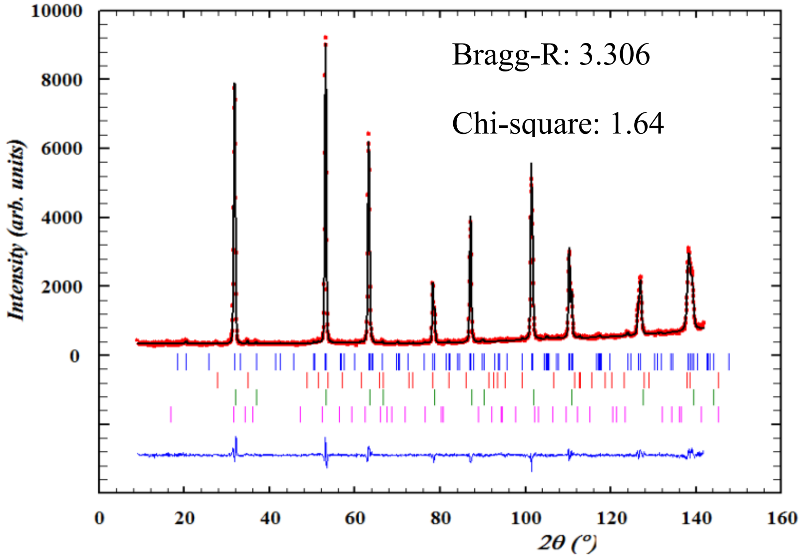

Rietveld refinement of neutron powder diffraction pattern collected at E9.

Sample A0075-6

Cu (Zn+Sn)	Zn/Sn	Cu	Zn	Sn	Se	type	%	%
0.8902	1.1341	1.859	1.111	0.980	4	A-B	63 % B	37% A

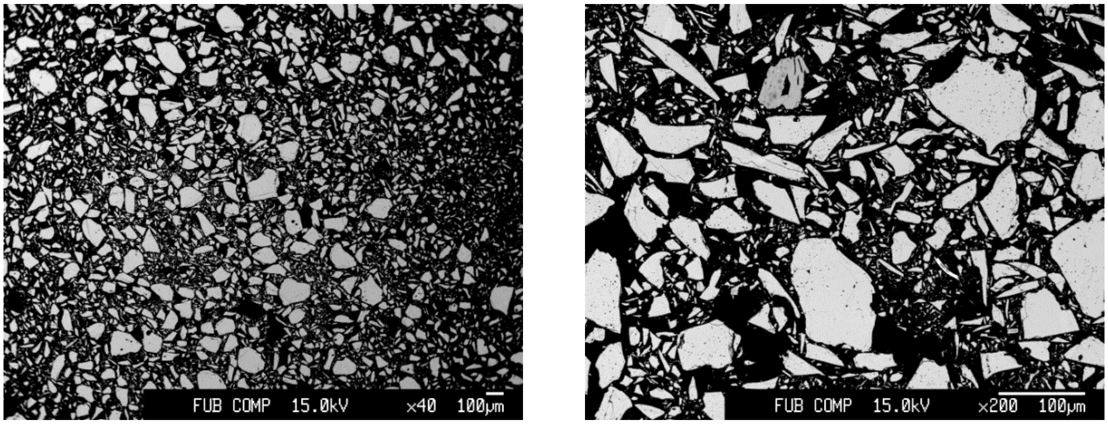

BSE micrograph

Refined phases: Kesterite (space group $I\bar{4}$)

ZnSe (space group $F\bar{4}3m$)

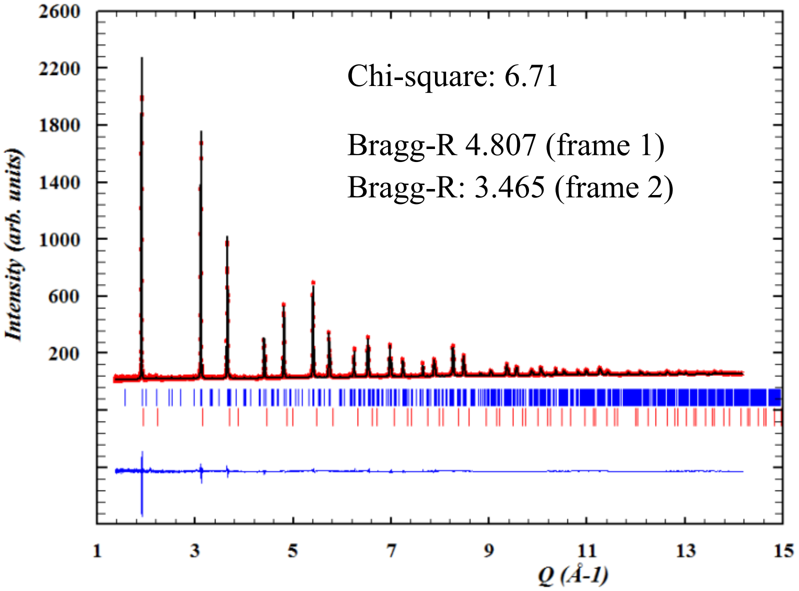

Rietveld refinement of neutron powder diffraction pattern (frame 1) collected at Oak Ridge.

Sample A0000-1

Cu (Zn+Sn)	Zn/Sn	Cu	Zn	Sn	Se	type	%	%
0.9778	1.0766	1.985	1.053	0.978	4	B-F	20 % F	80 % B

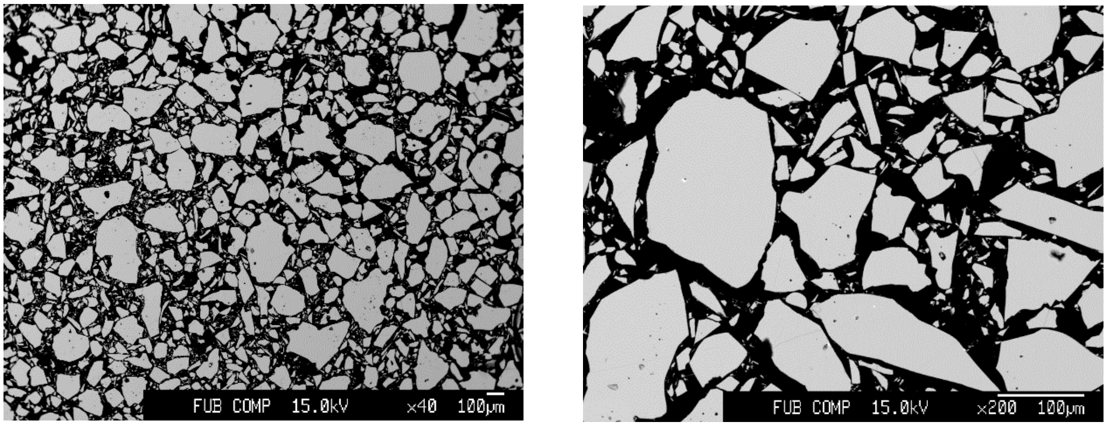

BSE micrograph

Refined phases: Kesterite (space group $I\bar{4}$)

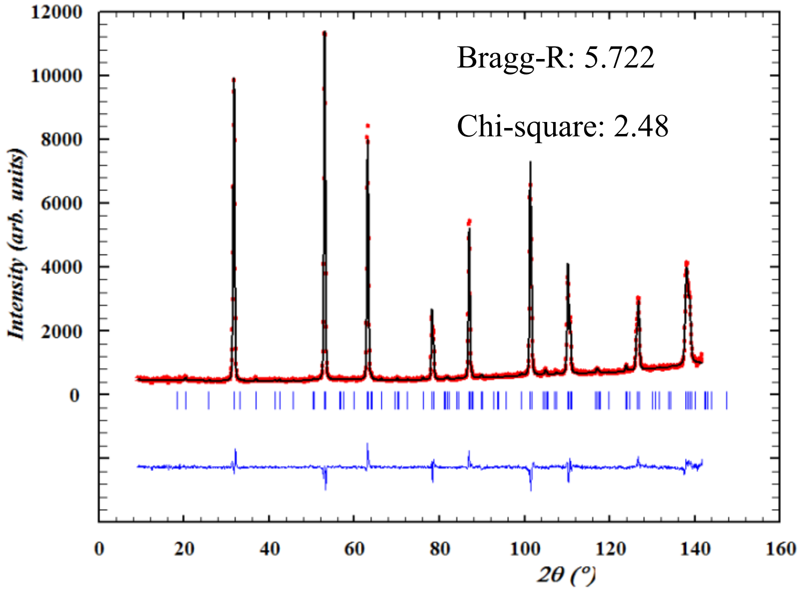

Rietveld refinement of neutron powder diffraction pattern collected at E9.

Sample A0000-3

Cu (Zn+Sn)	Zn/Sn	Cu	Zn	Sn	Se	type	%	%
0.9792	1.0753	1.986	1.051	0.978	4	B-F	21 % F	79 % B

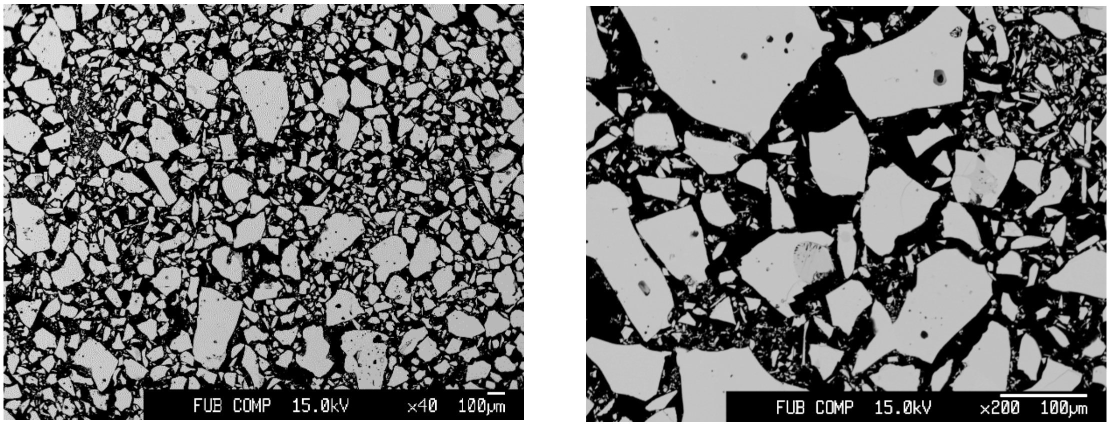

BSE micrograph

Refined phases: Kesterite (space group $I\bar{4}$)
CuSe (space group $P6_3/mmc$)

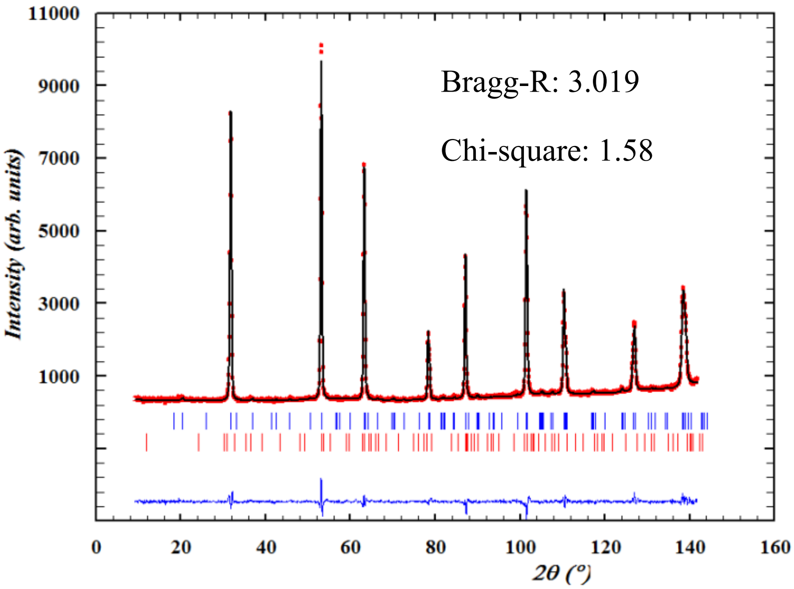

Rietveld refinement of neutron powder diffraction pattern collected at E9.

Sample A0075-3G

Cu (Zn+Sn)	Zn/Sn	Cu	Zn	Sn	Se	type	%	%
0.9587	1.1200	1.965	1.083	0.967	4	B-F	14 % F	86 % B

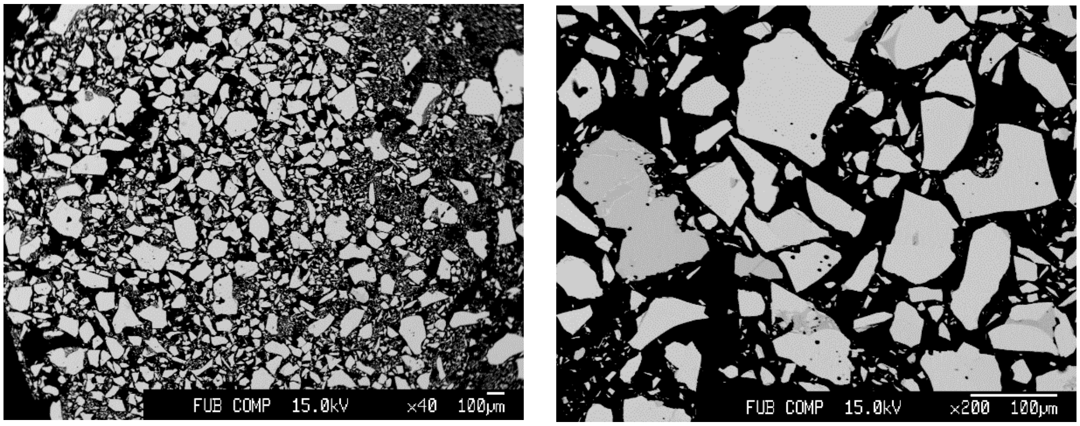

BSE micrograph

Refined phases: Kesterite (space group $I\bar{4}$)

CuSe (space group $P6_3/mmc$)

ZnSe (space group $F\bar{4}3m$)

Cu_2Se (space group $Fm\bar{3}m$)

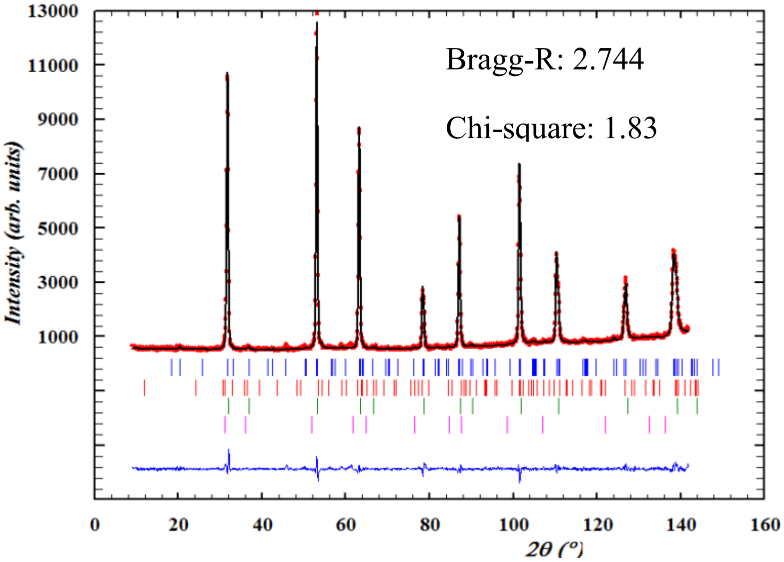

Rietveld refinement of neutron powder diffraction pattern collected at E9.

Sample B0025-3

Cu (Zn+Sn)	Zn/Sn	Cu	Zn	Sn	Se	type	%	%
0.9720	1.1140	1.984	1.076	0.966	4	B-F	24 % F	76 % B

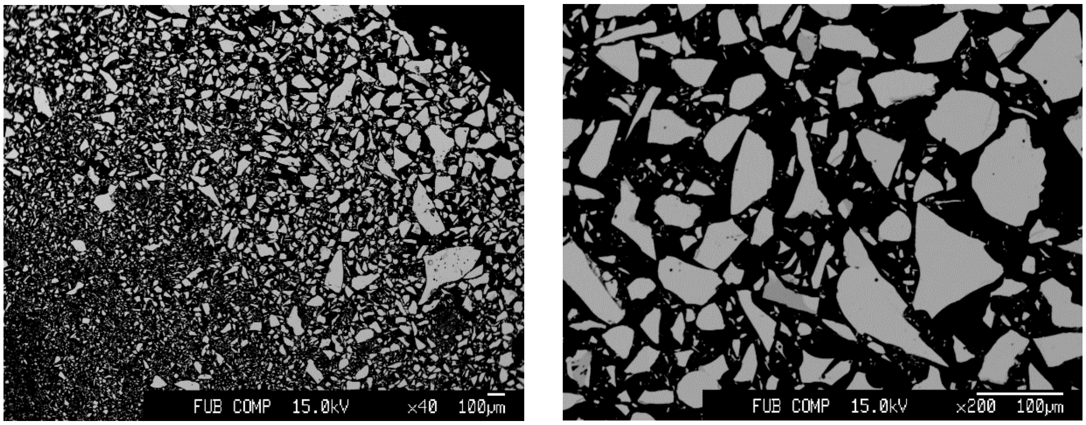

BSE micrograph

Refined phases: Kesterite (space group $I\overline{4}$)
CuSe (space group $P6_3/mmc$)
Cu_2Se (space group $Fm\overline{3}m$)

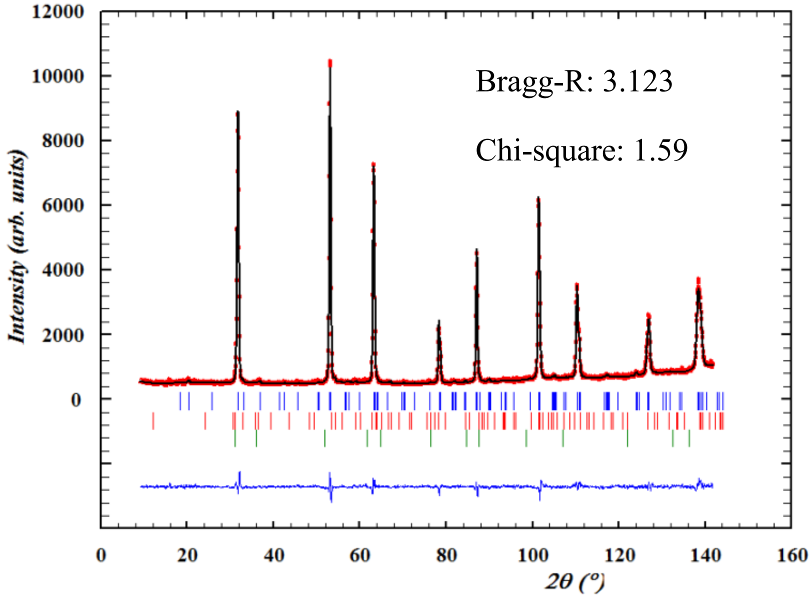

Rietveld refinement of neutron powder diffraction pattern collected at E9.

Sample B0050-4

Cu (Zn+Sn)	Zn/Sn	Cu	Zn	Sn	Se	type	%	%
0.9980	1.0418	2.007	1.026	0.985	4	B-F	45% F	55 % B

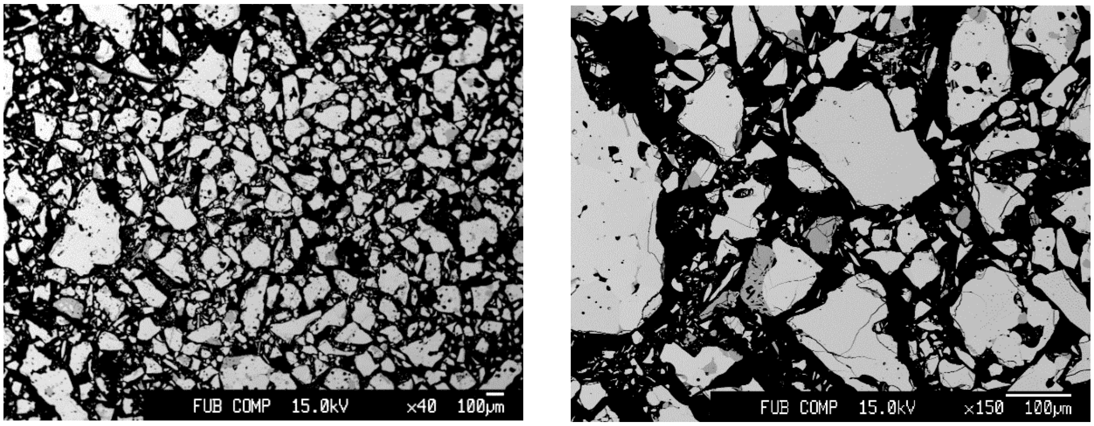

BSE micrograph

Refined phases: Kesterite (space group $I\bar{4}$)
CuSe (space group $P6_3/mmc$)
ZnSe (space group $F\bar{4}3m$)

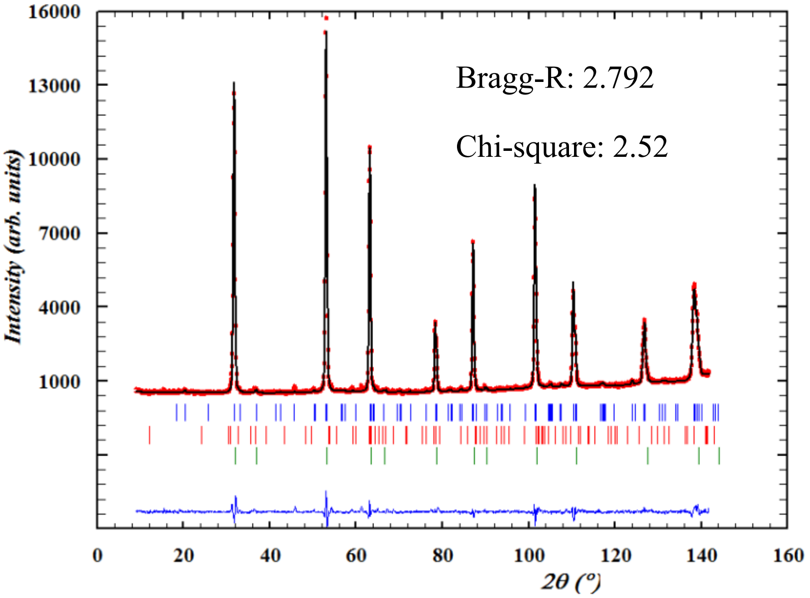

Rietveld refinement of neutron powder diffraction pattern collected at E9.

Sample B0075-4

Cu (Zn+Sn)	Zn/Sn	Cu	Zn	Sn	Se	type	%	%
1.0001	1.0456	2.011	1.028	0.983	4	B-F	50% F	50 % B

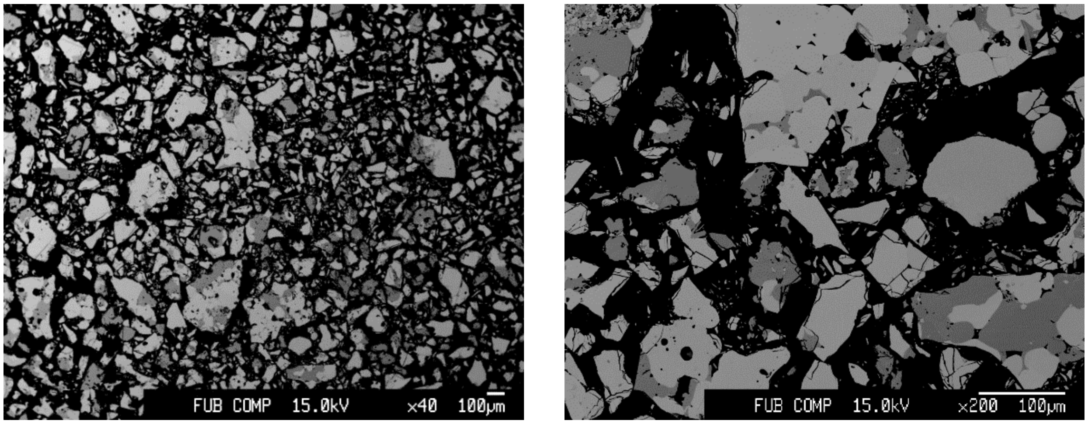

BSE micrograph

Refined phases: Kesterite (space group $I\overline{4}$)
CuSe (space group $P6_3/mmc$)
ZnSe (space group $F\overline{4}3m$)
SnO_2-Cassiterite (space group $P4_2/mnm$)

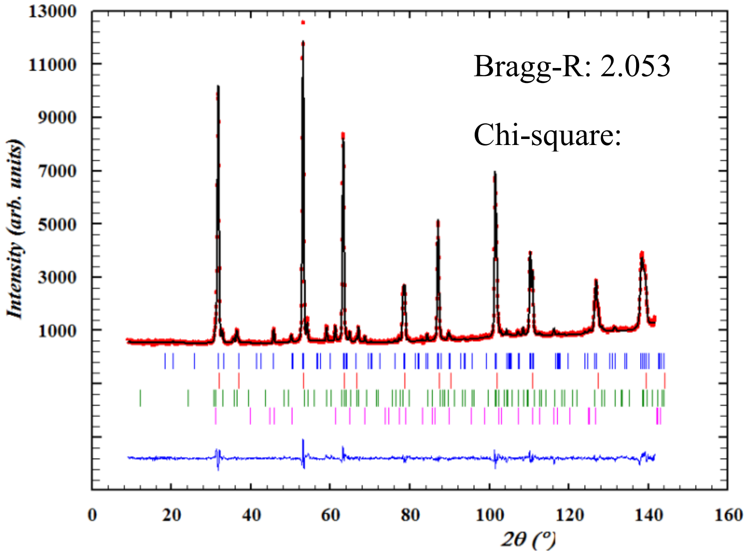

Rietveld refinement of neutron powder diffraction pattern collected at E9.

Sample B0075-5

Cu (Zn+Sn)	Zn/Sn	Cu	Zn	Sn	Se	type	%	%
0.9393	1.2137	1.953	1.142	0.941	4	B-F	19% F	81% B

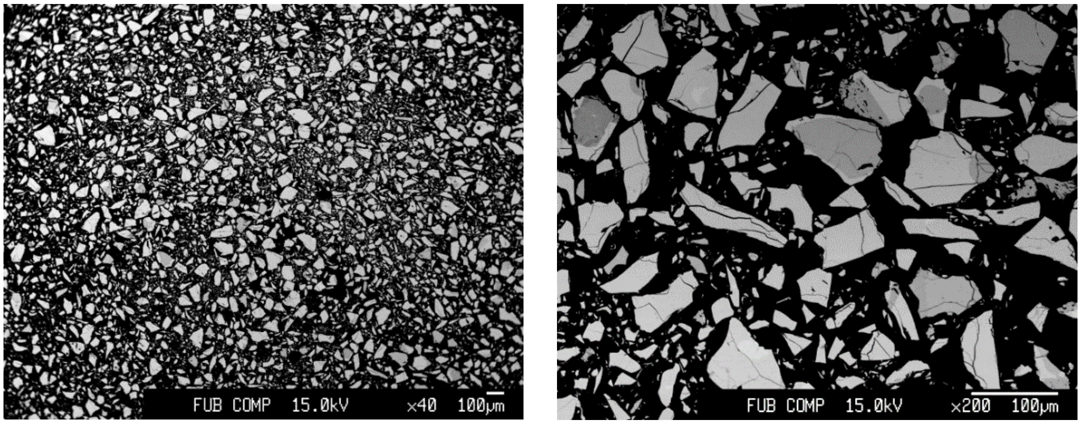

BSE micrograph

Refined phases: Kesterite (space group $I\bar{4}$)
CuSe (space group $P6_3/mmc$)
ZnSe (space group $F\bar{4}3m$)
Se (space group $P3_121$)

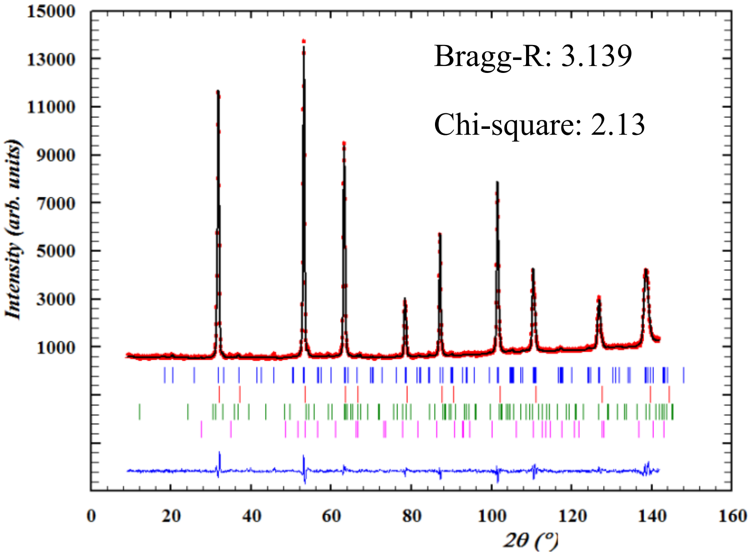

Rietveld refinement of neutron powder diffraction pattern collected at E9.

Sample C0025-5

Cu (Zn+Sn)	Zn/Sn	Cu	Zn	Sn	Se	type	%	%
1.0084	1.1002	2.036	1.058	0.962	4	B-F	59 % F	41% B

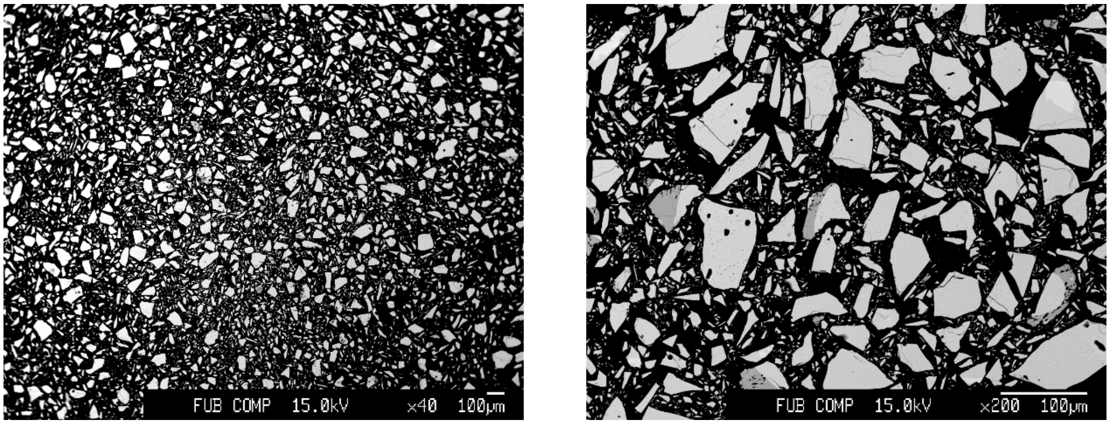

BSE micrograph

Refined phases: Kesterite (space group $I\overline{4}$)
CuSe (space group $P6_3/mmc$)

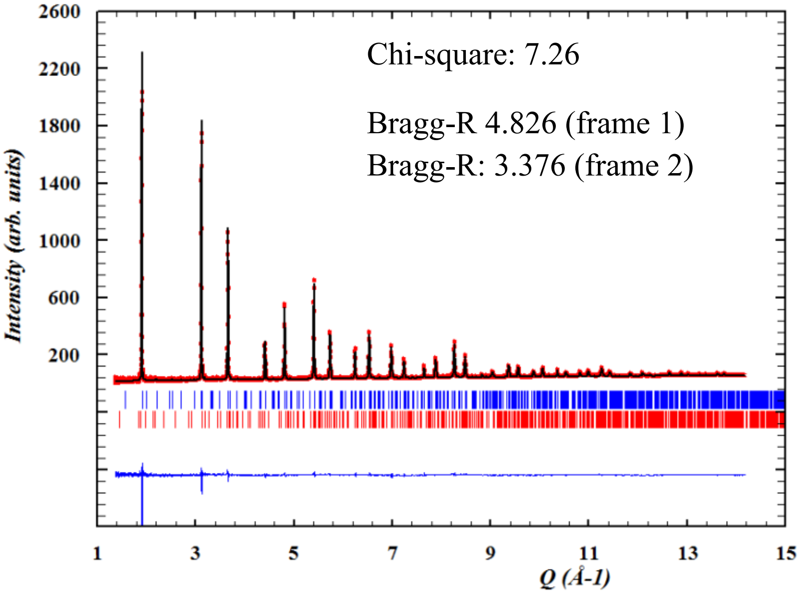

Chi-square: 7.26

Bragg-R 4.826 (frame 1)
Bragg-R: 3.376 (frame 2)

Rietveld refinement of neutron powder diffraction pattern (frame 1) collected at Oak Ridge.

Sample A100-6

Cu (Zn+Sn)	Zn/Sn	Cu	Zn	Sn	Se	type	%	%
0.9452	1.1487	1.950	1.104	0.961	4	B-F	10 % F	90% B

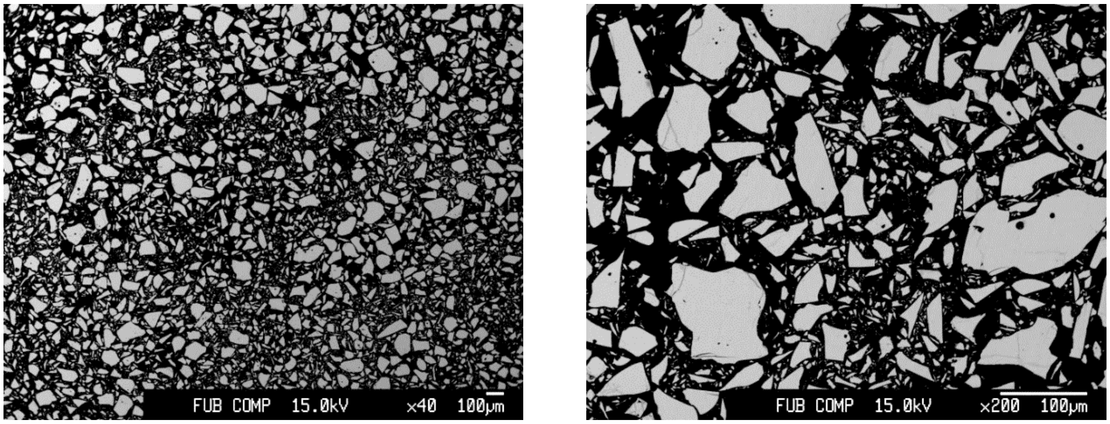

BSE micrograph

Refined phases: Kesterite (space group $I\overline{4}$)

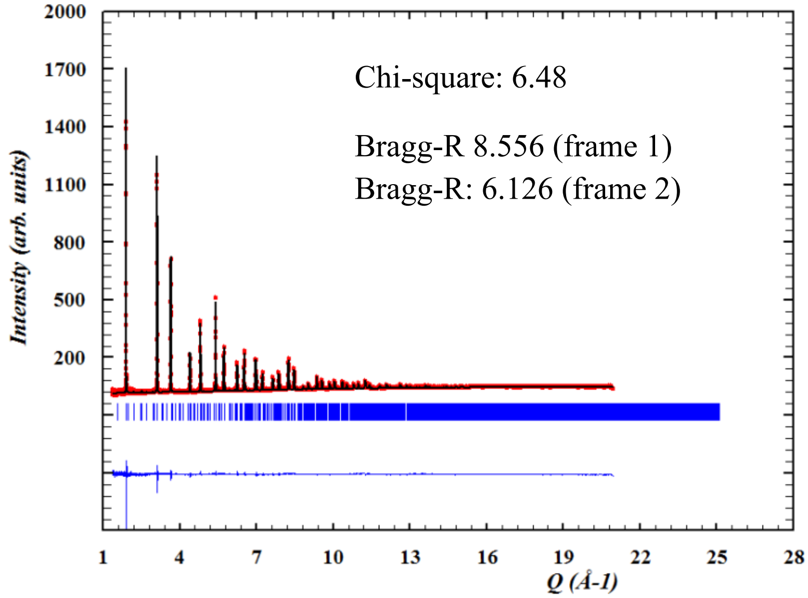

Rietveld refinement of neutron powder diffraction pattern (frame 1) collected at Oak Ridge.

Sample A0125-6

Cu (Zn+Sn)	Zn/Sn	Cu	Zn	Sn	Se	type	%	%
0.9102	1.2219	1.910	1.155	0.945	4	B-F	5 % F	95% B

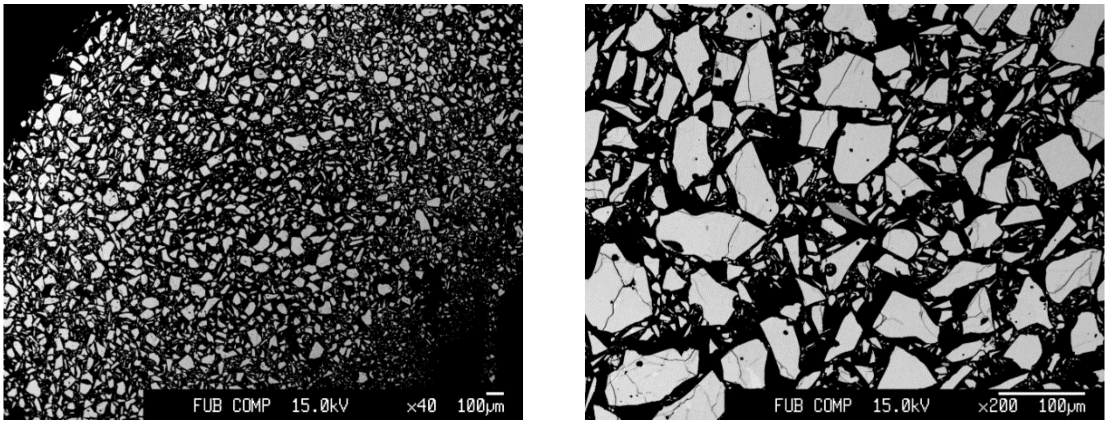

BSE micrograph

Refined phases: Kesterite (space group $I\bar{4}$)
ZnSe (space group $F\bar{4}3m$)

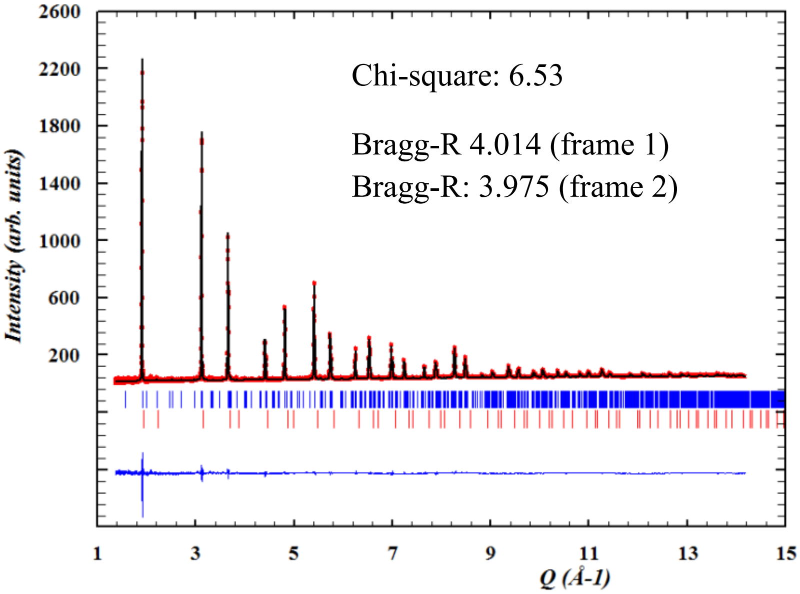

Rietveld refinement of neutron powder diffraction pattern (frame 1) collected at Oak Ridge.

Sample S0000-7

Cu (Zn+Sn)	Zn/Sn	Cu	Zn	Sn	Se	type	%	%
1.0070	1.0614	2.025	1.036	0.976	4	B-F	62% F	38% B

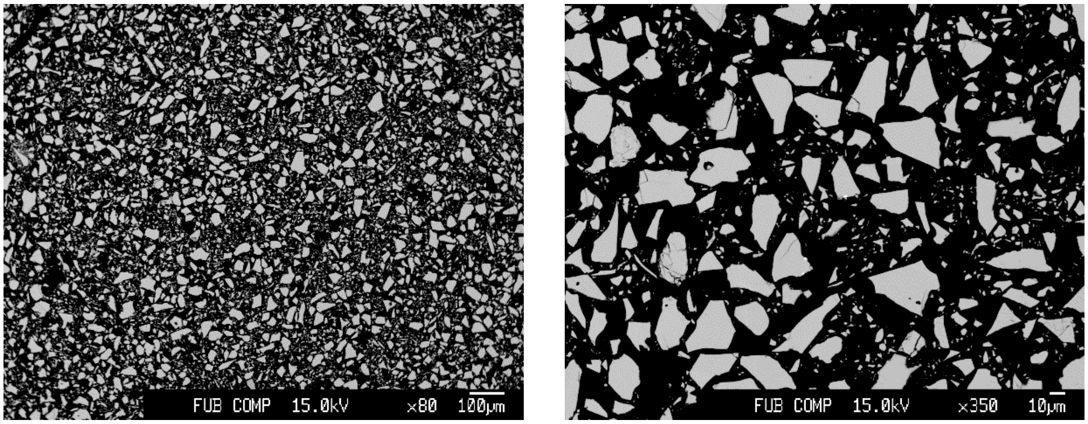

BSE micrograph

Refined phases: Kesterite (space group $I\bar{4}$)

Cu_2Se (space group $Fm\bar{3}m$)

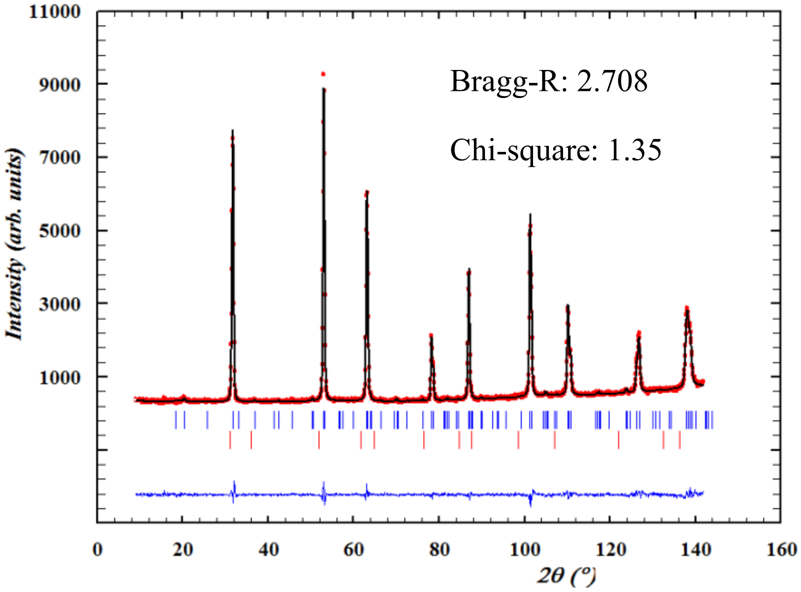

Rietveld refinement of neutron powder diffraction pattern collected at E9.

Sample C0025-7

Cu (Zn+Sn)	Zn/Sn	Cu	Zn	Sn	Se	type	%	%
0.9955	1.1315	2.023	1.080	0.954	4	B-F	46% F	54% B

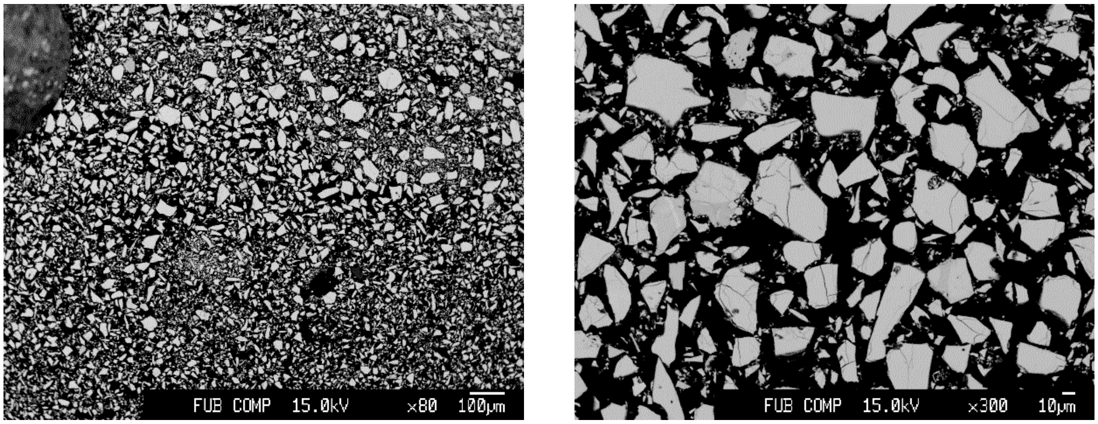

BSE micrograph

Refined phases: Kesterite (space group $I\bar{4}$)
CuSe (space group $P6_3/mmc$)
Cu_2Se (space group $Fm\bar{3}m$)

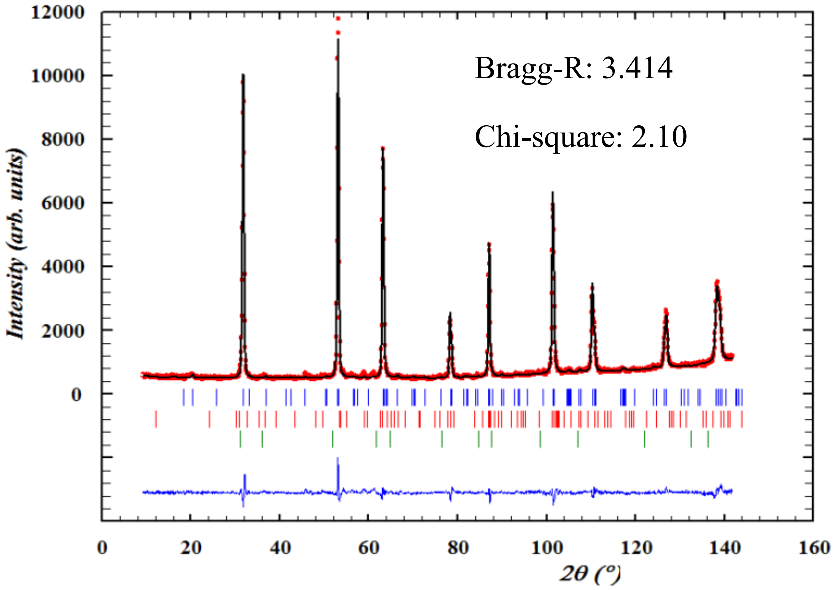

Rietveld refinement of neutron powder diffraction pattern collected at E9.

Sample D0050-9

Cu (Zn+Sn)	Zn/Sn	Cu	Zn	Sn	Se	type	%	%
1.0231	1.0850	2.055	1.045	0.964	4	B-F	78% F	22% B

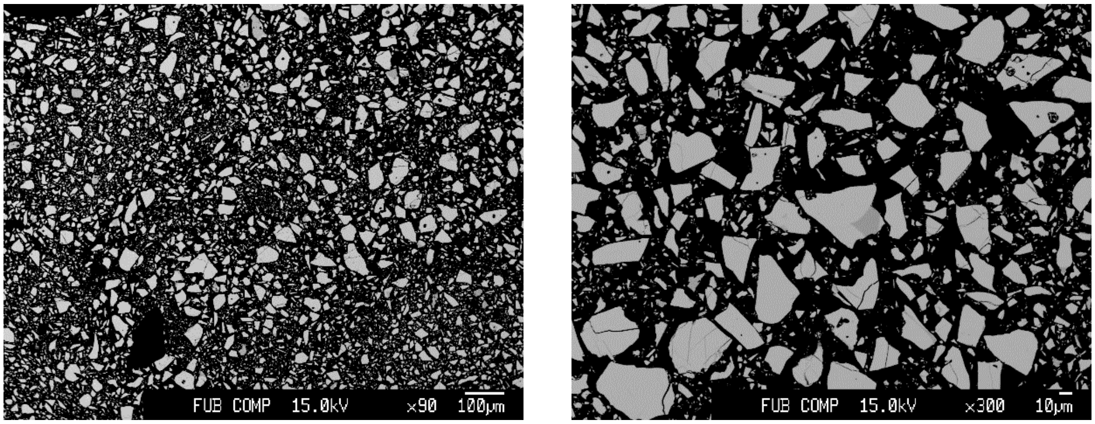

BSE micrograph

Refined phases: Kesterite (space group $I\bar{4}$)
CuSe (space group $P6_3/mmc$)
Cu_2Se (space group $Fm\bar{3}m$)

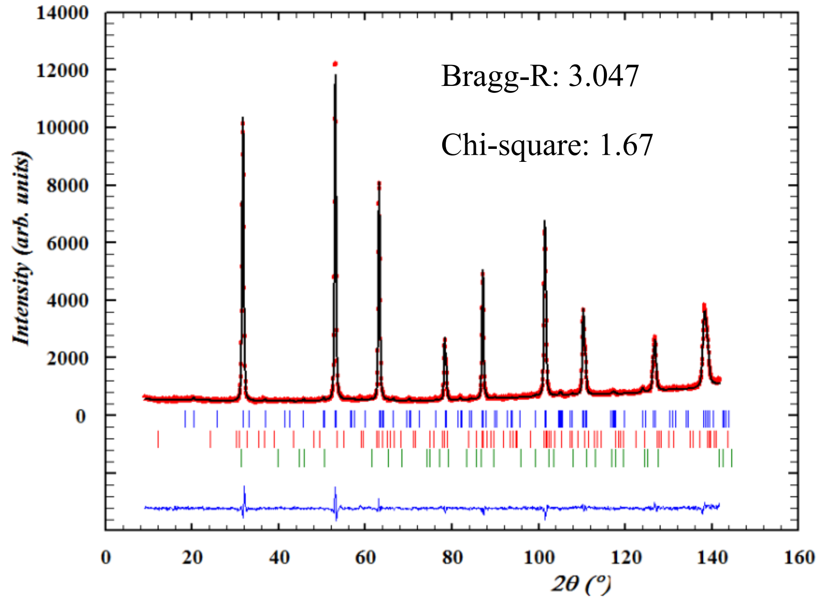

Rietveld refinement of neutron powder diffraction pattern collected at E9.

Sample C0025-2

Cu (Zn+Sn)	Zn/Sn	Cu	Zn	Sn	Se	type	%	%
1.0268	0.9952	2.039	0.990	0.995	4	D-F	82% D	18% F

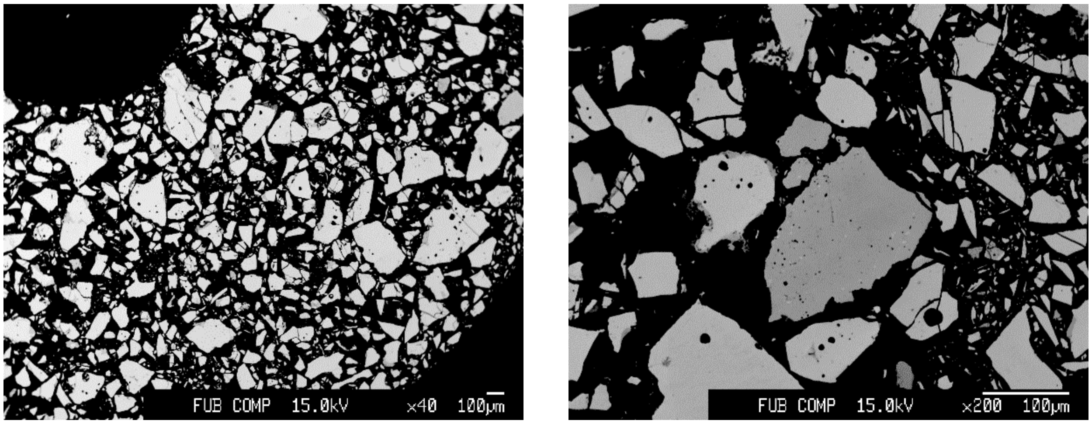

BSE micrograph

Refined phases: Kesterite (space group $I\overline{4}$)

ZnSe (space group $F\overline{4}3m$)

CuSe (space group $P6_3/mmc$)

Cu_2Se (space group $Fm\overline{3}m$)

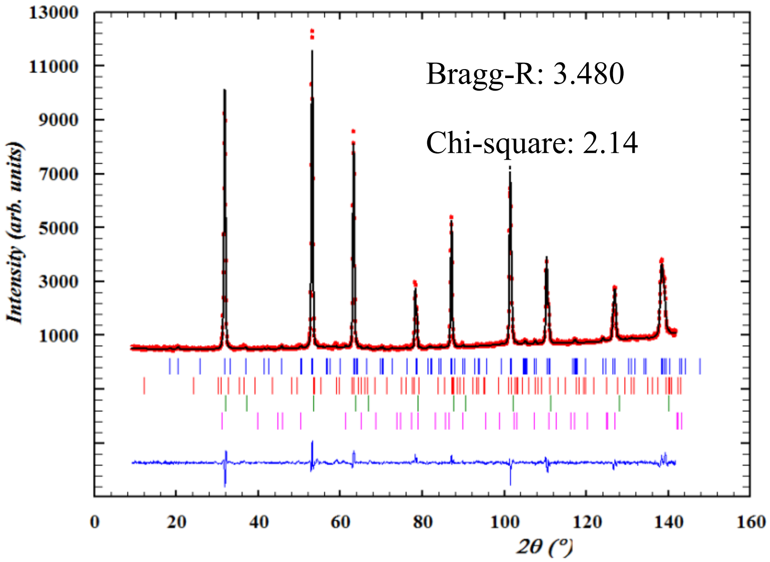

Rietveld refinement of neutron powder diffraction pattern collected at E9.

Sample C0025-4

Cu (Zn+Sn)	Zn/Sn	Cu	Zn	Sn	Se	type	%	%
1.0136	1.0173	2.025	1.007	0.990	4	D-F	28% D	72% F

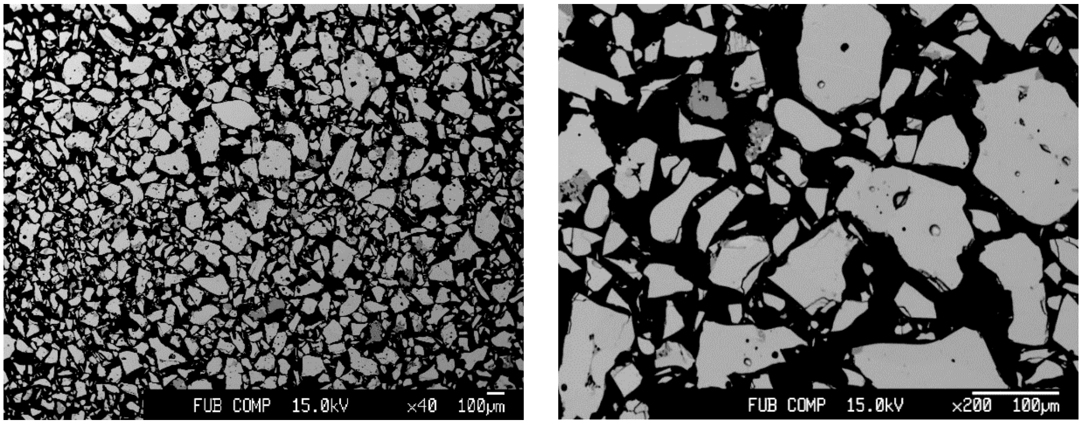

BSE micrograph

Refined phases: Kesterite (space group $I\bar{4}$)

ZnSe (space group $F\bar{4}3m$)

CuSe (space group $P6_3/mmc$)

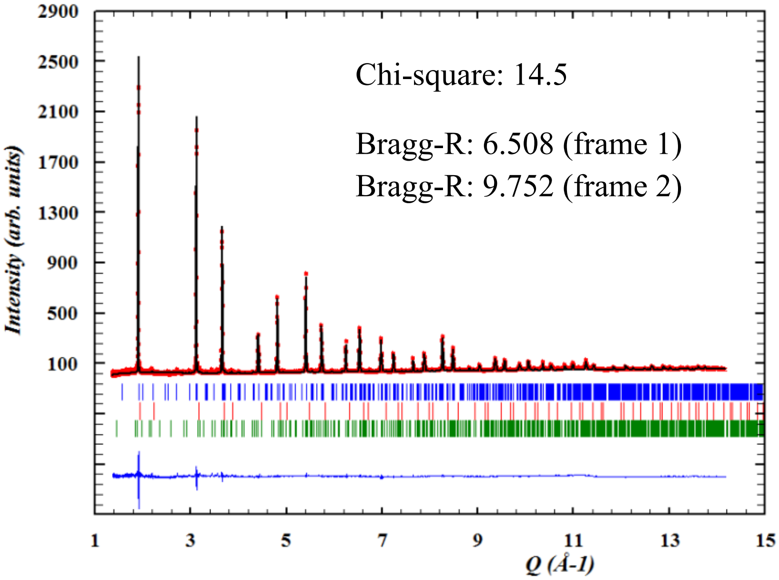

Rietveld refinement of neutron powder diffraction pattern (frame 1) collected at Oak Ridge.

Sample D0100-9

Cu (Zn+Sn)	Zn/Sn	Cu	Zn	Sn	Se	type	%	%
1.1003	0.9614	2.136	0.950	0.991	4	D-F	91% D	9% F

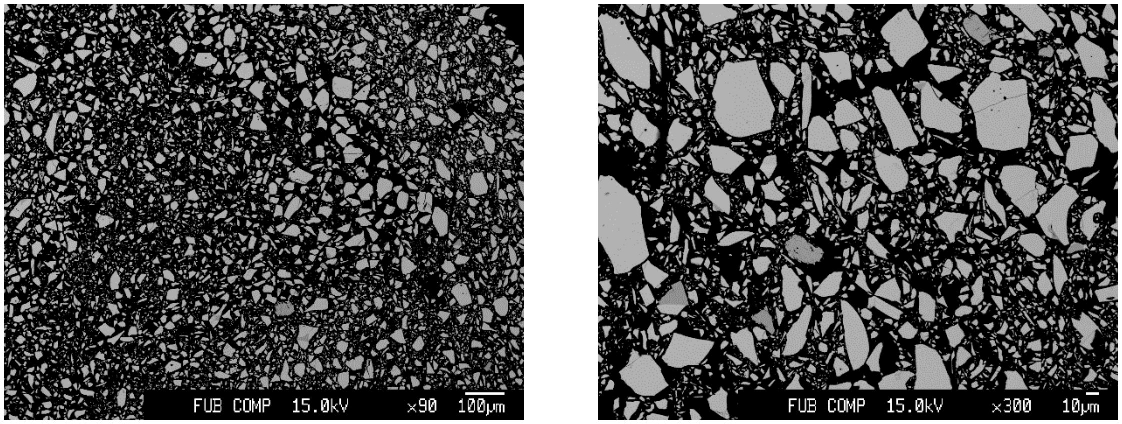

BSE micrograph

Refined phases: Kesterite (space group $I\bar{4}$)
Cu_2Se (space group $Fm\bar{3}m$)
CuSe (space group $P6_3/mmc$)
SnO_2-Cassiterite (space group $P4_2/mnm$)

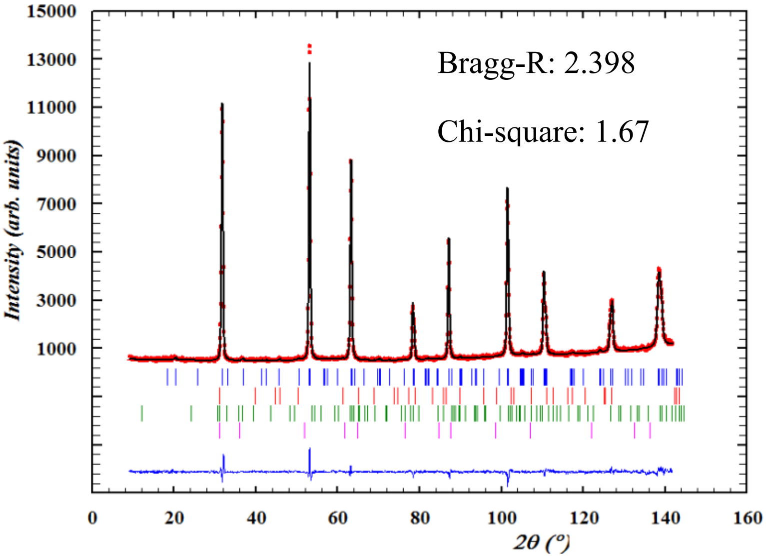

Rietveld refinement of neutron powder diffraction pattern collected at E9.

Sample D0150-9

Cu (Zn+Sn)	Zn/Sn	Cu	Zn	Sn	Se	type	%	%
1.1454	0.9098	2.185	0.909	0.999	4	D-F	99% D	1% F

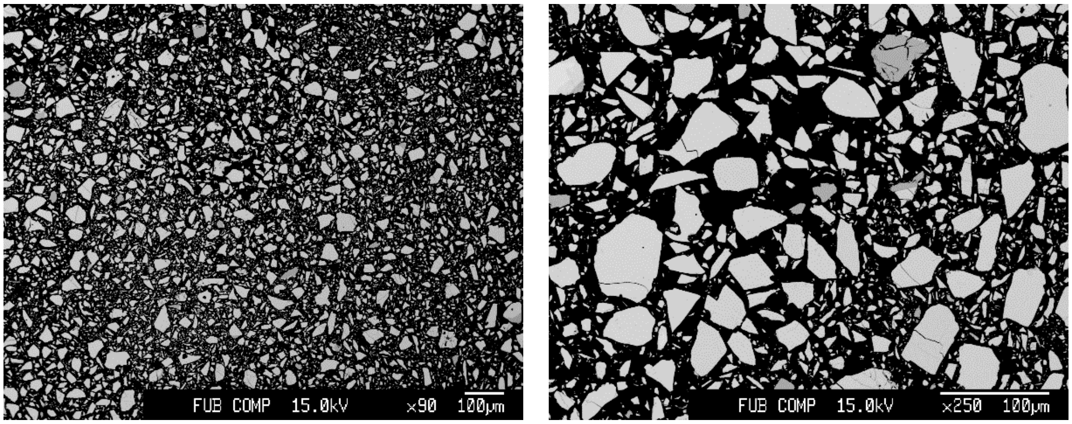

BSE micrograph

Refined phases: Kesterite (space group $I\bar{4}$)
CuSe (space group $P6_3/mmc$)

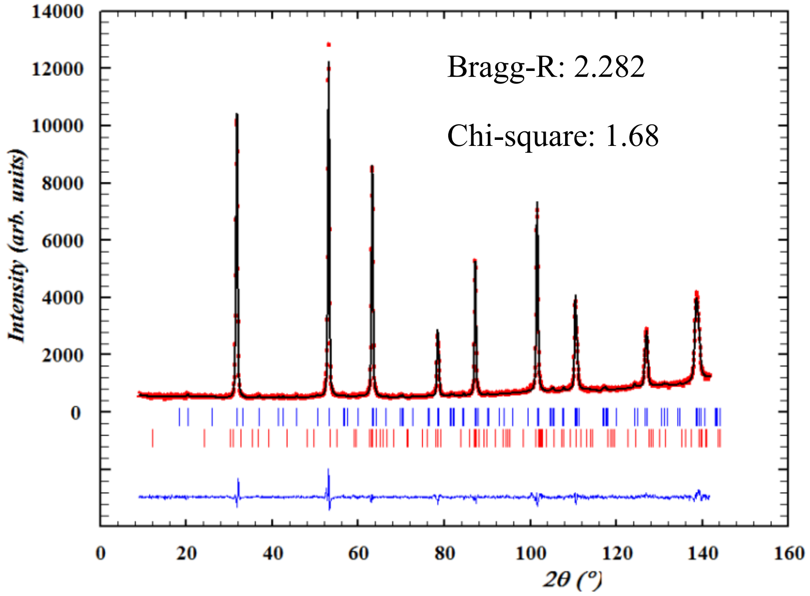

Rietveld refinement of neutron powder diffraction pattern collected at E9.

Sample C0050-4

Cu (Zn+Sn)	Zn/Sn	Cu	Zn	Sn	Se	type	%	%
1.1028	0.8830	2.117	0.901	1.020	4	C-D	67 % C	33% D

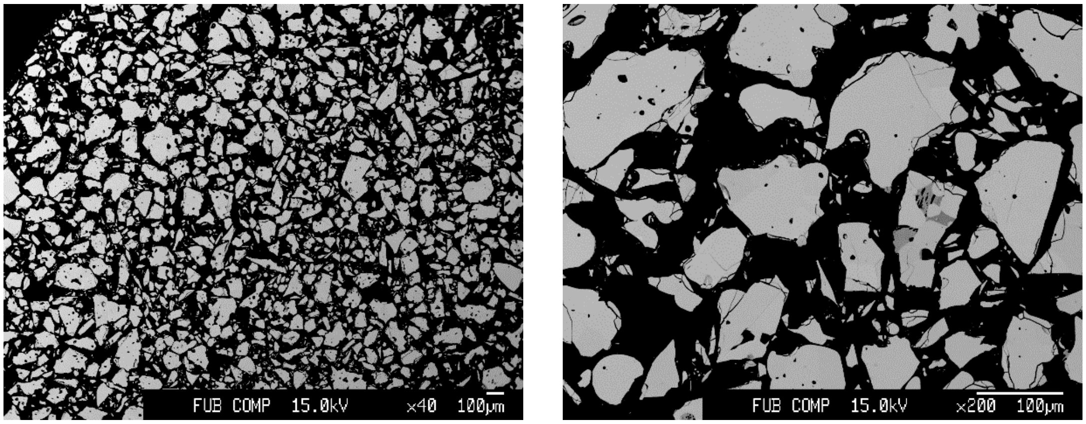

BSE micrograph

Refined phases: Kesterite (space group $I\overline{4}$)
CuSe (space group $P6_3/mmc$)

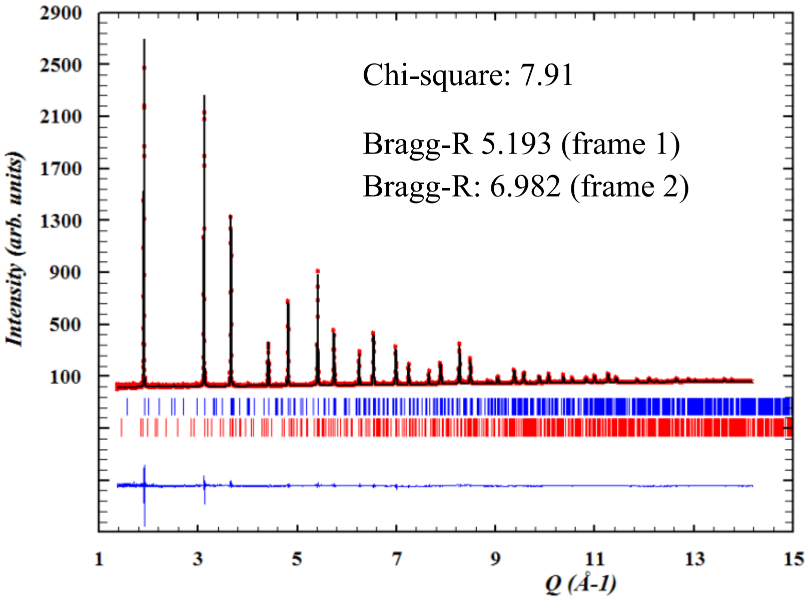

Rietveld refinement of neutron powder diffraction pattern (frame 1) collected at Oak Ridge.

Sample C0050-7

Cu (Zn+Sn)	Zn/Sn	Cu	Zn	Sn	Se	type	%	%
1.0881	0.8707	2.093	0.896	1.029	4	C-D	86 % C	14% D

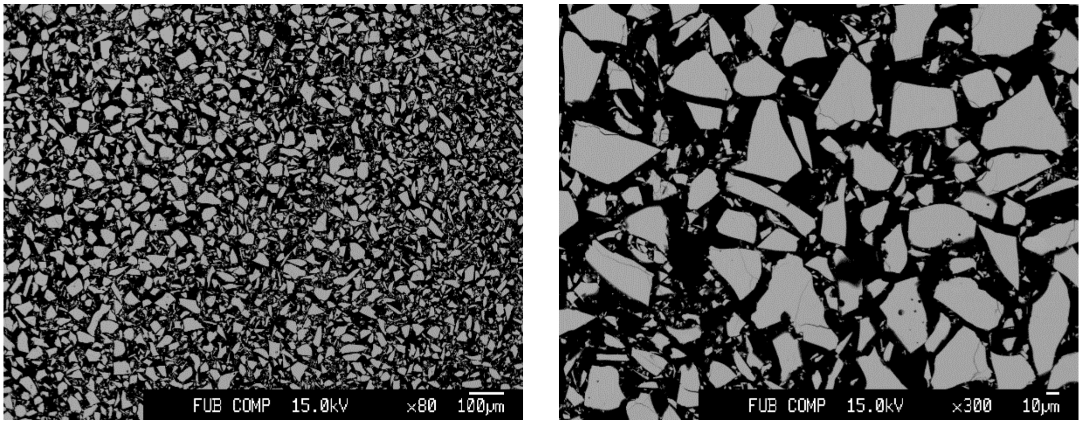

BSE micrograph

Refined phases: Kesterite (space group $I\overline{4}$)
CuSe (space group $P6_3/mmc$)

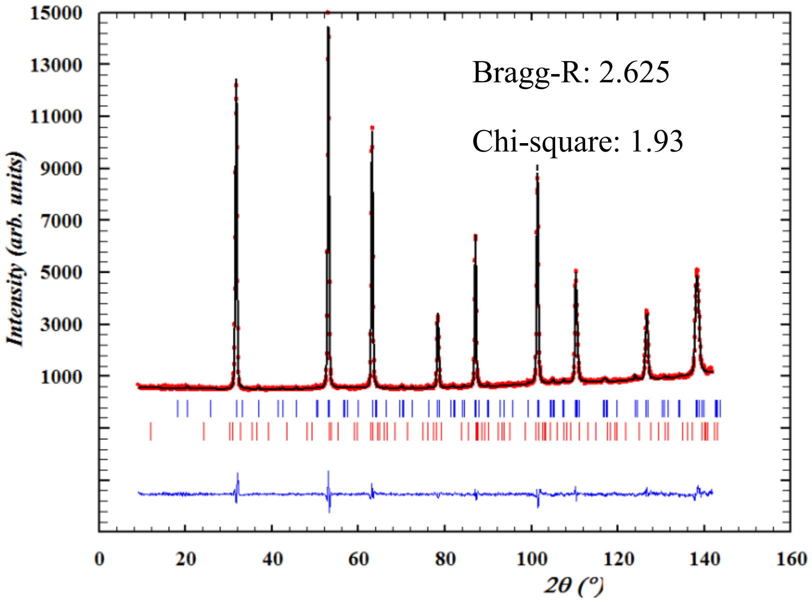

Rietveld refinement of neutron powder diffraction pattern collected at E9.

Sample C0075-7

Cu (Zn+Sn)	Zn/Sn	Cu	Zn	Sn	Se	type	%	%
1.1739	0.7766	2.181	0.814	1.048	4	C-D	81 % C	19% D

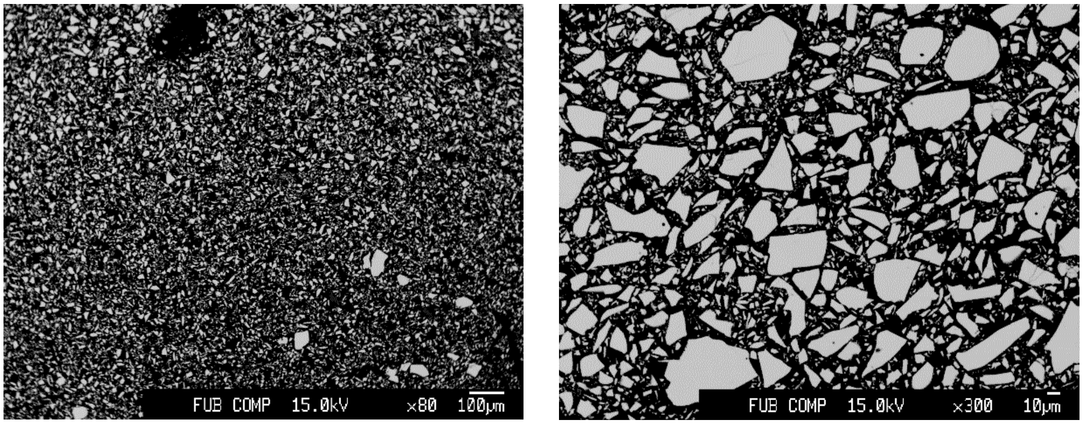

BSE micrograph

Refined phases: Kesterite (space group $I\bar{4}$)
CuSe (space group $P6_3/mmc$)

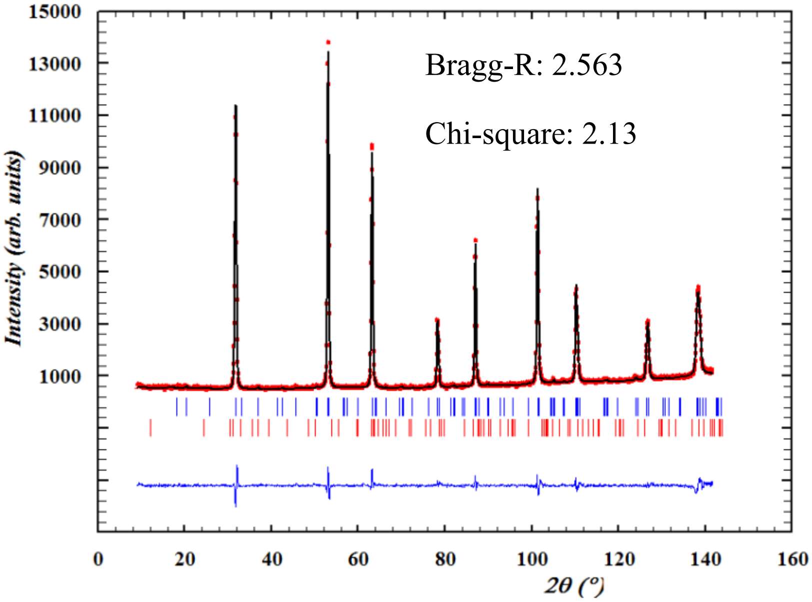

Rietveld refinement of neutron powder diffraction pattern collected at E9.

Table A.2: Samples overview: cation ratios and atomic % and type fractions by linear combination

No.	sample	Cu/(Zn+Sn)	err	Zn/Sn	err	atomic % WDX				chemical composition			
						Cu	Zn	Sn	Se	Cu	Zn	Sn	Se
2	A0050-1	0.911	0.016	1.127	0.016	23.924	13.912	12.341	49.824	1.892	1.101	0.977	4
3	A0100-1	0.833	0.014	1.129	0.016	22.783	14.505	12.846	49.865	1.766	1.125	0.996	4
4	A0125-1	0.816	0.014	1.147	0.016	22.536	14.766	12.868	49.831	1.74	1.141	0.994	4
7	A0025-3	0.967	0.017	1.045	0.015	25.112	13.271	12.701	48.916	1.961	1.036	0.992	4
14	B0025-5	0.854	0.015	1.189	0.017	23.244	14.786	12.438	49.532	1.81	1.154	0.971	4
15	B0050-5	0.846	0.015	1.192	0.017	23.032	14.810	12.420	49.737	1.797	1.158	0.971	4
18	A0025-6	0.950	0.016	1.099	0.016	24.762	13.647	12.418	49.172	1.947	1.073	0.977	4
19	A0050-6	0.920	0.016	1.113	0.016	24.184	13.852	12.444	49.521	1.902	1.09	0.979	4
20	A0075-6	0.890	0.015	1.134	0.016	23.815	14.216	12.535	49.434	1.859	1.111	0.98	4
1	A0000-1	0.978	0.017	1.077	0.015	24.767	13.133	12.198	49.903	1.985	1.053	0.978	4
6	A0000-3	0.979	0.017	1.075	0.015	25.331	13.404	12.465	48.800	1.986	1.051	0.978	4
8	A0075-3	0.959	0.017	1.120	0.016	25.051	13.804	12.325	48.820	1.965	1.083	0.967	4
9	B0025-3	0.972	0.017	1.114	0.016	25.232	13.679	12.279	48.811	1.984	1.076	0.966	4
12	B0050-4	0.998	0.017	1.042	0.015	25.714	13.147	12.619	48.520	2.007	1.026	0.985	4
13	B0075-4	1.000	0.017	1.046	0.015	25.795	13.183	12.608	48.414	2.011	1.028	0.983	4
16	B0075-5	0.939	0.016	1.214	0.017	24.990	14.586	12.018	48.406	1.953	1.142	0.941	4
17	C0025-5	1.008	0.017	1.100	0.016	25.644	13.322	12.108	48.926	2.036	1.058	0.962	4
21	A0100-6	0.945	0.016	1.149	0.016	24.909	14.088	12.264	48.739	1.95	1.104	0.961	4
22	A0125-6	0.910	0.016	1.222	0.017	24.431	14.761	12.080	48.729	1.91	1.155	0.945	4
23	S0000-7	1.007	0.017	1.061	0.015	25.816	13.199	12.436	48.533	2.025	1.036	0.976	4
24	C0025-7	0.996	0.017	1.132	0.016	25.861	13.790	12.187	48.112	2.023	1.08	0.954	4
27	D0050-9	1.023	0.018	1.085	0.015	26.434	13.446	12.392	47.728	2.055	1.045	0.964	4
5	C0025-2	1.027	0.018	0.995	0.014	25.947	12.604	12.665	48.783	2.039	0.99	0.995	4
10	C0025-4	1.014	0.018	1.017	0.014	25.990	12.930	12.710	48.369	2.025	1.007	0.99	4
28	D0100-9	1.100	0.019	0.961	0.014	27.315	12.168	12.658	47.859	2.136	0.95	0.991	4
29	D0150-9	1.145	0.020	0.910	0.013	27.929	11.616	12.768	47.688	2.185	0.909	0.999	4
11	C0050-4	1.103	0.019	0.883	0.012	27.039	11.498	13.021	48.441	2.117	0.901	1.02	4
25	C0050-7	1.088	0.019	0.871	0.012	26.798	11.463	13.166	48.564	2.093	0.896	1.029	4
26	C0075-7	1.174	0.020	0.777	0.011	27.715	10.321	13.289	48.665	2.181	0.814	1.048	4

sample	Cu/Zn+Sn	error	Zn/Sn	error	x	x err	y	y err	B frac.	error	A frac.	error	Cu	error	Zn	error	Sn	error
A0050-1	0.9113	0.009	1.1273	0.011	0.127	0.001	0.031	0.000	0.758	0.025	0.242	0.008	1.892	0.051	1.101	0.029	0.977	0.026
A0100-1	0.8330	0.008	1.1292	0.011	0.129	0.001	0.031	0.000	0.124	0.004	0.876	0.030	1.766	0.053	1.125	0.035	0.996	0.031
A0125-1	0.8155	0.008	1.1475	0.011	0.147	0.001	0.036	0.001	0.157	0.005	0.843	0.029	1.740	0.051	1.141	0.034	0.994	0.030
A0025-3	0.9669	0.010	1.0449	0.010	0.045	0.000	0.011	0.000	0.746	0.025	0.254	0.009	1.961	0.052	1.036	0.027	0.992	0.026
B0025-5	0.8538	0.009	1.1888	0.012	0.189	0.002	0.045	0.001	0.652	0.022	0.348	0.012	1.810	0.046	1.154	0.028	0.971	0.024
B0050-5	0.8458	0.008	1.1924	0.012	0.192	0.002	0.046	0.001	0.622	0.021	0.378	0.013	1.797	0.045	1.158	0.028	0.971	0.024
A0025-6	0.9500	0.010	1.0990	0.011	0.099	0.001	0.024	0.000	0.969	0.032	0.031	0.001	1.947	0.063	1.073	0.035	0.977	0.031
A0050-6	0.9197	0.009	1.1131	0.011	0.113	0.001	0.028	0.000	0.750	0.025	0.250	0.009	1.902	0.051	1.090	0.029	0.979	0.026
A0075-6	0.8902	0.009	1.1341	0.011	0.134	0.001	0.032	0.000	0.627	0.021	0.373	0.013	1.859	0.046	1.111	0.027	0.980	0.024
sample	**Cu/Zn+Sn**	**error**	**Zn/Sn**	**error**	**y**	**y err**	**k**	**k err**	**F frac.**	**error**	**B frac.**	**error**	**Cu**	**error**	**Zn**	**error**	**Sn**	**error**
A0000-1	0.9778	0.010	1.0766	0.011	0.019	2.66E-04	0.963	0.010	0.198	0.006	0.802	0.021	1.985	0.044	1.053	0.023	0.978	0.022
A0000-3	0.9792	0.010	1.0753	0.011	0.018	2.61E-04	0.964	0.010	0.214	0.007	0.786	0.021	1.986	0.043	1.051	0.023	0.978	0.022
A0075-3	0.9587	0.010	1.1200	0.011	0.029	4.12E-04	0.943	0.009	0.136	0.004	0.864	0.023	1.965	0.045	1.083	0.025	0.967	0.023
B0025-3	0.9720	0.010	1.1140	0.011	0.028	3.92E-04	0.946	0.009	0.240	0.008	0.760	0.020	1.984	0.042	1.076	0.023	0.966	0.021
B0050-4	0.9980	0.010	1.0418	0.010	0.010	1.46E-04	0.980	0.010	0.451	0.014	0.549	0.015	2.007	0.041	1.026	0.021	0.985	0.021
B0075-4	1.0001	0.010	1.0456	0.010	0.011	1.59E-04	0.978	0.010	0.503	0.016	0.497	0.013	2.011	0.042	1.028	0.022	0.983	0.021
B0075-5	0.9393	0.009	1.2137	0.012	0.051	7.17E-04	0.903	0.009	0.186	0.006	0.814	0.022	1.953	0.043	1.142	0.026	0.941	0.021
C0025-5	1.0084	0.010	1.1002	0.011	0.024	3.46E-04	0.952	0.010	0.588	0.019	0.412	0.011	2.036	0.045	1.058	0.023	0.962	0.021
A0100-6	0.9453	0.009	1.1487	0.011	0.036	5.07E-04	0.931	0.009	0.104	0.003	0.896	0.024	1.950	0.046	1.104	0.027	0.961	0.023
A0125-6	0.9102	0.009	1.2219	0.012	0.053	7.43E-04	0.900	0.009	0.051	0.002	0.949	0.025	1.910	0.048	1.155	0.029	0.945	0.024
S0000-7	1.0070	0.010	1.0614	0.011	0.015	2.14E-04	0.970	0.010	0.618	0.020	0.382	0.010	2.025	0.046	1.036	0.024	0.976	0.022
C0025-7	0.9955	0.010	1.1315	0.011	0.032	4.50E-04	0.938	0.009	0.464	0.015	0.536	0.014	2.023	0.042	1.080	0.022	0.954	0.020
D0050-9	1.0231	0.010	1.0850	0.011	0.021	2.94E-04	0.959	0.010	0.783	0.025	0.217	0.006	2.055	0.054	1.045	0.028	0.964	0.026
sample	**Cu/Zn+Sn**	**error**	**Zn/Sn**	**error**	**k**	**k err**	**m**	**m err**	**D fr frac.**	**error**	**F frac.**	**error**	**Cu**	**error**	**Zn**	**error**	**Sn**	**error**
C0025-2	1.0268	0.010	0.9952	0.010	0.027	2.68E-04	0.018	5.3E-04	0.823	0.035	0.177	0.008	2.039	0.073	0.990	0.035	0.995	0.000
C0025-4	1.0136	0.010	1.0173	0.010	0.014	1.36E-04	0.009	2.7E-04	0.282	0.012	0.718	0.033	2.025	0.071	1.007	0.035	0.990	0.000
D0100-9	1.1003	0.011	0.9614	0.010	0.100	1.00E-03	0.065	1.9E-03	0.909	0.039	0.091	0.004	2.136	0.083	0.950	0.036	0.991	0.000
D0150-9	1.1454	0.011	0.9098	0.009	0.145	1.45E-03	0.092	2.8E-03	0.995	0.042	0.005	0.000	2.185	0.092	0.909	0.038	0.999	0.000
sample	**Cu/Zn+Sn**	**error**	**Zn/Sn**	**error**	**z**	**z err**	**m**	**m err**	**C frac.**	**error**	**D frac.**	**error**	**Cu**	**error**	**Zn**	**error**	**Sn**	**error**
C0050-4	1.1028	0.011	0.8830	0.009	0.030	6.03E-04	0.117	0.001	0.673	0.035	0.327	0.017	2.117	0.081	0.901	0.049	1.020	0.040
C0050-7	1.0881	0.011	0.8707	0.009	0.033	6.68E-04	0.129	0.001	0.863	0.045	0.137	0.007	2.093	0.094	0.896	0.043	1.029	0.047
C0075-7	1.1739	0.012	0.7766	0.008	0.059	1.18E-03	0.223	0.002	0.809	0.042	0.191	0.010	2.181	0.092	0.814	0.042	1.048	0.046

Table A.3: Samples overview of lattice parameters, occupation factors and isotropic temperature factors of neutron diffraction data

No.	sample	neutrons		$V_{unit\ cell}$	Occ								Biso					Se-anon		
		a	*c*	Å^3	(2a)		(2c)		(2d)		(2b)		(2a)	(2c)	(2d)	(2b)	Se	x	y	z
2	A0050-1	5.697	11.340	367.992	1.028	30	0.96	47	1.069	62	1.002	33	1.899	2.559	2.559	0.963	0.807	0.7400	0.7429	0.6281
3	A0100-1	5.694	11.331	367.3641	0.976	38	0.905	27	1.02	36	1.005	40	1.239	2.577	2.577	0.408	1.148	0.7392	0.7439	0.6252
4	A0125-1	5.693	11.331	367.2602	0.931	32	0.875	33	1.005	43	0.984	36	1.177	1.056	1.056	0.863	0.809	0.7456	0.7385	0.6286
7	A0025-3	5.696	11.353	368.301	0.985	23	0.943	33	1.036	37	0.996	25	1.95	2.689	0.268	0.958	1.134	0.7437	0.7392	0.6304
14	B0025-5	5.697	11.353	368.5322	0.997	29	0.888	42	1.019	49	0.987	30	1.817	1.316	0.841	0.863	1.199	0.7393	0.7441	0.6287
15	B0050-5	5.697	11.353	368.529	1.007	26	0.893	41	1.068	55	0.987	30	1.715	1.306	1.306	0.840	1.111	0.7398	0.7434	0.6287
18	A0025-6	5.698	11.348	368.4401	1.013	32	0.852	42	1.131	56	1.024	37	1.813	1.746	1.003	1.000	0.952	0.7498	0.7371	0.6286
19	A0050-6	5.696	11.342	367.9665	1.024	42	0.963	52	1.061	67	0.969	47	2.421	1.319	1.319	1.282	0.74	0.7393	0.7455	0.6284
20	A0075-6	5.693	11.332	367.2661	0.946	32	0.898	37	1.068	49	1.005	36	1.247	1.226	1.226	0.986	0.903	0.7447	0.7394	0.6286
1	A0000-1	5.699	11.351	368.6397	1.008	26	0.983	33	0.989	32	1.005	26	1.782	4.062	0.02	0.583	0.786	0.7432	0.7393	0.6286
6	A0000-3	5.692	11.343	367.4409	1.014	23	0.935	38	1.083	48	0.97	29	1.497	1.493	1.493	0.902	0.821	0.7439	0.7409	0.6295
8	A0075-3	5.694	11.348	367.9172	0.999	28	0.926	49	1.101	65	0.98	31	1.814	1.577	1.577	0.829	0.96	0.7430	0.7418	0.6291
9	B0025-3	5.693	11.344	367.6741	0.994	25	0.941	33	1.04	38	0.979	25	1.762	3.316	0.439	0.757	0.99	0.7414	0.7416	0.6286
12	B0050-4	5.693	11.348	367.8603	1.006	25	0.989	33	1.015	37	1.008	27	1.935	3.024	0.459	1.216	0.961	0.7433	0.7407	0.6301
13	B0075-4	5.695	11.349	368.0304	1.003	39	0.941	44	1.068	62	1.003	44	1.694	1.428	2.37	0.628	0.835	0.7429	0.7433	0.6274
16	B0075-5	5.692	11.347	367.6703	1.014	34	0.956	44	1.004	48	1.002	34	2.626	3.072	0.153	0.46	1.12	0.7416	0.7432	0.6290
17	C0025-5	5.691	11.346	367.4319	0.976	32	0.95	36	1.095	47	1.044	44	0.773	1.233	1.233	1.399	0.826	0.7466	0.7402	0.6290
21	A0100-6	5.693	11.330	367.1911	0.947	37	0.893	42	1.088	55	1.013	42	0.871	1.342	1.342	0.768	0.76	0.7477	0.7380	0.6279
22	A0125-6	5.692	11.328	366.9872	0.963	23	0.919	37	1.048	42	1.008	23	1.546	2.263	0.797	0.627	0.911	0.7442	0.7391	0.6280
23	S0000-7	5.700	11.348	368.6461	0.987	28	0.952	25	1.047	34	1.005	33	1.465	0.999	1.88	0.985	0.938	0.7382	0.7457	0.6221
24	C0025-7	5.694	11.345	367.8907	1.020	33	0.964	30	1.015	34	1.004	28	3.506	1.772	1.564	0.065	1.474	0.7411	0.7487	0.6292
27	D0050-9	5.695	11.346	367.9402	0.997	22	0.956	30	1.078	35	0.985	23	1.616	2.943	0.616	0.909	1.206	0.7452	0.7374	0.6295
5	C0025-2	5.694	11.344	367.7758	1.002	26	0.957	40	1.046	48	1.012	28	1.693	2.511	0.755	1.118	1.105	0.7426	0.7394	0.6302
10	C0025-4	5.693	11.344	367.6225	0.98	30	0.96	46	1.089	50	0.989	31	1.231	2.214	0.572	0.894	0.753	0.7400	0.7442	0.6290
28	D0100-9	5.692	11.342	367.4288	1.011	27	0.949	26	1.065	39	0.993	33	2.13	0.786	2.058	0.929	1.131	0.7414	0.7454	0.6287
29	D0150-9	5.689	11.341	366.9476	0.997	21	0.961	29	1.03	31	0.977	24	2.197	2.516	0.314	0.899	1.199	0.7441	0.7385	0.6308
11	C0050-4	5.6874	11.3403	366.8179	0.999	22	0.926	34	1.103	43	0.997	24	1.344	1.171	1.171	0.999	0.87	0.7438	0.7396	0.6292
25	C0050-7	5.695	11.357	368.3484	0.992	20	0.973	27	1.052	29	1.019	30	2.389	3.018	0.241	1.146	1.064	0.7452	0.7378	0.6305
26	C0075-7	5.695	11.357	368.3092	0.989	28	0.929	38	1.123	53	1.002	34	2.004	1.415	1.792	1.883	1.277	0.7454	0.7399	0.6286

Table A.4: Samples overview of bond lengths and bond angles (tetrahedral angles) of the kesterite phase

No	sample	Bond distances (calculated acc. to ionic radii * / Cation - anion Se $^{-2}$ (1.84)								Bond distance (Rietveld refinements)							
		Cu^+-0.6		Cu^+-0.6		Zn^{2+}-0.74		Sn^{4+}-0.69		2a-Se		2c-Se		2d-Se		2b-Se	
2	A0050-1	2.440	0.0244	2.447	0.0245	2.566	0.0257	2.531	0.0253	2.427	0.0243	2.434	0.0243	2.454	0.0245	2.539	0.0254
3	A0100-1	2.410	0.0241	2.432	0.0243	2.573	0.0257	2.530	0.0253	2.407	0.0241	2.446	0.0245	2.477	0.0248	2.519	0.0252
4	A0125-1	2.410	0.0241	2.421	0.0242	2.573	0.0257	2.530	0.0253	2.433	0.0243	2.462	0.0246	2.415	0.0242	2.537	0.0254
7	A0025-3	2.440	0.0244	2.452	0.0245	2.566	0.0257	2.530	0.0253	2.444	0.0244	2.445	0.0244	2.415	0.0242	2.555	0.0255
14	B0025-5	2.427	0.0243	2.445	0.0244	2.566	0.0257	2.531	0.0253	2.434	0.0243	2.426	0.0243	2.457	0.0246	2.543	0.0254
15	B0050-5	2.440	0.0244	2.431	0.0243	2.563	0.0256	2.531	0.0253	2.433	0.0243	2.431	0.0243	2.451	0.0245	2.544	0.0254
18	A0025-6	2.440	0.0244	2.501	0.0250	2.526	0.0253	2.531	0.0253	2.446	0.0245	2.484	0.0248	2.398	0.0240	2.530	0.0253
19	A0050-6	2.440	0.0244	2.446	0.0245	2.566	0.0257	2.531	0.0253	2.436	0.0244	2.421	0.0242	2.462	0.0246	2.535	0.0254
20	A0075-6	2.454	0.0245	2.430	0.0243	2.559	0.0256	2.531	0.0253	2.433	0.0243	2.456	0.0246	2.421	0.0242	2.537	0.0254
1	A0000-1	2.440	0.0244	2.451	0.0245	2.573	0.0257	2.531	0.0253	2.432	0.0243	2.455	0.0245	2.429	0.0243	2.546	0.0255
6	A0000-3	2.440	0.0244	2.472	0.0247	2.552	0.0255	2.531	0.0253	2.442	0.0244	2.444	0.0244	2.424	0.0242	2.541	0.0254
8	A0075-3	2.44	0.0244	2.482	0.0248	2.545	0.0255	2.532	0.0253	2.440	0.0244	2.441	0.0244	2.433	0.0243	2.540	0.0254
9	B0025-3	2.440	0.0244	2.470	0.0247	2.556	0.0256	2.532	0.0253	2.431	0.0243	2.439	0.0244	2.440	0.0244	2.542	0.0254
12	B0050-4	2.440	0.0244	2.456	0.0246	2.566	0.0257	2.531	0.0253	2.445	0.0245	2.439	0.0244	2.422	0.0242	2.549	0.0255
13	B0075-4	2.440	0.0244	2.468	0.0247	2.554	0.0255	2.531	0.0253	2.434	0.0243	2.447	0.0245	2.449	0.0245	2.524	0.0252
16	B0075-5	2.440	0.0244	2.468	0.0247	2.564	0.0256	2.533	0.0253	2.439	0.0244	2.431	0.0243	2.443	0.0244	2.538	0.0254
17	C0025-5	2.440	0.0244	2.468	0.0247	2.555	0.0255	2.532	0.0253	2.445	0.0245	2.457	0.0246	2.414	0.0241	2.531	0.0253
21	A0100-6	2.451	0.0245	2.477	0.0248	2.541	0.0254	2.532	0.0253	2.434	0.0243	2.475	0.0247	2.411	0.0241	2.527	0.0253
22	A0125-6	2.454	0.0245	2.471	0.0247	2.549	0.0255	2.533	0.0253	2.426	0.0243	2.459	0.0246	2.425	0.0242	2.535	0.0253
23	S0000-7	2.440	0.0244	2.470	0.0247	2.552	0.0255	2.531	0.0253	2.392	0.0239	2.460	0.0246	2.509	0.0251	2.500	0.0250
24	C0025-7	2.440	0.0244	2.459	0.0246	2.566	0.0257	2.532	0.0253	2.458	0.0246	2.410	0.0241	2.461	0.0246	2.524	0.0252
27	D0050-9	2.440	0.0244	2.469	0.0247	2.552	0.0255	2.532	0.0253	2.436	0.0244	2.461	0.0246	2.409	0.0241	2.550	0.0255
5	C0025-2	2.440	0.0244	2.461	0.0246	2.557	0.0256	2.530	0.0253	2.439	0.0244	2.441	0.0244	2.419	0.0242	2.556	0.0256
10	C0025-4	2.440	0.0244	2.468	0.0247	2.552	0.0255	2.531	0.0253	2.437	0.0244	2.422	0.0242	2.451	0.0245	2.540	0.0254
28	D0100-9	2.440	0.0244	2.467	0.0247	2.545	0.0255	2.530	0.0253	2.443	0.0244	2.425	0.0243	2.452	0.0245	2.529	0.0253
29	D0150-9	2.440	0.0244	2.451	0.0245	2.555	0.0255	2.530	0.0253	2.443	0.0244	2.443	0.0244	2.405	0.0241	2.556	0.0256
11	C0050-4	2.440	0.0244	2.468	0.0247	2.540	0.0254	2.530	0.0253	2.434	0.0243	2.448	0.0245	2.420	0.0242	2.542	0.0254
25	C0050-7	2.440	0.0244	2.454	0.0245	2.554	0.0255	2.530	0.0253	2.446	0.0245	2.454	0.0245	2.405	0.0240	2.556	0.0256
26	C0075-7	2.440	0.0244	2.461	0.0246	2.537	0.0254	2.530	0.0253	2.440	0.0244	2.459	0.0246	2.423	0.0242	2.536	0.0254

** Shannon, R. (1976). "Revised effective ionic radii and systematic studies of interatomic distances in halides and chalcogenides." Acta Crystallographica Section A 32(5): 751-767.*

		Cation-anion-cation bond angles (Rietveld refinements)											
No	sample	(Cu2a)-(Se8g)-(Cu2c)		(Cu2a)-(Se8g)-(Zn2d)		(Cu2a)-(Se8g)-(Sn2b)		(Cu2c)-(Se8g)-(Zn2d)		(Cu2c)-(Se8g)-(Sn2b)		(Zn2d)-(Se8g)-(Sn2b	
2	A0050-1	111.51	1.1151	110.82	1.1082	108.38	1.0838	110.98	1.1098	107.79	1.0779	107.18	1.0718
3	A0100-1	111.69	1.1169	110.63	1.1063	109.62	1.0962	109.74	1.0974	107.98	1.0798	107.03	1.0703
4	A0125-1	110.23	1.1023	111.83	1.1183	108.15	1.0815	111.24	1.1124	106.87	1.0687	108.33	1.0833
7	A0025-3	110.65	1.1065	111.67	1.1167	107.33	1.0733	111.93	1.1193	107.04	1.0704	107.96	1.0796
14	B0025-5	111.67	1.1167	110.59	1.1059	108.07	1.0807	111.20	1.1120	108.05	1.0805	107.07	1.0707
15	B0050-5	111.50	1.1150	110.80	1.1080	108.00	1.0800	111.20	1.1120	107.80	1.0780	107.20	1.0720
18	A0025-6	109.30	1.0930	112.20	1.1220	108.10	1.0810	111.20	1.1120	106.60	1.0660	109.30	1.0930
19	A0050-6	111.68	1.1168	110.26	1.1026	108.21	1.0821	111.13	1.1113	108.34	1.0834	107.05	1.0705
20	A0075-6	110.42	1.1042	111.64	1.1164	108.16	1.0816	111.22	1.1122	107.05	1.0705	108.16	1.0816
1	A0000-1	110.77	1.1077	111.66	1.1166	108.09	1.0809	111.21	1.1121	107.05	1.0705	107.85	1.0785
6	A0000-3	110.63	1.1063	111.31	1.1131	107.72	1.0772	111.55	1.1155	107.41	1.0741	108.02	1.0802
8	A0075-3	110.85	1.1085	111.12	1.1112	107.87	1.0787	111.41	1.1141	107.58	1.0758	107.83	1.0783
9	B0025-3	111.20	1.1120	111.15	1.1115	108.08	1.0808	111.19	1.1119	107.53	1.0753	107.49	1.0749
12	B0050-4	110.75	1.1075	111.34	1.1134	107.43	1.0743	111.84	1.1184	107.35	1.0735	107.89	1.0789
13	B0075-4	110.89	1.1089	110.81	1.1081	108.59	1.0859	110.68	1.1068	107.92	1.0792	107.84	1.0784
16	B0075-5	111.18	1.1118	110.80	1.1080	107.90	1.0790	111.35	1.1135	107.89	1.0789	107.54	1.0754
17	C0025-5	110.05	1.1005	111.50	1.1150	107.88	1.0788	111.36	1.1136	107.28	1.0728	108.62	1.0862
21	A0100-6	109.76	1.0976	111.95	1.1195	108.44	1.0844	110.94	1.1094	106.78	1.0678	108.80	1.0880
22	A0125-6	110.54	1.1054	111.71	1.1171	108.42	1.0842	110.97	1.1097	106.99	1.0699	108.05	1.0805
23	S0000-7	111.94	1.1194	110.23	1.1023	110.93	1.1093	108.40	1.0840	108.35	1.0835	106.81	1.0681
24	C0025-7	111.28	1.1128	109.58	1.0958	107.85	1.0785	111.49	1.1149	109.05	1.0905	107.45	1.0745
27	D0050-9	110.31	1.1031	112.09	1.1209	107.70	1.0770	111.56	1.1156	106.67	1.0667	108.27	1.0827
5	C0025-2	110.88	1.1088	111.63	1.1163	107.41	1.0741	111.89	1.1189	107.05	1.0705	107.72	1.0772
10	C0025-4	111.53	1.1153	110.56	1.1056	107.91	1.0791	111.36	1.1136	108.09	1.0809	107.21	1.0721
28	D0100-9	111.23	1.1123	110.32	1.1032	108.07	1.0807	111.23	1.1123	108.34	1.0834	107.50	1.0750
29	D0150-9	110.55	1.1055	111.84	1.1184	107.12	1.0712	112.12	1.1212	106.88	1.0688	108.04	1.0804
11	C0050-4	110.66	1.1066	111.62	1.1162	107.79	1.0779	111.41	1.1141	107.14	1.0714	108.01	1.0801
25	C0050-7	110.32	1.1032	112.01	1.1201	107.23	1.0723	111.96	1.1196	106.76	1.0676	108.28	1.0828
26	C0075-7	110.33	1.1033	111.57	1.1157	108.06	1.0806	111.13	1.1113	107.22	1.0722	108.35	1.0835

Table A.5: Samples overview of defect concentrations

sample	Zn_{Sn}				Cu_i			Sn_{Zn}				Cu_{Zn}			
	Fracc.	defects/cm3	error +	error -	Fracc.	defects/cm3	error		defects/cm3	error +	error -	Fracc.	defects/cm3	error +	error -
A0050-1	0.023	6.25E+19	1.44E+19	1.13E+19											
A0100-1															
A0125-1															
A0025-3	0.008	2.172E+19	2.93E+18	3.83E+18											
B0025-5	0.029	7.869E+19	9.57E+18	1.98E+19											
B0050-5	0.029	7.869E+19	9.57E+18	1.98E+19											
A0025-6	0.023	6.243E+19	2.45E+19	4.27E+18											
A0050-6	0.021	5.707E+19	6.69E+18	2.67E+19											
A0075-6	0.02	5.446E+19	5.34E+18	1.91E+19											
A0000-1	0.022	5.968E+19	1.22E+19	7.09E+18	0.01552	4.21007E+19	2.71E+19								
A0000-3	0.022	5.987E+19	2.58E+18	2.35E+19	0.01545	4.20476E+19	2.72E+19								
A0075-3	0.033	8.969E+19	7.2E+18	2.74E+19	0.01498	4.07157E+19	2.72E+19								
B0025-3	0.034	9.247E+19	5.74E+18	2.65E+19	0.02585	7.03068E+19	2.72E+19								
B0050-4	0.015	4.078E+19	9.22E+18	4.49E+18	0.01808	4.91491E+19	2.72E+19								
B0075-4	0.017	4.619E+19	1.39E+19	1.14E+19	0.02221	6.03483E+19	2.72E+19								
B0075-5	0.059	1.605E+20	4.11E+19	2.68E+19	0.0363	9.87298E+19	2.72E+19								
C0025-5	0.038	1.034E+20	5.94E+19	2.73E+16	0.05596	1.523E+20	2.72E+19								
A0100-6	0.039	1.062E+20	3.86E+19	1.69E+19	0.01526	4.15587E+19	2.72E+19								
A0125-6	0.055	1.499E+20	3.43E+19	8.57E+18	0.0103	2.80664E+19	2.72E+19								
S0000-7	0.024	6.51E+19	1.62E+19	1.06E+19	0.03725	1.01045E+20	2.71E+19								
C0025-7	0.046	1.25E+20	2.8E+19	1.55E+19	0.05707	1.55128E+20	2.72E+19								
D0050-9	0.036	9.784E+19	6.79E+18	2.12E+19	0.06388	1.73615E+20	2.72E+19								
C0025-2	0.005	1.36E+19	3.42E+18	1.32E+18	0.02366	6.43327E+19	2.72E+19					0.015	4.08E+19	1.41E+19	1.97E+19
C0025-4	0.01	2.72E+19	3.53E+18	6.96E+18	0.02169	5.90007E+19	2.72E+19					0.003	8.16E+18	4.81E+18	2.61E+18
D0100-9	0.009	2.449E+19	4.08E+18	5.98E+18	0.07679	2.08993E+20	2.72E+19					0.059	1.61E+20	3.41E+19	6.68E+19
D0150-9					0.08544	2.3284E+20	2.73E+19					0.1	2.73E+20	2.4E+19	1.42E+20
C0050-4					0.03809	1.03839E+20	2.73E+19	0.02	5.45E+19	1.36E+19	1.3E+19	0.079	2.15E+20	5.79E+19	1.05E+20
C0050-7					0.01809	4.91111E+19	2.71E+19	0.029	7.87E+19	6.79E+18	1.92E+19	0.075	2.04E+20	4.53E+19	6.56E+19
C0075-7					0.04316	1.17184E+20	2.72E+19	0.048	1.3E+20	5.04E+19	2.81E+19	0.138	3.75E+20	1.46E+20	2.16E+20

sample	VCu				Zn_{Cu}				Cu-Zn disorder defect			
	Fracc.	**defects/cm3**	**error +**	**error -**	**Fracc.**	**defects/cm3**	**error +**	**error -**	**Fracc.**	**defects/cm3**	**error +**	**error -**
A0050-1	0.03	8.15235E+19	5.28541E+19	7.55E+18	0.078	2.11961E+20	1.8E+20	3.89E+19	0.1	2.71745E+20	1.48E+20	4.3E+19
A0100-1	0.1032	2.8092E+20	1.53577E+20	5.75E+19	0.121	3.29373E+20	1.05E+20	8.74E+19	0.05	1.36105E+20	2.94E+19	2.62E+19
A0125-1	0.125	3.40358E+20	9.0369E+19	1.61E+20	0.135	3.67587E+20	1.1E+20	1.52E+20	0.05	1.36143E+20	2.32E+19	4.33E+19
A0025-3	0.011	2.98669E+19	4.91627E+18	1.03E+19	0.028	7.60248E+19	2.01E+19	3.08E+19	0.102	2.76947E+20	5.73E+19	5.91E+19
B0025-5	0.066	1.79089E+20	3.24314E+19	4.67E+19	0.125	3.39183E+20	1.09E+20	1.82E+20	0.1	2.71347E+20	4.95E+19	1.02E+20
B0050-5	0.074	2.00798E+20	1.14705E+20	1.24E+19	0.129	3.5004E+20	2.55E+20	6.42E+19	0.121	3.28332E+20	1.48E+20	5.67E+19
A0025-6					0.05	1.35707E+20	3.9E+19	9.26E+19	0.384	1.04223E+21	2.91E+20	3.72E+20
A0050-6	0.029	7.88115E+19	5.45165E+19	8.74E+18	0.069	1.87517E+20	1.63E+20	4.92E+19	0.1	2.71764E+20	1.42E+20	6.46E+19
A0075-6	0.05	1.36141E+20	6.53897E+19	2.08E+19	0.091	2.47777E+20	2.03E+20	5.04E+19	0.15	4.08423E+20	1.7E+20	5.29E+19
A0000-1					0.031	8.40929E+19	2.43E+19	3.45E+19	0.05	1.35634E+20	2.36E+18	4.69E+19
A0000-3					0.029	7.89243E+19	3.35E+19	3.07E+19	0.2	5.44305E+20	1.83E+20	1.14E+20
A0075-3					0.05	1.359E+20	8.19E+19	6.19E+19	0.25	6.79501E+20	2.94E+20	2.07E+20
B0025-3					0.042	1.14232E+20	2.86E+19	4.97E+19	0.17	4.62366E+20	4.47E+19	1.55E+20
B0050-4					0.011	2.99027E+19	1.22E+19	1.04E+19	0.1	2.71842E+20	2.49E+19	8.94E+19
B0075-4					0.011	2.98888E+19	1.38E+19	1.55E+19	0.189	5.13545E+20	1.81E+20	1.8E+20
B0075-5					0.083	2.25746E+20	9.29E+19	1.26E+20	0.117	3.1822E+20	1.81E+19	1.55E+20
C0025-5					0.02	5.44319E+19	2.9E+19	1.49E+19	0.18	4.89887E+20	2.15E+20	4.61E+19
A0100-6					0.065	1.7702E+20	4.39E+19	1.58E+20	0.28	7.62546E+20	1.84E+20	2.92E+20
A0125-6					0.1	2.72489E+20	4.51E+19	1.81E+20	0.22	5.99476E+20	4.11E+19	2.45E+20
S0000-7					0.012	3.25515E+19	8.49E+18	1.17E+19	0.2	5.42526E+20	2.78E+19	1.82E+20
C0025-7					0.034	9.24188E+19	2.21E+19	3.62E+19	0.1	2.7182E+20	2.03E+19	8.47E+19
D0050-9					0.009	2.44605E+19	9.66E+18	5.35E+18	0.2	5.43567E+20	1.27E+20	8.88E+19
C0025-2									0.15	4.07857E+20	1.15E+20	1.37E+20
C0025-4									0.2	5.44036E+20	2.47E+20	1.39E+20
D0100-9									0.191	5.19829E+20	1.02E+20	1.07E+20
D0150-9									0.08	2.18015E+20	1.87E+19	7.89E+19
C0050-4									0.2	5.4523E+20	5.39E+19	2.32E+20
C0050-7									0.1007	2.73383E+20	5.61E+19	5.78E+19
C0075-7									0.15	4.07267E+20	2.08E+19	2.18E+20

Table A.6: Conferences contributions and publications

Conferences	**authors, title**
4th European Kesterite workshop. Berlin, Germany 2013	L.E. Valle-Rios, G. Gurieva, S. Schorr, Structural characterization of off-stoichiometric Cu2ZnSnSe4 (**poster**)
22nd Annual Conference of the German Crystallographic Society (DGK) Berlin, Germany 2014	L.E. Valle-Rios, Susan Schorr, Chemical and structural characterization of off-stoichiometric Cu2ZnSnSe4 (**poster)**
7th International Conference on Materials Science and Condensed Matter Physics (MSCMO), Chisinau, Moldova 2014	L.E. Valle-Rios, G. Gurieva, S. Schorr, Chemical and structural characterization of off-stoichiometric Cu2ZnSnSe4. (**poster)**
Autumn School on Microstructural Characterization and Modelling of Thin-Film Solar Cells Potsdam 2014	Valle-Rios, Laura-Elisa; Gurieva, Galina; Schorr, Susan: Chemical and structural characterization of off-stoichiometric Cu2ZnSnSe4. (**poster)**
5th European Kesterite Workshop. Tallinn, Estonia, 2014	L.E. Valle-Rios, G. Gurieva, S. Schorr, Chemical and structural characterization of off-stoichiometric Cu2ZnSnSe4 (**poster**)
Sixth Joint BER II and BESSY II User Meeting, Berlin, Germany 2014	L.E. Valle-Rios, K. Neldner, R. Gunder,S. Zander, D.M. Toebbens, S.Schorr, Structural characterization of off-stoichiometric Cu2ZnSnSe4 (CZTSe) from anomalous X-ray diffraction at KMC-2 (BESSY II). (**poster**)
23rd Annual Conference of the German Crystallographic Society (DGK), Göttingen, Germany 2015	L.E. Valle-Rios, D.M. Toebbens, S.Schorr, Chemical and structural characterization of off-stoichiometric Cu2ZnSnSe4. (**poster**)
Materials research society (MRS) - spring meeting, San Francisco, USA 2015	L.E. Valle-Rios, G. Gurieva, D.M. Toebbens, P.Whitfield, S.Schorr, Chemical and structural characterization of off-stoichiometric Cu2ZnSnSe4. (**poster**)
29th European Crystallographic Meeting Rovinj, Croatia (ECM) 2015	Valle-Rios, Laura-Elisa; Gurieva, Galina; Schorr, Susan: Intrinsic point defects formation in off-stoichiometric CZTSe kesterite type compounds. **(poster)**
GeoBerlin 2015 Berlin	Valle-Rios, Laura-Elisa; Gurieva, Galina; Schorr, Susan: Synthesis and structural characterization of off-stoichiometric Cu2ZnSnSe4 **(Talk)**
6th European Kesterite Workshop. Newcastle upon Tyne, UK2015	Valle-Rios, Laura-Elisa; Gurieva, Galina; Schorr, Susan: Intrinsic point defects formation in off-stoichiometric CZTSe kesterite type compounds. (**poster**)
Seventh Joint BER II and BESSY II User Meeting Berlin2015	Valle-Rios, Laura-Elisa; Gurieva, Galina; Franz, Alexandra; Whitfield, Pamela; Többens, Daniel; Schorr, Susan-point defects formation in off-stoichiometric CZTSe kesterite type compounds.(**poster**)
Conference "From the witches cauldrons in material sciences" , Goslar,Germany, 2016	Valle-Rios, Laura-Elisa; Gurieva,Galina; Schorr, Susan:Intrinsic point defects formation in off-stoichiometric CZTSe kesterite type compounds **(poster)**
32nd European Photoltaic Solar Energy conference and Exhibition, Munich, Germany,2016	Th. Dittrich, L.E Valle-Rios, G.Gurieva, S.Kapil, N.Rujismaphan, S.Schorr: Surface Photovoltage Study of Cu1.95Zn1.1Sn0.96Se4 single phase powder (**EUPVSEC contribution published)**
publications	**authors, title**
Journal of Alloys and Compounds 657 (2016), p. 408-413 doi:10.1016/j.jallcom.2015.09.198	Valle Rios, L.E.; Neldner, K.; Gurieva, G.; Schorr, S.: Existence of off-stoichiometric single phase kesterite.
Powder Diffraction, 31, pp 168-175. doi:10.1017/S0885715616000191.	Daniel M. Többens, Rene Gunder, Galina Gurieva, Julien Marquardt, Kai Neldner, Laura E. Valle-Rios, Stefan Zander and Susan Schorr: Quantitative anomalous powder diffraction analysis of cation disorder in kesterite semiconductors

Contributions in the publications

- Journal of Alloys and Compounds 657 (2016), p. 408-413. Valle Rios, L.E.; Neldner, K.; Gurieva, G.; Schorr, S.: "*Existence of off-stoichiometric single phase kesterite*"

Valle Rios L.E contributed with samples synthesis, chemical characteritarion by WDX, diffraction measurements by XRD, Rietved anaylisis of off-stoichiometic CZTSe compounds. Neldner K, has contributed equally with CZTS compounds. Both author has contibuted equiality in data analysis and writing the paper. Gurieva, G. and Schorr, S contributed with disccutions and interpretention of the results.

- Powder Diffraction, 31, pp 168-175. Daniel M. Többens, Rene Gunder, Galina Gurieva, Julien Marquardt, Kai Neldner, Laura E. Valle-Rios, Stefan Zander and Susan Schorr: "*Quantitative anomalous powder diffraction analysis of cation disorder in kesterite semiconductors*".

Rene Gunder, Galina Guerieva, Julien Marquardt, Kai Neldner, Laura E. Valle-Rios, Stefan Zander have contributed in the measurements of kesterite powder samples at KMC-2 beam line of BESSY II at the HZB and with disccutions. Daniel M. Többens has wrote the paper and performed the data analysis and conclusions. Susan Schorr contributed with disccutions and interpretention of the results.

Eidesstattliche Erklärung

Ich erkläre hiermit, dass ich die vorliegende Dissertation selbstständig verfasst und keine anderen als die angegebenen Quellen und Hilfsmittel benutzt habe.

Berlin, den 08.09.2016

Laura Elisa Valle Rios
Matrikelnummer: 4742218

Acknowledgment

First of all, I would like to express my most sincere gratitude to my supervisor Prof. Dr. Susan Schorr who believed in me and guided me during my PhD, this dissertation would not have been possible without her continuous support and nice discussions. Additionally, I am truly thankful to Dr. Galina Gurieva for all her kindly advices and valuable assistance. Together with all my colleagues at HZB and MatSEC graduate school who have been always extremely friendly and supporting, in particular Kai Neldner and Rene Gunder.

Furthermore, I would like to acknowledge all the members of my Institute at the Free University of Berlin, especially to PD Dr. Ralf Milke for reviewing this work and his assistance with the electron microprobe (EMPA).

Diffraction experiments have been crucial for the development of this work, therefore, I really appreciated the help given by Dr. Alexandra Franz during my measurements at the E9-FIREPOD, Dr. Pamela Whitfield from Oak Ridge National Laboratory and Dr. Daniel Többens from KMC-2 beamline at BESSY II. Concerning the temperature dependence resistivity data analysis, I acknowledge Dr. Maxim Guc. Apart from my host institution, I had the great opportunity to visit others intuitions, thus I would like to give a special thanks to: Prof. Susanne Siebentritt at the University of Luxembourg, Prof. Maximo Leon at the Autonomous University of Madrid, Prof. Ernest Arushanov at the Institute of applied Physics Academy of Sciences of Chisinau and to Dr. Jose Maria Delgado from Abengoa-Solar R&D at Seville. Beside them I would like to thank all their wonderful team members, but the list would be unfortunately too long to all be mentioned.

With my heart I acknowledge my dear colleagues from KESTCELLS project from all of whom I learned a lot on every meeting. Especially all the ESR with whom I shared unforgettable moments and developed a friendship that I am sure will last forever.

Last but not least, I thank all my family members, my best friends and to my partner for being so understanding and encourage me every day to be a better person.

This work has been funded by Marie Curie Initial Training Network (ITN)
Seventh Framework Programme (FP7)

KESTCELLS „Training for sustainable low cost PV technologies:
development of kesterite based efficient solar cells“

Project No. FP-PEOPLE-2012-ITN.316488.